Detection of Magnetic Fields and Diffuse Radio Emission in Abell 3667 and other Rich Southern Clusters of Galaxies

Melanie Johnston-Hollitt

Department of Physics & Mathematical Physics
University of Adelaide

A thesis submitted in fulfilment
of the requirements for the degree of
Doctor of Philosophy

July 2003

Statement of Originality

This thesis is the result of work undertaken between 1998 and 2002 in the Astrophysics Group in the Department of Physics and Mathematical Physics at the University of Adelaide and the CSIRO Australia Telescope National Facility.

843 MHz data from the Molonglo Observatory Synthesis Telescope and R-band CCD imaging of A3667 were kindly provided by Dr Dick Hunstead and the Astrophysics Department at the University of Sydney.

20 and 13cm ATCA data for the northwest region of A3667 taken by Röttgering et al. (1997) were obtained from the ATNF archive and re-analysed in conjunction with new data presented here for the southern region.

The *MIRIAD* software package was used for the data reduction and analysis of ATCA data, while programs from the KARMA suite were used for visualisation. The *AIPS* software package was used for the reduction and analysis of VLA data. The 2dfdr software suite was used for the initial reduction of the A3667 spectroscopic data, and I am grateful to the 2dF Galaxy redshift team for allowing the use of their spectral templates.

Radio spectral analysis of the diffuse radio emission in A3667 was performed using the SYNAGE++ package in collaboration with Matteo Murgia of the IRA, Bologna, Italy.

X-ray analysis of the ROSAT PSPC archival observations of A3667 was undertaken using the ESO MIDAS software with the assistance of Federica Govoni of the IRA, Bologna, Italy.

The optical spectra for A3667 were collected by Dr Terry Bridges under the 2dF service observations program for the project *2dF observations of the Abell cluster A3667* for which the investigators were Johnston-Hollitt (PI), Corbett and Hunstead. The target selection and observation files were completed with the assistance of Dr Elizabeth Corbett. Reduction of the final spectra was performed with some assitance from Dr Elizabeth Corbett and the work was significantly enhanced by the guidance of Dr Dick Hunstead.

VLA observations of the source 0917+75 are from the ongoing observational program *High Resolution Observations of the Relic 0917+75*, by Johnston-Hollitt (PI) and Clarke. Data reduction was performed with the assistance of Dr Tracy Clarke.

The interpolated Galactic RM maps are generated using MATLAB. Coding of the maps was performed in collaboration with Christopher Hollitt and the work owes a great deal to thoughtful discussions with both Christopher Hollitt and Prof. Ron Ekers.

With the above exceptions, this thesis contains no material which has been presented for another degree at this or any other university and, to the best of my knowledge and belief, contains no copy or paraphrase of work published by another person, except where duly acknowledged in the text.

I give consent to this copy of my thesis, when deposited in the University Library, being available for loan and photocopying.

Melanie Johnston-Hollitt
July 2003

Acknowledgements

When I look back across my candidature I realise that I have been extremely privileged to have worked with such a large group of excellent researchers. I am profoundly grateful to have been given the opportunity to pursue my dream of studying at least a small part of this mysterious Universe. I have a great many people to thank for assisting me in this endeavour.

Throughout the course of my thesis I have been lucky to have such a diverse selection of advisors from whom to seek guidance. My principal supervisor Prof. Ron Ekers provided the initial concept for the project and though the thesis took a fairly crooked path from the original intent to its final destination, Ron was throughout the entire process, a source of guidance, inspiration and fantastic amounts of information. Though I often found myself "thrown in the deep end", on the few times I forgot how to swim Ron did not let me drown. I feel enormously fortunate to have worked with Ron as I have learnt far more about what it is to be an astrophysicist than is simply contained in this thesis.

The assistance of my co-supervisor Dr Dick Hunstead was in many ways complementary to that of Ron. I was continually amazed by the enthusiasm that Dick displayed for both this and other projects. Dick's assistance with the optical analysis in this project has been invaluable and though I complained at the time, his ever-ready green pen for correcting and proof-reading abstracts, posters, papers and this thesis has been a tremendous service.

My university supervisor Dr Roger Clay gave great support as a referee for many funding applications, provided funding for travel in Australia and was a critical reader of the manuscript. Also through Roger I gained a great deal of invaluable high level teaching experience.

I am greatly indebted to my many collaborators for both their assistance and professionalism toward all work, be it for this thesis or otherwise. In particular I wish to thank Dr Tracy Clarke, Dr Elizabeth Corbett, Dr Chris Fluke, Dr Neil Killeen, Dr Matteo Murgia, Dr Haida Liang, Dr Mark Wieringa, Dr Bruce Dawson, Jose Bellido, Prof. Jim Rose, Dr Wayne Christiansen and Matt Fleenor.

There are many people at the ATNF who not only made my work easier but who

made me want to be doing it. I thank; Dr Dave Rayner for all his assistance with the vagaries of *MIRIAD* and for providing a balanced perspective on the HWWS 98 committee; Dr Bob Sault for providing insight to mosaicing and polarimetry; Dr Neil "read the manual" Killeen for answering stupid questions about *MIRIAD* imaging and rotation measures; Elaine Pacey for always making I sure I got to see Ron, for help with all matters administrative and for keeping everything in Ron's office running basically smoothly! There was many a time Elaine tried to steer me away from Tim Tams for lunch, a course doomed to failure, but I appreciated the effort anyway - at least I was convinced to wear my shoes with the laces tied!! I thank Ms. Helen Sim for all the media related assistance, for her ever fascinating conversations on all topics from Australian science policy to the particular perspective in the works of Jan Van Eck, but most of all her friendship. Thanks are also extended to Dr Lister Staveley-Smith, Dr Jessica Chapman, Dr Tasso Tzioumis, Dr Tony Wong, Dr Roopesh Ojha, Dr Mike Kesteven, Anne Barends, and Betty Siegman (like Elaine, gone but not forgotten).

Staying in the Marsfield Lodge was a great pleasure due to the very funky Vicki Drazenovic and Elsa - the place has never been so nice!!

On my many trips to the ATCA at Narrabri I was always pleased to have the assistance of the wonderful team of unsung heroes who kept the telescope running and made visitors feel welcome. In particular the tireless work of Robin Wark ensuring that both duty astronomers and new observers are provided with all the relevant information and then arriving at 2:00 am in the middle of a thunder storm "just to make sure", must be acknowledged. (I am especially grateful that Robin never put the hideous photo of me as a vac student up on the photo wall!). I thank Dr Dave McConnell and Robin for their patience during the times I had to call in the middle of the night or early morning to get advice on fixing all manner of antenna problems - it was a great learning experience! For endless trips to the airport and assistance with all matters administrative I thank Jo Houldsworth, Kylee Forbes, Anni Reynolds and her predecessor Tina Earl.

No thesis in astrophysics is ever completed without the help of various "computer gurus" so I would like to extend my profound thanks to several people both at Adelaide and in Sydney. At ATNF I am indebted to Dr Shaun "the legend" Amy for always having a cheerful solution to even the most obscure computer matter, Dr Richard Gooch for all his assistance with the Karma package and in particular, for putting the three map overlay into Kview, Malte Marquarding for trying to teach me AIPS++ and helping with image overlaying, Andrew Wright for coding the RM database search pages, and Vince McIntyre and Henrietta May for always finding me disk space at very short notice! At Adelaide I am profoundly grateful for the help of Dr Ken Simpson and Ian Borchardt who stopped me beating my head against the department's machines a number of times by providing ingenious ways of getting around the bizarre computer setup at Adelaide.

Though I did not frequent my offices much either in Adelaide or Sydney, I am grateful

to my office mates, Hayley Bignall, Tracy Getts and Daniel Mitchell for not being too surprised when I did show up, for not stealing my desks and generally being good company. Additionally, I would like to thank Hayley for doing my remote observations while I was overseas.

I thank Bob Hurn at Adelaide for periodically letting me take over his office, computer, printer, scanner and telephone when there was nowhere else for me to work.

During the course of my thesis, I have been privileged to be able to travel extensively not just between the University of Adelaide and the ATNF but also to overseas institutions on five separate occasions. During each of these international journeys there have been many people and organisations who have contributed to the success of these visits. I would like to take this opportunity to offer thanks to the people and organisations which made each journey possible.

In 1999 I visited institutions and attended meetings in Canada, the USA, Northern Ireland and Poland. I am grateful to the following organisations for providing funding for this endeavour: The Department of Physics and Mathematical Physics of University of Adelaide, the Graduate Centre of the University of Adelaide, the University of Illinois, the Polish Academy of Science, the Astronomical Society of Australia and the South Australian branch of the Australian Institute of Physics. I would further thank the following individuals for their hospitality and support during this trip: Dr Jacques Vallée for his hospitality during my visit to the HIA in Victoria, British Columbia; Dr Andrew Gray, Dr Tom Landecker and the staff at the DRAO for making my trip to Penticton a pleasant one, in particular I thank Dr Sean Dougherty for bringing my lost camera all the way back to Australia!! During my stay at the University of Toronto I am grateful to Prof. Phil Kronberg, Dr Torsten Enßlin and Tracy Clarke for their enlightening discussions on magnetic fields and diffuse radio emission. I am particularly grateful for the provision of office space and the use of the Astronomy Department's poster printing facilities. I thank the staff of the Armagh Observatory for their generous support of my visit both scientifically and financially. I thank the organisers of the meeting *Plasma Turbulence and Energetic Particles in Astrophysics*, in particular Dr Michal Ostrowski for arranging funding for my attendance through the Polish Academy of Science and Dr Michal Urbanik for meeting me at the Krakow train station when I thought I was hopelessly lost!

For travel in 2000 I am indebted to the International Astronomical Union for provision of a Young Scientist Travel Grant to attend the IAU General Assembly in Manchester. Further funding to visit the Istituto di Radioastronomia, in Bologna was provided under the CSIRO-CNR scientific exchange scheme. Whilst in Bologna I am grateful for interactions both scientifically and socially with Dr Luigina Feretti, Dr Gabriele Giovannini, Prof. Roberto Fanti and Dr Carla Fanti, Dr Gianfranco Brunetti, Dr Tiziana Venturi, Dr Paula Parma, Federica Govoni and Matteo Murgia. I am further indebted to Dr Luigina Feretti for helping to organise my visit, teaching me much about image

analysis in *AIPS* and sharing her views on diffuse radio emission. I would like to particularly thank Federica Govoni for her assistance with X-ray reductions, the fantastic trip to Venice, the visit to the telescope at Medicina and her seemingly boundless generosity. I further thank the organisers of the Oxford workshop *Fields and Particles in Radio Galaxies*, in particular Dr Katherine Blundell for arranging an excellent meeting.

Travel in 2001 to the VLA was supported by the Australian Government through the Access to Major Facilities Scheme. My visit to the University of California Berkeley was supported partially by the ATNF and the generosity of Prof. Ron and Jay Ekers, who graciously allowed me to stay with them for a month while writing part of this thesis. During my visits to the AOC in Socorro, I was pleased to stay in the "Chateau de Havoc" and I thank Havoc and Dr Tracy Clarke for their hospitality. I would also like to thank Tracy for showing me the sights of Socorro, teaching me the correct way to climb in and out of a VLA dish, and her enlightening discussions on the comparative dangers of the Northern and Southern Hemisphere's deadly creatures. My stay at the AOC was a great learning experience and I would like to thank the NRAO staff for making me feel welcome and, in particular, the postdocs for making it fun!! I thank Prof. Leo Blitz and the staff of the RAL at the University of California, Berkeley for providing me with access to an office and amenities that made the writing of a large section this thesis possible. Whilst in Boston, I thank Lisa Kewley and Reuben Durham for their hospitality. For my trip to JHU I am grateful to Prof. Colin Norman.

My travel in June 2002 to the VLA was supported by a Don R. Stranks Travelling Fellowship and funding from the Department of Physics and Mathematical Physics at the University of Adelaide. My visit to the University of North Carolina at Chapel Hill was partly funded by Prof. Jim Rose. Whilst in Socorro, I again thank Dr Tracy Clarke and the staff of the AOC for their hospitality. In North Carolina I thank Prof. Jim Rose, Dr Wayne Christiansen and Matt Fleenor for showing me amazing Southern hospitality.

Travel to Maastricht in August 2002 was funded by the National Radio Sciences Committee of the Australian Academy of Science and the Faculty of Sciences at Adelaide University. While my attendance at the URSI general Assembly was funded by an URSI Young Scientist Award. The URSI meeting would not have been the same without Aaron P. Chippendale and Steve Tingay my fellow inmates from the URSI ghetto, Mitch who saved me from the fate of dirty hair with stolen hotel shampoo and Naomi McClure-Griffiths.

To my ATNF friends: Hayley "I'm up for anything" Bignall, Aaron "chicken Monday" Chippendale, Naomi F. U. McClure-Griffiths, Malte Marquarding, Tracy "Galaxy Girl" Getts, D.J. Pisano, Erwin de Blok, Daniel Mitchell, Erik Muller, Lucyna "Illusion" Kedziora-Chudczer - Thanks, it was fun.

I would like to thank my sister Sonya, for proof reading this manuscript, even though she did not really understand it!

Finally and most importantly, I would like to thank my husband Chris Hollitt - he knows what for.

The Australia Telescope Compact Array is part of the Australia Telescope which is funded by the Commonwealth of Australia for operation as a National Facility managed by CSIRO. The Molonglo Observatory Synthesis Telescope is operated with the support of the Australian Research Council and the Science Foundation for Physics within the University of Sydney. The Two Degree Field spectrographic system is part of the Anglo-Australian Telescope, operated by the Anglo-Australian Observatory. The Very Large Array is part of the National Radio Astronomy Observatory a facility of the National Science Foundation operated under cooperative agreement by Associated Universities, Inc. This research has made use of the NASA/IPAC Extragalactic Database (NED) which is operated by the Jet Propulsion Laboratory, California Institute of Technology, under contract with the National Aeronautics and Space Administration. The Digitized Sky Surveys were produced at the Space Telescope Science Institute under U.S. Government grant NAG W-2166. The images of these surveys are based on photographic data obtained using the Oschin Schmidt Telescope on Palomar Mountain and the UK Schmidt Telescope. The plates were processed into the present compressed digital form with the permission of these institutions.

The presentation of this thesis was made possible through the use of LaTeX 2ε.

List of Publications

Some of the material in this thesis has been presented in the following publications:

- **Are Violent Cluster Mergers a Possible Source of Cosmic Rays – Observational Evidence from A3667**, Johnston-Hollitt, M., Clay, R. W., & Ekers, R. D., 1999, in *Plasma Turbulence and Energetic Particles in Astrophysics*, Proceedings of the International Conference, Cracow (Poland), 5–10 September 1999, Eds: Ostrowski, M., and Schlickeiser, R., Obserwatorium Astronomiczne, Uniwersytet Jagiellonski, Krakow 1999, p. 292-295.

- **The Dual Radio Relics of A3667**, Johnston-Hollitt, M., Clay, R., Ekers, R. D. , Wieringa, M. H., & Hunstead R. W., 2002, in *The Universe at Low Radio Frequencies*, Proceedings of the IAU Symposium 199, Pune (India), November 1999, Eds: Rao, A. P., Swarup, G. and Gopal-Krishna, ASPconf Series, p157.

- **The Cluster Environment in A3667**, Johnston-Hollitt, M., Ekers, R. D., & Hunstead, R. W., 2001, in *Particles and Fields in Radio Galaxies*, Proceedings of the 2000 Oxford Workshop held August 2000, Oxford (UK), Eds: Laing, R., and Blundell, K., ASPconf Series, p432.

- **An Estimated All-Sky Rotation Measure Map**, Johnston-Hollitt, M., Hollitt, C. P., & Ekers, R. D., 2002, in Proceedings of the URSI General Assembly held 17–24 August 2002, Maastricht (The Netherlands) p2172.pdf. (Published on compact Disk)

The following publications are the result of work conducted in collaborative projects during my Ph.D. candidature, but not presented in this thesis:

- **Multifrequency Observations of PKS 2255-282**, Tornikoski, M., Tingay, S. J., Muecke, A., Chen, A., Connaughton, V., Jauncey, D. L., Johnston-Hollitt, M., Kemp, J., King, E. A., McGee, P., Rantakyro, F., Rayner, D., Reimer, O., & Tzioumis, A. K., 1999, AJ, 118, 1161.

- **SUGAR data and the Origin of the Highest Energy Cosmic Rays**, Clay, R. W., Dawson, B. R., Kewley, L., & Johnston-Hollitt, M., 2000, PASA, 17, 207.

- **Southern Hemisphere Observations of a 10^{18} eV Cosmic Ray Source Near the Direction of the Galactic Centre**, Bellido, J. A., Clay, R. W., Dawson, B. R., & Johnston-Hollitt, M., 2001, Astropart. Phys., 15, 167.

- **Multiple Merging Events in the Double Cluster A3128/A3125**, Rose, J. A., Gaba, A. E., Christiansen, W. A., Davis, D. S., Caldwell, N., Hunstead, R. W., & Johnston-Hollitt, M., 2002, AJ, 123 1216.

Abstract

This thesis investigates the properties of magnetic fields in galaxy clusters via both statistical Faraday rotation measures and diffuse source polarimetry, and investigates the nature and generation mechanisms for diffuse radio emission in the ACO cluster A3667. Chapter one gives an introduction to galaxy clusters and discusses both their history and emission processes. Chapter two provides a detailed discussion of the instruments used during the course of this research. Chapter three presents the results of a statistical study into cluster magnetic fields via Faraday rotation measurements (RMs). The results agree well with previous findings and support cluster fields of 1–2 μG. Chapter four presents an interpolated all-sky rotation measure map generated to allow for more accurate modelling of the Galactic contribution to calculated rotation measures. Large scale features in the RM sky are discussed and good agreement is found between these results and previously observed magnetic field directions in the spiral arms. These data do not suggest a field reversal in the outer spiral arm. Chapter five gives an analysis of multifrequency radio observations of the ACO cluster A3667, presenting a detailed investigation into the diffuse emission in the cluster. Major results presented include the discovery of filamentary structure with a power-law spectral index and high polarisation. Generation mechanisms for this emission are discussed in light of these results. Chapter six presents analysis of redshift data for objects in A3667 down to a magnitude of $m_B = 18.3$. The previously reported secondary subgroup in the north of the cluster is less obvious and no subgroup structures are evident in the velocity data. This suggests that if a merger is present in A3667 it must be entirely within the plane of the sky. Chapter seven presents the conclusions and future directions.

Contents

List of Tables

List of Figures

Chapter 1

Introduction

In my youth I regarded the Universe as an open book, printed in the language of physical equations, whereas now it appears to me as a text written in invisible ink, of which in our rare moments of grace we are able to decipher a small fragment

Arthur Koestler, 1980

1.1 Magnetic Fields: an Introduction

Magnetic fields are assumed to be pervasive throughout the universe on all scales, from the fields surrounding planets right up to fields in the intracluster and intergalactic media. In recent years the role of magnetic fields in both galactic and extragalactic regimes has gained increased attention across many astrophysical disciplines. For example, the magnetic field is a key factor in studies of large-scale structure formation, galaxy and star formation, and cosmic ray generation. Cosmic magnetic fields, on all scales, have been studied since the late seventies with varying degrees of success. While it is clear that magnetic field research has progressed considerably in this time, the mostly indirect measurement techniques have meant that it has been difficult to address many basic issues. Questions as to how strong magnetic fields are, how uniform they are, what the seeding and amplification mechanisms are, and, most importantly, what their contribution is to the energy density of the intergalactic medium, remain topics of animated debate.

1.2 Measurement of Magnetic Fields

There are several methods of estimating magnetic fields from polarised emission. These include optical, radio, and even infrared polarisation techniques (Sofue et al. 1986; Beck 1986; Heiles 1986). The three most commonly used are optical scattering, Zeeman splitting and Faraday rotation, which will be discussed herein. It should be noted that measurements made via these processes are all indirect, requiring additional information or observations in order to accurately assess the magnitude of the magnetic fields.

Optical Polarisation

Observations show that the percentage polarisation of optical starlight is proportional to the distance the light has travelled through the Galactic plane and is strongly correlated with extinction by dust. Elongated dust grains suspended in a magnetic medium will act as magnetic dipoles, aligning preferentially with their minor axes parallel to the magnetic field. As the grain size is of the order of the wavelength of optical radiation, aerosol scattering of background light passing through the dust will give rise to partial polarisation of the transmitted light. This scattering will be most significant for light which has its electric vector parallel to the major axis of the dust grains. Therefore, the transmitted light is most likely to be that which is polarised parallel to the minor axis of the dust, i.e., with the polarisation in the same direction as the magnetic field.

In order to use this technique to accurately calculate the magnetic field strength, a detailed model of the dust alignment mechanism is required. Such a model must take into account both the column density and composition of the dust. Such models have been used with some success to infer the magnetic field magnitude and direction in the plane of the galaxy from the amount of scattering and linear polarisation of the transmitted light. Obviously this technique will only work in regions were dust is present and as dust is also a major contributor to extinction, this technique is limited mainly to Galactic observations.

Zeeman Splitting

The Zeeman effect can be simply described as the splitting of atomic or molecular spectral lines by the action of a magnetic field. The effect was first observed as a broadening of the yellow sodium doublet lines in an experiment conducted by Zeeman in 1896 (Zeeman 1897). Subsequently, Lorentz used classical theory to explain the phenomenon as a shift in the gyrofrequency of electrons due to the application of a magnetic field perpendicular to the plane of rotation about the nucleus. As electrons would be rotating in both clockwise or anti-clockwise directions with respect to the magnetic field, this would result in both a negative and positive frequency shift accounting for the broadening of the lines about the central frequency. Later, when quantum theory was introduced, Zeeman splitting was reinterpreted by Heisenberg and Pascual as a difference in the energy state due to coupling of the magnetic field and the electron spin state.

The effect is to produce emission of two circularly polarised components of opposite handedness, each frequency shifted (one positively and one negatively) with respect to the original line frequency. Depending on the magnetic field direction with respect to the observer's sightline, either both circular components are visible or both circular components and the original line will be observed. For an arbitary orientation, elliptical polarisation will be observed.

The Zeeman effect provides the most direct measure of magnetic field strength, but its difficulties of detection limit its use to Galactic objects.

Faraday Rotation

Faraday rotation is similar to Zeeman splitting in that it is a process where the application of an external magnetic field will, in certain circumstances, produce a measurable change to an electromagnetic wave. In the case of Faraday rotation, incident polarised electromagnetic radiation passing through a magnetised plasma will have its plane of polarisation rotated by an amount determined by the properties of the plasma and the magnetic field strength. The amount of rotation experienced is strongly dependent on the frequency of the radiation. Comparisons of the amount of rotation at different frequencies produces a metric known as the rotation measure or RM. Rotation measures along the line of sight from a background object, such as a distant radio galaxy or quasar, are used as probes of the foreground magnetic fields through which the radiation has passed. If the properties of the plasma are known (electron density and path length) it is possible to use the RM to compute an averaged field strength along that line of sight. As Faraday rotation is of principal importance to this thesis, a detailed explanation is given in chapter 3.

Although Faraday rotation is not a direct measure of magnetic field strength, it can easily be used to probe the fields of distant objects, unlike optical polarimetry and Zeeman splitting. This ability to detect the presence of distant magnetic fields makes it of great value in examining fields in clusters of galaxies.

1.3 Magnetic Fields in Galaxies: An Historical Perspective

The first substantiated discovery of polarised emission from a Galactic source was made by Meyer (1919) who measured polarised optical light from the reflection nebula NGC2261. Following this discovery, many Galactic sources were discovered to have significant polarised emission in the optical band. However, it was not until 1942, that polarised emission was found in a source external to the Milky Way (Öhman 1942). Öhman is also credited by inference with the discovery of the first magnetic fields in the external galaxy, M31. Following this, several similar studies confirmed optical polarisation of nearby galaxies (Heeschen 1973; Bingham et al.1976; Scarrott et al. 1977). These optical measurements were interpreted as evidence of coherent large scale magnetic fields in the arms of spiral galaxies (Elvius 1978).

Progress in the field was slow and it was not until the advent of radio telescopes and observations of radio synchrotron emission that research into astrophysical magnetic fields really began to flourish.

The use of Zeeman splitting of the 21cm (radio frequency) line of neutral Hydrogen (HI) as a probe of magnetic field strengths was first proposed by Bolton & Wild (1957). However, the detection is observationally difficult; in the case of HI the splitting is only 2.8 MHz per gauss of magnetic field. Since the Galactic magnetic field strengths are typically on the order of tens of microgauss (μG) the frequency shift for HI is around 10 Hz either side of the 1420 MHz line. This 10 Hz shift is much less than the width of

the HI absorption line so it cannot be examined directly. Rather, as the effect results in two oppositely handed circularly polarised components, the technique is to observe a strong absorption line and look for circular polarisations of opposite handedness at the edges (Longair 1981).

Early attempts to find Zeeman splitting due to Galactic magnetic fields were unsuccessful (Galt et al. 1960; Weinreb 1962) or marginal (Davies 1964; Schwarz & Lasenby 1990). This gave an upper limit on Galactic field strengths of 10 μG (Galt et al. 1960). It was not until the early 1980's and 1990's that confirmed detections for Zeeman splitting due to the Galactic field were made. Initially, OH lines were found to exhibit the splitting (Crutcher & Kazes 1983) and then later HI measurements were made (Plante et al. 1994). Magnetic fields of up to 10 μG have been estimated from Zeeman splitting in HI, while fields of up to 100 μG have been determined from a few OH absorption lines. It is thought that these results are indicative only of the fields within the HI and OH clouds and not a good measure of the intragalactic field strength.

However, although Zeeman splitting was difficult to observe, synchrotron polarisation in the radio continuum was found in great abundance. Galactic radio polarisation at 408 MHz was discovered simultaneously in 1962 by Westerhout et al. and Wielebinski et al. Subsequent radio surveys (Berkhuijsen & Brouw 1963; Wielebinski & Shakeshaft 1962) continued to examine the Galactic field via the polarisation position angles measured at 408 MHz, while surveys at new radio wavelengths were also initiated (Berkhuijsen et al. 1964).

In the late 70's Rainer Beck began a program to map magnetic fields in spiral galaxies via radio polarimetry using the Effelsberg 100m dish and the Westerbork Radio Synthesis Telescope (WRST), and later the VLA. His work and that of others, concurred with the optical results from a decade earlier in finding coherent large scale magnetic fields in spiral galaxies (Beck et al. 1978) (See Figure 1.1 and 1.2). Through this research Beck and collaborators demonstrated that in some cases the magnetic field follows the spiral arms (Beck et al. 1980; Beck 1981; Krause et al. 1984; Beck et al. 1985b) while in others it did not and the field appeared to be turbulent (Klein et al. 1983). They also found that the degree of field uniformity seemed to correlate with the total optical luminosity (Beck & Reich 1985a). Later, as more galaxies were examined, these discrepancies were interpreted as differences in field structure of three main types; axisymmetric, bisymmetric or ringed fields (Beck 1986).

In the 80's numerous studies of extragalactic rotation measures produced via Faraday rotation were also conducted (Simard-Normandin et al. 1981; Broten et al. 1988; Vallée et al. 1986; MacLeod et al. 1988). These observations were used to investigate the nature of magnetic fields both within our own and other spiral galaxies (Vallée et al. 1986) and to determine characteristics of the Galactic field along the line of sight. However, the difficulty of the observations resulted in a lack of suitable data making this process difficult. In contrast to other spiral galaxies, the average magnetic field in the Milky Way was found to be weak and turbulent (Beck & Reich 1985a). Later in the 80's and early 90's the extragalactic RM values were combined with pulsar dispersion measure values in an attempt to disentangle the internal magnetic field structure of the Milky Way (Lyne & Smith 1989; Han & Qiao 1994; Han et al. 1997; Manchester

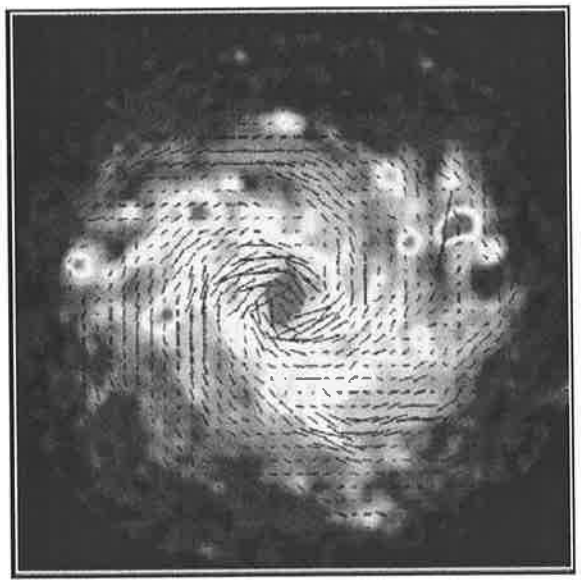

Figure 1.1: Radio image of the spiral galaxy NGC694, produced by Rainer Beck. The pseudocolour shows combined data from the VLA and Effelsberg at 6cm and the vectors indicate the direction of the magnetic field which clearly follows the spiral arms.

et al. 1998; Han et al. 1999a).

Beck and collaborators also made use of large scale Faraday rotation mapping of nearby galaxies in order to further elucidate their magnetic field structures and theories about how such fields are formed (Beck 1986; Sofue et al. 1986; Gräve & Beck 1987; Loiseau et al. 1987; Beck et al. 1997; Beck et al. 1989; Beck et al. 1990; Horellou et al. 1990). With such a wealth of material on magnetic structures in nearby galaxies, statistically based interpretation could be performed. It was concluded that the large-scale magnetic field structure in spiral galaxies was either axisymmetric or bisymmetric, that the fields run roughly parallel to the optical arms with the uniform field component strongest in the interarm regions and a turbulent field present in the spiral arms (Beck 1991a). Observational work has continued with galaxy fields now interpreted in terms of these standard models (Buczilowski et al. 1991; Neininger et al. 1991; Beck 1991b; Horellou et al. 1990; Neininger et al. 1993; Beck et al. 1994; Ehle et al. 1996; Han et al. 1999a; Chyzy et al. 2000). Further discussion of the current state of understanding of magnetic fields in galaxies can be found in Beck et al. (1996).

1.4 Clusters of Galaxies

The discovery that astronomical objects are not isotropically distributed on the sky arose in the late nineteenth century when detailed and systematic cataloguing of the heavens from photographic plates began. However, at this time it was not known that the preference for stars and "nebulae" to "clump" suggested anything more than

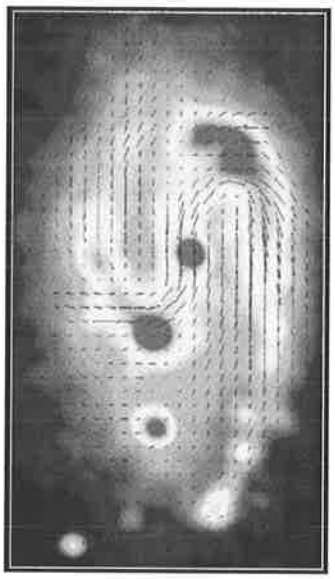

Figure 1.2: Radio image of the barred spiral galaxy NGC3627, produced by Soida et al. The pseudocolour shows combined data from the VLA and Effelsberg at 3.5cm and the vectors indicate the direction of the magnetic field which clearly follows the spiral arms.

coincidence. It was not until the pioneering work of Henrietta Leavitt in 1912 that showed that Cepheid variable stars could be used as an astronomical yardstick that astronomers obtained clues to the distance scales of the Universe. Using Leavitt's period-luminosity relation for Cepheid variables, in 1923 Edwin Hubble was able to calculate the distance to the Andromeda nebula proving for the first time that this object was indeed beyond and apart from the Milky Way - it was the first confirmed external galaxy. After the discovery that the sky was filled with galaxies it did not take long for the notion of clustering to arise. It was shown using the new redshift measure that not only did galaxies appear to clump in the same part of the sky but those galaxies clumping together were all at the same distance. Thus, the concept that galaxies coalesce into gravitationally bound systems was born.

The early to mid-twentieth century saw several major clustering studies undertaken (Shapley & Ames 1932; Abell 1958; Zwicky et al. 1968). These early surveys catalogued cluster positions, richness and other optical properties. However, despite the optical properties of clustering having been well established, it was not until the 1960s that the diffuse thermal and relativistic plasma components of galaxy clusters were discovered.

The '60s saw the beginning of X-ray observations, with early balloon-borne instruments later giving way to satellites. It was during this time that the first X-ray emissions from galaxy clusters were detected and interpreted (Felten et al. 1966; Friedman & Byram 1967). In the early '70s the UHURU Satellite detected extended emission from several clusters, including Virgo, Coma and Perseus (Kellogg et al. 1971; Gursky et al. 1971; Forman et al. 1972). These observations were initially not thought to be associated with the cluster itself, but rather assumed to be the blending of cluster

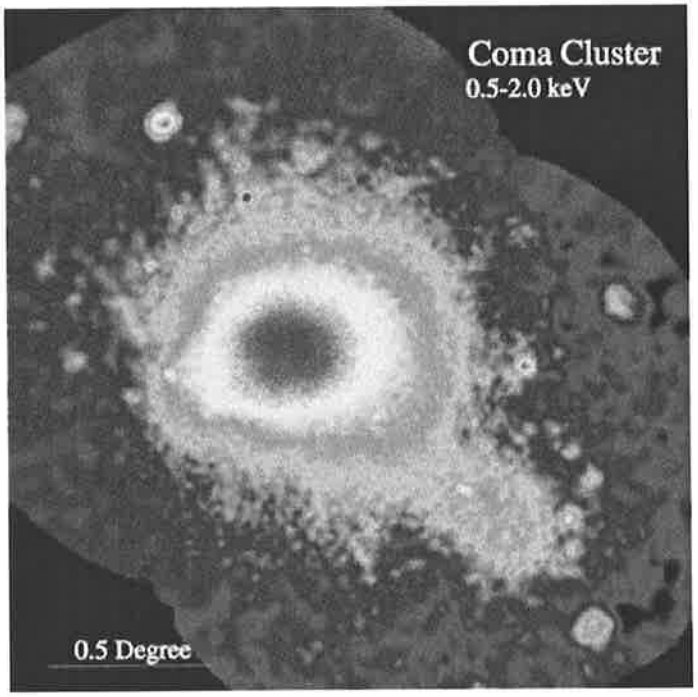

Figure 1.3: ROSAT X-ray image of the Coma cluster.

point sources (Kellogg et al. 1971). However, the Uhuru catalogue quickly revealed the correlation between rich clusters of galaxies and bright X-ray sources (Gursky et al. 1972).

Following this discovery, the field expanded rapidly with a large number of studies on X-ray properties of clusters being conducted in the late '70s and early '80s. It was found that galaxy clusters are the most commonly observed bright sources of extended X-ray emission. X-ray spectral analyses from UHURU and subsequent satellite missions revealed that the emission is mainly via bremsstrahlung of the thermal intracluster gas. This gas component was found to have temperatures between $10^7 - 10^8$ K (Malina et al. 1978) and have densities of $10^{-2} - 10^{-4}$ cm^{-3}. As the X-ray emission traces the cluster's gravitational potential, the surface brightness distribution can provide some information about the physical state of clusters (Jones & Forman 1992 in Clarke 2000). One such example of "clumpiness" in the X-ray surface distribution is shown in Figure 1.3 which shows a ROSAT image of the Coma cluster, clearly indicating substructure. Since most of the X-ray emission in clusters is due to thermal bremsstrahlung, the surface brightness distribution provides information on the plasma density distribution in the cluster, which in turn gives information about the cluster's dynamical history. Smooth X-ray profiles, often seen with strongly peaked central regions indicative of a "cooling-flow" (Fabian et al. 1981), are assumed to reflect relaxed, non-interacting clusters, while more disturbed X-ray emission is usually interpreted as evidence of interaction or mergers between clusters. The extreme difference in X-ray surface brightness between co-called cooling and non-cooling flow clusters is illustrated in Figure 1.4. Clusters with disturbed or clumpy X-ray emission do not exhibit the

sharp central peak and it is assumed that a merger event has disrupted the cooling flow. However, the very existence of cooling flows and consequently these interpretations, are still being debated.

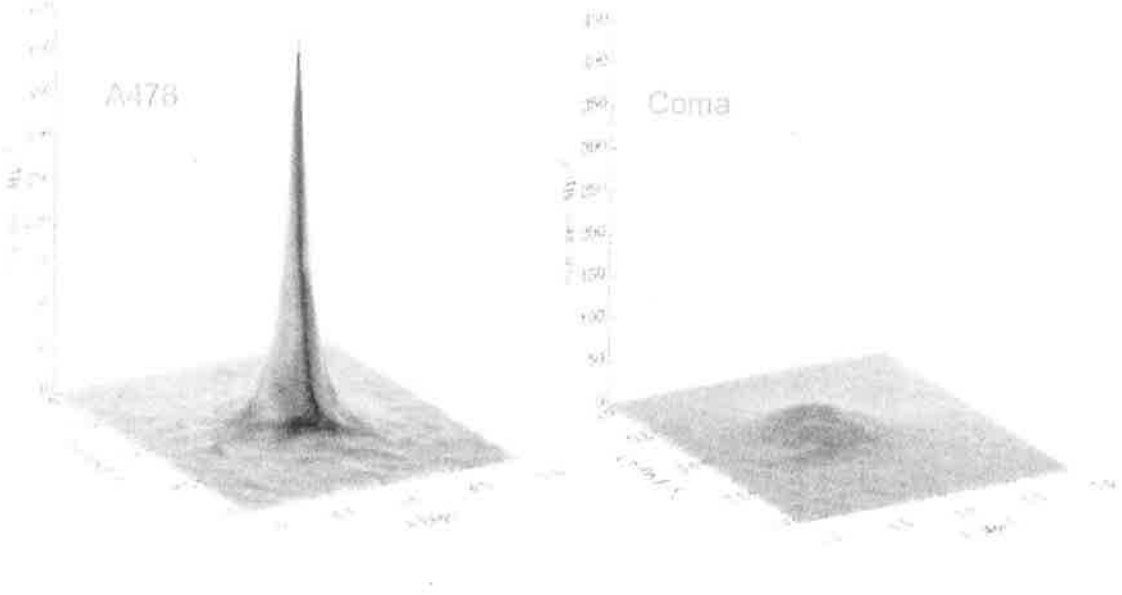

Figure 1.4: Examples of cooling and non-cooling flow clusters. These clusters have similar X-ray luminosities and have been scaled to appear as if both are at the same redshift. Abell 478, which is considered a "cooling flow" cluster exhibits a central surface brightness of over an order of magnitude more than that of the Coma cluster (Allen 1999).

Radio observations reveal the presence of both radio galaxies embedded within the cluster and, less frequently, regions of diffuse synchrotron emission. Radio sources located in the central regions of galaxy clusters often show very distorted morphologies and pairs of long extended "tails" trailing out from the optical host galaxy. It has been argued that these "head-tail" galaxies are indicative of turbulence within the hot plasma that fills the cluster potential well.

Diffuse radio emission, while not associated with any particular optical sources, has a long-standing statistical association with the position of rich galaxy clusters and is therefore assumed to be a cluster related phenomenon. Characteristics of such emission fall into two classes; *halos* a term first coined by Gavazzi (1978) and the unfortunately named, *relics*. Although both classes of diffuse emission are believed to be generated via synchrotron emission and have low surface brightnesses and steep spectral indices, they differ strongly in position within the cluster, morphology and polarisation characteristics. Halos are centrally located with roughly circular morphologies, typically about 500 kpc in diameter, and exhibit low fractional polarisation of typically less than 10% (Feretti & Giovannini 1996). The so-called relics are located on the clus-

ter periphery, exhibit very high fractional polarisations of around 40 - 60% and have very irregular morphologies in a range of sizes from tens of kpc (Slee et al. 2001) up to the order of a Mpc (Röttgering et al. 1997). The irregularity of this emission was the driving argument for the initial assumption that such objects were the remnant synchrotron lobes of now dormant radio galaxies, hence the name relic. However, for the larger diffuse emission regions there are strongly compelling arguments against this theory (Röttgering et al. 1997), which will be discussed in detail in chapter 5.

Galaxy clusters have been observed to contain only a halo (Coma; Bozyan,1968) only a relic (A1367; Gavazzi,1978) or both a relic and a halo (A2256; Bridle & Fomalont, 1976).

1.4.1 Emission Mechanisms in Clusters of Galaxies

Clusters are observed both through their constituent galaxies and via energetic processes in the plasma that fills their centre, usually termed the intracluster medium (ICM). Although emission mechanisms in individual galaxies produce radiation which spans the entire spectrum, the ICM emits only via a few specialised processes. These processes will be outlined in the proceeding sections.

Synchrotron Emission

The most prevalent form of astronomical emission in the radio regime is generated via the process of synchrotron emission, which results from charged particles (usually electrons) spiralling in magnetic fields. In galaxy clusters this is found in individual cluster members and in regions of diffuse radio emission (Wilson 1970).

In the presence of a uniform magnetic field, a high-energy charged particle will move in a spiral path with constant pitch angle, θ. It will have constant velocity, $\mathbf{v}$, in the direction of the magnetic field, $\mathbf{B}$, and will gyrate about the field lines at the gyrofrequency, ν_g. In the non-relativistic case the gyrofrequency can be described by

$$\nu_g = \frac{eB}{2\pi c m_e} \tag{1.1}$$

where e is the charge, B the magnetic field strength, m_e the mass and c is the speed of light. For relativistic particles the gyrofrequency is described by

$$\nu_g = \frac{eB}{2\pi\gamma m_0} \tag{1.2}$$

where m_0 is the rest mass of the electron and γ is the Lorentz factor, $\gamma = (1-v^2/c^2)^{-\frac{1}{2}}$.

The vectorial trajectory of these particles can be seen to have two distinct components, one describing the circular motion about the magnetic field lines and the other describing the forward motion. These components may be described by

$$\frac{d}{dt}(\gamma m_e \mathbf{v}) = \frac{e}{c}\mathbf{v} \times \mathbf{B} \tag{1.3}$$

$$\frac{d}{dt}(\gamma m_e c^2) = e\mathbf{v}\cdot\mathbf{E} = 0 \tag{1.4}$$

where $\mathbf{v}$ is the vector describing the particle's velocity and $\mathbf{E}$ and $\mathbf{B}$ are the electric and magnetic field vectors respectively. In combination these components will produce a helical path centred about the field line. Fig 1.5 shows this helical trajectory about a given field line.

The particle is being accelerated due to its circular motion and will thus emit photons. The emitted radiation is beamed in the direction of motion of the particle within a cone described by a half-angle of $\phi = \frac{1}{\gamma}$. The radiation is Doppler-shifted and is thus observed at frequencies much higher than the gyrofrequency of the particle in its orbit, such that

$$\nu \approx \frac{3}{2}\gamma^2 \nu_g \sin\theta \tag{1.5}$$

where θ is the pitch angle. The complete derivation can be found in Longair (1997).

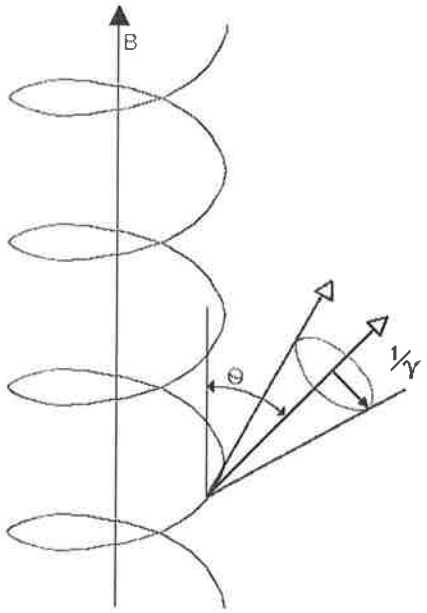

Figure 1.5: The trajectory of a relativistic electron spiralling in a magnetic field, $\mathbf{B}$ with pitch angle, θ. The resultant synchrotron emission will be emitted in a highly beamed cone the width of which is found to be $\frac{1}{\gamma}$.

The energy of the emitted photons will be distributed among the harmonics of the gyration frequency. The total radiation loss rate can be described by

$$-\left(\frac{dE}{dt}\right) = \frac{e^4 B^2}{6\pi\epsilon_0 c m_e^2}\frac{v^2}{c^2}\gamma^2 \sin^2\theta \tag{1.6}$$

where ϵ_0 is the permittivity of free space.

If we remember that $c = (\mu_0\epsilon_0)^{-1}$, the previous equation can be rearranged so as to express it in terms of the Thomson cross-section, σ_T, and the energy density in the magnetic field, U_{mag}, such that

$$-\left(\frac{dE}{dt}\right) = 2\sigma_T c U_{mag}\left(\frac{v}{c}\right)^2 \gamma^2 \sin^2\theta \tag{1.7}$$

where $U_{mag} = B^2/2\mu_0$.

In the ultra-relativistic limit $v \to c$ this can be approximated to

$$-\left(\frac{dE}{dt}\right) = 2\sigma_T c U_{mag}\gamma^2 \sin^2\theta \tag{1.8}$$

Returning to equation 1.7: If we now consider an ensemble of particles with an isotropic distribution of pitch angles, and average over that distribution, such that $p(\theta)d\theta = \frac{1}{2}\sin\theta \mathrm{d}\theta$, the average energy loss rate of the ensemble can be obtained:

$$\left\langle -\left(\frac{dE}{dt}\right)\right\rangle = 2\sigma_T c U_{mag}\left(\frac{v}{c}\right)^2 \gamma^2 \frac{1}{2}\int_0^\pi \sin^3\theta d\theta \tag{1.9}$$

$$= \frac{4}{3}\sigma_T c U_{mag}\left(\frac{v}{c}\right)^2 \gamma^2 \tag{1.10}$$

Equation 1.9 expresses the average energy loss of an ensemble of particles of average energy E, that are randomly scattered through many pitch angles during their lifetime. The energy is distributed among the harmonics of the gyrofrequency. For an ultra-relativistic population these harmonics are so closely spaced that the energy distribution becomes continuous.

For a power-law distribution of electron energies $N(E)dE = \kappa E^{-x}dE$ and an isotropic distribution of pitch angles, the synchrotron emissivity can be approximated (Longair 1981) to

$$j(\nu) = \frac{2\sigma_T c}{3\mu_0(m_e c^2)^{x-1}}\kappa B^{\frac{(x-1)}{2}}\nu^{\frac{-(x-1)}{2}} \tag{1.11}$$

where κ is a constant and x is the power law index of the electron energy spectrum. The flux density of synchrotron emission at a certain frequency, S_ν, is found to be proportional to that frequency to some power such that $S_\nu \propto \nu^\alpha$, where the value α is termed the spectral index of the synchrotron radiation. The value of x can be related to the spectral index, α, by $\alpha = -(x-1)/2$.

For an isotropic distribution of electrons following a power-law spectrum it can be further shown that fractional linear polarisation is given by

$$p_l = \frac{x+1}{x+\frac{7}{3}}\frac{B_o^2}{B_o^2 + B_t^2} \tag{1.12}$$

where B_o and B_t are the ordered and turbulent magnetic field components. It follows that if the magnetic field is uniform then equation 1.12 becomes

$$p_l = \frac{x+1}{x+\frac{7}{3}} \tag{1.13}$$

The observed spectrum of high-energy cosmic rays provides information on the likely values of x. Currently the observed cosmic ray flux between 10^{15} and 10^{18} eV is well described by a power law spectrum with $x \approx 2.6$. Using this value the maximum fractional linear polarisation achievable from a purely uniform magnetic field is roughly 73%. However, it should be noted that in this energy regime this cosmic ray population is likely to be of Galactic origin. As the acceleration processes in the Milky Way are likely to be different to those in other objects, such as radio-loud galaxies, this spectrum may not be useful in evaluating the maximum linear polarisation achievable in extragalactic sources. The origin of ultra-high-energy cosmic rays (10^{18} to 10^{22} eV) is thought to be entirely extragalactic and would be a more appropriate indicator of the achievable linear polarisation. However, this energy spectrum is currently difficult to assess due to the low number of events. In the future, new instruments such as the Fly's Eye (Baltrusaitis et al. 1985) and Pierre Auger Array (Boratav 2001) should improve our understanding of this high-energy spectrum, which may lead to a revision of the maximum linear polarisation possible.

Thermal Bremsstrahlung

Bremsstrahlung or "braking radiation" is the process which results in the emission of photons from one charged particle accelerating in the field of another. Bremsstrahlung may occur in both high-energy relativistic and non-relativistic particle populations as well as ionised thermal gases. The most common situation is thermal bremsstrahlung, which occurs in a fully ionised gas with a Maxwellian distribution of electron energies. Photons are emitted as the electrons collide with nuclei due to their random thermal motions. In a simple descriptive sense, each collision event can be regarded as producing a photon, and the energy of the photon corresponds approximately to the change in energy suffered during the collision. As the velocity distribution of the electron population is Maxwellian for some average temperature, the resultant photon spectrum will provide information on this average temperature.

In addition to the temperature, T, the details of the thermal bremsstrahlung spectrum depend on a number of factors, including the density of electrons, n_e, the density of ions, n_i and the ion charge, Z. To provide a full explanation of thermal bremsstrahlung would require a detailed quantum mechanical treatment which is beyond the scope of this thesis. Below is the relevant equation for the spectrum from Rybicki & Lightman (1979):

$$\epsilon_\nu = \frac{2^5 \pi e^6}{3 m_e c^3} \left(\frac{2\pi}{3 k m_e} \right)^{\frac{1}{2}} Z^2 n_e n_i T^{-\frac{1}{2}} e^{-\frac{h\nu}{kT}} G_{(\nu,T)} \tag{1.14}$$

where ϵ_ν is the emissivity of thermal bremsstrahlung, e is the electron charge, m_e is the electron mass, k is Boltzmann's constant, h is Planck's constant, ν is the frequency

and $G_{(\nu,T)}$ is the Gaunt factor - a slowly varying factor which accounts for the quantum mechanical nature of the process.

We now know that thermal bremsstrahlung generates most of the observed X-ray emission in galaxy clusters. This effect was first noted in the early '70s when it was believed that the observed soft X-ray excess seen in rich galaxy clusters was either due to thermal bremsstrahlung (Gorenstein et al. 1973) or inverse Compton scattering (Harris & Romanishin 1974). At the time it was not possible to use the observed X-ray spectrum to decide which of the competing models was correct. Using what were, at the time, plausible assumptions about the physical condition in the ICM (including magnetic field strengths), it was argued that the observed power-law spectrum in the X-ray could be generated either by bremsstrahlung from a nonuniform plasma or by inverse Compton scattering from a non-uniform ensemble of relativistic particles in a turbulent magnetic field (Bridle & Fomalont 1976). The literature from the '70s is filled with papers arguing the virtues of one model versus the other and it was not until quite late in the decade that the debate was resolved in favour of bremsstrahlung as the dominant mechanism. The discovery of iron lines in the X-ray emission spectra from Coma, Virgo and Perseus (Serlemitsos et al. 1977) was the key point in favour of a thermal origin for at least the bulk of the emission. These features were consistent with cosmic level iron abundances in the ICM and could be explained easily by a simple hot plasma model.

Since the hot cluster gas is bound in the gravitational potential well, observations of cluster X-ray emission not only give information on the gas temperature but also provide insight into the cluster's physical extent. This, in turn, gives clues to the dynamical history of the cluster.

Inverse Compton Scattering

Under certain conditions relativistic electrons may lose energy when interacting with photons. In this case, the photon is scattered off the electron with a higher energy obtained from the electron. This process is known as Inverse Compton Scattering (IC).

Longair (1981) gives the inverse Compton loss rate as

$$\frac{dE}{dt} = \frac{4}{3}\sigma_T c U_{rad} \gamma^2 \tag{1.15}$$

where σ_T is the Thomson cross-section, c is the speed of light, U_{rad} is the radiation energy density and γ is the Lorentz factor.

If we consider that the radiation field is isotropic and monochromatic with frequency, ν_0, then the average frequency of the scattered radiation, $\overline{\nu}$ is

$$\overline{\nu} = \frac{4}{3}\gamma^2 \nu_0 \tag{1.16}$$

and the spectral emissivity, $I(\nu)d\nu$, is given by

$$I(\nu)d\nu = \frac{3\sigma_T c}{16\gamma^4}\frac{N(\nu_0)}{\nu_0^2}\nu\left[2\nu\ln\left(\frac{\nu}{4\gamma^2\nu_0}\right)+\nu+4\gamma^2\nu_0-\frac{\nu^2}{2\gamma^2\nu_0}\right]d\nu \qquad (1.17)$$

where $N(\nu_0)$ is the photon number density. At low frequencies, $\nu \ll \gamma^2\nu_0$ which means that the square bracketed term, in equation 1.17 goes to a constant value and it can be seen that the scattered radiation has a spectrum proportional to the frequency.

The first suggestions that Inverse Compton scattering can occur in *tenuous regions of space* was originally put forward by Felten & Morrison (1966). This concept was extended to galaxy clusters in the early '70s, where cosmic ray electrons scattering off photons from the ubiquitous cosmic microwave background radiation were put forward as an explanation for the observed soft X-ray excess (Harris & Romanishin 1974). Using typical parameters for cosmic ray electrons ($\gamma = 1000$) and the energy density associated with the microwave background, $U_{rad} = 0.25\text{eV cm}^{-3}$ it can be seen that IC scattering gives rise to X-ray photons of order 0.4 keV (Longair 1981).

Early attempts to reconcile the observed soft X-ray emission with IC scattering soon demonstrated the critical nature of the magnetic field in these calculations. In clusters which possessed diffuse radio emission it had been suggested that X-ray and radio emissions were related via IC scattering (Harris & Romanishin, 1974; Hanisch, 1980). In this case, if the X-ray was derived from IC scattering then

$$L_{IC} = L_{sync}16.75\frac{U_c}{B_{perp}} \qquad (1.18)$$

where L_{IC} and L_{synch} are the X-ray and radio luminosities respectively derived from IC scattering and synchrotron emission, U_c is the energy density in the cosmic microwave background (CMB) and B_{perp} is the magnetic field perpendicular to the line of sight.

Using the radio halo luminosity and an equipartition magnetic field for the Coma cluster of 0.2 μG, Hanisch (1980) demonstrated that this predicts an X-ray luminosity an order of magnitude lower than observed. If there is X-ray scattering off the synchrotron photons in the halo then equation 1.18 still holds but now U_c becomes the energy density of the radio photons. In this case, the predicted X-ray emission is 5 times lower than that observed. The cluster magnetic field value is critical to this argument and even though the validity of using an equipartition magnetic field is questionable, the field would have to be 100 times stronger in order to account for all of the X-ray emission by this mechanism. This is a very convincing argument that even if IC scattering is present, bremsstrahlung must be the dominant emission mechanism.

Recently, a far ultra-violet excess has been observed toward several clusters, this has been attributed to scattering of very low energy cosmic rays ($\gamma = 300$) (Sarazin & Lieu, 1998; Sarazin , 1999). However, the IC model for this emission is still under debate (Bowyer & Berghöfer, 1998; Durret et al., 2002).

Cluster Magnetic Fields

The presence of magnetic fields in galaxy clusters is revealed by both statistical Faraday rotation studies and the presence of diffuse synchrotron emission associated with the

ICM.

As mentioned above, diffuse radio emission is believed to be generated via synchrotron emission. We know therefore that at least in the clusters where such emission is observed there must be an intracluster magnetic field.

Faraday rotation studies to detect magnetic field in clusters have been undertaken since the late 70s. Work began with Dennison (1979) and has continued through to the study, contemporaneous to this one, performed by Clarke (2000). As magnetic fields in galaxy clusters are central to this thesis a detailed discussion of their history may be found in chapters 3 and 5, which discuss Faraday rotation measure studies and diffuse radio emission regions results respectively.

1.5 Notation and Conventions

Standard conventions are used throughout to describe polarisation. Specifically the IAU (1974) adoption of the IEEE (1969) convention for describing circular polarisation is used, wherein a **Right-Handed (clockwise) Polarised Wave** is defined as an elliptically polarised electromagnetic wave in which the rotation of the electric field vector with time is clockwise for a stationary observer looking in the direction of the wave normal. Thus, for an observer looking from the point of view of a receiver pointed toward the apparent source, the direction of rotation will be reversed.

Standard conventions are used throughout to describe the rotation of the polarisation position vector of an electromagnetic wave undergoing **Faraday Rotation**. A positive rotation measure corresponds to a clockwise rotation of the polarisation position vector as seen when the magnetic field is directed towards the observer.

The **spectral index**, α, in this thesis follows the $S_\nu \propto \nu^{+\alpha}$ convention.

Throughout this thesis $\imath$ is used to denote $\sqrt{-1}$, H_o =75 km s^{-1} Mpc^{-1} and $q_o = 0.5$ and an Einstein-de Sitter cosmology is assumed.

The **projected separation between two points on the sky** is estimated by:

$$D = \frac{0.58\theta c(1 - \frac{1}{\sqrt{1+z}})}{H_0(1+z)} \tag{1.19}$$

where θ is the angular separation between the points in arc-minutes, z is the redshift, c is the speed of light in kms^{-1} and D is given in kpc.

The **luminosity distance to an object** is given by:

$$D_{lum} = \frac{2c}{H_0}(1+z)\left[1 - \frac{1}{\sqrt{1+z}}\right] \tag{1.20}$$

Unless otherwise stated all co-ordinates are given using the J2000 **equinox.**

1.6 Summary

This chapter outlines the history of research into galaxy clusters and discusses the emission mechanisms at work with in the cluster environment.

Chapter 2

Instrumentation and Analysis Techniques

2.1 Introduction

During the course of this investigation several different instruments and instrumental techniques were employed. The main observations for this study were taken with radio telescopes. However, observational data were also obtained optically and archival material at many wavelengths was also used.

Most of the observational data were obtained with the Australia Telescope Compact Array (ATCA) located in Narrabri, New South Wales, in three separate observing projects. Data were also collected using the the Two Degree Field (2dF) spectrographic system on the Anglo-Australian Telescope, in Coonabarabran, NSW and a small amount was obtained from the Very Large Array (VLA) in Socorro, New Mexico. To supplement these results, archival radio data from the Molonglo Observatory Synthesis Telescope and X-ray data from the ROSAT satellite were also utilised.

Due to the physical nature of clusters, being large in angular extent with diffuse low surface brightness radio features, it was necessary to adopt observing techniques that allowed large fields of view to be covered with high surface brightness sensitivity. As spectral characteristics and polarimetry were a key part of this study, additional effort was also placed into obtaining matched resolutions and full polarisation calibration solutions. This chapter will outline the instrumentation and analysis techniques employed in this study.

2.2 The Australia Telescope Compact Array

The Australia Telescope Compact Array is a six-element aperture synthesis radio telescope located near the town of Narrabri in northern New South Wales, Australia. Along with the Parkes 64m single dish and the Mopra millimetre antenna near Coonabarabran, it forms part of the *Australia Telescope*. Construction of the ATCA was undertaken as part of the Australia Telescope project, which commenced in 1983 with

funding from the Australian Federal Government as a Bicentennial Project. The ATCA was officially opened on 2 September 1988. The ATCA is operated as a National Facility by the CSIRO - Australia Telescope National Facility (ATNF). Time on the telescope is allocated via peer review with currently a 60/40 percent split between Australian and overseas proposals.

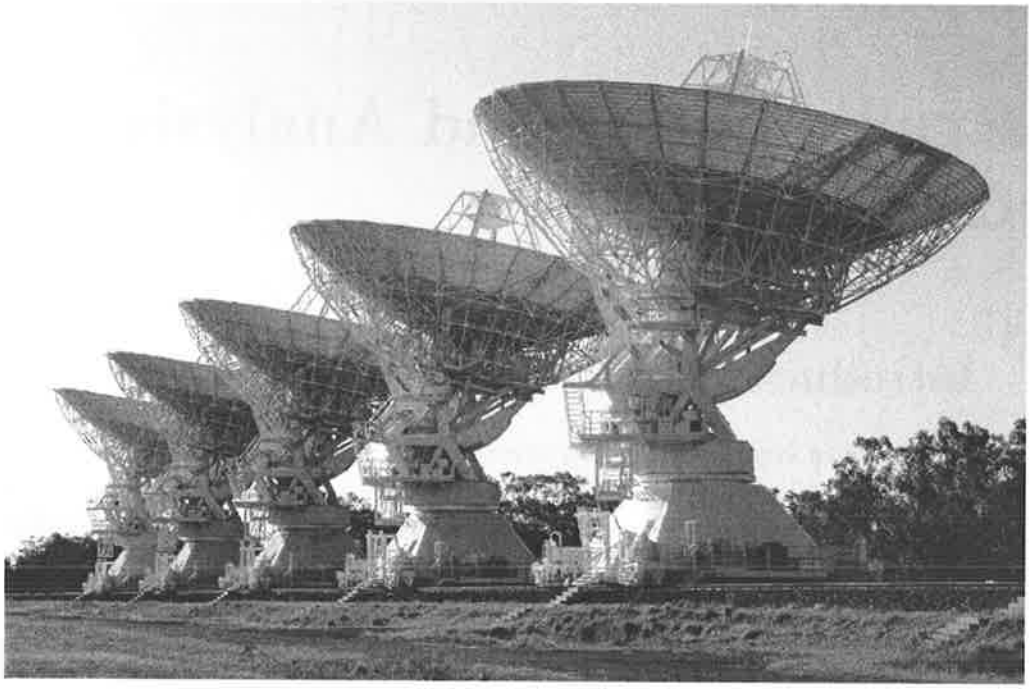

Figure 2.1: Five of the six antennas of the ATCA, Narrabri, New South Wales. Photo courtesy of S. Amy.

2.2.1 ATCA Design Aspects

The ATCA consists of six 22 m altitude-azimuth (alt-az) Cassegrain-focus antennas. For the observations in this thesis the ATCA had only East-West baselines with antennas spaced over a 6 km range (Frater & Brooks 1992). Five of the antennas are located on a 3 km track containing 35 optical-fibre-linked antenna base stations, while the remaining sixth antenna is located a further 3 km away giving a maximum baseline of 6 km.

The base stations are arranged on the track in non-redundant spacing configurations. Moving the antennas to various stations allows the observer to match the spatial frequency coverage to the requirements of the observing program. The ATCA has a number of antenna location configurations that allow observers to target radio data at different resolutions, for example the compact '375m' configuration, which has baselines ranging from 32 to 375 m will probe structures up to an angular size of 21 arcminutes at 20cm, whereas the '6D' configuration, with maximum baseline length of 6km when

used at the highest frequency of 3cm will be sensitive to structures of angular size one arcsecond.

Each antenna is equipped with two wideband corrugated feedhorns located on a rotating turret. When a frequency band is selected, the turret turns, ensuring that the appropriate feed is always at the focus of the dish. The rotating turret system has a major advantage over other receiver-changing systems, in that polarisation calibrations can be reliably performed over almost the entire primary beam, allowing greater flexibly when measuring polarised emission off-axis.

Each feedhorn contains a pair of orthogonal-linear probes with associated front-end electronics that allows two independent frequencies and two polarisation channels to be recorded simultaneously. In the current configuration, the ATCA can record both 20cm (1.25 - 1.78 GHz) and 13cm (2.20 - 2.50 GHz) bands simultaneously with up to a 128 MHz bandwidth divided into 32 spectral channels in each. Alternatively, the 6cm (4.40 - 6.70 GHz) and 3cm (8.00 - 9.20 GHz) bands may be observed simultaneously, again with up to 128 MHz bandwidth of 32 spectral channels at each frequency. It is also possible to record at two locations in one 'band' simultaneously, for example at both ends of the 6cm band, at say (4.500 – 4.628 GHz) and (6.500 – 6.628 GHz).

Since the completion of observations for this thesis, the ATCA was upgraded to a 2-dimensional array via the addition of a short North-South track extension called the "NS-spur". The primary purpose of this upgrade is to allow new observations at millimetre wavelengths. Receivers and feedhorns for the mm system were undergoing trials on three of the six antennas during preparation of this document.

2.3 ATCA Observing Techniques

Though the ATCA has only a small number of antennas, its wideband correlator gives the instrument a continuum sensitivity comparable with existing arrays such as the VLA and WSRT which have many more dishes. This feature, combined with the flexibility of the correlator and the fast drive times, provide the ATCA with some powerful and unique observing modes. Several different observing modes were crucial for aquisition of the data presented in this study. The following sections detail the observational techniques applied during this work.

2.3.1 Continuum Observations

Although the number of baselines of the ATCA is small (${}^6C_2 = 15$), and the instantaneous (u, v)-coverage is only one-dimensional due to the array's East-West orientation, it is possible, through a combination of earth-rotation synthesis and the wide continuum observing bandwidth, to recover both the (u, v)-coverage and the improved sensitivity of a larger number of dishes in a 2-dimensional array.

2.3.2 Multifrequency Synthesis

In its so-called *continuum mode* the correlator on the ATCA uses a minimum of 32 frequency channels, of which 16 are independent, across its 128 MHz bandwidth. In this way visibility data from each channel can be correctly gridded in the spatial frequency domain at its correct location in wavelengths. This process, known as "multifrequency" or "bandwidth" synthesis, is most effective in the lowest frequency band where the fractional bandwidth of each channel is greatest. It has a distinct advantage over simply averaging all visibilities into a single channel (as in the 50 MHz VLA band) which results in a much reduced effective field of view due to "bandwidth smearing".

Bandwidth smearing results when a point source which is offset from the observation's phase centre is observed in a configuration which averages all data into a single channel. The source will appear smeared in a radial direction from the phase centre. Bandwidth smearing causes a decreased amplitude for the source due to a number of spatial frequencies being represented by only a single point in the (u, v)-plane. An approximate calculation for the limit on the acceptable field of view for a given band, $\Delta\nu$ is

$$\frac{\Delta\nu}{\nu_c} \gg \frac{\theta_{res}}{\theta} \tag{2.1}$$

where ν_c is the centre of the observing band, θ_{res} is the instrumental resolution, i.e., the synthesised beam, and θ is the furthest distance from the phase centre before significant smearing occurs.

Since the VLA has a bandwidth of 50 MHz, which is 12.5 times greater than that of the ATCA's 4MHz channels, then the effective field of view of the VLA will be 12.5 times smaller than the ATCA if using the same observing frequency and resolution.

At 20cm wavelength on the ATCA, the ratio, A, of observed amplitude to true amplitude in a 4 MHz channel is given by:

$$A = 1 - \frac{\theta b}{130}$$

where θ is the distance from the phase centre in arcmin and b is the baseline length in km. For sources close to the phase centre and observations at the higher frequencies where the fractional bandwidth is relatively small the effect of bandwidth smearing is negligible. Using a 6 km array at 20cm you would require 32 channels across a 128 MHz band in order to recover the full field of view.

A further advantage of using 32 separate channels over a single 128 MHz band is that narrow-band radio frequency interference (RFI) can be removed from the individual channels it is affecting rather than rendering the entire band useless.

The ATCA is therefore able to correctly recover some of the sensitivity lost due to the small number of antennas.

2.3.3 Earth-Rotation Synthesis

The ATCA as an East-West array has only 1D instantaneous (u, v)-coverage and can thus only observe a 1D projection of the baseline distribution on the (u, v)-plane. In order to overcome this, sources are usually observed for a period of 12 hours, which corresponds to one half of a revolution of the earth. This produces a set of concentric ellipses in the (u, v)-plane which trace the baseline projections as the hour angle changes. The ellipticity of the coverage is a function of the source declination. In a 12 hour synthesis, the projected baseline distribution will move across half the (u, v)-plane and symmetry arguments allow the entire ellipse to be determined.

However, it is often not necessary to observe a particular source for 12 hours in order to detect a particular source. Thus, a large number of sources may be interleaved in any given 12 hour period by observing for several short intervals of say two minutes. This observing mode stems from the properties of earth-rotation synthesis and will be discussed in the next section.

2.3.4 Short Observations

As noted in the previous section, to detect a source, it is often not necessary to have a full 12 hour synthesis. However, as the instantaneous (u, v)-coverage is only 1-dimensional it is not possible to obtain a good image from a single short observation or "cut". On the other hand, if several such short "cuts" are taken at well separated hour angles over the range $-90° < \mathrm{HA} < +90°$, then the source may be imaged effectively. By interleaving a number of sources together in an observing period one can image a large number of bright point sources in a single 12 hour run. This is a good technique for observing a large number of small angular size sources quickly. This is particularly advantageous when looking at large numbers of sources contained in several different clusters of galaxies that are distributed across the sky (as long as slew times between sources are kept to a minimum). Further details on the application of this technique to the ATCA can be found in Burgess & Hunstead (1995).

2.3.5 Mosaicing

In conventional aperture synthesis observations, the size of the primary beam will place a limit on the angular extent of the objects that may be observed. In studies of clusters, particularly those at low redshift, this has previously been a significant barrier to imaging the entire cluster region. However, with the advent of radio mosaicing (Ekers & Rots 1979) it has become possible to image very large regions of the sky by combining separate pointings into a single image.

Since the inception of this concept, the word "mosaic" has taken on two distinct meanings in astronomical contexts. In the simplest case, a "mosaic" is a large image formed from the combination of smaller individual sub-images, usually by butting together the individual images. It is possible however, to form a radio mosaic by combining the data from all points in the (u, v)-plane before deconvolution (Cornwell 1988)

to produce a superior radio map. This process is often called "Non-Linear Mosaicing" after the non-linear algorithms required to process the data (Cornwell & Braun 1989). It is this second form of radio non-linear mosaicing, hereafter simply called mosaicing, which is discussed below.

Consider an interferometric pair of antennas of size D, with projected baseline d. In the (u, v)-plane such an antenna pair will measure the integral of all spacings from d − D to d + D. In a conventional single pointing, the information in this range of spacing has been combined into a single point in the (u, v)-plane. Through mosaicing it can be recovered for the range of spacings d − D to d + D (Sault et al. 1996). This gives an effective increase in the (u, v)-coverage through the finer sampling and hence larger angular size sources are correctly imaged. In the case of the ATCA, which has D = 22 metres, the shortest available baseline, d, is 31m, this means all information down to a (u, v)-distance of 9m can be recovered, greatly reducing the need for additional single dish data.

Mosaicing has three main advantages over conventional radio imaging. The first, and most obvious, is the increased viewing area which allows structures of larger angular extent than the primary beam to be completely imaged. Secondly, mosaicing allows for more accurate spectral indices and line profiles to be calculated and finally provides an improved and more uniform signal-to-noise ratio across the entire field. This third point makes mosaicing a far more powerful technique than simply abutting individual images together. The improvement in signal-to-noise arises as adjacent pointings are not independent in the (u, v)-domain and therefore when combined they will produce a fundamentally better image. In the case of diffuse, low surface brightness emission in clusters of galaxies the improvement in signal-to-noise is particularly useful.

It has been shown that a Nyquist sampling in the plane of the sky gives sufficient information to recover the full range of spatial frequencies (Cornwell 1989). Originally it was common practice to adopt a rectangular pointing grid pattern for mosaic images, which gives a Nyquist rate of $\frac{\lambda}{2d}$, where d is the angular distance between pointing centres. However, it was soon discovered that a hexagonal pointing grid pattern, which has a Nyquist rate of $\frac{\lambda}{\sqrt{3}d}$ gives better solid angle coverage.

Two methods are advocated for the exact way in which data should be combined. These methods, which both fall under the category of "joint deconvolution" are either to mosaic the dataset together using a linear algorithm (Linear Mosaic) and then deconvolve the entire dataset simultaneously (Sault et al. 1996; Staveley-Smith et al. 1997) or to apply a non-linear deconvolution algorithm during the mosaic process (Cornwell 1988). Both processes have been shown to recover almost exactly the same information (Sault et al. 1996).

2.3.6 Polarisation Mosaicing

The rotation turret system on the ATCA enables the production of accurate Stokes Q and U images (see section 2.4.1 for definition of Stokes parameters) away from the pointing centre of the observation. This makes the ATCA operationally well equipped to obtain mosaiced images in both total intensity and polarisation.

The on-axis instrumental polarisation is typically below 2-3%. After calibrating for instrumental polarisation errors, this can be reduced to around 0.1%. The off-axis polarisation error increases roughly as the square of the distance from the pointing centre at least up to the half-power point. At 20, 13, 6 and 3 cm, the instrumental polarisation is about 1.6%, 9%, 1.6% and 3% of the apparent total intensity at the half-power point, respectively (The Australia Telescope Compact Array Users' Guide 1999). Figure 2.2 shows the ATCA's instantaneous linearly polarised response as a function of source position within the primary beam for the centre of the 20cm and 13cm frequency bands (The Australia Telescope Compact Array Users' Guide 1999).

Since the ATCA antennas have an alt-az mount, the off-axis response varies with parallactic angle, and will be smeared out by a factor of a few by a long synthesis. This smearing is a function of declination. The *MIRIAD* task OFFPOL can be used to simulate off-axis polarimetric response of a long synthesis observation. Mosaicing can smear out the off-axis response still further, in some cases by as much as an order of magnitude. Though the off-axis polarisation response is not normally considered an issue in mosaiced images, it is possible to account for its variation by either employing a different spatial weighting function or observing with super-Nyquist sampling.

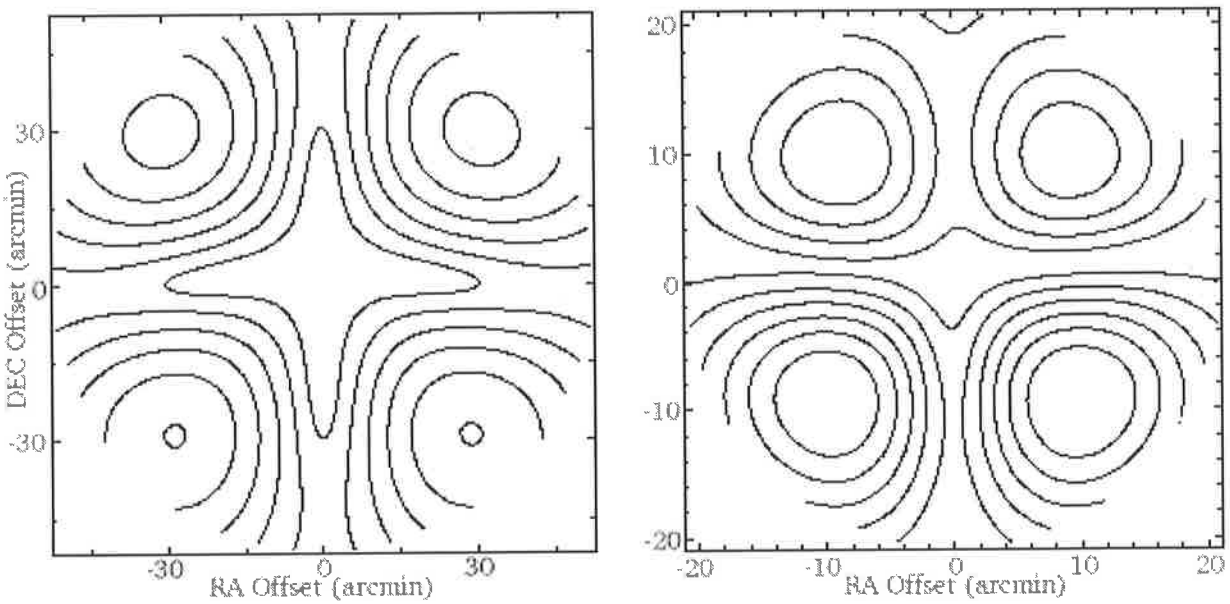

Figure 2.2: The ATCA instantaneous linearly polarised response as a function of source position within the primary beam. The contours are the linearly polarised response to an unpolarised point source with a true (not apparent) flux of 1 unit. Left panel: 20 cm response, with contours at increments of 0.001, shown out to the half power beam width of 35 arcminutes; Right panel: 13 cm response, with contours at increments of 0.01, shown out to the half power beam width of 20 arcminutes (The Australia Telescope Compact Array Users' Guide 1999).

2.4 Interferometric Polarisation with the ATCA

The basic principles behind radio interferometry rely on the relationship between the *spatial coherence function*, C_ν and the radio brightness distribution, B_ν of the source being imaged. The *spatial coherence function* is more commonly termed the "visibilities" or "antenna correlation functions". This relationship may be described mathematically after the formalism of Clark (1999):

$$C_\nu(\mathbf{r}_1, \mathbf{r}_2) = \int B_\nu(\mathbf{s}) e^{-2\pi\imath\nu\mathbf{s}\cdot(\mathbf{r}_1,\mathbf{r}_2)/c} d\Omega \tag{2.2}$$

where the *spatial coherence function* is measured between the points $\mathbf{r}_1$ and $\mathbf{r}_2$ and the integral performed across the entire sky for some frequency, ν. Here, the brightness distribution, B_ν is given in power per area per solid angle per frequency, more commonly termed *flux density* and given the units of Jansky, where $1\text{Jy} = 10^{-26}\ \text{Wm}^{-2}\text{Hz}^{-1}$.

To obtain B_ν one must first measure the spatial coherence function, C_ν. C_ν can be expressed as the expectation value of the product of the electric radiation field as measured at $\mathbf{r}_1$ and $\mathbf{r}_2$, such that:

$$C_\nu(\mathbf{r}_1, \mathbf{r}_2) = \langle E_\nu(\mathbf{r}_1) E^*_\nu(\mathbf{r}_2) \rangle$$

where $E_\nu(\mathbf{r}_1)$ and $E_\nu(\mathbf{r}_2)$ represent the measurable electric fields at positions $\mathbf{r}_1$ and $\mathbf{r}_2$; $*$ represents a complex conjugation.

It is generally assumed that all sources of interest lie within a small angle of the unit vector, $\mathbf{s}$ (phase centre vector). This allows equation 2.1 to be re-expressed such that B_ν is a function of (l, m), the direction cosines with respect to $\mathbf{s}$, and C_ν is a function in the (u, v)-plane. The advantage of this re-expression is that the spatial coherence function is now expressed in the domain in which the electric fields are measured by an interferometer.

$$C_\nu(l, m) = \int\int B_\nu(l, m) e^{-2\pi\imath(ul+vm)} dl dm \tag{2.3}$$

Another advantage of this formalism is that C_ν and B_ν are related by Fourier theory. Therefore:

$$B_\nu(l, m) = \int\int C_\nu(u, v) e^{2\pi\imath(ul+vm)} du dv \tag{2.4}$$

This is now in the form where the B_ν is expressed in terms of the observable spatial coherence function C_ν, or visibilities.

The above treatment, while adequate, has neglected the vector nature of electromagnetic radiation, consequently no information on the polarisation state can be inferred. In order to fully recover the vectorial nature of the incoming wave, a single receiver is insufficient, rather a combination of two orthogonally mounted feeds is required. This will then result in not a single spatial coherence function, but rather a set of functions to describe the nature of the incoming wave. The treatment for this array of spatial coherence functions will be considered in the following section.

2.4.1 Polarimetry at the ATCA

One of the greatest strengths of the ATCA is that it has excellent polarisation characteristics over its large bandwidth. Most large aperture-synthesis arrays such as the VLA use circularly polarised feeds. The ATCA, however, uses dual linear polarisation probes, which measure the two orthogonal linear polarisations, denoted X and Y. In order to correctly account for the use of linear feeds the *MIRIAD* software suite (Sault et al. 1995) was used for the data reduction and calibration of all ATCA data presented in this thesis.

Stokes Parameters

One convenient and commonly used notation to indicate the state of a polarised radiation field is in terms of the four Stokes parameters, $I(l,m)$, $Q(l,m)$, $U(l,m)$ and $V(l,m)$, usually simply called I, Q, U, and V (Stokes et al. 1852). The Stokes parameters are a particularly convenient way to describe the vector nature of electromagnetic radiation and can be related through a series of equations to the set of four correlations (visibility or spatial coherence functions). These functions represent the 4 multiplicative terms derived from the orthogonal feed measurements of the two linear polarisations X and Y. These terms are $X \times X$, $Y \times Y$, $X \times Y$ and $Y \times X$; generally denoted XX, YY, XY and YX.

Consider a propagating electric field, $\mathbf{E}$. If E_x and E_y are the components of the electric field resolved into two perpendicular axes normal to the direction of propagation from a point source, we can write

$$E_x = e_x(t)\cos[2\pi\nu t + \delta_x(t)], \quad \text{and} \tag{2.5}$$

$$E_y = e_y(t)\cos[2\pi\nu t + \delta_y(t)]. \tag{2.6}$$

where e_x and e_y are the components of the complex amplitude of the electric field and δ is a time-variable phase term. The four Stokes parameters are defined as:

$$I = \left\langle e_x^2(t)\right\rangle + \left\langle e_y^2(t)\right\rangle,$$

$$\begin{aligned} Q &= \langle e_x^2(t)\rangle - \langle e_y^2(t)\rangle\,, \\ U &= 2\,\langle e_x(t)e_y(t)\cos[\delta_x(t)-\delta_y(t)]\rangle\,, \quad \text{and} \\ V &= 2\,\langle e_x(t)e_y(t)\sin[\delta_x(t)-\delta_y(t)]\rangle\,, \end{aligned} \tag{2.7}$$

where the angle brackets indicate a time average, or expectation value. Here, I represents the total intensity, Q and U represent the linearly polarised component and V represents the circularly polarised component. These four parameters fully describe the polarisation state of the incident radiation. Together with the frequency they provide all the information required to characterise any electromagnetic radiation.

Returning to the set of correlations or spatial coherence functions as per the formalism developed in section 2.4, it is evident that this may be given as:

$$\begin{aligned} C_{\rm XX}(\mathbf{r}_1,\mathbf{r}_2) &= \langle E_x(\mathbf{r}_1)E_x^*(\mathbf{r}_2)\rangle, \\ C_{\rm YY}(\mathbf{r}_1,\mathbf{r}_2) &= \langle E_y(\mathbf{r}_1)E_y^*(\mathbf{r}_2)\rangle, \\ C_{\rm XY}(\mathbf{r}_1,\mathbf{r}_2) &= \langle E_x(\mathbf{r}_1)E_y^*(\mathbf{r}_2)\rangle, \\ C_{\rm YX}(\mathbf{r}_1,\mathbf{r}_2) &= \langle E_y(\mathbf{r}_1)E_x^*(\mathbf{r}_2)\rangle. \end{aligned}$$

In turn, the correlation functions maybe related to the Stokes *visibilities* via the following equations:

$$\begin{aligned} C_{XX}(u,v) &= I(u,v)+Q(u,v), \\ C_{YY}(u,v) &= I(u,v)-Q(u,v), \\ C_{XY}(u,v) &= U(u,v)+iV(u,v), \\ C_{YX}(u,v) &= U(u,v)-iV(u,v). \end{aligned}$$

The Stokes visibilities are related to the Stokes parameters through the same Fourier relationship that relates the brightness to the spatial coherence.

The Stokes visibilities may now be expressed in terms of the measurable cross-correlations, such that:

$$I(u,v) = (C_{XX}(u,v)+C_{YY}(u,v))/2, \tag{2.8}$$
$$Q(u,v) = (C_{XX}(u,v)-C_{YY}(u,v))/2, \tag{2.9}$$
$$U(u,v) = (C_{XY}(u,v)+C_{YX}(u,v))/2, \tag{2.10}$$
$$V(u,v) = (C_{XY}(u,v)-C_{YX}(u,v))/2\imath, \tag{2.11}$$

where I describes intensity, Q and U the linearly polarised components and V the circular component in the visibility domain.

Despite the usefulness of the Stokes description, astronomically it is more usual to understand the polarisation as either total polarisation, p_t, fractional linear p_l, or fractional circular polarisation, p_c and the polarisation position angle, ψ (increasing from north through east). This means it is also useful to consider the following equations:

$$p_t = \frac{\sqrt{Q^2+U^2+V^2}}{I}, \quad \text{and} \tag{2.12}$$

$$p_l = \frac{\sqrt{Q^2+U^2}}{I}, \tag{2.13}$$

$$p_c = \frac{V}{I}, \tag{2.14}$$

$$\psi = \frac{1}{2}\arctan\left(\frac{U}{Q}\right), \quad 0 \leq \psi \leq \pi. \tag{2.15}$$

2.4.2 In the Not-so-ideal World

The previous sections describe the situation for an ideal set of receivers, which stay both perfectly orthogonal to each other and maintain a constant orientation with the source of interest. In practice, however, this is not the case.

For an alt-azimuth antenna such as the ATCA, the feeds will rotate with respect to the sky over the course of the observation. This implies that the X feed will not constantly sample the x-component, E_x, of the incoming wave. Similarly, the Y feed will not sample the y-component, E_y. However, the values that are measured by each feed, E_X and E_Y may be correctly related back to the actual E_x and E_y by incorporating a correction due to the change in parallactic angle θ, such that:

$$E_X = E_x\cos\theta + E_y\sin\theta, \tag{2.16}$$

$$E_Y = -E_x\sin\theta + E_y\cos\theta. \tag{2.17}$$

$$\tag{2.18}$$

It is also unlikely, in a real antenna, that each feed will maintain a perfect response, meaning that some y-oriented radiation will leak into the X feed and vice-versa. This cross-polarisation term can be accounted for by the feed "leakages", D_X and D_Y (assuming there is a linear response).

$$E'_X = E_X + D_X E_Y, \tag{2.19}$$

$$E'_Y = E_Y + D_Y E_X. \tag{2.20}$$

$$\tag{2.21}$$

The leakage terms are, in general, complex. However, their components are loosely associated with physical effects. The real part is a measure of the angle between the actual feed orientation and the true orientation on the sky, while the imaginary term corresponds to a term called the "ellipticity" which is a measure of the axial ratio of the polarisation of the feed; for a more in-depth treatment see Morris et al. (1964).

Finally, the complex gains of each feed must be accounted for before calibration.

$$E''_X = G_X E'_X, \tag{2.22}$$
$$E''_Y = G_Y E'_Y. \tag{2.23}$$
$$\tag{2.24}$$

2.5 ATCA calibration

As shown above, calibration of a real interferometer requires an estimate of the gains, leakages and parallactic angle to be made for each feed on every antenna for every correlation. The observed correlations can then be corrected by applying the set of equations derived in the previous sections in order to obtain the "true" correlations. This process is known as calibration.

In order to determine the required set of parameters to perform a calibration a combination of instrumental and astronomical procedures is normally employed. Instrumental procedures such as gain calibration through noise injection normally provide a coarse calibration which is refined by the observation of a strong unresolved, unpolarised astronomical source called a "calibrator". By examining the correlation products which arise from observations of such a source, the required calibration parameters may be obtained.

It should be noted that one of the striking differences between calibration of antennas with linear feeds, as compared to those with circular feeds, is that astronomical sources are often slightly linearly polarised. In the case of a circular-feed antenna this makes no difference. However, when calibrating a linear-feed antenna with such a source the XX and YY visibilities will not provide independent measurements of the total intensity I making the overall calibration more difficult.

2.5.1 Standard Calibration on the ATCA

There is a standard procedure for the calibration of ATCA data in the *MIRIAD* software suite (Sault et al. 1995). *MIRIAD* consists of a number of software routines called "tasks" which can be run either through the *MIRIAD* package, from a command line interface, or within complex shell scripts.

A short stepwise treatment for the basic calibration procedure follows (see Figure 2.3. For full details of this process the "Miriad User's Manual" (Sault & Killeen 1998) should be consulted.

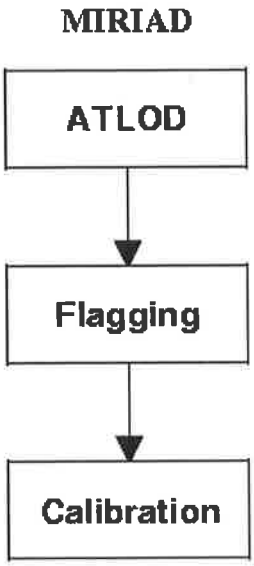

Figure 2.3: ATCA data reduction flow chart.

Importing Data to *MIRIAD*

The ATCA correlator outputs data in the RPFITS format (Norris et al. 1992) which must be translated into *MIRIAD*'s native format before processing may begin. The task ATLOD is used to both load the data into *MIRIAD* and to perform three data handling operations. The first of these is to correct for the XY-phase difference measured by the noise injection diode. Following this, it is usual to discard the channels at the edge of the band and average the remaining data. For continuum imaging it is usual to observe the 128 MHz band in 32, 4-MHz channels. Only every second channel is independent (due to windowing) and after removing the channels on the edge of the band and averaging every second channel this leaves 13, 8-MHz channel. However, the ATCA correlator is flexible and it is possible to observe with different bandwidths and numbers of channels for other experiments such as spectral line observations. Full details of the possible correlator configuration can be found in The Australia Telescope Compact Array Users' Guide (1999). Finally, ATLOD will remove any channels affected by internal interference generated by the correlator.

Flagging

During the observations any data collected while the telescope is not on source will be automatically marked as "bad" by the system. However, there are a number of reasons certain data should be excluded from the final image and it is during the offline processing that most of this occurs. At this stage it is usual that the observer will remove corrupted data by "flagging". Flagging is a laborious process that involves

visually inspecting the visibilities and removing those which are clearly caused by instrumental error or radio frequency interference (RFI). In the case of large datasets this process alone may take days to weeks if performed manually. As a result of this, *MIRIAD* allows for data to be clipped. Clipping is a process wherein data are automatically flagged via a software routine. The routine inspects and removes data based on its statistical deviation from the mean. The software default is to remove all correlations which are greater than five standard deviations from the mean, though it is possible for the user to increase or decrease this threshold. Clipping is much faster than manually flagging and is often the best initial procedure for large datasets or cases of very strong intermittent RFI. Of course for complex sources with a great deal of structure, care must be taken when applying the clipping algorithm.

Calibration

There are many variations on the calibration procedure which can be employed for different datasets. Here only the standard and preferred procedure is considered. Information on other calibration techniques is given in the "Miriad User's Manual".

The first step in the calibration procedure is to determine the absolute flux density scale using the primary calibrator PKS B1934−638. Two *MIRIAD* tasks are employed during this process. The first of these, MFCAL, determines the complex, time-dependent bandpass function for each feed. In order to accomplish this, MFCAL has been programmed with the spectrum of PKS B1934−638. The second task, GPCAL, solves for the time-dependent, complex feed gain and time-independent complex leakages. GPCAL will also account for any residual XY-phase differences left after ATLOD's correction. In both cases it assumes there is no polarised emission from PKS B1934−638. In general, this is a valid approximation and for the case of linear polarisation solutions will pose no problems. On the other hand, it has been found that PKS B1934−638 does have weak circular polarisation at ATCA wavelengths (Rayner 2000) which must be considered when processing circular polarisation data. However, since circular polarisation was not considered in this thesis, the standard calibration procedures are adequate.

The next step in the calibration process involves the use of a "secondary", or "phase" calibrator. The role of the secondary is primarily to provide a reference for atmospheric phase effects. In order to achieve this, the calibrator would ideally be a strong source in the same field of view as that of the target. In practice it is more common to find a suitable secondary calibrator a few degrees away from the target so that the atmospheric lines of sight are not too dissimilar. The calibration procedure for the secondary is almost identical to that of the primary. First, MFCAL is used to determine the bandpass function. Since MFCAL will not have been supplied with the source spectrum a flat spectrum is assumed across the band. In general, this is a valid approximation; further information about the bandpass effects can be found in Sault & Wieringa (1994). Following this, GPCAL is again used to determine the gains and leakages for the secondary and finally the task GPBOOT is employed to apply the flux density scale derived from the primary.

Having produced a properly calibrated secondary calibrator dataset, the solutions may now be copied over to the target source. This is done with the task GPCOPY. The target source is now in theory ready to image. In practice, however, this process is usually iterative, often requiring a return to the flagging stage in order to get the best set of calibration solutions. A flow chart of this process is given in Figure 2.4.

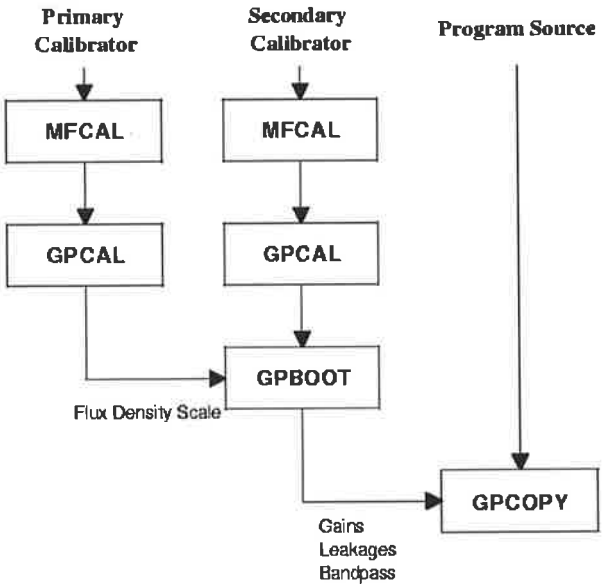

Figure 2.4: ATCA data calibration flow chart. Note that this set of procedures is optimal only where there is good parallactic angle coverage for the secondary calibrator. In other circumstances the *MIRIAD* manual (Sault & Killeen 1998) should be consulted to determine the best calibration process.

2.6 ATCA Imaging

Once the data are properly calibrated, images can be made. Although the options for imaging a (uv)-dataset are very flexible, they do follow a basic pattern outlined in Figure 2.5. The first stage is transformation from the Fourier domain to the image domain. Following this, side-lobe patterns are removed via "cleaning" and deconvolution.

2.6.1 Transforming to the Image Plane

In *MIRIAD* images are made using the task "invert" which Fourier transforms the data from the Fourier domain to the image domain. This produces an image known as a "dirty image".

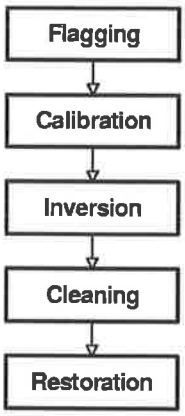

Figure 2.5: ATCA data imaging flow chart.

Since the ATCA correlator provides information at each frequency channel it is possible to either combine all of this information into a single image or to image each channel separately. When combining the data from each channel into a single image, "invert" uses the option for multi-frequency synthesis (mfs). Since the ATCA allows for two frequency bands to be observed simultaneously it is also possible to select these bands to overlap slightly, essentially giving a wider band-width for the observation. Invert is capable of taking these two sets of observations and making a single continuum image using the mfs option. Eventually, though, simple, multi-frequency synthesis will break down due to variations in source flux density with frequency.

As synthesis telescopes only sample the $(u - v)$-plane at discrete locations, there is incomplete knowledge of the Fourier transform of a source's intensity distribution. Thus, the "dirty image" that is produced is the convolution of the Fourier transforms of the true source visibility function and the sampling function, often called the "dirty beam". Although sources are visible in dirty maps, fine details are often lost in the resultant sidelobe pattern from incomplete sampling of the $(u - v)$-plane. Thus, is it desirable to attempt to remove the effects of incomplete sampling from the image. This process is known as "cleaning" and will be discussed in the next section. In the case of multi-frequency synthesis of sources with very steep spectral indices or images that require a very high dynamic range, msf must be combined with a special cleaning algorithm "mfclean".

2.6.2 Removing the Sidelobe Pattern

In order to better study radio sources, it is necessary to remove or "clean" the telescope sidelobe pattern from the image. To do this an algorithm is employed to perform a two part procedure wherein the location of radio sources are found and a model of the "dirty beam" pattern is "subtracted" from the image via deconvolution. There are several different algorithms that are derived from the original "clean" algorithm developed by Högbom in 1974. There are also Maximum entropy algorithms which work in a

different way to perform the same task of removing the sidelobes. The virtues of each class of algorithm have been debated extensively in the last 20 years. A comparison of the two techniques is well beyond the scope of this thesis. For further information see "Synthesis Imaging in Radio Astronomy II", 1999, ASPconf Vol 180.

In practice, the algorithms make a model of the sky by estimating the true source distribution in the unsampled parts of the (uv)-plane. Therefore the solutions will not be unique and the task of image reconstruction becomes one of choosing the "best" image from the possible set of solutions provided. More details can be found in "Synthesis Imaging in Radio Astronomy II", 1999, ASPconf Vol 180.

2.7 The 2dF Spectroscopic System

The Two Degree Field Spectroscopic system (2dF) is an optical fibre based multi-source spectrograph (Lewis et al. 2002) on the 3.9m Anglo Australian Telescope (AAT) at Siding Spring, NSW. The system is comprised of a wide field corrector, an atmospheric dispersion compensator, a robot fibre positioner and two spectrographs each accepting 200 optical fibres. It is designed to allow acquisition of up to 400 spectra simultaneously within a two degree diameter field. The two spectrographs can provide wavelength coverage from of 440 to 110nm.

A tumbling mechanism with two field plates allows the next field to be configured while the current field is being observed, making the system much more efficient than previous instruments. The robot positioner can place fibres at a rate of 10 per minute, with a precision of 20 microns or 0.3 arcseconds, which adds to the speed of data acquisition. All the elements, including the spectrographs, are mounted on a top-end ring to give ease of handling and keep the fibre length short to maximise UV throughput. Interchange times between 2dF and other AAT configurations can be handled in a semi-automatic fashion in under one hour. Figure 2.6 shows the major components of the system.

Under favourable conditions a typical galaxy with a blue magnitude, m_B, of 19 gives a spectrum with signal-to-noise ratio of better than 10 per pixel in less than an hour (Lewis et al. 2002).

2.7.1 Observing Set-up

Positional Calibration

To successfully record spectra, the robot must position the fibres directly on the galaxy position on the plate, thus accurate target co-ordinates are essential. Target positions for 2dF are usually measured from Schmidt telescope photographic plates. On most occasions this is performed by the Automatic Plate Measuring, or SuperCOSMOS plate measuring machines, which provide co-ordinates with a relative accuracy of 0.2 - 0.3 arcseconds across the entire 2.1 degree field. This requires use of reference stars from an astrometric catalogue and must take account and correct for proper motions; currently the Tycho-2 catalogue is used (Høg et al. 2000) for this purpose.

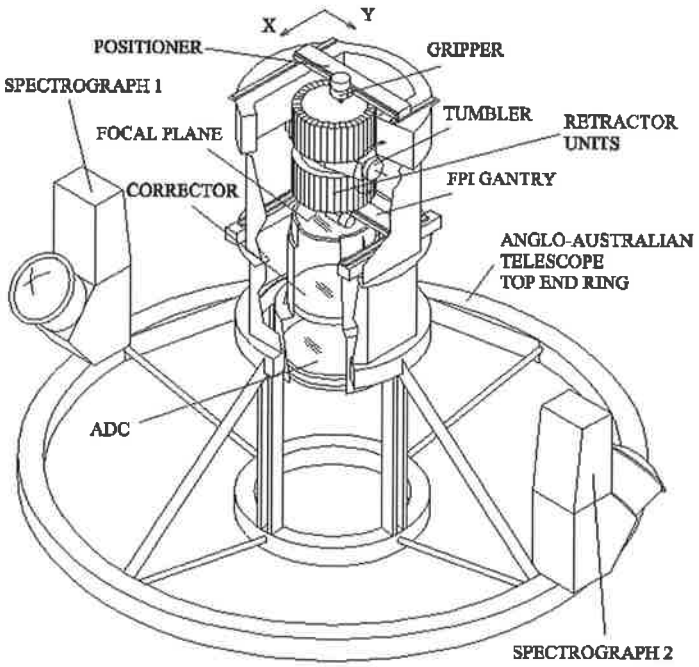

Figure 2.6: Schematic of the major components of the 2dF spectrographic system (Bailey et al. 2002)

Fibre positioning requires conversion from astronomical co-ordinates (RA, Dec) to physical plate co-ordinates (X,Y). The conversion parameters are calculated from the measured positions of a set of standard stars and a set of fiducial plate markers. The fiducial plate markers serve to remove any non-perpendicularity between the optical axes and the gantries as well as mechanical shifts between the field plates and the gantries. After this correction is made, the reference stars may be used to fit for other parameters. To do this an expected position for each star is determined after correction for atmospheric refraction, known pointing errors and distortion introduced by the corrector plate. This is then matched to the observed centroids of the stars. A linear least-squares minimisation is then performed to determine the fitting parameters. These include the X and Y scales, the rotation or skewness of the field and the field offset determined by the difference in centre of the optical distortion pattern and the optical axis.

Fibre Allocation

Fibre allocation is performed off-line using the CONFIGURE software. The initial inputs to CONFIGURE are the field centre and a list of target sources and fiducial stars. The software then assigns fibres to objects, taking into account the hardware constraints, such as fibre collisions. Due to the physical size and shape of the magnetic buttons used to hold the fibres on the plate the minimum separation between targets is around 30 arcseconds, though this varies with location in the field. Options in the

software allow the observer to assign different priorities to objects and set the hour angle in order to optimise fibre allocation. CONFIGURE then performs an iterative fibre allocation, randomly swapping fibre allocations at each step in order to maximise target coverage and minimise crossed fibres. Observers also have the option to swap or allocate fibres to either targets or "sky" positions manually before saving the final set-up. An example of a target field configuration using CONFIGURE is given in Figure 2.7, and a photograph of a configured plate is given in Figure 2.8.

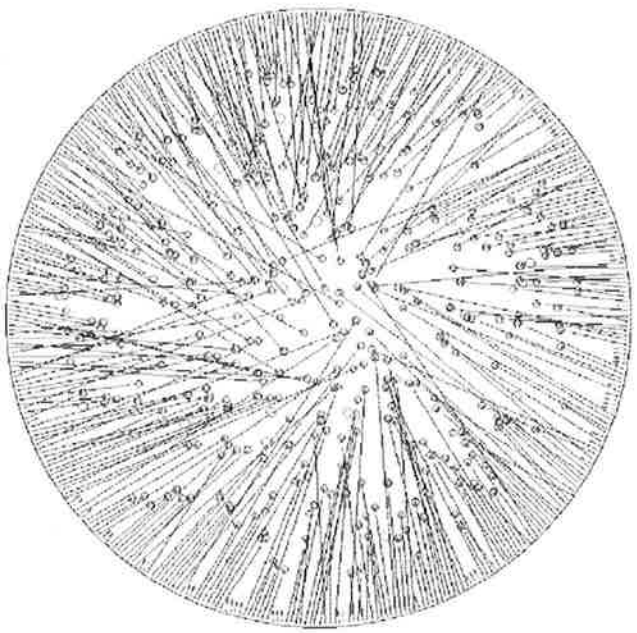

Figure 2.7: An example of a target field configuration from CONFIGURE. Red circles indicate fiducial stars, the small black objects are the target sources, while blue squares are the sky fibres and grey squares show broken fibres (Bailey et al. 2002).

Observations

In addition to the observations of a particular target field, a fibre flat and arc exposure are required in order to calibrate the observations. The fibre flat, is done first with a quartz lamp and is used for locating the data on each CCD during data reduction. The arc exposure provides the wavelength calibration of the spectra. Optional additional exposures include offset sky exposures and twilight sky flats which are used to calibrate the fibre throughput variation (though this can also be accomplished using the night sky emission lines in the object data).

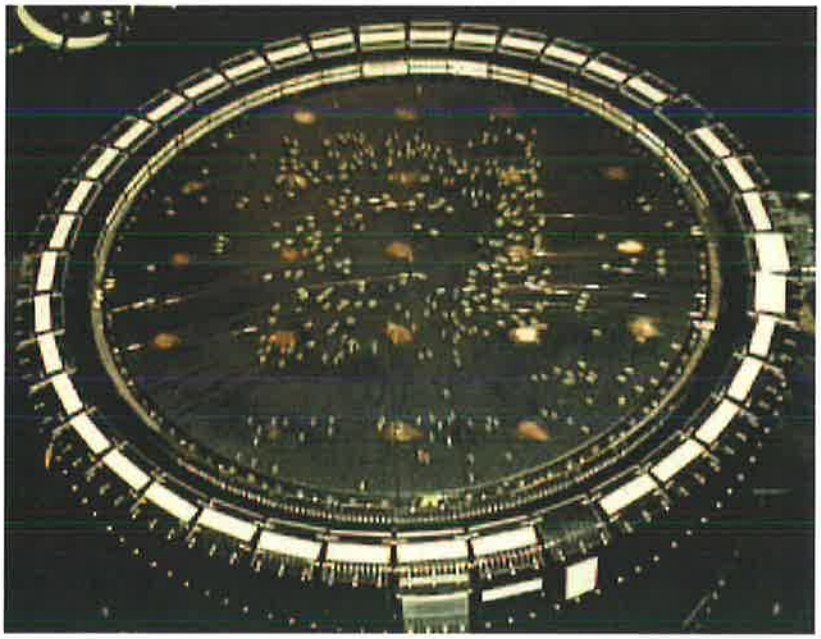

Figure 2.8: Photograph of the 2dF spectrographic system fibres positioned on a plate (Bailey et al. 2002)

Data Reduction

Data are reduced via a pipeline process developed for the Two Degree Field Galaxy Redshift Survey (2dFGRS) (Colless 1998; Colless et al. 2001). The software, 2dfdr, provides a complete pipeline reduction for an evening's observations in less than an hour. However, the package also provides flexible options for users to reduce the data and fit spectra manually, or to inspect and adjust automatically fitted spectra. The software outputs a set of paramters including the absorption determined redshift, the emission determined redshift, quality parameters for each redshift, the B_j magnitude and the spectral classification based on a set of standard spectra. Further details of the software outputs will be discussed in section 6.4, while further discussion on 2dfdr and its options can be found in Bailey et al. (2002).

2.8 Summary

The instrumentation and data analysis techniques described in this chapter are those which have been directly used to analyse the ATCA and 2dF observations presented in this thesis.

Chapter 3

Rotation Measure Studies in Clusters

3.1 Introduction: Magnetic Fields in Clusters

One of the standard ways to obtain estimates of the magnetic field is through the use of a population of background radio galaxies as probes of the Faraday rotation along the line of sight (Clarke 2000).

3.2 Faraday Rotation

Passing a linearly polarised electromagnetic wave through a magnetised plasma will result in rotation of the electric vector by an amount proportional to the strength of the field through which it passes. This effect, known as Faraday Rotation, was first proposed for astronomical sources by Cooper & Price (1962), who used it to explain the observed wavelength dependence of the polarisation position angle seen in Centaurus A. The phenomenon can be described by:

$$\chi = \chi_{in} + (RM)\lambda^2, \tag{3.1}$$

where χ_{in} is the intrinsic position angle of the radiation in radians, and λ is the wavelength in metres. If χ is plotted against λ^2, the y-intercept will correspond to the intrinsic position angle of the source and the slope of the line will give the Rotation Measure (RM). The rotation measure is a quantity proportional to the integral product of the magnetic field strength and electron density along the line of sight.

Faraday rotation can be understood by considering a linearly polarised wave as the combination of two opposite-handed elliptically polarised waves. In the case where the synchrotron gyrofrequency, ν_g, (as defined in section 1.4.1) is much less than the plasma frequency, the refractive indices as seen by each of the two elliptical modes can be given as (Longair 1981):

$$n^2 = 1 - \frac{\left(\frac{\nu_p}{\nu}\right)^2}{1 \pm \left(\frac{\nu_g}{\nu}\right)} cos\theta \tag{3.2}$$

where n is the refractive index, ν_g is the gyrofrequency, ν is the observing frequency, $\nu_p = 9.1 \times 10^3 n_e^{1/2}$ is the plasma frequency (where n_e is the electron density), and θ is the angle between the wave propagation direction and the magnetic field.

As the two elliptical waves move through the medium they will experience different refractive indices which will result in different phase velocities. From Longair (1981) it can be seen that under the conditions where $\nu_p/\nu \ll 1$ and $\nu_g/\nu \ll 1$ the difference in refractive index can be given as

$$\Delta n = \frac{\nu_p^2 \nu_g}{\nu^3} cos\theta \tag{3.3}$$

Following this the corresponding phase difference can be shown to be

$$\Delta\phi = \frac{2\pi\nu\Delta n dl}{c} \tag{3.4}$$

After travelling some distance, dl, if one again considers the linear polarisation vector by adding the two orthogonal elliptical components back together, one sees that the differing phase velocities of the elliptical components gives rise to a rotation of the overall linear vector.

$$\Delta\chi = \frac{\pi\nu_p^2 \nu_g}{c\nu^2} cos\theta dl, \tag{3.5}$$

where χ is the polarisation position angle as given in equation 3.1 above.

Integrating equation 3.5 over the distance travelled through the plasma, L, gives

$$\chi = \frac{\pi}{c\nu^2} \int_0^L \nu_p^2 \nu_g cos\theta dl, \tag{3.6}$$

Now the gyrofrequency, ν_g, is directly related to the magnetic field strength via $\nu_g = 2.8B \times 10^6$Hz, meaning that $\nu_g cos\theta = 2.8B_{||} \times 10^6$Hz, where $B_{||}$ describes the magnetic field parallel to the line of sight. Substituting this into equation 3.6 gives

$$\chi = \frac{\pi 2.8 \times 10^6}{c\nu^2} \int_0^L \nu_p^2 B_{||} dl, \tag{3.7}$$

Further, the plasma frequency, ν_p is related to the electron density, n_e, such that $\nu_p = 9.1 \times 10^3 n_e^{0.5}$ Hz. Substituting this into equation 3.7 gives

$$\chi = \frac{\pi 2.8 \times 10^6 (9.1 \times 10^3)^2}{c\nu^2} \int_0^L n_e B_{||} dl, \tag{3.8}$$

Substituting ν^2 for c^2/λ^2 and converting dl into parsecs rather than metres gives

$$\chi = 8.1 \times 10^5 \lambda^2 \int_0^L B_{||} n_e dl \text{ rad m}^{-2}, \tag{3.9}$$

Since the rotation measure is defined as $RM = \chi/\lambda^2$, this leads to the standard RM equation given below. It can be seen now that the degree of rotation is given by the relation between the RM, line of sight magnetic field and the electron density.

$$(RM) = 8.1 \times 10^5 \int_0^L B_{||} n_e dl \text{ rad m}^{-2}, \tag{3.10}$$

where $B_{||}$ is the line-of-sight component of the magnetic field in Gauss, n_e is the electron density in cm^{-3} and dl is the path length in pc.

The rotation measure is determined by the measurable quantities of position angle, χ and wavelength, λ. By obtaining measurements of the position angle of the electric vector at a number of different wavelengths it is possible to determine the RM.

It can be seen from equation 3.1 that the integral can be separated for different Faraday screens, implying that the position angle measured will be the linear sum of all rotations along the line-of-sight. Thus, a more general form of equation 3.1 is:

$$\chi = \chi_{in} + \sum_i (RM)_i \lambda^2, \tag{3.11}$$

Where $\sum_i (RM)_i$ denotes the linear sum of all RM contributions along the line of site.

For extragalactic radio sources there are at least four RM terms to consider; the RM due to internal conditions in the probe source, the RM of the objects along the line of sight, the RM due to our own Galaxy and the RM caused by the Earth's ionosphere.

A further complication is the consideration of redshift, which gives a correction to the wavelength emitted. In general, the observed RM, which is the sum of all RM components, must also be corrected for redshift such that:

$$(RM)_{obs} = \sum_i^F [\frac{(RM)_i^F}{(1+z_F)^2}], \tag{3.12}$$

Where RM_{obs} is the measure RM and $\frac{RM_i^F}{(1+z_F)^2}$ denotes each RM component along the line of sight as a function of redshift. As the clusters examined in this study were all at redshifts less than 0.06, the redshift correction will be minimal (around ten percent).

3.3 Sources of Error in Rotation Measure Fits

Aside from the multiple components along the line of sight, there are a number of other difficulties to be considered when attempting to obtain a unique RM fit to a series of points plotted in the $\chi - \lambda^2$ plane. As well as errors relating to measurement uncertainties such as noise, there are several effects which lead to a breakdown of the $\chi \propto \lambda^2$ relation. These will be discussed individually in this section. Throughout this

section χ_{in} will denote the intrinsic value of the position angle, χ will represent the position angle that would be measured in the absence of any errors, i.e., the combination of linear position angles along the lines of sight. Finally ψ will be used for measured position angle values, which are those values which contain an error component.

3.3.1 Error due to Noise

One way to obtain either the total polarisation, P, or the value of the position angle, ψ, at a certain frequency is to begin with the Stokes Q and U parameters. Section 2.4 gives details of how P and ψ are obtained from U and Q.

Since Q and U have a linear relationship to the observables they will have Gaussian error distributions and be subject to noise from both measurement and calibration. The effect of noise in the measurement of U and Q will be propagated to an error in both P and ψ. As P is a vector in the complex plane the measured vector $\mathbf{P_{meas}}$ will have a vectorial relationship to both the real value of $\mathbf{P}$ and some noise vector, $\delta\mathbf{P}$.

$$\mathbf{P_{meas}} = \mathbf{P} + \delta\mathbf{P} \tag{3.13}$$

Figure 3.1 demonstrates the effect of this noise vector graphically in the complex plane.

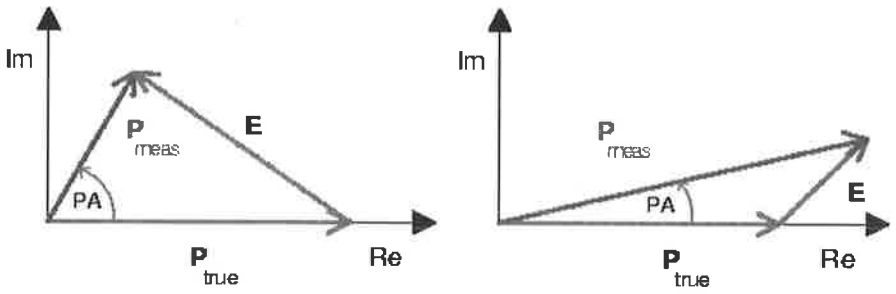

Figure 3.1: Following the example in Killeen et al. (in prep); measurement errors give rise to a spurious vector component, $\delta\mathbf{P}$, which adds to the polarisation vector, $\mathbf{P}$, producing an error in the position angle measurement, PA.

Assuming Gaussian noise, $\delta\mathbf{P}$ follows a symmetric distribution which becomes Gaussian at large signal-to-noise ratios. The amplitude of $\mathbf{P_{meas}}$ follows a Rice distribution (Vinokur 1965; Wardle & Kronberg 1974), becoming Gaussian at high signal-to-noise ratios. A more detailed discussion of these distributions can be found in Thompson et al. (1986).

3.3.2 $n\pi$-Ambiguity

The most common problem with the traditional fitting of a straight line to a series of points in the $\chi - \lambda^2$ plane is that it is impossible to distinguish how many times the electric vector has rotated before detection. This is to say, that if the position angle at a certain wavelength is measured with the value ψ radians, it is not possible to distinguish this from $\psi + \pi$, or in fact $\psi + n\pi$. This is referred to as the $n\pi$-ambiguity.

If only two points have been measured it will be impossible to assess whether an ambiguity is present. In such a case, the fit giving the lowest RM value is generally used. This is an unsatisfactory situation as it biases the RM distribution toward lower values. Even with three or more points with finite errors, if the RM is sufficiently large as to allow a rotation of more than π radians between adjacent values in wavelength-squared space, it may not be possible to recover the correct RM value. Figure 3.2 demonstrates example of an hypothetical ambiguity where the fit to the data suggests a value of 5.9 rad m^{-2} when in fact the true value is 200 rad m^{-2}.

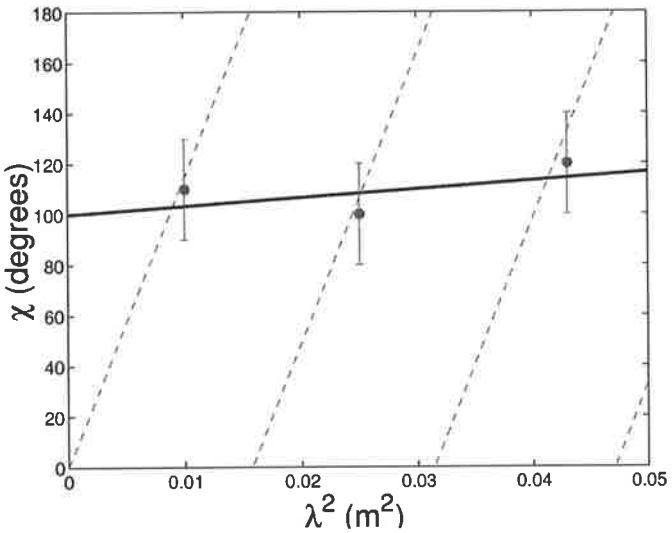

Figure 3.2: Again following the example in Killeen et al. (in prep); a simple least-squares fit to the position angle, χ, measured at three frequencies (ν = 1.4, 1.85 and 3.2 GHz) for a Faraday screen with rotation measure RM = 200 rad m^{-2} results in an incorrect measurement of RM = 5.9 rad m^{-2}. The true variation of χ with λ is shown as the dashed line.

In this case a solution may be found either by assuming that there is no rotation between adjacent points and performing a linear-least squares fit to the data, or by employing an algorithm which allows (usually a single) rotation between adjacent point to calculate the statistical best fit. Neither of these approaches is guaranteed to return the correct RM value.

However, by carefully selecting the wavelengths it is possible to minimize the possibility of suffering an ambiguity in the data fitting. By selecting two very closely spaced wavelengths for which only extremely high RMs will result in a rotation greater than π

radians between them, in combination with one, or preferably two, more widely spaced wavelengths, it is possible to adequately recover most RM values (or in the worst case give a lower limit to the RM). Figure 3.3 demonstrates how the selection of wavelength is critical in an attempt to obtain a unique RM fit.

It should be noted that this technique is only viable when the errors are sufficiently small, so as to allow the RM to be constrained. In order to achieve this there must be sufficient flexibility in the allowable frequency choices on the instrument. As this is the case on the ATCA, the above technique was employed here.

3.3.3 Depolarisation

Depolarisation may occur due to either instrumental effects or intrinsic properties of the radio source. In the case of instrumental effects, depolarsiation can arise due to either bandwidth or beamwidth choices. Internal depolarisation in the radio source will also produce a depolarisation signature.

Internal Depolarisation

Internal depolarisation within a radio source has been the subject of many papers dating back to the work of Burn (1966). Internal Depolarisation is not strictly speaking an error, it is worth mentioning, as the signature of internal depolarisation is similar to the error introduced by beam depolarisation (see below). Internal depolarisation results when the synchrotron emitting electrons are mixed in a medium rich in thermal electrons. Faraday rotation will occur as the polarised light moves through the thermal electrons before leaving the radio galaxy. As shown in equations 3.4 and 3.5 the change in phase of each elliptical mode and thus the amount of Faraday rotation is proportional to the distance travelled. In the case of internal depolarisation, light from different depths in the medium, and therefore having different phases will interfere, causing the polarised flux density to change with source depth. This follows a characteristic sinc squared function. However, the total flux density, I, does not vary with source depth, meaning that overall the degree of polarisation decreases inversely with the observing wavelength. This effect is known as internal depolarisation. In the presence of a uniform magnetic field, internal depolarisation still produces a polarisation angle relation which is proportional to λ^2, but only over discrete ranges of $\pi/2$ radians. At position angle values of $\chi_{in} + n\pi/2$ radians (where χ_{in} is the intrinsic polarisation position angle) the source is completely depolarised and the polarisation position angle jumps discontinuously. Thus, by observing a wavelength range over which a $\pi/2$ rotation is likely to occur it is possible to detect this effect. More recently the work of Tribble (1991) and Sokoloff et al. (1998) describe the process in some detail.

Bandwidth Depolarisation

Performing an accurate RM fit depends critically on the accurate measurement of the position angle at each frequency. This is particularly important because of the small

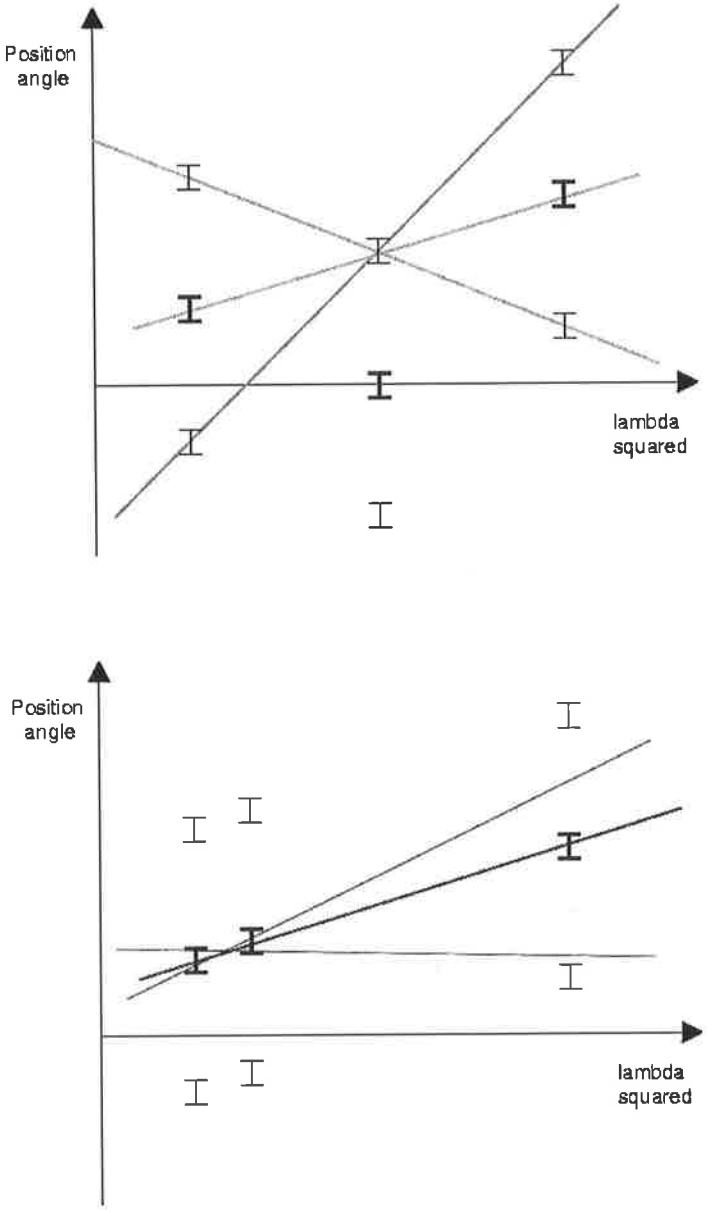

Figure 3.3: Illustration of the effect of wavelength selection on the uniqueness of an RM fit after those found in Ruzmaikin & Sokoloff (1979). The top figure shows a set of three values of the position angle measured at equal spacings in λ^2 space, marked in blue. Due to the $n\pi$-ambiguity it is impossible to distinguish these measured values from points on the plane which are plus or minus $n\pi$ radians away, marked here in black. This means there are at least three possible fits to these data, each marked by a grey line. Hence, the RM can not be uniquely determined. The bottom panel shows the same dataset but with the middle observing wavelength chosen so as to be close to one of the other points in λ^2 space. Again the measured values are shown in blue and their corresponding plus or minus $n\pi$ radian points in black. Assuming there is not one full rotation between adjacent measurements, the closely spaced values provide a constraint on the acceptable values of the third data point (shown by grey lines) meaning that a unique fit to the data can be obtained.

number of points typically used. As it is not possible in practice to make measurements in a single monochromatic band (there would not be a large signal-to-noise ratio for most radio sources), it is important to consider the effect of a finite bandwidth on the resultant value of ψ.

As seen in section 2.4 the total linear polarisation, p, may be expressed as

$$p = \sqrt{Q^2 + U^2}, \tag{3.14}$$

and the polarisation position angle, χ, as

$$\psi = \frac{1}{2} \arctan\left(\frac{U}{Q}\right), \tag{3.15}$$

where Q and U are the Stokes parameters corresponding to the two orthogonal linear polarisation states.

If the complex linear polarisation, P, is now assigned the value

$$P = \sqrt{Q^2 + iU^2} = pe^{2i\psi}, \tag{3.16}$$

after the notation of Conway & Kronberg (1969), one can now discuss bandwidth depolarisation mathematically.

Consider the situation where a large continuum band centred at frequency ν_c and with width $\Delta\nu = \nu_1 - \nu_2$ is employed to obtain a position angle, ψ. Assuming that p is independent of frequency, the integrated complex polarisation over the bandwidth is

$$P_{I,\nu_c} = p \int_{\nu_1}^{\nu_2} e^{2i\psi(\nu_c)} d\nu. \tag{3.17}$$

Substituting the expression for the position angle given by equation 3.1, setting $\psi_{\rm in} = 0$ without loss of generality, and assuming the fractional bandwidth $\Delta\nu/\nu_c \ll 1$, one can show that

$$P_{I,\nu_c} = p \frac{\sin(\alpha)}{\alpha} e^{i2RM\lambda_c{}^2} \tag{3.18}$$

where $\alpha = 2(RM)\lambda_c^2 \Delta\nu/\nu_c$ and λ_c is the wavelength equivalent to the central frequency, $\nu_c = (\nu_1 + \nu_2)/2$.

This means that if the polarisation vector changes significantly over the observing bandwidth the measured value, ψ, which will be the average across the band, will be less than the true value, χ. Bandwidth depolarisation will be a problem for either sources of very large rotation measures or observations using very wide bandwidths. Due to the correlator configuration on the ATCA, which allows the band to be split into narrow frequency channels, bandwidth depolarisation was not an important source of error in this study.

Beam Depolarisation

Beam depolarisation is the result of averaging the position angle values from all components within the beam. In the case where multiple unresolved RM components are present or there is an RM gradient in the source on scales smaller than the telescope beam, beam depolarisation will occur. In the limit of a linear RM gradient across the source, beam depolarisation will give the same effect as internal depolarisation. However, it is possible to distinguish between internal depolarisation and beam depolarisation as internal depolarisation is proportional to the magnitude of the RM, whereas beam depolarisation is proportional to the magnitude of the RM gradient. The effects of beam depolarisation become most extreme when there is a change of more than $\pi/2$ radians across the beam. For the observing frequencies chosen in this study, this would correspond to RM gradients of 39 and 680 c m^{-2} $arcsec^{-1}$ at 1.4 and 6.2 GHz respectively. Observational evidence suggests that such gradients are only likely to be measured for the central radio sources embedded in cooling flow clusters (Feretti et al. 1999). As cooling flow clusters have been deliberately excluded from this study, beam depolarisation is not likely to pose a great source of error, though of course should not be excluded.

More details on the effects of depolarisation are found in Burn (1966), Tribble (1991), and Sokoloff et al. (1998).

3.3.4 Effect of Off-axis Polarisation Errors

Figure 2.2 showed the off-axis instrumental polarisation error for the ATCA at 20 and 13 cm. The 20, 6 and 3 cm responses vary less than 2 percent to the half power point, making them essentially uniform across the primary beam (allowing accurate polarimetry to be performed away from the beam centre). However, the 13cm polarisation response degrades more rapidly to around 10% at the half power point, making it difficult to obtain accurate polarisation values over a large part of the primary beam.

Hence all sources appear slightly polarised at around the 2 percent level at the edges of the primary beams for 20, 6 and 3 cm and at more than 10 percent at the edge of the 13cm beam. For polarised sources that lie on the edge of the primary beam, this introduces a spurious vector component to the value of P, which is an additional source of error in positional angle. As mentioned in section 2.3.6 these errors are dependent on source declination. As the polarisation response of the ATCA is known it is possible to model and remove this suprious vector with the *MIRIAD* task OFFPOL. However, in this study all sources were observed only near the beam centre so as to avoid this complication.

3.4 Previous RM studies in Clusters

The notion of significant extragalactic magnetic fields, specifically those in clusters of galaxies was first discussed by Burbidge (1958). However, it was not until recently that the existence of such intracluster fields outside the lobes of radio galaxies could be

statistically confirmed (Kim et al. 1991) and still later that convincing numerical values could be ascribed to them (Clarke 2000). Part of the difficulty of investigating cluster magnetic fields through Faraday rotation is that such a study may only be undertaken statistically. This is due to the vector addition of all contributing Faraday screens along the line of sight, making it impossible to disentangle the cluster rotation measure components from either internal rotation in the source, a Galactic rotation measure component, or an ionospheric component, i.e. equation (3.11). However, comparison of a sample of sources with lines of sight through the intra-cluster medium, as compared to a control sample, provides a statistically valid approach for the confirmation of an enhancement of the rotation measure in cluster regions. Several analyses of this kind have been performed with increasing degrees of success.

Dennison (1979) first attempted a statistical study of cluster rotation measures by comparing a sample of 16 cluster radio sources to 16 controls. Unfortunately, the sample size was too small for the result to be conclusive. Following this, Lawler & Dennison (1982) reported a broadening of the scatter in their RM data of 50 rad m^{-2} in a cluster sample of 24 sources when compared with only 10 rad m^{-2} their control. They interpreted this as evidence of a cluster field with $\mathbf{B}$ of the order of 1μG with a scale length greater than 20 kpc. This result is only marginal as there was no account taken of error broadening of the sample. Hennessy et al. (1989) conducted the first statistical RM study to perform fits at four different wavelengths, which largely removed the problem of the $n\pi$-ambiguity in the RM (see section 3.3.2). Their study found no significant difference between their cluster (16 sources) and control samples and they reported an upper limit on the RM width excess in clusters (as compared to the control population) of 55 rad m^{-2}. This led to an upper limit on the cluster magnetic field of $\mathbf{B} = 0.07\mu$G for a uniform untangled field with core radius of 500 kpc. Goldshmidt & Rephaeli (1993) questioned this result for $\mathbf{B}$ and recalculated it, assuming a scale length of 20 kpc over the 500 kpc core radius. They assumed an electron density of 3×10^{-3} cm^{-3}, which gave a net field strength of less than 0.2 μG. All three studies are considered too small to be statistically significant (Goldshmidt & Rephaeli 1993). Kim et al. (1990) investigated the magnetic field in the Coma cluster using 18 sources in the cluster field, 11 comprising the cluster sample and 7 in the control. The authors themselves drew attention to the problem of the small source sample, but nevertheless concluded a "first order result" of $\mathbf{B}$ less that 2 μG derived from an *average* RM width excess of 30 rad m^{-2}. Unfortunately, on closer examination, a question arises as to the validity of those points used in the Kim et al. (1990) analysis for which only two wavelengths were used to calculate the RM. As mentioned in section 3.3.2 only RMs of at least four (or a very carefully chosen three) wavelengths may produce a unique fit. Given the small sample size and lack of uniqueness of a two-frequency fit for half of the sample, it is not possible to draw any significant conclusion from these data.

Following these observations Kim, Tribble & Kronberg (1991) improved their source statistics by examining a large number of rotation measures from the literature (Simard-Normandin et al. 1981; Broten et al. 1988; Hennessy et al. 1989; Kim 1988; Lawler & Dennison 1982; Vallée et al. 1986) supplemented by unpublished data from Kronberg. 152 source RMs were obtained and compared with the positions of Abell clusters. This

produced a catalogue with 53 sources comprising the cluster sample and 99 sources in the control. This study contains the largest cluster sample to date.

The Kim et al. (1991) study, hereafter denoted KTK, divided both the cluster and control sample into various subsamples. The cluster sample was divided into two sections based on whether a source fell within one sixth of the Abell radius. The control sample contained a subsample of isolated giant elliptical galaxies with properties similar to central dominant (cD) galaxies. The study found that the distribution of RMs for the cluster sample was broader than the control at the 99.9% confidence level. Further, there was seemingly no difference between the elliptical galaxy sample and the rest of the control, from which it was inferred that the excess RM width in the cluster sample was due to the intracluster medium and not some bias due to preferential observation of cluster galaxies. At the 99% confidence level the excess RM width was in the range 51–84 rad m^{-2}. Assuming a field which was uniform through the cluster core but locally tangled on scales of 10 kpc, a **B** value of between 0.5 and 1.25 μG was obtained; this was in contrast to a value derived using the model of $B(r) \propto n(r)$ (Jaffe 1980), which gave 1–2.25 μG for the inner cluster sample and 1.9–4.7 μG for the outer cluster sample. These results have been examined in detail for robustness and it was found that there is a significant statistical difference between the cluster and core samples (Goldshmidt & Rephaeli 1993). However, there is some concern as to the validity of the RM fits in this sample also. Questions have also arisen as to the numerical validity of the KTK results in light of the fact that some of the "clusters" examined in their study were undetected at X-ray wavelengths by the *Einstein* satellite (Clarke 2000). The lack of X-ray flux indicates that the clusters are either quite poor, or are not gravitationally bound systems with significant intracluster gas. RMs along the line of sight towards these objects will have a considerably lower value than those directed at X-ray bright clusters and thus will introduce a lowering numerical bias to the result. This implies that the KTK result is likely to be *more* signifigant, both in terms of detection and implied **B** value, than first thought and therefore should be re-examined.

All of the afore-mentioned studies, with the exception of Hennessy et al. (1989), suffer from lack of well-defined source selection criteria, which may lead to bias in the sample. This was the impulse for Goldshmidt & Rephaeli (1993) to re-examine the KTK sample. Clarke (2000) attempted to address the lack of a large well-defined cluster RM sample by observing radio sources toward 24 X-ray luminous Abell clusters using a strict set of selection criteria. The Clarke data comprised of both a cluster and control sample with 27 and 89 sources respectively. The cluster sample was chosen from 24 Abell clusters with X-ray luminosity greater than 1×10^{44} erg s^{-1} in the 0.1 to 2.4 KeV band (Ebeling et al. 1996). In order to reduce Galactic contamination of the RM sample, clusters were selected no closer than 13 degrees from the Galactic Plane and an averaging technique was employed in an attempt to correct for this effect (see Chapter 4 for further discussion). A statistically significant width difference between the RM distributions for the (Galaxy corrected) cluster and control samples was observed with the standard deviations of each distribution differing by almost an order of magnitude ($\sigma_{cluster} = 113$ rad m^{-2} to $\sigma_{control} = 15$ rad m^{-2}). Further, the two samples were found to be drawn from different populations at the 99.4% confidence level. Using, electron

densities obtained from ROSAT X-ray observations, Clarke also statistically examined the strength of the cluster magnetic field. Two magnetic field models were investigated. The first was a simple "slab" model, wherein the magnetic field is assumed to be uniform in both magnitude and direction throughout the cluster. This predicted field strengths of around 0.5 μG. The second, and more sophisticated model, used tangled magnetic fields with particular cell sizes; this produced field strengths of the order of 1 – 1.5 μG. A further investigation of cell sizes via RM mapping of sources in three of the sample clusters suggested that the field had large scale uniformity at around 100 kpc with smaller 10 kpc features. The structure observed in the RM mapping suggested that a tangled cell model was more likely, and the uniform slab values were rejected. In conclusion, Clarke asserted that field strengths of ≥ 1 μG were unlikely in rich X-ray luminous galaxy clusters.

3.5 Current Study

The samples of all previous studies have deliberately steered away from investigating radio probes within the very cores of clusters (the median distance from the cluster centre for sources in the Clarke sample is 445 kpc). This is due, in part, to the difficulty of the task, and in part to the notion that in the very centre of clusters strong radio sources will interact with the ICM giving rise to RMs which are not indicative of the true cluster RM. Other studies have shown that radio sources embedded in so-called "cooling-flow" clusters have extreme RM values (Taylor et al. 1994). However, no study directed toward the radio sources behind the cores of non-cooling-flow clusters has yet been undertaken. This work investigates a sample of radio background probes directed toward seven rich X-ray-luminous southern galaxy clusters which do not exhibit a cooling-flow profile. Originally the program was designed to fill the general gap in knowledge of cluster magnetic fields left after the KTK sample by observing sources which were projected both through galaxy cluster and a control sample of non-cluster sources. However, when I became aware of the work in progress by Clarke the observational program was redesigned in order to have less overlap with that study. The final aim of this study was to determine the extent to which the RM excess observed by Clarke (2000) is enhanced in the cores of clusters.

3.5.1 Source Selection

As this study was to use the ATCA, the first selection criterion was, of necessity, to choose those clusters which could reasonably be viewed from the Southern hemisphere. Thus an initial declination cut-off was imposed to select only clusters south of $-30°$.

To determine magnetic field strength along the line of sight through a cluster of galaxies it is necessary to have two pieces of information. The first is some field strength estimate, generated, in this case by Faraday rotation measures, and the second is an independent estimate of the electron density, n_e, along the line of sight. As X-ray emission via the process of bremsstrahlung is assumed to trace the cluster potential

well (Jones and Forman in (Clarke 2000)), X-ray data may be used to obtain an independent estimate of n_e. Thus, by considering RMs from radio probes drawn from a sample of clusters with measured thermal X-ray emission, it is possible to decouple the effect of the gas from equation 3.5 and obtain a estimate of the integrated field along the line of sight.

However, as demonstrated in Section 3.2, the measured RM will be the linear combination of all RMs along the line of sight. If we assume that the gas density in the intercluster medium is sufficiently low so as to render the resultant RMs from any possible magnetic fields in this region close to zero, equation 3.11 can be rewritten as:

$$\chi = \chi_{in} + [(RM)_{Cluster} + (RM)_{Galactic} + (RM)_{ionospheric}]\,\lambda^2 \tag{3.19}$$

This is not an unreasonable assumption even for sources at high redshift which have long path lengths through intercluster space, as no redshift:RM correlation has ever been observed (Kronberg & Simard-Normandin 1976; Welter et al. 1984; Vallée 1990).

This leaves the observed RMs as the linear combination of the source intrinsic, cluster, Galactic and ionospheric Faraday rotation contributions. Ionospheric Faraday rotation has been studied in some detail (Burkard 1961) and is believed to contribute less than 5 rad m^{-2} at the ATCA observing frequencies (Whiteoak, J., private communication 2001). The ionospheric contribution will of course vary depending on the Solar Cycle and the value of less than 5 rad m^{-2} is a average over a long time period. As these observations were carried out just after a minimum in the 11 year Solar Cycle, this estimate should be sufficient. The presence of a Galactic contribution to the RM error may be minimised by appropriate selection criteria. This leaves the intrinsic RM which cannot be removed. The effect of the intrinsic RM will be discussed in a subsequent section.

In the first instance care must be taken to ensure that the RM sample is minimally contaminated by the Galactic magnetic field. In order to do this an extensive study of the effect of the Galaxy on the RM sky was undertaken (see Chapter 4) and only clusters more than 30° from the Galactic plane were considered. At these Galactic latitudes it was found that the $RM_{galactic}$ was of the order of 10 rad m^{-2}. The precise effect of the galaxy on potential cluster RMs is discussed in detail in the following Chapter.

To further reduce the effect of Galactic contamination, a third selection criterion was used in this study: that the clusters studied must be X-ray luminous. The rationale identified here is that clusters with high X-ray luminosity will have a large gas content (high n_e), which, even in the presence of weak magnetic fields, will give rise to relatively large RMs. Large cluster RM contributions will then tend to dominate over the smaller Galactic RMs at these Galactic latitudes. Clusters with X-ray luminosities greater than 2×10^{44} ergs s^{-1} in the 0.1– 2.4 keV band were selected from the XBAC sample (Ebeling et al. 1996). This is a brighter cut-off than that chosen by Clarke (2000) who selected all clusters down to 1×10^{44} erg s^{-1} from the same sample.

A further concern was to select those clusters for which there was a high probability

Table 3.1: Selection criteria for the Southern Rich Abell clusters used in the statistical study of rotation measure in cores of non-cooling-flow clusters.

Criteria	Parameter	Range
Southern Sample	Declination	dec $\leq -30°$
Low $RM_{galactic}$	Galactic Latitude	$\|b\| \geq 30°$
Large Angular Size	Redshift	z ≤ 0.06
Independent n_e	X-ray Luminosity	$L_x \geq 2 \times 10^{+44}$ erg s^{-1}

of finding a polarised background source projected through the cluster core. If one assumes that the density of polarised background radio sources, which is a function of the telescope sensitivity, is constant across the sky, then the probability of finding a suitable background source behind the cluster core goes as the angular size of the core projected on the sky. That is to say, the larger the area of sky covered by the cluster the more likely it will be to find an acceptable probe behind it. As clusters appear to be approximately of equal physical size, this becomes a question of angular size, which is a function of redshift. At high redshifts, clusters will occupy a small solid angle and thus it becomes very unlikely to find a suitable background source. In order to give maximum probability of detecting a polarised probe, a low redshift cut-off for the sample was established. Only clusters with z less than 0.06 were examined. Table 3.1 re-iterates these criteria.

3.5.2 Observations of Southern X-ray Luminous Clusters of Galaxies

Applying the selection criteria outlined in Section 3.5.1 a list of nine suitable rich Southern X-ray luminous clusters was obtained. One cluster, A3532, which straddled the border for both the $-30°$ declination and Galactic latitude cut-off was discarded. Properties of the selected clusters are outlined in Table 3.2.

Archival total intensity ATCA data at 20cm were available for seven of these clusters. These data were examined to obtain a list of sources which might act as suitable probes to the cluster magnetic field. As this study was to focus on the cluster core, initially only sources which fell within the fifty percentile contour of the X-ray distribution and had a peak flux density at 20cm greater than 12 mJy per beam (using a 6 arcsecond beam) were selected. However, as this gave only twelve potential sources the criteria were relaxed to 4 mJy per beam in the fifty percentile X-ray contour and to also include sources which were projected through any part of the X-ray emission region and that had a peak flux density greater than 12 mJy per beam (using a six arcsecond beam). Two additional sources located behind the diffuse radio emission in A3667 was also included (see chapter 5). This generated a list of 39 candidate sources which are listed in Table 3.5.2. The double cluster A3395 was removed from the sample as the X-ray image shows clear signs of substructure, making it difficult to determine

Table 3.2: Southern Rich Abell clusters used in the statistical study on rotation measures in cores of non-cooling flow clusters. Col 1 is the ACO cluster name; col 2 the J2000 Right Accession; col 3 the J2000 Declination; col 4 the redshift; col 5 the X-ray flux in the 0.1–2.4 KeV band from Ebeling et al. (1996) and col 6 shows if 1.4 GHz data were present in the ATCA archive.

Name	RA_{J2000}	Dec_{J2000}	z	$L_x \times 10^{+44}$ (erg s^{-1})	Archival
A3667	20 12 30.1	-56 49 00	0.0560	8.76	yes
A3571	13 47 28.9	-32 51 57	0.0397	7.36	yes
A3558	13 27 54.8	-31 29 32	0.0477	6.27	yes
A3266	04 31 11.9	-61 24 23	0.0545	6.15	yes
A3562	13 33 31.8	-31 40 23	0.0502	3.33	yes
A3128	03 30 12.4	-52 33 48	0.0590	2.12	yes
A3158	03 42 39.6	-53 37 50	0.0590	5.31	no
A3395	06 27 31.1	-54 23 58	0.0506	2.80	yes

a suitable X-ray centre.

The cluster, A3158, for which there were no archival radio data was also observed at 20 and 13 cm for use in a future expanded study. A list of the sources found in A3158 is given in Table A.3 in Appendix A.

Table 3.3: Sources examined for the pilot study to determine suitable candidates for the statistical RM study. Column 1 gives the cluster that sources were seen in projection through; col 2 is the source identification; col 3 is the J2000 right accension and col 4 is the J2000 declination.

Sources examined for Pilot Survey			
Cluster	Source	RA_{J2000}	Dec_{J2000}
A3266	A3266_5e	04 29 57.160	-61 28 39.36
A3266	A3266_11	04 30 21.960	-61 46 27.89
A3266	A3266_1	04 31 56.910	-61 18 29.37
A3266	A3266_9	04 31 36.340	-61 44 35.83
A3266	A3266_2	04 31 13.090	-61 25 12.13
A3266	A3266_3	04 30 42.130	-61 27 18.13
A3266	A3266_4e	04 30 21.950	-61 31 59.90
A3266	A3266_5e	04 29 57.160	-61 28 39.36
A3266	A3266_10	04 30 25.930	-61 45 09.95
A3266	A3266_8	04 31 0.520	-61 11 50.19
A3128	A3128_3	03 30 57.110	-52 28 12.58
A3128	A3128_5	03 51 10.070	-52 28 46.71
A3128	A3128_7	03 30 1.960	-52 34 15.40
A3128	A3128_10	03 31 15.000	-52 41 47.98

continued on next page

continued from previous page			
Cluster	Source	RA_{J2000}	Dec_{J2000}
A3558	A3558_1e	13 28 29.880	-31 19 31.75
A3558	A3558_2	13 28 59.300	-31 26 24.96
A3558	A3558_5	13 27 53.500	-31 30 24.86
A3558	A3558_7	13 29 4.5100	-31 31 10.09
A3558	A3558_8	13 28 31.530	-31 35 06.04
A3558	A3558_10	13 92 13.300	-31 21 54.60
A3558	A3558_11	13 27 50.390	-31 21 01.98
A3558	A3558_13	13 28 02.580	-31 45 21.77
A3562	A3562_1	13 34 08.790	-31 28 37.76
A3562	A3562_3	13 33 37.370	-31 30 47.18
A3562	A3562_4	13 43 37.450	-31 32 52.74
A3562	A3562_5	13 34 22.480	-31 39 08.31
A3562	A3562_6e	13 33 31.566	-31 41 02.77
A3562	A3562_9	13 32 27.550	-31 23 55.57
A3571	A3571_1	13 47 54.100	-32 37 00.60
A3571	A3571_3e	13 48 07.620	-32 46 15.00
A3571	A3571_5e	13 47 25.280	-32 52 16.40
A3571	A3571_6	13 47 56.760	-33 01 08.54
A3571	A3571_8	13 47 26.400	-32 29 30.39
A3667	A3667_1	13 47 54.100	-32 37 00.60
A3667	A3667_A	20 11 09.272	-56 26 59.59
A3667	A3667_26e	20 11 27.540	-56 44 06.60
A3667	A3667_28	20 09 29.540	-57 00 59.42
A3667	A3667_16	20 15 18.740	-56 34 23.32
A3667	A3667_17	20 09 25.368	-56 33 26.76

In order to have sufficient points in the $\chi - \lambda^2$ plane to give an unique fit to the RM, sources were required to have at least 5σ detection of polarisation at the four frequencies chosen for this study (see Section 3.3.2 for details). However, unlike the study of Clarke who was able to make use of the polarimetric data from the NVSS for selection of suitable polarised probe sources, this study had out of necessity to begin with a polarimetric pilot survey of the selected sources.

3.5.3 Observations

In order to establish percentage polarisation the 40 candidate sources were targeted for ATCA observation in continuum mode at 20 and 13 cm and both ends of the 6cm band (4.7 and 6.7 GHz). The sources were initially observed for a period of 1 hour in "cuts" mode (see Section 2.3.4). Data were examined using the UVFLUX routine in *MIRIAD* . This routine provides information on the amplitude and associated noise in each of the Stokes values. The outputs of the process are given in Table A.1 of Appendix A. The results of UVFLUX were then used to determined the total polarised

flux and percentage polarisation observed for all sources at each frequency, the full set of results are given in Table A.2 of Appendix A while a condensed version is given here in Table 3.4. It should be noted that UVFLUX is most useful for determining characteristics of point sources. However the cores of the extended sources were also examined using the software in this initial pilot program. This was not the optimal way to investigate the extended sources as, in general, while the core maybe the brightest part of the source in these images, it is likely to be less polarised then the surrounding low surface brightness material. However, it was felt this was an acceptable procedure for the initial survey.

Table 3.4: 4.7 and 6.7 GHz properties of sources used in statistical RM study. Column 1 is the source identification; col 2 is the observed flux density at 4.7 GHz in mJy; col 3 is the observed polarised flux density at 4.7 GHz in mJy; col 4 is the percentage polarisation at 4.7 GHz; col 5 is the observed flux density at 6.7 GHz in mJy; col 6 is the observed polarised flux density at 6.7 GHz in mJy; col 7 is the percentage polarisation at 6.7 GHz and col 8 shows if the source was selected to go to the next observing phase.

Pilot Survey Results							
Source	$S_{4.7}$ (mJy)	$P_{4.7}$ (mJy)	$\%P_{4.7}$	$S_{6.7}$ (mJy)	$P_{6.7}$ (mJy)	$\%P_{6.7}$	Used
a3128_10	50.3 ± 0.2	1.7 ± 0.3	3.4	46.5 ± 0.4	0 ± 0.4	0.1	Y
a3128_1e	3.4 ± 0.2	1.6 ± 0.3	46.7	0.8 ± 0.3			N
a3128_3	3.8 ± 0.2	1.7 ± 0.3	45.5	1 ± 0.3			N
a3128_5	42.4 ± 0.4	2.6 ± 0.3	6.1	24 ± 0.4	2.5 ± 0.4	10.4	Y
a3128_7	2.8 ± 0.2	1.5 ± 0.3	53.6	1.7 ± 0.3	0.1 ± 0.4	6.4	N
a3266_1	5.5 ± 0.3	1 ± 0.3	18.2	2.3 ± 0.4	0.3 ± 0.5	14.7	N
a3266_10	20.2 ± 0.3	0.6 ± 0.4	3.2	11.9 ± 0.4	1 ± 0.5	8	N
a3266_11	10.1 ± 0.3	0.4 ± 0.3	4.3	6.7 ± 0.4	0.5 ± 0.5	7.8	N
a3266_2	2.4 ± 0.2	0.9 ± 0.3	39	0.7 ± 0.3			N
a3266_3	9.1 ± 0.7	1.4 ± 0.4	15.4	3.8 ± 0.5	0.3 ± 0.5	7.9	Y
a3266_4e	114 ± 1.2	2.7 ± 0.4	2.4	76.3 ± 1.3	0.9 ± 0.5	1.2	Y
a3266_5e	3.2 ± 1			-0.8 ± 0.6			N
a3266_8	67.5 ± 0.6	0.3 ± 0.4	0.5	40.8 ± 0.5	1.3 ± 0.5	3.1	N
a3266_9	10.5 ± 0.3	0.7 ± 0.4	6.3	5.9 ± 0.4	0.5 ± 0.5	8.3	N
a3558_10	8.4 ± 0.3	2.7 ± 0.3	32.2	4.4 ± 0.4	0.8 ± 0.5	17.3	Y
a3558_11	3.1 ± 0.2	2.8 ± 0.3	89.4	0.4 ± 0.4			N
a3558_13	10.3 ± 0.3	2.9 ± 0.3	28.5	6.3 ± 0.4	0.3 ± 0.5	4.6	Y
a3558_1e	5.4 ± 0.2	2.3 ± 0.3	42	1.4 ± 0.4			Y
a3558_2	4.1 ± 0.3	3.1 ± 0.3	77.4	0.5 ± 0.4			N
a3558_5	1.8 ± 0.3	2.8 ± 0.3	152	1.4 ± 0.4			N
a3558_7	36.2 ± 0.3	2.3 ± 0.3	6.3	24.9 ± 0.4	0.5 ± 0.5	1.9	Y
a3558_8	29.5 ± 0.4	5.6 ± 0.3	18.8	11.7 ± 0.5	1.2 ± 0.5	10	Y
a3562_1	3.9 ± 0.3	2.4 ± 0.4	62.2	0.9 ± 0.4			N

continued on next page

continued from previous page

Source	$S_{4.7}$ (mJy)	$P_{4.7}$ (mJy)	$\%P_{4.7}$	$S_{6.7}$ (mJy)	$P_{6.7}$ (mJy)	$\%P_{6.7}$	Used
a3562_3	5.2 ± 0.2	3.1 ± 0.4	59.7	2.1 ± 0.4	0.8 ± 0.6	37	Y
a3562_4	1.6 ± 0.2	2.8 ± 0.4	179.5	-0.1 ± 0.4			Y
a3562_5	4.5 ± 0.2	2.8 ± 0.4	62.7	2 ± 0.4			Y
a3562_6e	2.7 ± 0.3	2.3 ± 0.4	87.6	0.8 ± 0.5			Y
a3562_9	6.4 ± 0.3	2.4 ± 0.4	37.9	2.7 ± 0.5	0.8 ± 0.7	30.5	N
a3667_1	0.8 ± 0.7			-4.5 ± 0.7	0.3 ± 0.6	-5.5	N
a3667_11	1.4 ± 0.3	1.4 ± 0.4	101.7	0.1 ± 0.4			N
a3667_16	1 ± 0.3			-1.1 ± 0.4			N
a3667_17	2.3 ± 0.3	1.6 ± 0.3	69.9	-0.3 ± 0.4			Y
a3667_26e	7.1 ± 0.5	1.6 ±	22.3	9.6 ± 0.5	0.2 ± 0.5	1.7	Y
a3667_28	5.3 ± 0.3	1.3 ± 0.3	24.8	3.6 ± 0.4	0.4 ± 0.6	9.8	N
a3667_a	7.3 ± 0.3	1.1 ± 0.3	14.8	2.8 ± 0.4	0.7 ± 0.5	25.4	Y
a3571_1	5.6 ± 0.3	2.1 ± 0.4	36.5	2.4 ± 0.4	0.4 ± 0.6	18	Y
a3571_3e	24.4 ± 0.3	5.1 ± 0.4	20.7	11.8 ± 0.5	0.5 ± 0.6	4	Y
a3571_5e	3 ± 0.2	2.5 ± 0.4	84.8	0.4 ± 0.4			N
a3571_6	1.8 ± 0.2	1.9 ± 0.4	101.6	-0.1 ± 0.4			N
a3571_8	35.6 ± 0.3	2.2 ± 0.4	6.1	23.2 ± 0.5	0.7 ± 0.6	3.2	N

Unfortunately, the observations centred at 6.7 GHz were in a region of the band where only spectral line observing is usually performed as the system temperatures are quite high. As a result, these data were of very poor quality and it was not possible to determine reliable source characteristics at this frequency. For all subsequent observations the frequency was shifted to 6.2 GHz to avoid the high system temperatures at the very edge of the band. Nevertheless, the 4.7 GHz data were used to obtain a list of 18 suitable cluster probes for re-observation. Sources were selected if they had a 5σ detection in both I and one of either Q or U and the total linear percentage polarisation was less than 45%. As these data are not corrected for Ricean noise bias it is important to selected in regions of high signal-to-noise ratios in order to reduce this effect. Thus, the 5σ cut off in either Q or U was selected.

This gave a list of 15 sources. However, for the cluster A3562, this gave only one source (a3562_4e). For this cluster the last criterion was relaxed and this gave an additional 3 sources. Two anomalies occured in the sources selection here; the first was that the source a3571_8, which did fulfill the selection criteria, was accidentally omitted from the follow-up source selection, the second is that the sources a3667_28 and a3667_17 were accidentally switched and a3667_17 was observed in the follow-up study. This turned out to be fortuitous as a3667_17 turned out to be sufficiently polarised for a RM fit to be obtained and as the source was seen in projection through the Mpc-scaled region of diffuse emission in A3667 this was of great interest (see Chapter 5). Thus, from 39 potential targets 15 were selected and an additional 3 added. This is a similar attrition rate to that experienced by Clarke who began with roughly 250 sources and obtained less than 60 useable sources (Clarke 2000, private communication).

Table 3.5: The 20cm flux of the sources selected for the statistical RM study. Col 1 is the source identifications; col 2 is the J2000 right accension; col 3 is the J2000 declination; col 4 is the peak flux density at 1.4 GHz in mJy; col 5 is the known optical identifcation and col 6 is the redshift.

1.4 GHz properties of sources used in statistical RM study					
Source	RA_{j2000}	Dec_{j2000}	$S(peak)_{1.4}$	Optical Id	z
A3128_5	03 51 10.070	-52 28 46.71	186.0		
A3128_10	03 31 15.000	-52 41 47.98	44.0	APMBGC 155-096-118	0.0665
A3266_3	04 30 42.130	-61 27 18.13	9.7	J0430419-612716	0.0632
A3266_4e	04 30 21.950	-61 31 59.90	165.9	J0430219-613201	
A3558_1e	13 28 29.880	-31 19 31.75	22.0		
A3558_7	13 29 4.510	-31 31 10.09	76.5		
A3558_8	13 28 31.530	-31 35 6.04	98.6		
A3558_10	13 92 13.300	-31 21 54.60	14.7		
A3558_13	13 28 2.580	-31 45 21.77	17.7	J1328026-314520	0.0429
A3562_3	13 33 37.370	-31 30 47.18	27.1		
A3562_4	13 43 37.450	-31 32 52.74	13.9		
A3562_5	13 34 22.480	-31 39 8.31	13.2		
A3562_6e	13 33 31.566	-31 41 2.77	20.0	A3558:[MGP94] 4108	0.0482
A3571_1	13 47 54.100	-32 37 0.60	11.7		
A3571_3e	13 48 7.620	-32 46 15.00	101.7		
A3667_A	20 11 9.272	-56 26 59.59	35.1		
A3667_26e	20 11 27.540	-56 44 6.60	93.4	SC 2008-565:[PMS88] 037	0.0552
A3667_17	20 09 25.368	-56 33 26.76	48.5		

The 18 sources given in Table 3.5 were re-observed in the short observation mode on the ATCA at 1.4, 2.4, 4.7 and 6.2 GHz over the period from Feb 1999 to November 2000. This was to both improve the signal-to-noise ratio and thus reduce the effect of Ricean noise bias and to obtain a 4th frequency for the fitting since the 6.7 GHz data were not useable. Observations at 1.4 and 2.4 GHz were carried out simultaneously using a 6 km configuration while the observations at 4.7 and 6.2 GHz were performed using a 1.5 km configuration so as to match the resolution of the lower frequency observations. Data were then reduced in the *MIRIAD* suite using standard calibration procedures (see Section 2.5). Tapering in the $uv-$plane was applied in order to lower the resolution of each observing frequency to that of the 1.4 GHz images. Images of all four Stokes parameters were then made at all four frequencies and total polarisation and position angle images were calculated. In all cases the images were used to measure the polarisation and position angle of the brightest part of each source. For the extended sources this meant that the core was used initially. It was then planned that a proper treatment of the extended sources would follow. Unfortunately time constraints prevented this from occuring. Nevertheless, useful data were obtained for RM fitting.

3.5.4 Polarisation Data

It has been well established that while the total intensity of radio sources usually decreases inversely with the observing frequency, the percentage polarisation increases. Thus, there was always some risk that sources selected with sufficient polarised flux at the two higher frequencies would not be detectably polarised at the lower frequencies. This turned out to be the case for some of the sources in the final sample. There were also other problems with five sources not well detected in polarisation at any of the frequencies used in the final sample. Of these 1 was only just detected in the pilot survey above the 5σ level in the un-corrected for Ricean bias data and it is thus not suprising that it turned out not to be polarised. However, the other 4 sources all had greater than 10σ detections for polarisation at 4.7 GHz in the pilot survey, and it is a puzzle as to why they were not at least detected again at this frequency. Table 3.5.4 gives the measurable position angles for each source at each frequency. As only sources which had a measurable postion angle for at least three frequencies could be used for reliable RM fitting, this reduced the sample to 11. The source "a3558_1e" was partly resolved into a double radio galaxy with considerable polarisation in both lobes at three of the observing frequencies. Position angle measurements were taken separately from each lobe, this provided an additional line of sight through the ICM bring the total number of RM obtained to 12.

Table 3.6: Observed Position angle results for the RM Source Sample. Col 1 gives the source name; col 2 is the measured position angle at 1.4 GHz in degrees; col 3 is the measured position angle at 2.4 GHz in degrees; col 4 is the measured position angle at 4.7 GHz in degrees; col 5 is the measured position angle at 6.2 GHz in degrees; col 6 is the distance from the cluster centre, often called the impact parameter, in kiloparsecs and col 7 is the sources rotation measure in rad m^{-2}.

Observed Position Angle Results							
Source	$\psi_{1.4}$	$\psi_{2.4}$	$\psi_{4.7}$	$\psi_{6.2}$	Notes	$Dist_{kpc}$	RM
a3128_5	57 ± 4	9 ± 4	-49 ± 1	-51 ± 1	extended	457	43.7± 3.9
a3128_10	23 ± 10	16 ± 4	22 ± 5	35 ± 10	point		-75.9± 9.2
a3266_3					extended		
a3266_4e	-13 ± 8	-2 ± 0.8	-72 ± 2	-82 ± 4	extended	501	99.7± 5.8
a3558_1en	4 ± 1	-42 ± 3	-55 ± 7		extended	423	25.0 ±7.5
a3558_1es	-48 ± 1	16 ± 3	-27 ± 8		extended	423	66.4 ±6.1
a3558_7			-12±6		point		
a3558_8	-56 ±0.4	-74 ± 1	-86 ± 1	-85 ± 3	point	375	-61.4 ±3.8
a3558_10					point		
a3558_13					point		
a3562_3	-25 ± 2	74± 6	-84 ±3		pointish		250.7 ±4.9
a3562_4					point		
a3562_5	-21 ± 3		-68 ±3	-70 ± 2	point	526	19.6± 4.7
a3562_6e			54 ± 4		headtail		

continued on next page

continued from previous page							
ource	$\psi_{1.4}$	$\psi_{2.4}$	$\psi_{4.7}$	$\psi_{6.2}$	Notes	Dist_{kpc}	RM
a3571_1					point		
a3571_3e	-48 ± 2	-58 ± 2	-75 ± 3	-89 ± 3	double	262	161.0 ±4.5
a3667_17	-22 ± 1	70± 2	39 ±2	52 ± 4	point	2276	-174.6 ±4.3
a3667_26e	-79 ± 3	51 ± 2	-53 ± 5	-43 ± 3	headtail	678	-86.2 ±4.9
a3667_a	-47 ± 1	68 ± 9	32 ± 3	41 ± 4	double	1700	-107.7± 4.3

3.5.5 RM Fitting

Plots of the position angle and frequency were examined. Due to the small number of points to consider it was not necessary to write a complicated fitting routine to find the best fit. Data were adjusted by hand under the assumption that there would be no rotation between the two closely spaced points at 4.7 and 6.2 GHz and that a maximum of 360 degrees ambiguity was likely to have occurred in the 1.4 GHz value. Assuming no rotation between the closely space values at 4.7 and 6.2 GHz allows for $|\text{RM}| \leq 1350$ rad m^{-2} to be fitted unambiguously. The resultant points were then passed through a standard linear least-squares fitting routine in Microsoft Excel. It was found in many cases that the 2.4 GHz points were difficult to reconcile with the other three measurements, giving slightly discrepant values. Despite efforts to minimise errors this is likely to be a result of the polarisation response of the 13cm feed on the ATCA. Though sources were observed near the beam centre in order to have the best polarisation characteristics at all frequencies it appears that some effect is still evident in the 13 cm data. Thus, the 13cm points were given less weighting during the fitting procedure. Figures 3.4 and 3.5 show the resultant plots, while the RMs obtained are listed in Table 3.6. Surprisingly the fitting worked extremely well with the worst case fit to the data still giving a 99 % confidence to a straight line.

It should be noted that the use of observations from a period spanning 18 months gives some concern as the data are not all from the same epoch. Nevertheless the quality of the RM fits is excellent and it is therefore assumed that there is no variation in the observed source RMs over this time scale.

3.5.6 Comparison to Other Data

The RMs obtained from the fitting procedure were then corrected for the contribution from the Galactic rotation measure, G_{RM} . This was done by using an interpolated all-sky rotation measure map generated from published RM catalogues. The map is an estimate of the Milky Way's contribution to the RM sky. The next chapter discusses in detail how this map was generated. The Galactic contribution was subtracted from the measured RM to give a residual RM, (RRM) which represents a combination of the cluster RM and the intrinsic source RM. Previous studies have used the standard deviation of the distribution of extragalactic RMs at high galactic latitudes, beyond the influence of the Galaxy, to argue that the contribution from internal RMs is small.

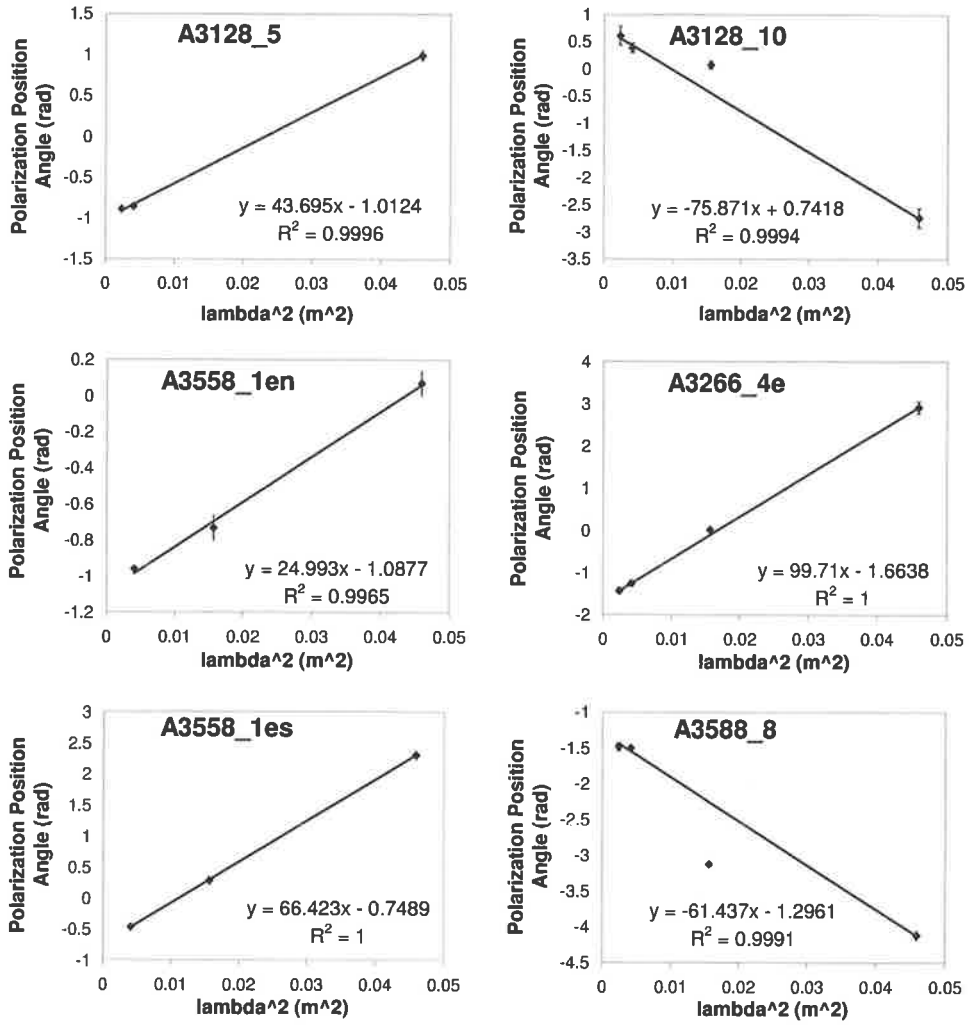

Figure 3.4: RM fits for the cluster sample examined here. The graph shows the equation of the line where the RM corresponds to the slope, the R^2 statistic which is a measure of the goodness of fit to a straight line is also given (an R^2 value of 1 corresponds to a perfect fit) .

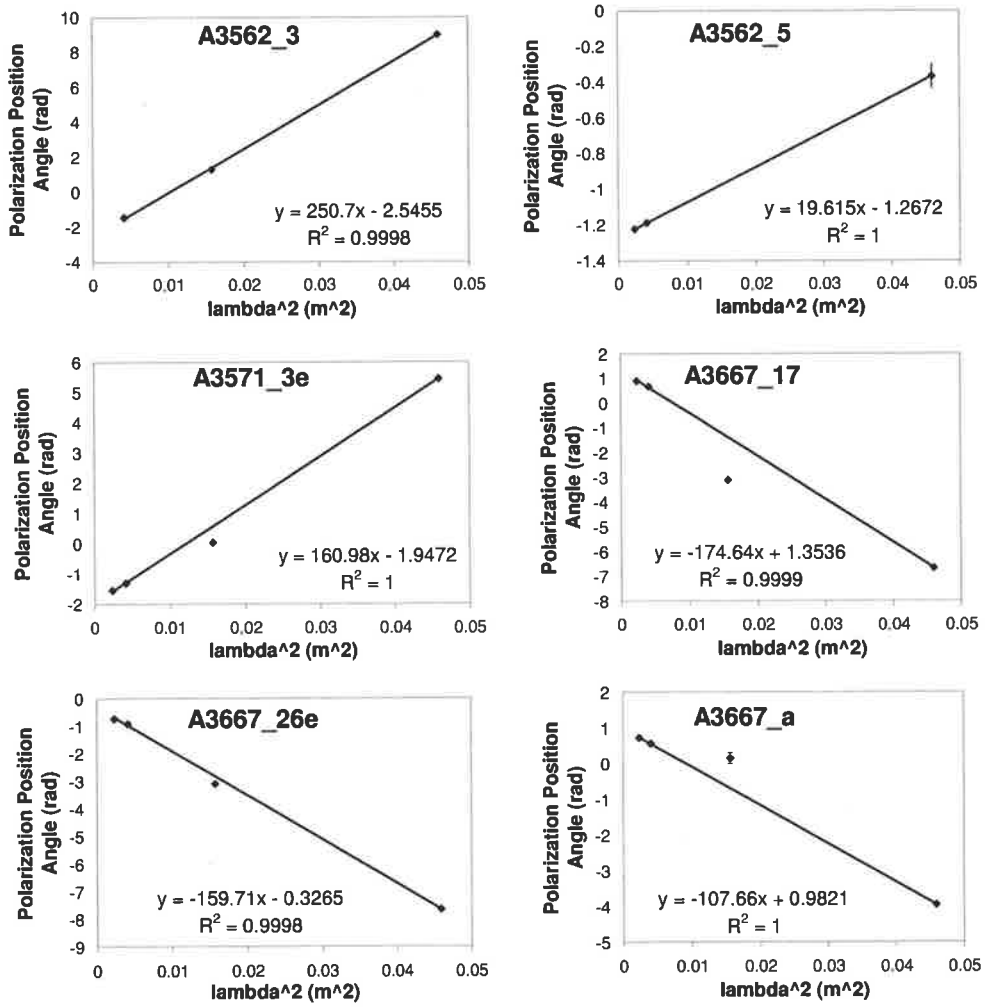

Figure 3.5: RM fits for the cluster sample examined here. The graph shows the equation of the line where the RM corresponds to the slope, the R^2 statistic which is a measure of the goodness of fit to a straight line is also given (an R^2 value of 1 corresponds to a perfect fit) .

The standard deviation of around 400 extragalactic RMs at greater than 30 degrees from the Galactic plane was found to be 10 rad m^{-2} (see Section 4.5). This suggests that the intrinsic RM component should be small and that RRM should adequately represent the Cluster contribution to the measured RM. Previously it was assumed that the distribution was Gaussian and thus the likelihood of encountering a moderate to high intrinsic RM was very low. However, further analysis of the high Galactic latitude extragalactic RM population has shown the distribution is exponential at above the 99.9% confidence level (see Section 4.5). This means that it is more likely to observe a background source with a significant internal contribution to the measured RM than previously thought. This reinforces the requirement to examine cluster magnetic fields statistically.

Clarke (2000) also corrected for the Galactic contribution via examining published RMs in a 15 degree radius about each cluster. In order to directly compare the two datasets, the RRMs from the Clarke sample were recalculated using the interpolated map. In most cases this made a 5-10% in the RRM values. The two samples were then plotted together on two graphs showing distance from the cluster centre (the so-called impact parameter) versus RRM and |RRM|. These plots are shown in Figures 3.6 and 3.7 respectively. Each plot shows the entire combined dataset out to an impact parameter of 9000 kpc in the top panel and restricted impact parameter range of 0 to 3000 kpc in the lower panel. The RRM of the southern cluster sample presented here (see Table 3.5.6) agrees well with the northern sample of Clarke which drops to a background level at around 800 kpc from the cluster core. The two labelled points are both from A3667 and are background sources to the largest and brightest diffuse radio emission region yet discovered (Röttgering et al. 1997). These two points are significantly above the RM level suggested by the other data. They are further beyond the region of X-ray emission in A3667 and should fall at a background level, the fact that they do not strongly suggests that these RMs are probing the magnetic field of the diffuse radio emission. The implications of this are discussed in Chapter 5.

The data for both lobes of the source A3558.1e show quite different RRMs (-0.5 and 41.9) despite being closely spaced. This may either be interpreted as due to tangling of the cluster magnetic field on scales of order of 10 kpc, or as a difference in the internal properties of the radio lobes. Observations of radio jets in low power radio sources have shown that the magnetic field is aligned along the jet and becomes tangled in the resultant lobes due to entrainment. Thus, it is likely here that we are seeing a combination internal and environmental effects.

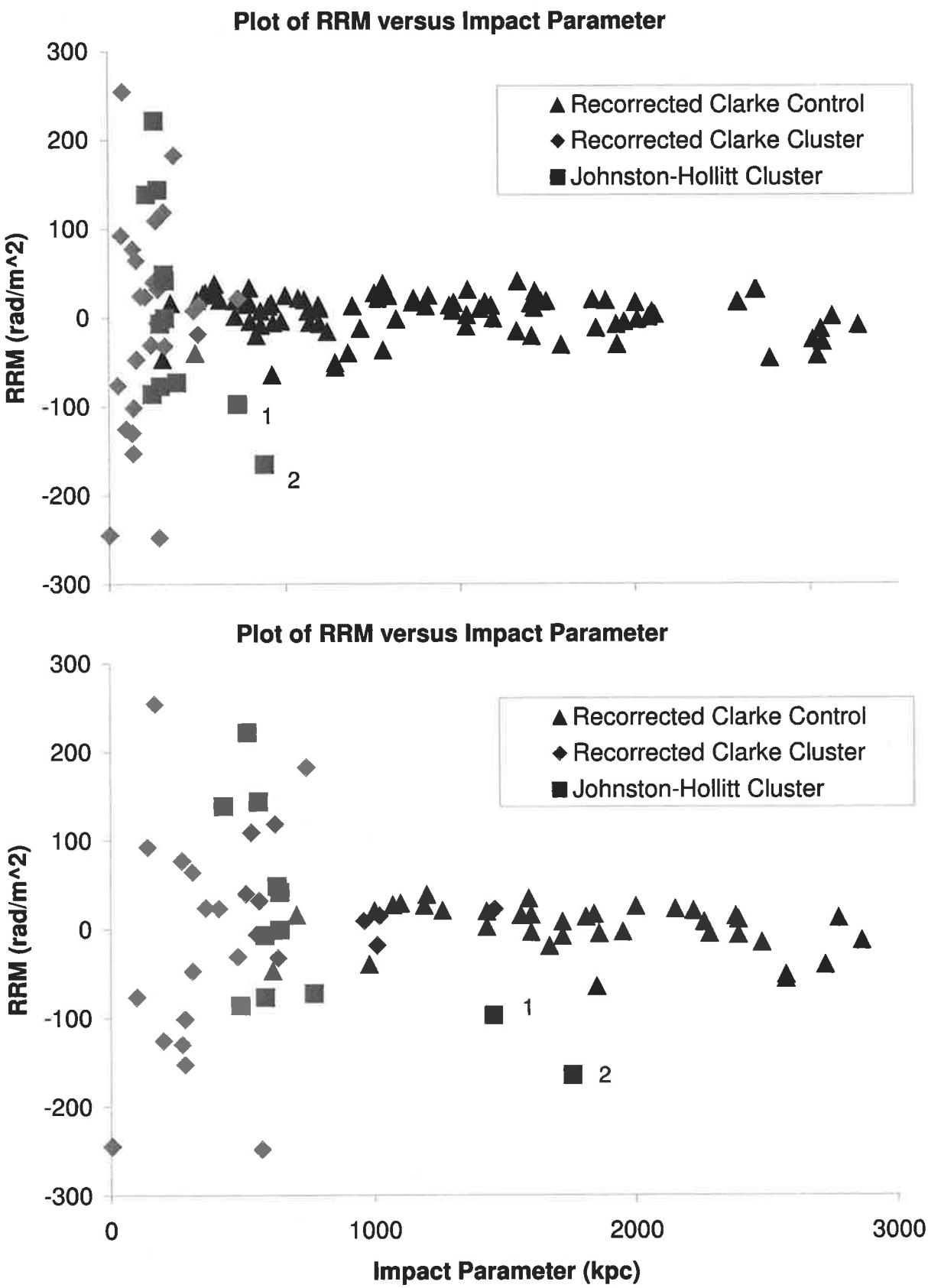

Figure 3.6: Impact Parameter versus Residual Rotation Measure. The labeled points correspond to sources seen in projection through a region of diffuse synchrotron emission in A3667 (see Chapter 5).

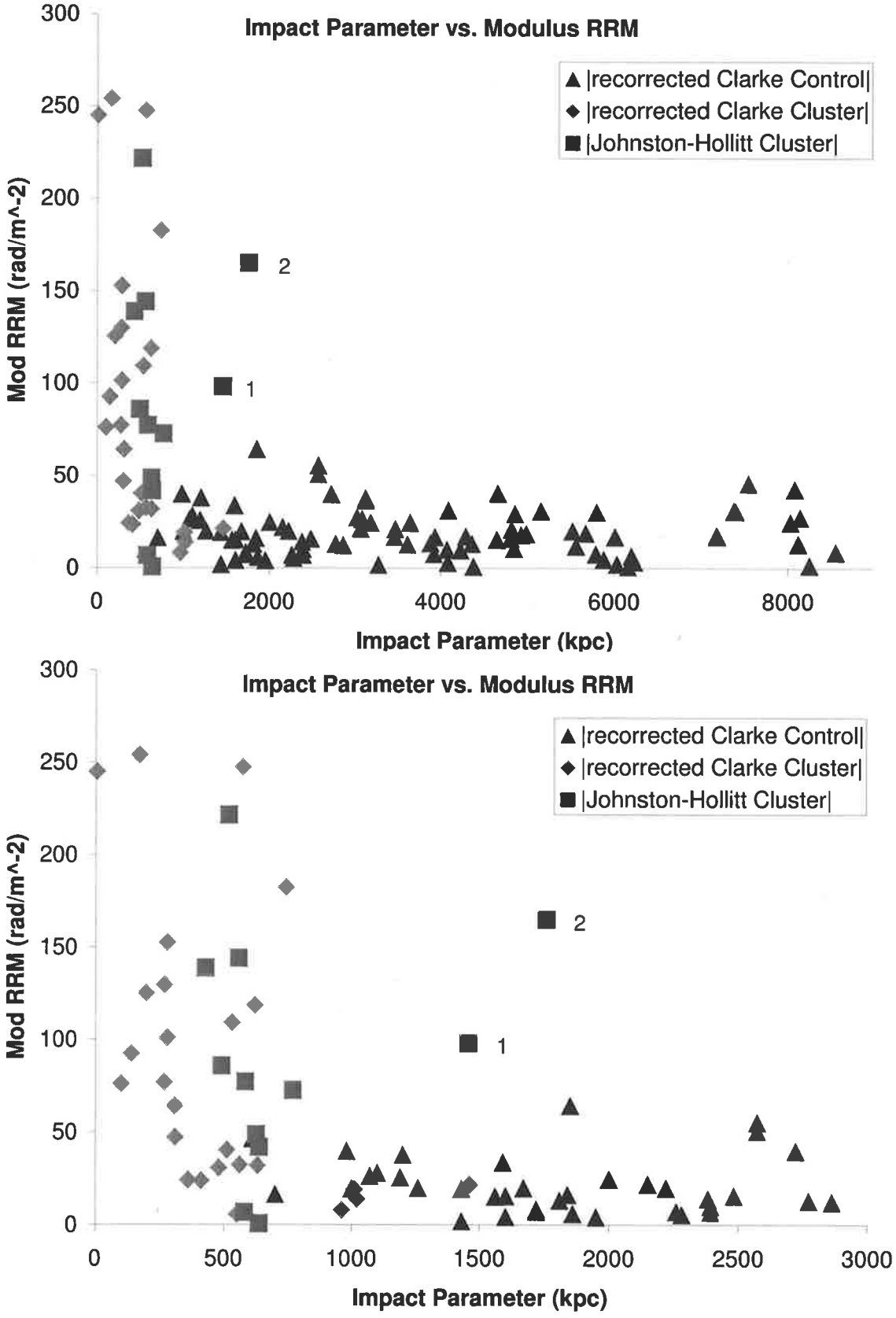

Figure 3.7: Impact Parameter versus Residual Modulus Rotation Measure. The labeled points correspond to sources seen in projection through a region of diffuse synchrotron emission in A3667 (see Chapter 5).

Table 3.7: Residual RM corrections. Column 1 gives the source name; col 2 is the J2000 galactic longitude; col 3 is the J2000 galactic latitude; col 4 is the Galactic contribution to the rotation measure at these co-ordinates as calculated with an interpolated all-sky rotation measure map (see Chapter 4) and col 5 is the residual rotation measure for each source once the Galactic contribution is subtracted.

Residual RM corrections				
Source	l	b	G_{RM}	RRM
A3266.4e	272.29	-40.23	-44.3	144.0
A3128.5	262.75	-48.20	-4.9	48.6
A3128.10	264.82	-50.91	-3.2	-72.7
A3558.1en	312.15	30.88	24.5	-0.5
A3558.1es	312.15	30.88	24.5	41.9
A3558.8	312.11	30.62	24.5	-85.9
A3562.3	313.37	30.50	29.1	221.6
A3562.5	313.52	30.34	26.3	-6.7
A3571.3e	316.49	28.60	22.2	138.8
A3667.A	341.32	-33.21	-9.5	-98.2
A3667.26e	340.98	-33.25	-9.5	-76.7
A3667.17	341.19	-32.97	-9.5	-165.1

With the exception of the points in A3667, these data agree well with the Clarke sample and support the finding that cluster magnetic fields are of the order 1–2 μG assuming a tangled cell model.

3.6 Summary

A discussion of Faraday rotation and its associated measurement errors was presented. Results of a search to detected excess Faraday rotation toward the cores of several Southern rich non-cooling flow clusters were presented. It was found that results of this study agreed well with those of the contemporaneous study of Clarke (2000), supporting the notion that a statistically significant broadening of the RM distribution is measured out to around 800 kpc for nearby galaxy clusters. This suggests cluster magnetic fields to be of the order of 1–2 μG assuming a tangled cell model.

Chapter 4

An Estimated All-Sky Rotation Measure Map

4.1 Introduction

This chapter was motivated primarily by the need to determine the physical extent and strength to which the magnetic field of the Milky Way interferes with obtaining accurate line-of-sight RMs for distant objects such as clusters of galaxies. It has been shown that the distribution of RMs obtained for distant objects has a statistical broadening, implying an enhancement of the magnetic field in these objects (see Section 3.6.3). In the case of galaxy clusters, this broadening is seen at distances out to 800 kpc from the cluster core (Clarke 2000). However, such measurements must account for an intrinsic source RM, the object RM and a Galactic contribution. Previous work of this type has assumed the probe source RM to be negligible. Such studies have then attempted to account for the Galactic component by averaging RMs of extragalactic background sources in some arbitrary radius on the sky around the object of interest. This value is then subtracted from the measured object RM to give a Residual Rotation Measure (RRM) (Govoni et al. 2001). Although this approach may, in some cases, give a good approximation to the actual Galactic RM contribution, it suffers from two major problems, being the arbitrarily sized averaging radius and the loss of spatial information on the Galactic contribution provided by the background sources. Applying this technique can result in a single large intrinsic RM source dominating the averaging, which will result in an over subtraction. Several authors have made an attempt to correct for the second problem by calculating the source RM distribution in their averaging area and removing those sources with RMs of more than an arbitarily designated number of standard deviations from the mean RM (Hennessy et al. 1989; Athreya et al. 1997; Clarke 2000). The standard deviation cut-off chosen is arbitrary (3, 1.3 and 2 were used in the three studies cited here) and due to the paucity of available extragalactic RMs this technique often suffers from poor statistics.

In order to provide a better solution a method was sought which would give greater weighting to nearby points but that would prevent single large RM values from dom-

inating the calculated value. Presented here is an estimated all-sky rotation measure map which is not subject to an arbitrarily chosen averaging scale and preserves the source spatial information. After investigating several interpolation algorithms, the 2-dimensional solution for Poisson's equation in combination with a statistical culling algorithm was chosen.

4.2 Interpolation

As mentioned above, a technique was sought to better interpolate the known RM data in order to estimate the Galactic contribution at any given point in the sky. Using code developed by Christopher Hollitt a range of algorithms were trialled for this purpose including, simple averaging, gaussian filtering and Delaunay triangularisation. After initial calculations the 2-dimensional solution to Poisson's equation was the preferred algorithm.

Unlike other common 2-dimensional interpolation techniques the 2-dimensional solutions of Poisson's equation allows a convergent interpolated solution for the rotation measure to be computed, whilst retaining the physical information provided by the source spatial distribution on the sky. It also uses all RM data over the entire sky, weighted against distance from the point of interest to determine an interpolated value. This algorithm uses information from a large number of sources in any calculation while allowing the points closest to the region of interest to provide the majority of information. The use of a statistical culling algorithm removes probe sources which are assumed to have an high intrinsic RM component.

Over 1000 extra-galactic RMs taken from several catalogues (Tabara & Inoue 1980; Simard-Normandin et al. 1981; Broten et al. 1988; Hennessy et al. 1989; Rudnick & Jones 1983; Lawler & Dennison 1982) were initially examined. Only those with a believable RM fit over at least three wavelengths were selected. In the case of sources appearing in more than one reference, the more reliable fit was used. This produced a final catalogue of 801 sources which was utilised in the two stage process. Appendix B gives the list of sources used.

First, a culling algorithm removed sources for which there was a three sigma deviation from the local median modulus RM. This was similar to previous techniques (Hennessy et al. 1989; Athreya et al. 1997) but rather than using a defined radius about an individual point the algorithm tests the population of at least the nine nearest neighbours. Moreover, unlike previous techniques, this technique estimates sigma from the median modulus value rather than simply the mean. The estimation process was then performed by obtaining a convergent solution to the 2 -Dimensional Poisson's equation (see Appendix B).

Figure 4.1 shows the resultant estimated RM map with the position of the measured data marked as crosses. The dashed line shows 30 degrees either side of the Galactic plane, which was the cut-off used to select clusters of galaxies for the RM study in Chapter 3 so as to minimise Galactic contamination.

The source density of this dataset is approximately 0.013 sources per square degree,

whereas the density of sources in the plane of the galaxy, as defined by $|b| \leq 30°$ is 0.01 per square degree. As the source density is quite low, particularly in the region of the Galactic plane, only large-scale features may be reliably inferred. However, with the imminent release of new Galactic plane survey data and the advent of better instruments such as the SKA, it is expected that this situation will be greatly improved. Never-the-less this map performs well for the purpose for which it was intended; as a tool for the removal of the Galactic contribution from the measured RM value along a particular line of sight.

4.3 Evaluation

In order to assess the robustness of the interpolated map it was compared to maps generated via simple low pass filtering (via Gaussian convolution) of the same culled dataset using different spatial scales. Figures 4.2 through 4.4 show the resultant images.

The low pass filtering is stable on scales of greater than 25 degrees, producing consistent large-scale features. This is similar to the stability scale determined by Frick et al. (2001) via wavelet analysis. The interpolated image also correctly reproduces these structures.

4.4 Structure Analysis

With such a dataset it is possible to statistically determine the region in which our Galaxy significantly affects RM measurements and even though this is only an approximation to the magnetic field influence of our galaxy there are two key results. Firstly, it can be seen that the influence of our galaxy on RM values extends to roughly 30 degrees either side of the Galactic plane, perhaps slightly more in the southern hemisphere. Secondly, it confirms the presence of large-scale positive and negative RM regions seen in the contemporary wavelet analysis study of Frick et al. (2001) which makes use of a similar dataset.

Comparison of these features with the position of the spiral arms as deduced from electron density models (Taylor & Cordes 1993) demonstrates that these features are likely to be correlated with the magnetic field in the interarm region between the Perseus and Sagittarius spiral arms. Figure 4.5 shows the spiral arms positions with the positive and negative RM regions marked in yellow and blue respectively. The number and position of field reversals in the Milky Way are critical to distinguish the gobal field as either axisymmetric or bisymmetric (Vallée 1996) and proponents of various models often have widely varing interpretations of the global direction of each arm and its associated interarm regions (Vallée, 1991; Clegg et al., 1992; Han & Qiao, 1994; Rand & Lyne, 1994; Vallée, 1996). It is generally agreed that the field rotates in a clockwise direction in the interarm region between the Perseus and Sagittarius-Carina arms and an anti-clockwise direction in the region between the Sagittarius-Carina and Scutum-Crux arms. In addition, the weight of the literature supports a clockwise

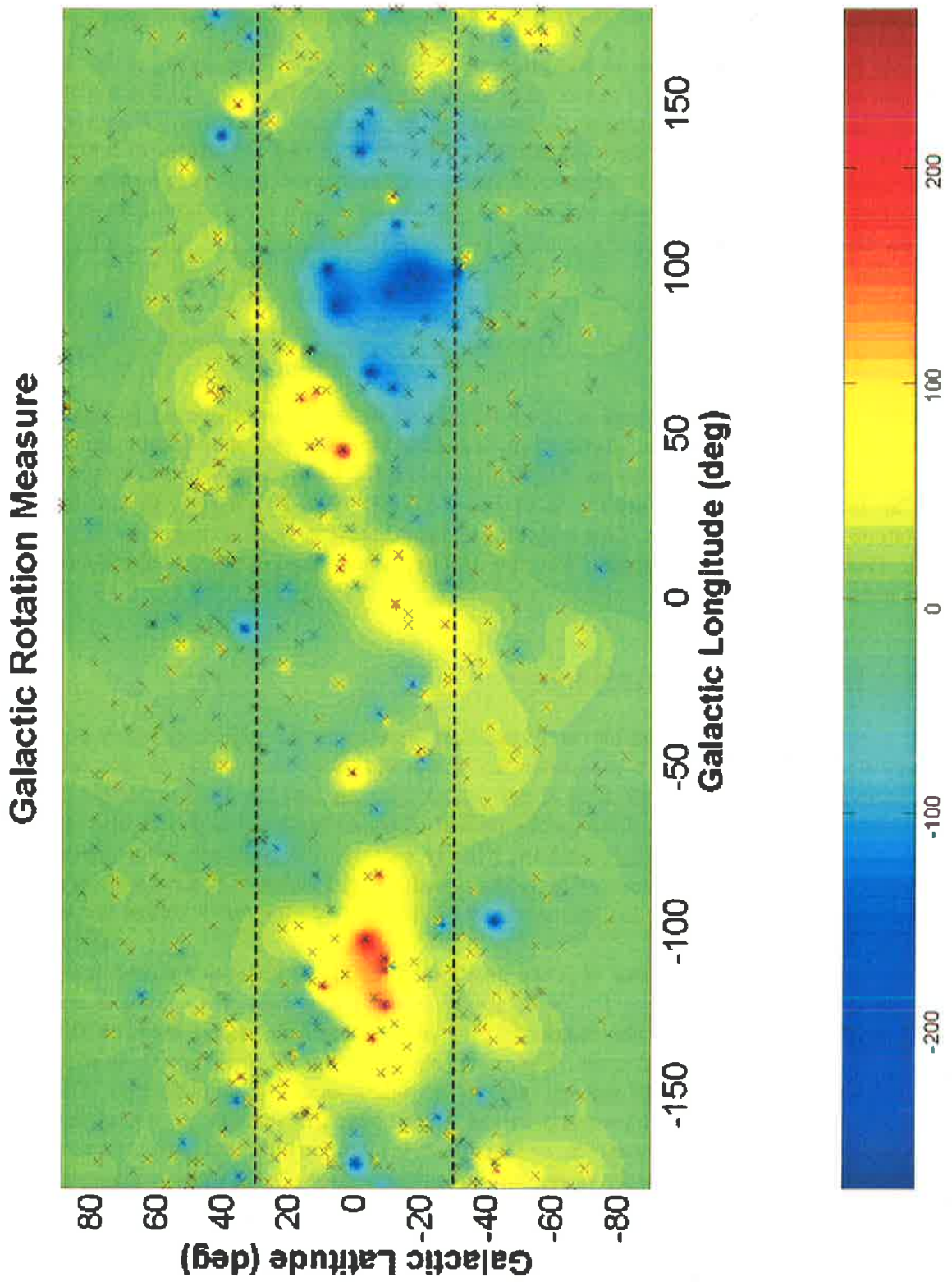

Figure 4.1: Interpolated All Sky Rotation Measure Map, created from over 800 published RM values calculated for extrag-alactic sources. Measured data are marked as crosses, the dashed line shows the cut off used to minimize contamination of the cluster RMs measured in the previous chapter.

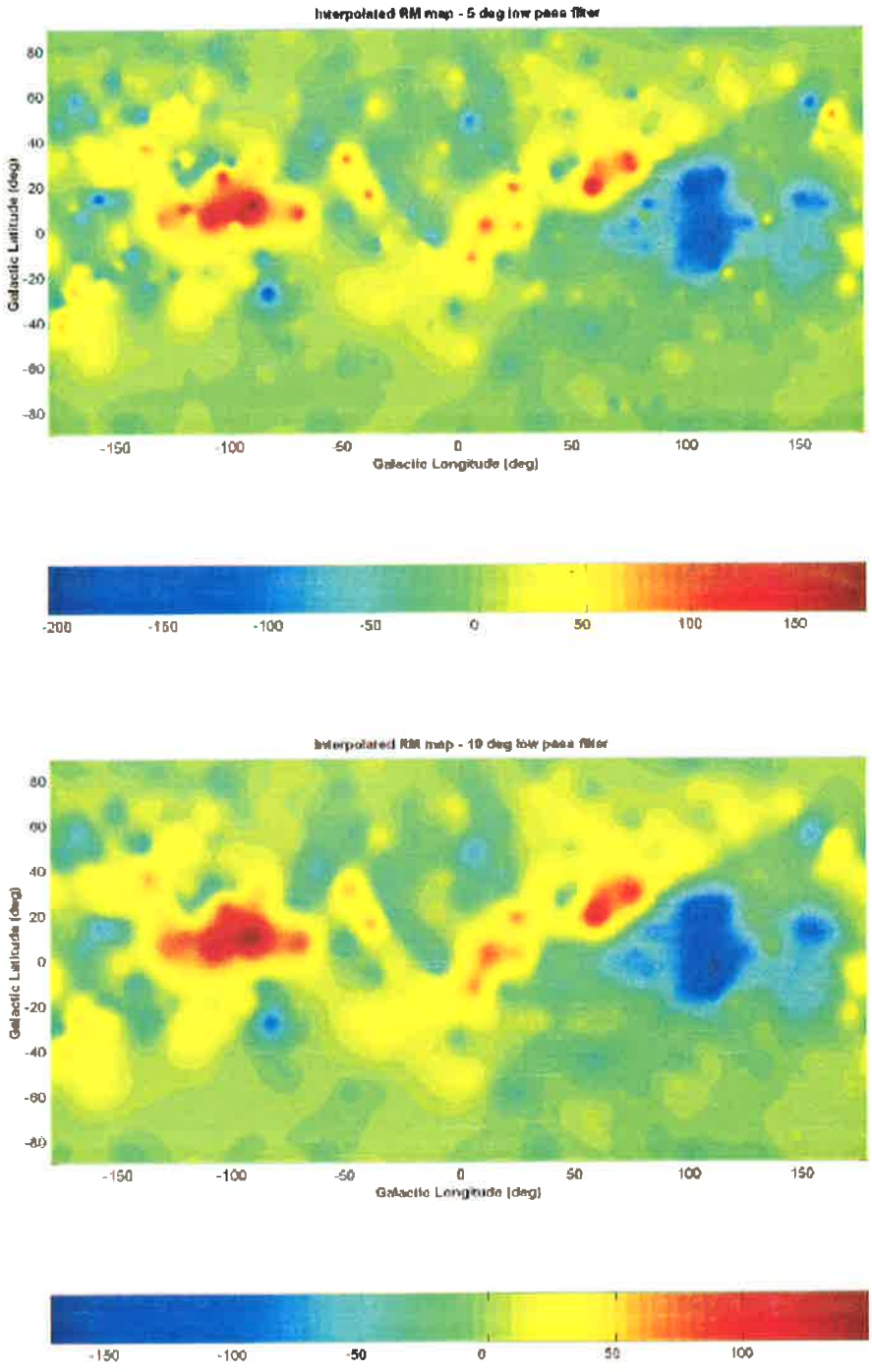

Figure 4.2: Low pass filtered RM sky using 5 and 10 degree filters.

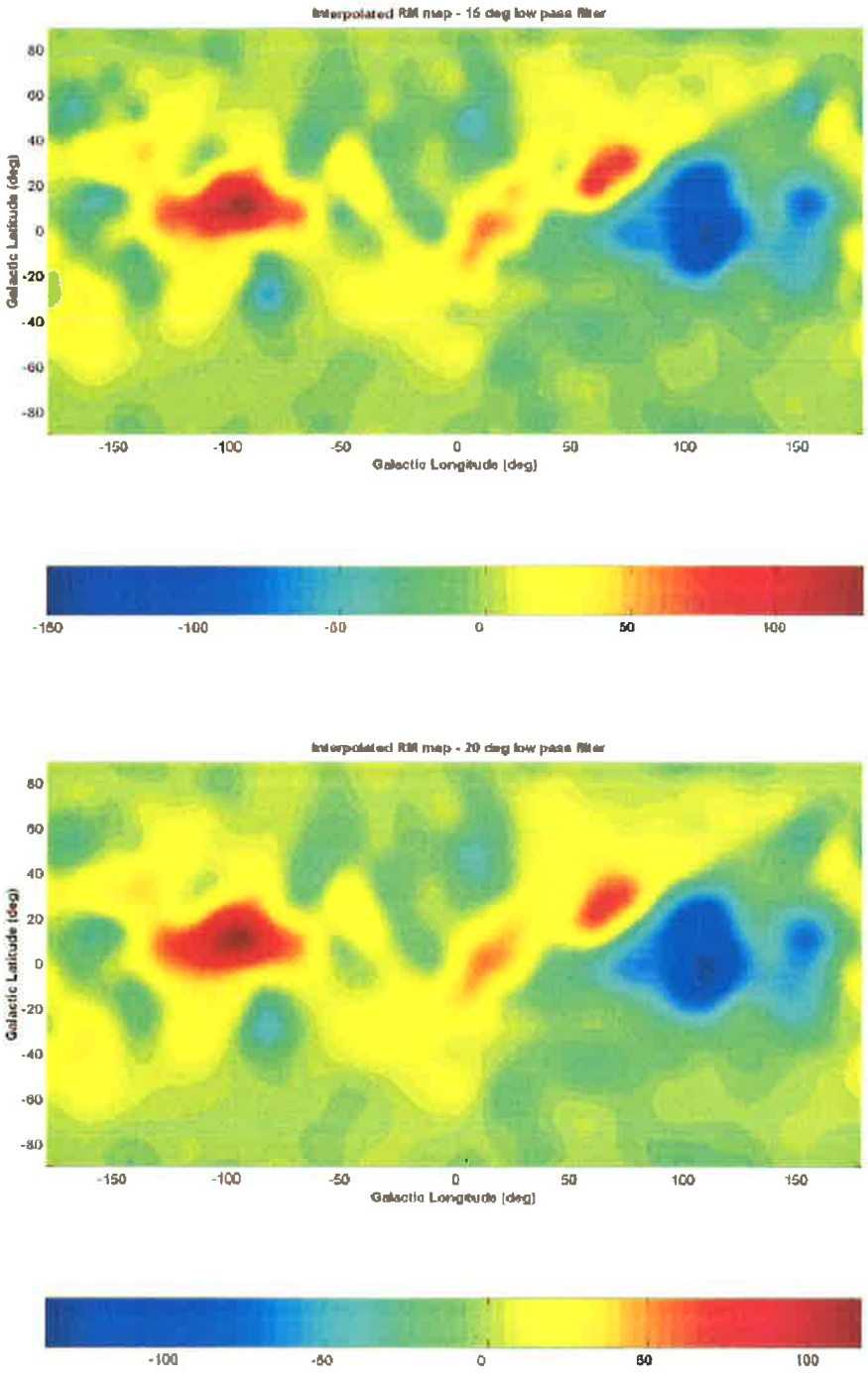

Figure 4.3: Low pass filtered RM sky using 15 and 20 degree filters.

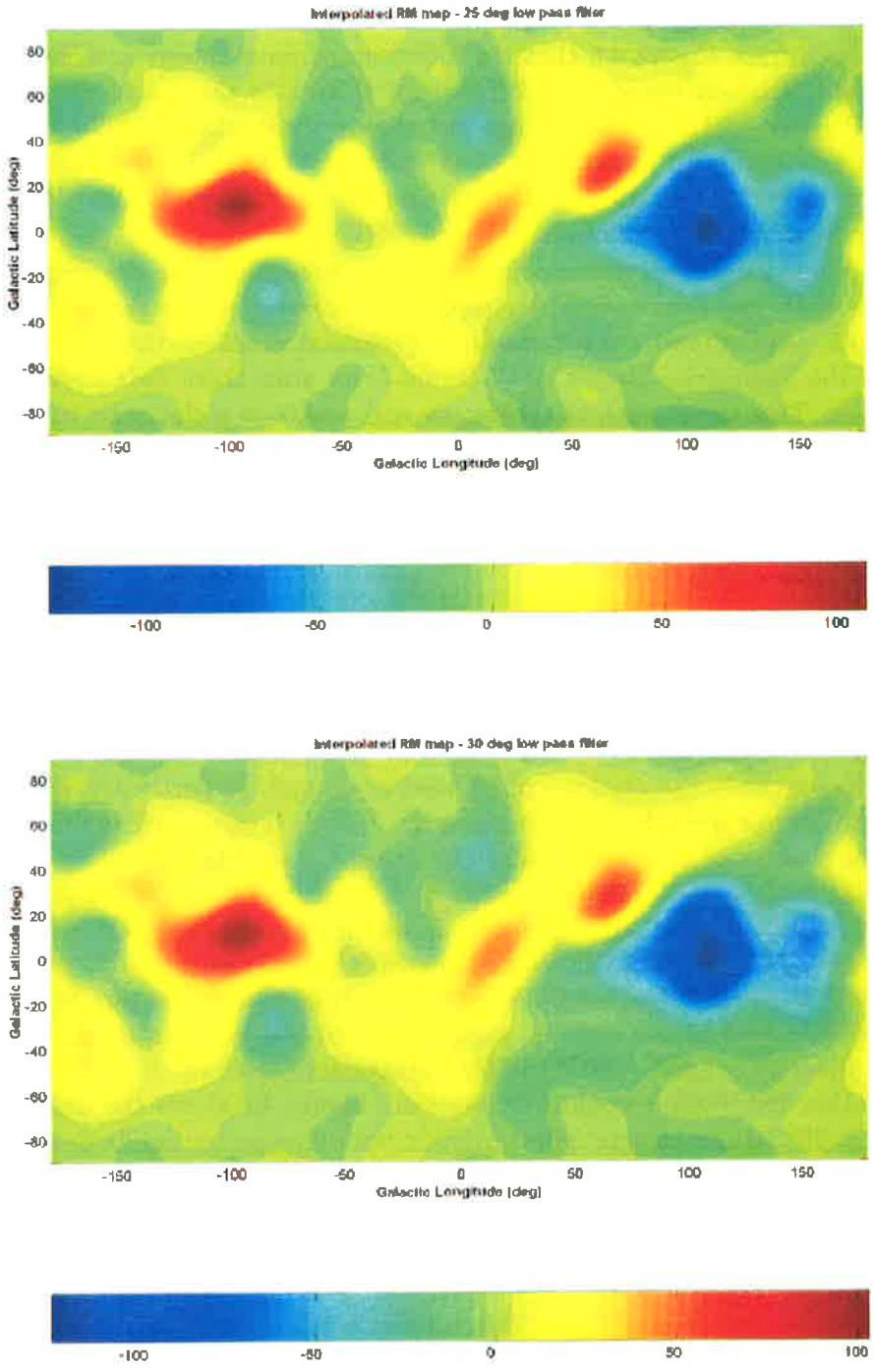

Figure 4.4: Low pass filtered RM sky using 25 and 30 degree filters.

rotation in the interarm region between the Scutum-Crux and Norma arms. However, the field direction between the other spiral arms in the outer and inner parts of the galaxy is an area of contention.

It can be seen from Figure 4.5 that the interpolated data appear consistent with a clockwise field direction beyond the Perseus spiral arm, in the region between the Perseus and Perseus +I arm , which is not included in the model of Taylor & Cordes (1993) but is located in the upper right of the plot beyond the Perseus arm (Vallée 1996). This is inconsistent with pulsar dispersion measures (Han & Qiao 1994) but agrees with models including other data (Vallée 1996).

The interpolated data are not conclusive for other regions. In the regions corresponding to both the Perseus/Sagittarius-Carina interarm region the interpolated data show both positive and negative features (coloured green on the plot). In the area between the Sagittarius-Carina and Scutum-Crux arms these data show a positive RM region. This agrees with the literature and points to a clockwise rotation of the magnetic field.

4.5 Source Statistics

Since the high degree of polarisation suggests ordered internal magnetic fields in the probe source, there will be an internal rotation measure component which will be added into the final result in spite of any culling performed.

In order to investigate the statistical behaviour of the sample, subsets of the data at various distances from the Galactic plane were examined. In particular, the region greater than 30 degrees from the Galactic plane was heavily investigated as this was the area where the clusters of galaxies examined in Chapter 3 were located. The standard deviation of 474 extra-galactic RMs at greater than 30 degrees from the Galactic plane was found to be 10 rad m^{-2}. Furthermore, it was discovered that at high galactic latitudes the source distribution follows an exponential. This result is both interesting and unexpected as at these latitudes one expects little or no contribution to the RM from the magnetic field of the Galaxy, suggesting that the exponential distribution must be a product of internal rotation in the extragalactic sources. It was previously thought that this distribution would be Gaussian. Figure 4.7 shows the distribution of RM at $|b| \leq 30°$ for the galactic plane overlaid with an exponential fit to the data. Figure 4.8 shows the same data but with a log-linear plot. Chi-squared testing shows this data to be exponential of the form Number of occurences = A exp(0.0037 $\times$ RM) (where A is a scaling constant in this case A=289) to greater than the 99.9% confidence. In comparsion, the distribution obtained from all data, i.e. including those RM's seen on lines-of-sight through the Galaxy shows a marked deviation from the exponential fit, especially for sources greater with modulus RMs greater than 50 rad m^{-2}.

Only by understanding the contribution of this internal component and accounting for it statistically can a true insight into the validity and robustness of such maps be obtained. This will be the focus of future work.

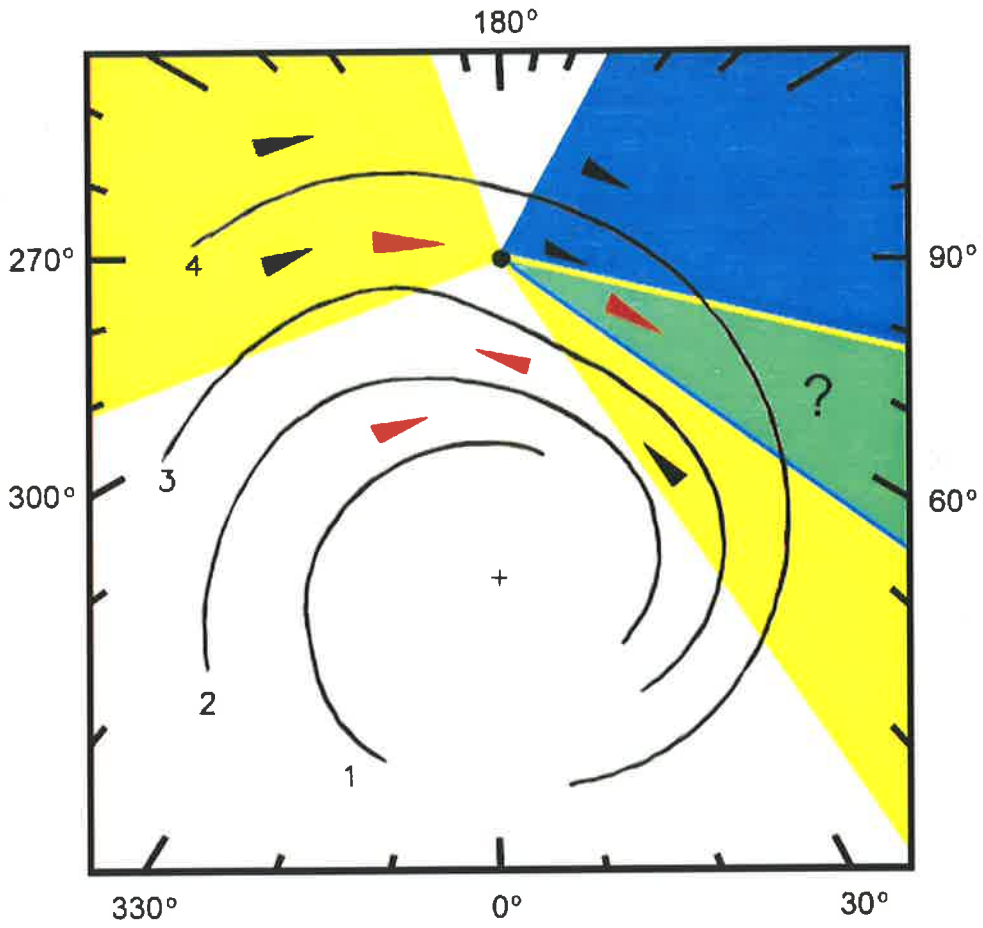

Figure 4.5: Location of spiral arms in the Milky Way after the model of Taylor & Cordes (1993). The circle in the centre shows the location of the solar system, while the coloured lines correspond to lines of sight through the galaxy where large scale features are seen in the interpolated RM map. As in the Interpolated RM map (Fig 4.1) yellow corresponds to a positive Rotation Measure and blue to a negative RM. The spiral arms are numbered, with 4 being the Perseus arm, 3 the Sagittarius-Carina arm, 2 the Scutum-Crux arm and 1 the Norma arm. The suggested outer arm, Perseus + I, is not shown here but is located beyond the Perseus arm in the upper right of this figure. The field directions agreed upon in the literature are shown as red arrows. The suggested field directions from the present study are shown as black arrows.

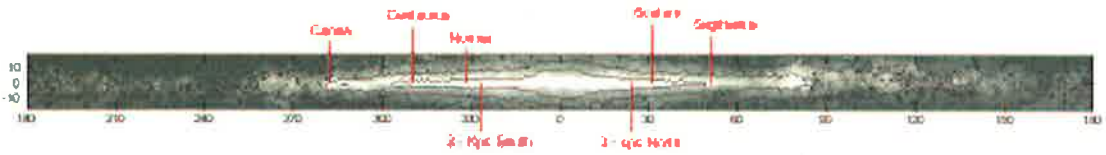

Figure 4.6: Cross section of the radio Milky Way showing the location of the sprial arms. The longitude has been reversed in order to make comparison to Figure 4.5 easier.

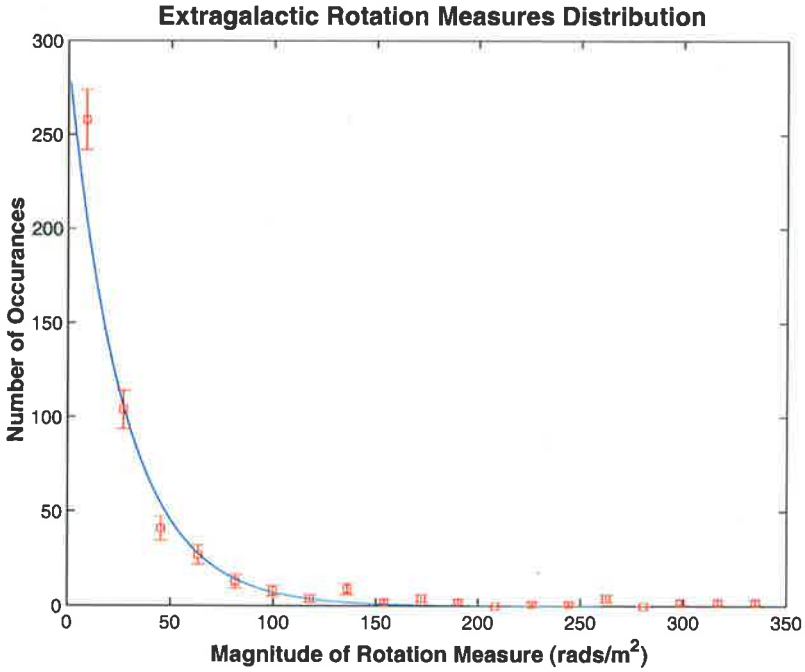

Figure 4.7: Plot of the extra-galactic RM distribution for sources greater than 30 degrees from the galactic plane. The dots represent the data, while the line is the chi-squared fit to the data.

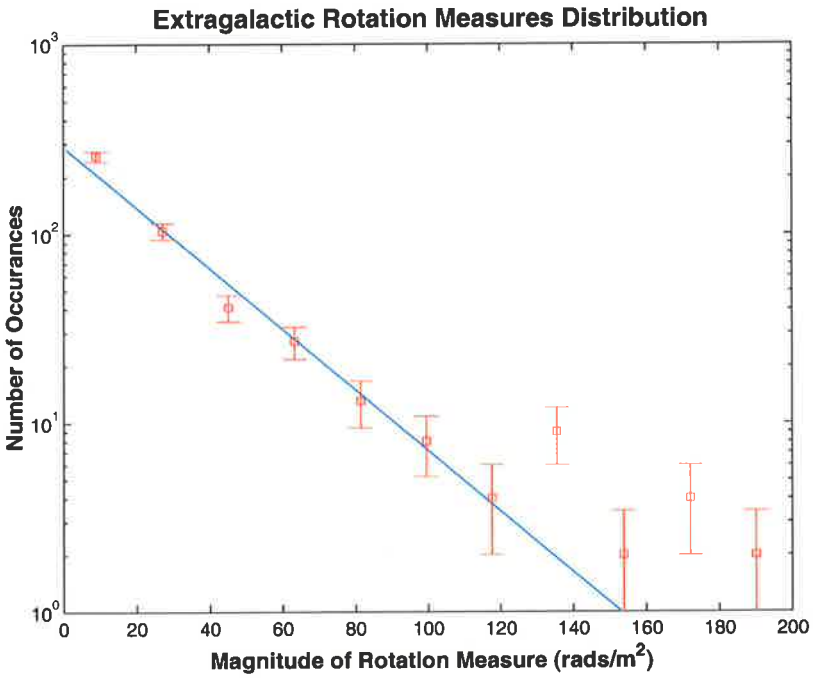

Figure 4.8: Plot of the extra-galactic RM distribution for sources greater than 30 degrees from the galactic plane shown as a log-linear plot. The dots represent the data, while the line is the chi-squared fit to the data.

4.6 Discussion

With the completion, or near completion, of major polarimetric surveys such as the Southern Galactic Plane Survey (McClure-Griffiths et al. 2001), and the Canadian Galactic Plane Survey (English et al. 1998), a wealth of new information on the magnetic field structure of our galaxy will soon become available. The expected boost in available data for this work is a factor of 5–10. Tantalising preliminary results have recently appeared, giving new insight into both the RM structure of the sky as seen through the Galaxy and the role of the magnetic field in diffuse Galactic plasma (Gaensler et al., 2001; Brown & Talyor, 2001). As these new data become available, better modelling and subtraction of the effect of the local field will be possible. This technique will continue to be useful in evaluating the rotation measure sky. However, since the greatest source of error is the lack of information on the behaviour of the Galactic magnetic field, it is likely that there are better ways to handle such a dataset. Radio astronomers face a similar problem when making images from incompletely sampled *uv*-data, as there is a non evenly spaced set of measurements over which one wishes to interpolate. However, in the case of radio astronomical imaging one can construct a model of the source because something is known about how simple radio sources behave. This can then be fed back into the processing. This gives an extra piece of information to allow a good map to be produced even from poor data (ie VLBI). However, here there is as yet, no model for what the magnetic structure of the Milky Way on all but the largest scales. Thus, the greatest source of error lies with the technique and can not be approximated in a simple way. In future, the Maximum Entropy Method, will be investigated as a better way of determining the interpolated RM sky and the errors associated with it.

4.7 Summary

This chapter presented an estimated all-sky rotation measure map generated from over 900 published rotation measures. This map was used in Chapter 3 to correct for the Galactic contribution to sources which were in the background of clusters of galaxies. Discussed here were the large scale features in the RM sky and comparisons made between these features and the position of Galactic spiral arms. Finally RM source statistics were addressed.

Chapter 5

Diffuse Radio Emission in A3667

5.1 Introduction

The presence of magnetic fields in galaxy clusters has been investigated in the previous chapter via Faraday rotation of extragalactic radio sources. However, this is not the only way such fields demonstrate their presence. Diffuse synchrotron emission also demonstrates the existence of such fields. In this chapter the galaxy cluster A3667 which is in the unique position of having two so-called radio 'relics', being regions of diffuse radio emission observed on the edge of galaxy clusters, will be investigated in detail.

5.2 Diffuse Radio Emission in Galaxy Clusters

Large scale diffuse radio emission was first discovered at low frequencies in the Coma cluster (Abell 1656) in the late 60's and early 70's (Bozyan, 1968; Wilson, 1970; Donivan et al., 1974; Jaffe et al., 1976). The detection was difficult due to the low surface brightness of the source and early attempts to uncover more such sources were mostly unsuccessful with a detection only in Abell 2256 (Bridle & Fomalont 1976) and marginal inferences for Perseus (Abell 0426) (Ryle & Windram 1968) and Abell 401 (Harris & Romanishin 1974) reported (later shown to be a blending of points sources rather than diffuse emission (Feretti & Giovannini 1996)). These early detections were problematic in that those undertaken on an interferometer (Ryle & Windram and Wilson using Cambridge and Jaffe et al. and using Westerbork) did not have the short spacing required to see large scale structure directly; it was inferred from extrapolations of the visibility functions. Conversely those observations performed with a single dish (Bozyan, Donivan et al. and Harris & Romanishin all using Arecibo) did not correct the observed brightness distribution for the known point sources. Bridle & Fomalont (1976) appears to be the first interferometric observation directly showing the large scale structure of the diffuse cluster emission.

The late seventies saw two more sources discovered, one in Abell 1367 (Gavazzi 1979), and the other in Abell 2319 (Harris & Miley 1978). Throughout the 80s the

Coma source dominated the research into diffuse emission with several groups reporting detections at increasingly shorter wavelengths (Hanisch et al., 1979; 1400 & 430 MHz Hanisch, 1980; Sastry & Shevgaonkar, 1983; Schlickeiser et al., 1987). However, despite the prolific study of Coma, or perhaps because of it, diffuse emission in other galaxy clusters began to be investigated, but the number of sources still remains relatively low with only around 50 sources known to date (Giovannini & Feretti 2000).

The origin of this emission was speculated upon by several authors. Jaffe (1977) was the first to investigate possible acceleration mechanisms in detail. He showed that second order Fermi acceleration can not give enough energy to the particles and first order Fermi is unlikely for geometric reasons and that neither convective or radiative process can compete with losses over the observed sizes of the emission regions.

By the early 80's three competing explanations had been proposed. The first of these, the *primary electron model*, proposed particle diffusion from radio galaxies as the cause of the diffuse emission (Jaffe, 1977; Rephaeli, 1979). This was the original "relic" hypothesis which assumes that particles from old radio galaxies have drifted away from the host galaxy which has then become dormant. In this scenario the spectral index of the diffuse emission would be steep and since emission times scales are known the size of diffuse emission would give an estimate of the bulk particle velocity.

The *secondary electron model* had energetic protons leaking from radio galaxies. In this scenario secondary electrons are formed via inelastic collisions between the relativistic protons and the thermal ions in the intracluster medium (Dennison 1979).

However, soon discovered that the spectral index of the diffuse emission in Coma was 1.3 which is not as high as expected for simple diffusion (Hanisch 1980). However, calculating an average spectral index over a large frequency range using data from different telescopes is difficult and it can be argued that this is not a sufficient condition to discount the model. What is much more concerning is the bulk diffusion speeds required in the larger relics in many cases this exceeds both the ion sounds speed and the Alfven speed (Hanisch et al., 1979; Hanisch, 1980). Thus, the primary and secondary electron models were put in serious doubt.

Finally the *in-situ acceleration model* where continuous acceleration occurs at the site of the observed emission was suggested (Jaffe, 1977; Roland, 1981). Acceleration processes proposed for the in-situ model included galactic wakes (Roland 1981) and bow shocks (Blandford & Ostriker 1978) and finally shocks from cluster-cluster mergers (Harris et al. 1980; Tribble 1993).

The first peripheral diffuse radio emission region found on a cluster edge was the one in A1367 (Gavazzi, 1978; Hanisch, 1980). Confusingly these peripheral sources came to be known as "relics" after the model thought to generate them. Fortunately even at the time of their discovery several authors thought they were NOT generated through the relic radio galaxy model, which was the dominant model at the time. In the case of A1367 there is no suitable host galaxy found in the optical and so it was concluded very early on that the particles must be accelerated in situ (Gavazzi 1978). Hanisch (1980) favoured inverse Compton scattering to link both radio and X-ray emission in galaxy clusters, however in the case of A1367 there is no X-ray emission in the region of the diffuse radio emission and so he concluded it must be a Head-Tailed galaxy phenomena

(Miley et al. 1972). However, further observations also ruled this hypothesis out.

In the models of Harris et al. (1980) and Tribble (1993), shock fronts on a scale large enough to accelerate Mpc sized fronts could be created, explaining the large extent of the observed emission, without having to worry greatly about diffusion times. This combined with the X-ray driven notion of cluster sub-structure became the most popular explanation for diffuse radio emission, spawning a whole field of research into cluster mergers and their connection to radio sources. Proponents of the model expanded on the theory producing ever more sophisticated scenarios to explain particular clusters in detail (Enßlin et al. 1998; Roettiger et al. 1999) and often the models were altered significantly to fit an individual clusters available data. It was not until the work of Ricker & Sarazin (2001) that a purely general merger induced shock model was applied to real data.

In all of these shock models the source of the particles was still a mystery. Several authors proposed tailed radio galaxies as the source of the particles (Röttgering et al. 1997; Enßlin et al. 1998), however this was often problematic as the jet axis was often not aligned to the direction of the diffuse emission (see Section 5.11). To over come this problem the concept of *fossil plasma* has recently developed (Enßlin 1999). In this model, long dormant patches of plasma litter the heavens, waiting to wakened by the acceleration of a passing shockwave, so that they may burst forth once more into radio brilliance. The most significant advantage of this model is that it provides an explanation as to why diffuse emission is not observed in all clusters which are in a supposed post merger state.

5.3 A3667

The ACO Cluster, A3667 (Abell et al. 1989), is arguably the most interesting and consequently most studied cluster in the Southern sky. However, although the physical picture of the cluster is constantly evolving as more multiwavelength data is obtained, it seems that many basic questions about the dynamical history of A3667 remain unanswered. The work presented in this chapter details the most sensitive radio images yet made of the entire cluster region and places them in context with the current understanding of cluster mergers and the generation of diffuse radio emission regions.

5.3.1 Physical Picture of A3667

A3667 is a rich, X-ray luminous, Southern galaxy cluster which has the distinction of being one of only a handful of galaxy clusters to have a cold gas front at the centre and the only cluster yet seen with two diffuse radio emission regions.

A3667 is relatively close, having a published redshift of 0.0550 based on the measurement of 123 galaxies in the cluster (Sodre et al. 1992). The Abell richness class is 2 and the Bautz-Morgan type is I–II (Haigh et al. 1997) indicating the presence of many galaxies in this region. Proust et al. (1988) report 423 galaxies with blue magnitudes up to $m_b = 19.0$ in the cluster field and, based on the isodensity plots for this

sample, conclude a bimodal optical galaxy distribution (see Section 6.2). The velocity dispersion is high at 970 km s^{-1} (Girardi et al. 1998), which places A3667 amongst the clusters of largest velocity dispersion (Sodre et al. 1992). ROSAT observations revealed a high X-ray luminosity with $L_x = 8.74 \times 10^{44}$ h_0^2 ergs s^{-1} in the 0.4–2.4 keV range (Ebeling et al. 1996), making it one of the brightest X-ray sources in the Southern sky. Further, the X-ray isophotes are distorted in the direction of the reported bimodal optical distribution and observations from the Einstein Satellite are reported as showing clear evidence of substructure (Sodre et al. 1992). Observations of the temperature of the X-ray gas with ASCA by Markevitch et al. (1999) showed the central part of the cluster to be cool and the X-ray surface brightness profile along the elongation axis suggests a shocked region is present. These features are shown in Figures 5.1 and 5.2 respectively.

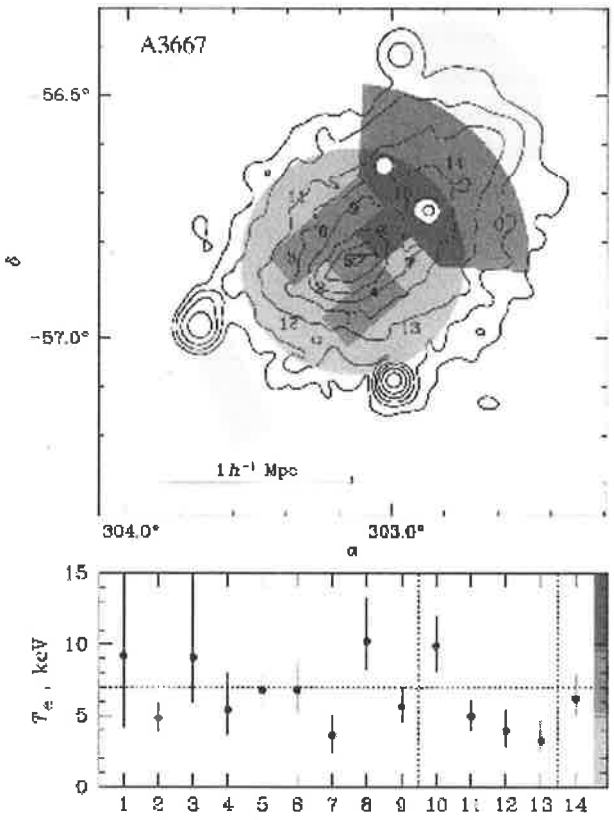

Figure 5.1: Temperature observations of the X-ray emitting gas in A3667 taken with ASCA (Markevitch et al. 1999).

Recent Chandra observations confirmed this interpretation revealing the central part of the cluster to contain a cold gas front moving through the warm intercluster medium (Vikhlinin et al. 2001). This gas, shown in Figure 5.3, has a very sharp leading edge possibly indicating supersonic velocity.

However, by far the most dramatic features of A3667 are the two symmetrically

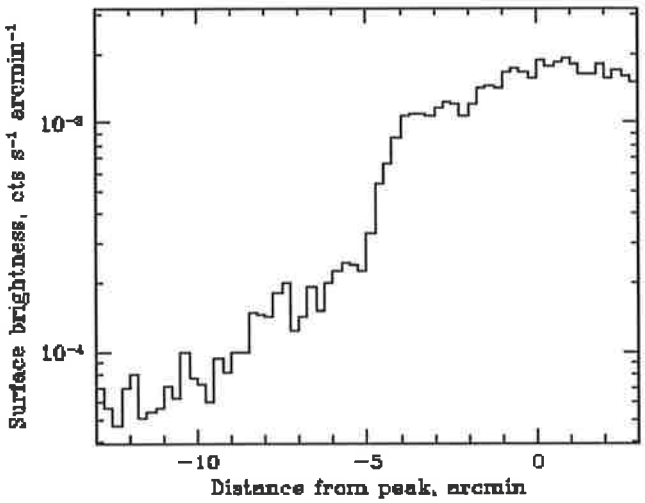

Figure 5.2: X-ray Surface profile brightness for A3666 (Markevitch et al. 1999).

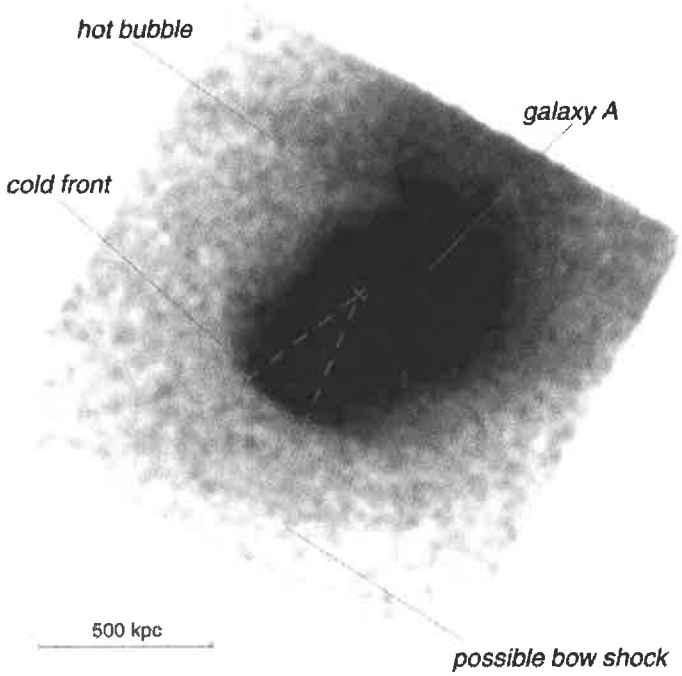

Figure 5.3: Chandra observations of the cold gas front in A3667 (Vikhlinin et al. 2001). Here galaxy A is the cD galaxy of A3667.

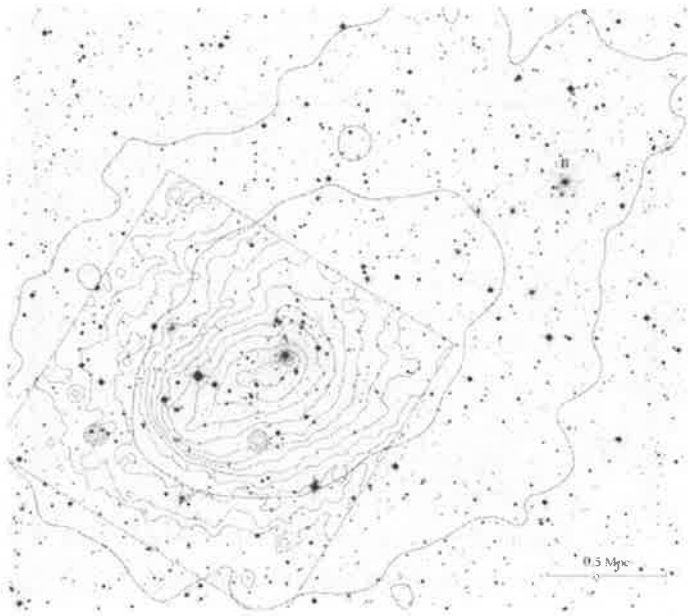

Figure 5.4: Chandra observations of the cold gas front in A3667 overlaid on a DSS image (Vikhlinin et al. 2001). Here galaxy A is the cD galaxy of A3667 and B is the cD galaxy of the sub-group reported by Proust et al. (1988).

located regions of diffuse radio emission, first detected in a 843 MHz image taken with the Molonglo Observatory Synthesis Telescope, MOST (Röttgering et al. 1997). This image is shown in Figure 5.5.

The combination of these features has been interpreted as evidence that the cluster is observed in a post merger state (Röttgering et al., 1997; Knopp et al., 1996; Roettiger et al., 1999; Markevitch et al., 1999; Vikhlinin et al., 2001).

A few authors have tried to explain the emission in A3667, using primarily shock models derived from the initial concept of Tribble (1993). Based on a model for the Coma cluster, Enßlin et al. (1998) considered matter falling into the gravitational potential of the cluster as the source of the shocks which generated the North western diffuse emission. The seed particles in this scenario are provided by the central head-tail galaxy B2007-569. Predictions of the model included the percentage polarisation for the Southern DRER and an overall geometry which would be testable through Faraday mapping of the diffuse regions.

On the other hand Roettiger et al. 1999 proposed a model wherein fore and aft shocks generated by a cluster-cluster merger give rise to the diffuse emission. Using magneto-hydro-dynamical (MHD) N-body calculations, Roettiger et al. modelled the resultant X-ray and radio emission produced by a slight off-axis merger of two cluster groups. Comparison of these data with the observed radio and X-ray data show there is reasonable morphological agreement between theory and observation, however this is not surprising since the model was generated after the MOST image had been published. An image of the simulated radio and X-ray data is shown in Figure 5.6, while the location of shocks from the model is shown in Figure 5.7. Predictions of the

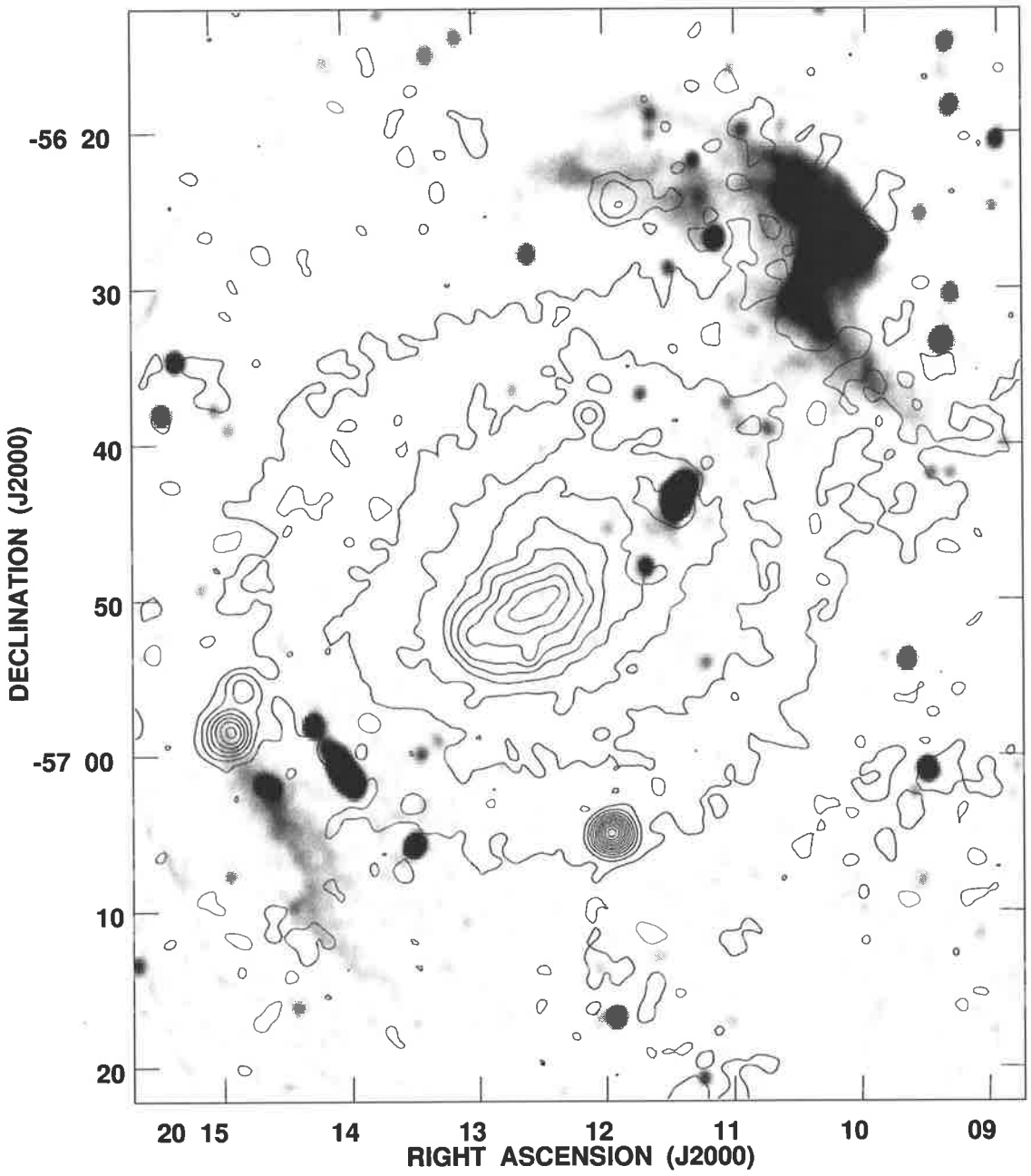

Figure 5.5: 843 MHz observations of A3667 taken with MOST, overlaid with X-ray contours from ROSAT. Figure from Röttgering et al. (1997).

MHD code, include a spectral gradient in the Southern DRER in the direction of the supposed merger axis, a magnetic field strength in the region of 0.6 μG and strong radio emission in the cluster core.

A3667 is unique in that it possesses both the largest and brightest diffuse radio emission regions and a wealth of multiwavelength data for the entire cluster region. This provides the unique opportunity to perform a detailed study of possible generation mechanisms for the diffuse emission and test DRER generation theories.

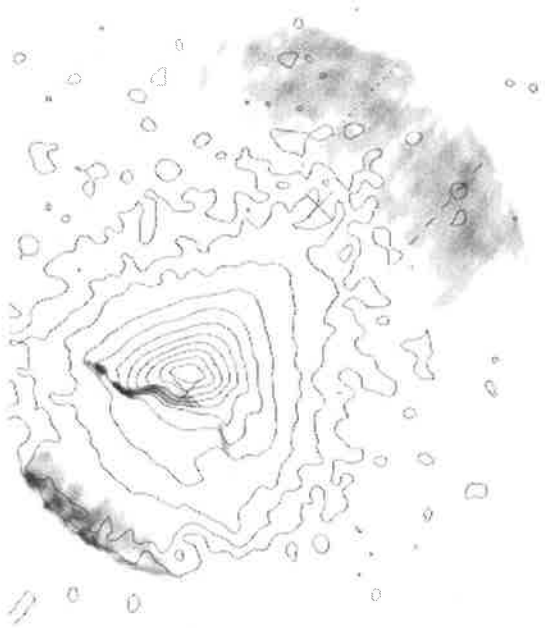

Figure 5.6: Simulated radio and X-ray data for A3667, generated from a MHD N-body code describing a cluster-cluster merger (Roettiger et al. 1999). Grey scale show the regions of predicted radio emission, while contours represent the extent of the thermal X-ray gas.

5.4 Diffuse Emission in A3667

The diffuse radio source to the Northwest of A3667 is not a recent discovery. It has been observed with increasing frequency since the early 60s when it was first included as one of the brightest sources in the MSH catalogue (Mills et al. 1961) with a flux density of 81 Jy at 85.5 MHz being reported. Even the complex shape and low surface brightness have been known for the last 30 years. Ekers (1969) attempted to model the source using limited data from the two element ANRAO interferometer but found the brightness distribution too complex. Shortly after, it was imaged at 408 MHz with Molonglo by Schilizzi & McAdam (1975) who commented on the unusual twisted shape and low surface brightness. Goss et al. (1982) improved upon the resolution

Figure 5.7: Shock location for a MHD N-body code describing a cluster-cluster merger (Roettiger et al. 1999).

of Schilizzi & McAdam (1975) by observing the source at 1415 MHz with the Fleurs Synthesis Telescope. They reported a total flux density of 1.5 ± 0.2 Jy for the source and argued that as this was in good agreement with the result of Ekers (1969) who observed 1.9 Jy, that there was little or no flux missing for the source despite their low sensitivity to large-scale structure. It was not until the source was mosaiced with the ATCA by Röttgering et al.(1997) that a clear picture of the extent of the source was obtained, revealing that all previous observations were missing part of the source structure. Röttgering et al.(1997) improved the flux density estimate further, giving a lower limit of 2.4 ± 0.2 Jy at 1.4 Gz and 1.4 Jy at 2.4 GHz. Also in Röttgering et al.(1997), though not directly discussed in the paper, was a second diffuse source to the Southeast of the cluster. This source was seen in a new 843 MHz image taken with the Molonglo Synthesis Telescope (see Figure 5.5). Both sources were shown to border the edge of the X-ray emission as observed with ROSAT.

5.4.1 This Study

The 1.4 and 2.4 GHz mosaics made by Röttgering et al.(1997) only covered half of the cluster region centring on the North eastern DRER. It was decided that the cluster would be reobserved in order to extend the mosaics to cover the entire cluster region. Further, the polarimetry data taken by Röttgering et al. (1997) was never published. It was the focus of this study to examine the entire cluster for diffuse emission making use of both the total intensity and polarimetric data. Additional observations of the

NW DRER at 4.7 GHz were also undertaken in a pilot study to assess the feasibility of mosaicing the diffuse emission at higher frequencies, and three point spectral index curves between 0.8, 1.4 and 2.4 GHz were investigated.

5.5 Observations

5.5.1 Mosaicing at 20 and 13 Centimetres

Radio imaging of the cluster was performed at 1.4 and 2.4 GHz using the Australia Telescope Compact Array. A 30 point-mosaic consisting of 16 pointings from the archive (Röttgering et al. 1997) and 14 new pointings was generated. The locations of the pointing centres for archival and new observations are shown in Figure 5.8. A total of 9 × 12 hours of observation in five different array configurations were used to image the entire cluster. Table 5.1 gives the observational details. The mosaic pattern of the new observations was chosen in a rectangular grid so as to match the archival spacings. This was done as it was felt that the gain in efficiency obtained by using an hexagonal grid would be lost in increasing difficulty of the processing.

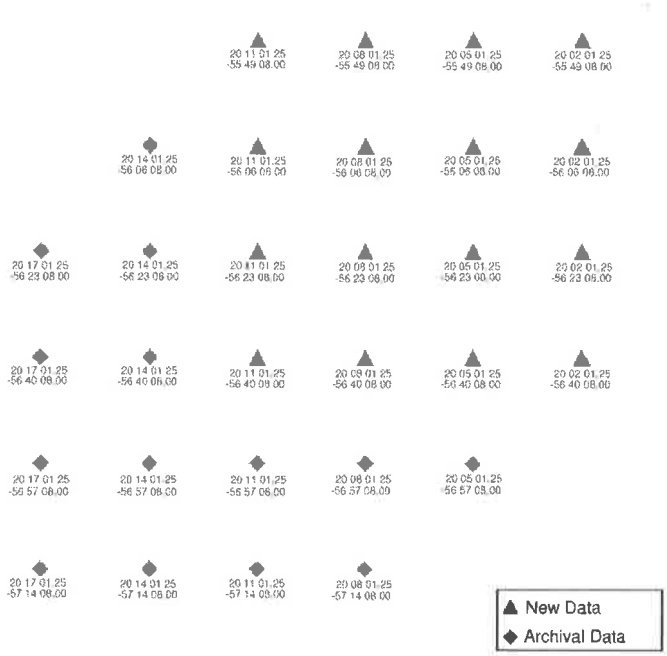

Figure 5.8: Location of mosaic pointing centres for 1.4 and 2.4 GHz observations of A3667. The triangles correspond to archival data, while the diamonds are from this study.

All data, including the archival material, was reprocessed using the *MIRIAD* software package and combined into single mosaics at each of the four Stokes parameters for each of the two observing frequencies. During processing it was discovered that producing a jointly deconvolved mosaic on such a large dataset was too computer

Table 5.1: 1.4 & 2.4 GHz observations of the NW DRER in A3667. Observations prior to 1999 were taken from the ATCA archive. Column 1 gives the data of the observation; Column 2 the integration time in minutes; Column 3 the array configuration where the first digit corresponds to the maximum baseline length in meters, except in the case of a 6 which denotes 6 km; Column 4 gives a flag for the source of the data, a 1 indicates archival data from the NW of the cluster and a 2 corresponds to date from the SE observed for this thesis.

Date	Integration Time (min)	Array Configuration	Area
1993 September 06	709	6C	1
1993 September 10	627	750c	1
1993 September 21	580	6D	1
1993 October 03	633	375	1
1999 January 06	706	375	2
1999 February 05	353	750C	2
1999 February 06	234	750C	2
1999 February 22	658	6C	2
1999 April 25	696	1.5C	2
1999 August 25	748	6D	2

intensive even after removing the long baselines. As a result, all images presented here are linear mosaics. It is hoped that in the future Moore's Law will allow a joint deconvolution mosaic to be produced for the entire dataset.

5.5.2 6 Centimetre Observations

Due to the steep spectral index observed in most DRERs, it was unlikely that anything but the brightest parts of the NW source would be visible at 4800 MHz. Nevertheless an observing program was accepted to attempt detection of the NW diffuse source at 6cm. Initially time was scheduled in March 2000, however due to a power cable melting and taking out an antenna, the observations had to be rescheduled for later in the year. The scheduled observations were supplemented with unallocated time obtained under the ATCA duty astronomer program. Table 5.2 gives details of the observations.

The total integration time for usable data was 1234 minutes (20.5 hours). The other ATCA frequency band was used to observe at 8640 MHz in the hope of also getting a detection at this frequency. However, no detection at 8.6 GHz was made, in hindsight it would have been better to improve the 4.8 GHz sensitivity by using this band to observe at a different part of the ATCA's 6cm band.

Table 5.2: 4800 GHz observations of the NW DRER in A3667. Unfortunately the data collected in September 2000 were corrupt, with no phase information being recorded for the secondary calibrator. Self calibration on these data proved unsuccessful, so they could not be used in the final analysis.

Date	Integration Time (min)	Array Configuration
2000 April 04	161	6D
2000 April 12	165	1.5D
2000 September 08	548	6A*
2000 November 11	528	6C
2002 January 29	218	6B
2002 January 30	162	6B

5.6 Total Intensity 1.4 GHz Imaging

Figure 5.9 shows the high resolution (6 arcseconds) 1.4 GHz image of A3667 overlaid with X-ray contours from the ROSAT PSPC observation. The RMS sensitivity of this image is 0.05 mJy beam^{-1}, which is a factor of four better sensitivity than the lower resolution (18 arcseconds) image produced by Röttgering et al. (1997), making it the most sensitive radio image of this cluster to date. This image clearly shows the two diffuse radio emission regions and their symmetrical arrangement in the cluster about the thermal gas.

Figures 5.10 and 5.11 show enlarged images of the Northern diffuse emission at high resolution. A clearly filamentary structure is evident in the source. The linear size of the entire source is estimated to be 1.7 Mpc, while the length of the filaments varies from around 250 to 400 kpc. The source also exhibits knots of enhanced emission such at the bright region seen on the upper west edge of the source. Figures 5.12 and 5.13 show enlarged images of the Southern emission.

5.6.1 Low Resolution Imaging

As the diffuse emission is likely to be partly resolved out at a resolution of 6 arcseconds, lower resolution images were made at 1.4 and 2.4 GHz in order to better examine the diffuse structure. Images were made at resolution of 43 arcseconds by applying an appropriate *uv*-taper. This resolution was chosen to match that of the 0.8 GHz data available from MOST (Hunstead et al., 1998) which was to be used in conjunction with these data to generate spectral index maps (see Section 5.8). 1.4 GIIz images of the diffuse emission are shown in Figures 5.14 and 5.15. It can be seen that the extent of both sources is much larger than in the high resolution imaging and in the case of the NW DRER the extension of the source in the lower Western region is much greater than that shown by Röttgering et al. (1997). These low level features appear also in both the 2.4 GHz and new MOST maps confirming their reality. The total flux at 1.4

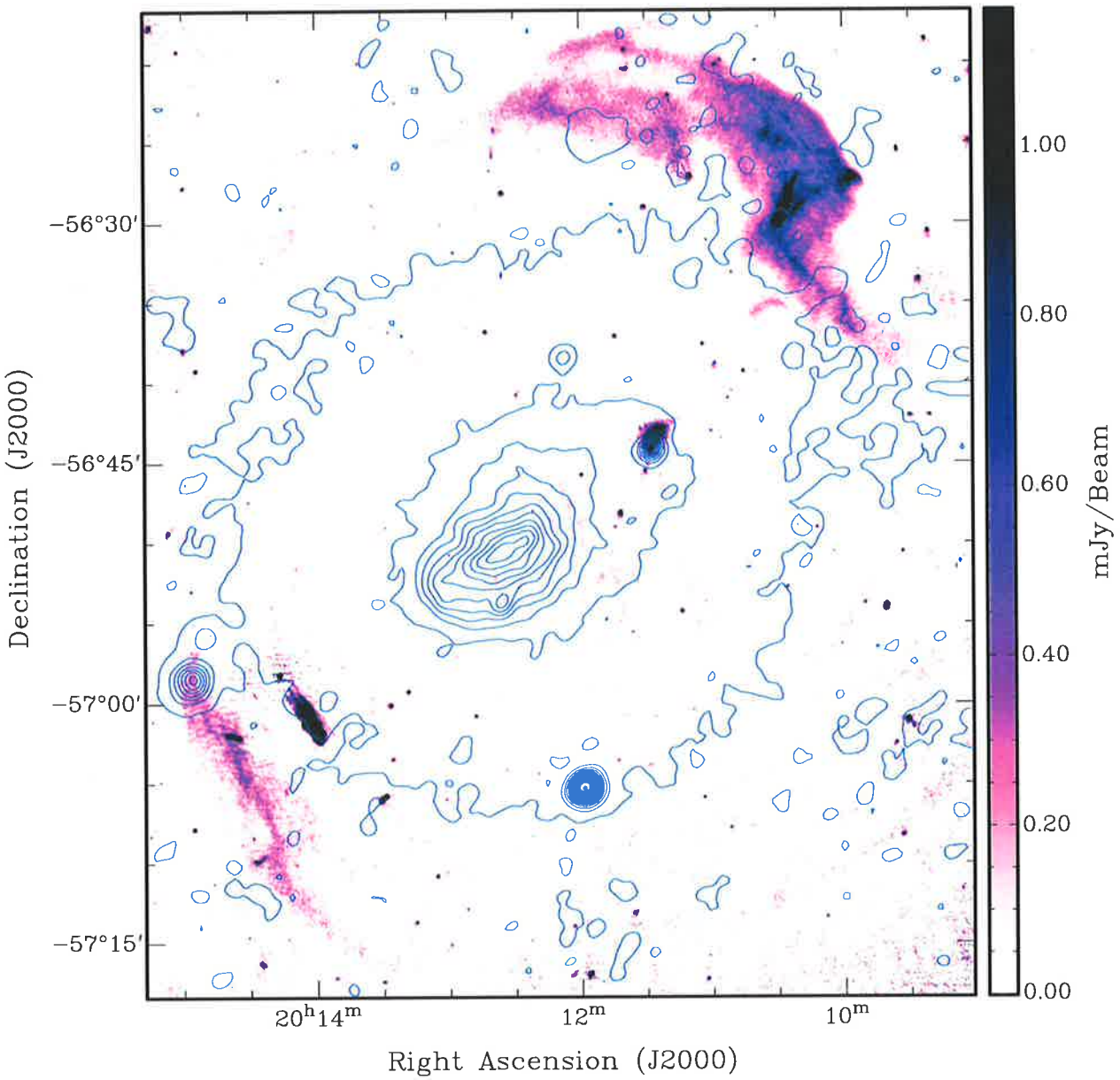

Figure 5.9: 1.4 GHz ATCA data for A3667 shown at 6 arcesond resolution and overlaid with contours from the ROSAT PSPC observation. X-ray contours are given at 2.25, 7.25, 12.25, 17.25, 22.25, 27.25, 32.25, 37.25, 42.25, 47.25 and 52.25 times the background.

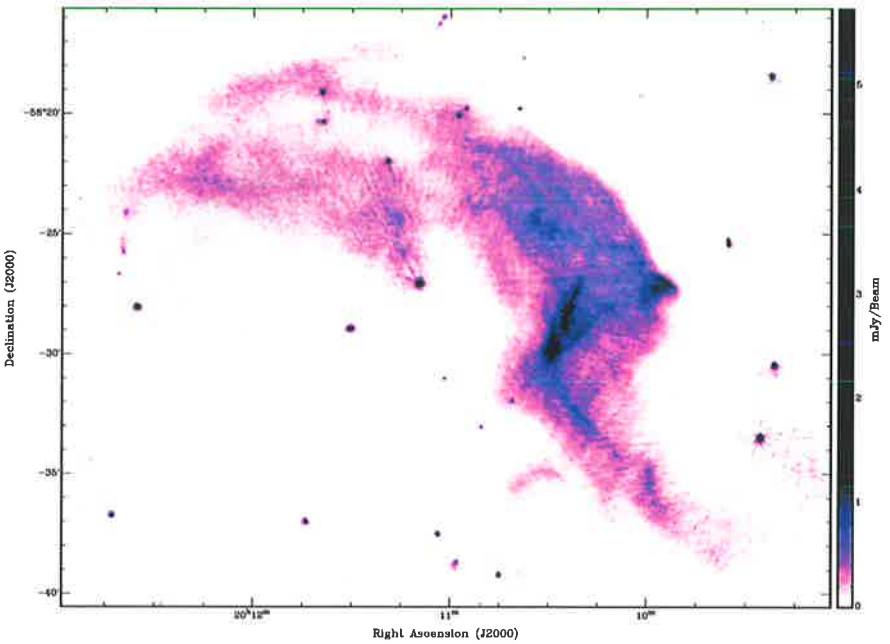

Figure 5.10: The northern DRER shown at 1.4 GHz and 6 arcseconds resolution. Filamentary structure is clearly present in this source, as well as small regions of enhanced emission.

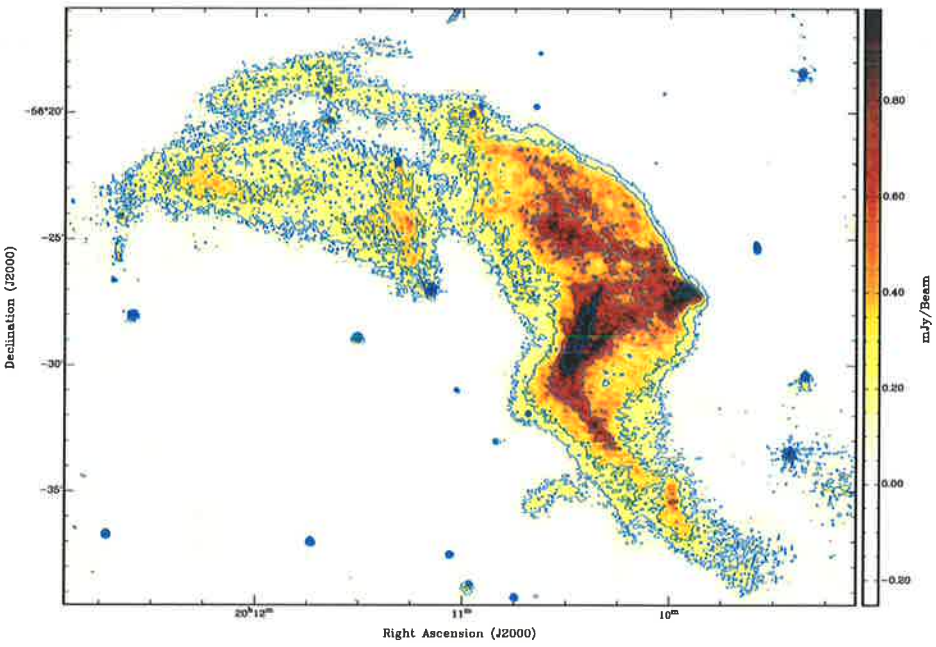

Figure 5.11: The northern DRER shown at 1.4 GHz and 6 arcseconds resolution. Contours are given at 0.14, 0.28, 0.56, 1.1, 2.3, 4.5 and 9 mJy beam^{-1}.

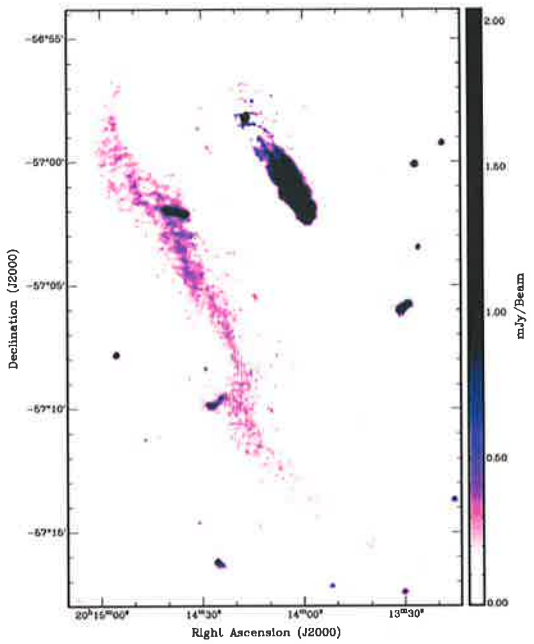

Figure 5.12: The southern DRER shown at 1.4 GHz and 6 arcseconds resolution. While no filamentary structure is seen here, there are regions of enhanced emission similar to those found in the Northern source. The strong lobed source embedded in the north of the diffuse emission is a suspected background FRII galaxy.

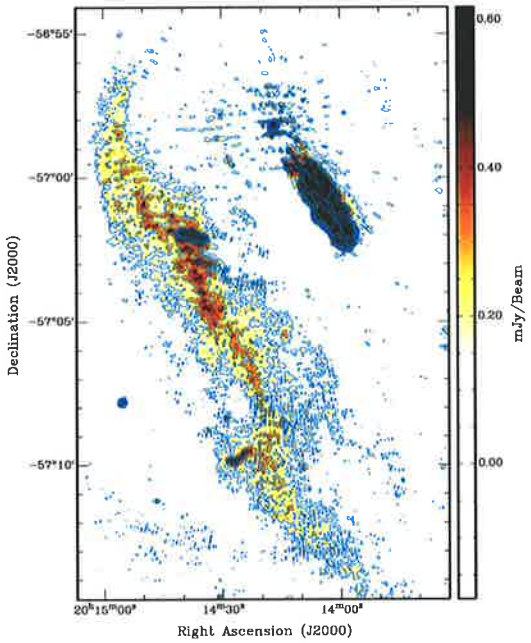

Figure 5.13: The southern DRER shown at 1.4 GHz and 6 arcseconds resolution. Contours are given at 0.14, 0.28, 0.56, 1.1, 2.3, 4.5 and 9 mJy beam^{-1}.

GHz for the NW emission is calculated as 3.7 ± 0.3 Jy which is almost 1.5 times higher than that reported by Röttgering et al. (1997). This discrepancy is mostly likely due to more of the source structure being detected. Despite this increase in source size, there is still quite a large negative bowl surrounding the NW emission, which suggests that even in these new images not all of the flux has been recovered. In contrast there is no negative bowl for the SW emission and a total flux of 0.3 ± 0.02 Jy is estimated from these data.

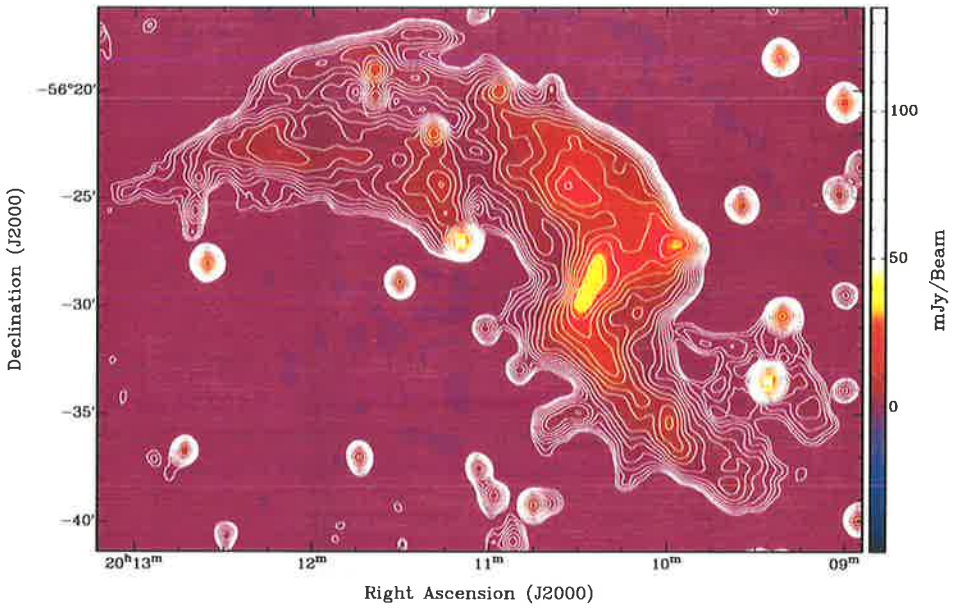

Figure 5.14: The Northern DRER shown at 1.4 GHz and 43 arcseconds resolution. The RMS sensitivity of the image is 0.1 mJy beam^{-1}. Contours are given at 0.27, 0.38, 0.54, 0.76, 1.1, 1.5, 2.1, 3.0, 4.2, 6.0, 8.4, 12, 17, 24 and 34 mJy beam^{-1}.

The low resolution imaging has also revealed marginal evidence of a central halo. This possible halo is shown in Figure 5.16. This emission is very weak, with a total flux at 1.4 GHz of 33 ± 6 mJy. The detection of this halo is thrown into some doubt, as though it is clearly several sigma above the noise and is in the correct position for a central halo (see Figure 5.17 which is the X-ray overlay) it is also in the position most likely to be due to addition of the side lobes from the two bright head-tail galaxies in the field. Not surprisingly nothing is seen in this region in the 2.4 GHz image, as if a halo were present it would be too weak to detect, and if the effect is due to the side lobe pattern, moving to a different frequency will change their intersection location. The potential halo is also not detected in the MOST image. Though these data are not as sensitive at the 1.4 GHz image, having an RMS noise of 0.6 mJy beam^{-1}, it would be expected that a halo would be brighter at 0.8 MHz than at 1.4 GHz. However, assuming a typical halo spectral index of -1, this would only give a total flux at 0.8 GHz of 56 mJy, which spread out over such a large area would be undetected in this

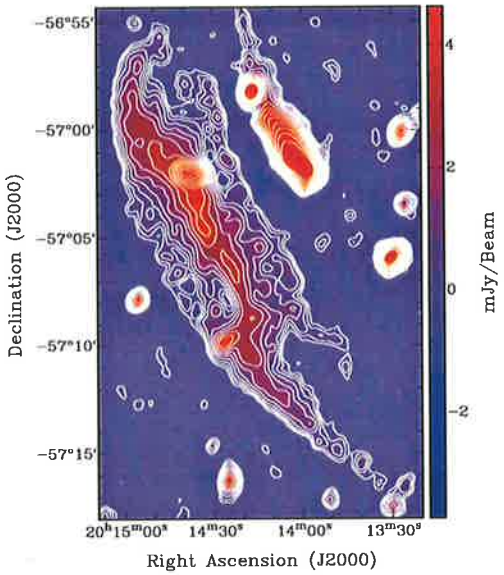

Figure 5.15: The Southern DRER shown at 1.4 GHz and 43 arcseconds resolution. The RMS sensitivity of the image is 0.1 mJy beam^{-1}. Contours are given at 0.27, 0.38, 0.54, 0.76, 1.1, 1.5, 2.1, 3.0, 4.2, 6.0, 8.4, 12, 17, 24 and 34 mJy beam^{-1}.

image. A deeper image either at 1.4 or 0.8 GHz will be required to confirm or deny this possible detection. Follow up observations on the ATCA at 1.4 GHz have been scheduled for July 2003.

5.6.2 Other Sources

Aside from the diffuse emission A3667 also harbours several objects of extended radio morphology. These objects, being two head-tail sources and a suspected FRII galaxy are presented as radio images in Figures 5.18, 5.20 and 5.22 respectively and as optical/radio overlays in Figures 5.19, 5.21 and 5.23.

The first of these objects, shown in Figure 5.18 is the head-tail radio galaxy B2007-569 (Goss et al. 1982), which is seen toward the cluster centre in Figure 5.9. The optical counterpart to this source, galaxy 072 from Sodre et al. (1992), seen in Figure 5.19 has a redshift of 0.053 (Danziger et al. 1983) defining it as a cluster member. X-ray emission from this object is also clearly visible in the ROSAT PSPC image. This galaxy would lie within the region of most gravitational interaction between the reported subgroups (see Figure 6.1) and constant dynamical friction may explain the strong multiwavelength activity.

The second head tail source can be seen in Figure 5.9 just north west of the Southern diffuse emission region. This galaxy seen in figure 5.20 presents a more obvious picture of a narrow angled tail source than B2007-569. It has two clearly evident radio jets

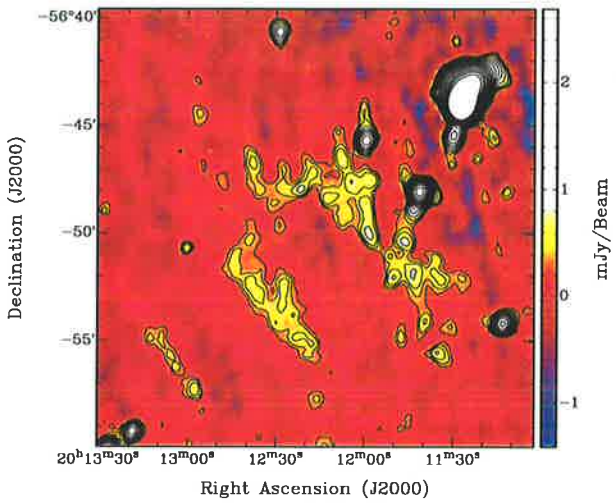

Figure 5.16: Possible weak halo in the centre of A3667 detected at 1.4 GHz with a 43 arcsecond beam. The RMS sensitivity of the image is 0.1 mJy beam^{-1}. Contours are given at 0.27, 0.38, 0.54, 0.76, 1.1, 1.5, 2.1, 3.0, 4.2, 6.0, 8.4, 12, 17, 24, 34, mJy beam^{-1}.

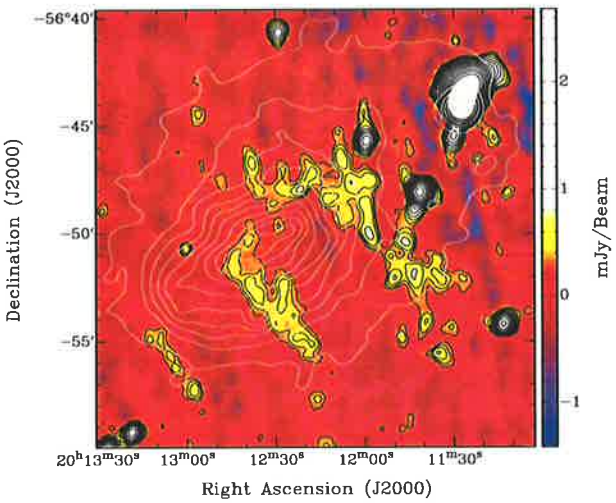

Figure 5.17: Possible weak halo in the centre of A3667 detected at 1.4 GHz with a 43 arcsecond beam is shown here overlaid with contours with the ROSAT PSPC data. The RMS sensitivity of the radio image is 0.1 mJy beam^{-1}. Radio contours (black) are shown at 0.27, 0.38, 0.54, 0.76, 1.1, 1.5, 2.1, 3.0, 4.2, 6.0, 8.4, 12, 17, 24, 34, mJy beam^{-1}, whereas X-ray contours (pink) are shown at 7.25, 12.25, 17.25, 22.25, 27.25, 32.25, 37.25, 42.25, 47.25 and 52.25 times the X-ray background.

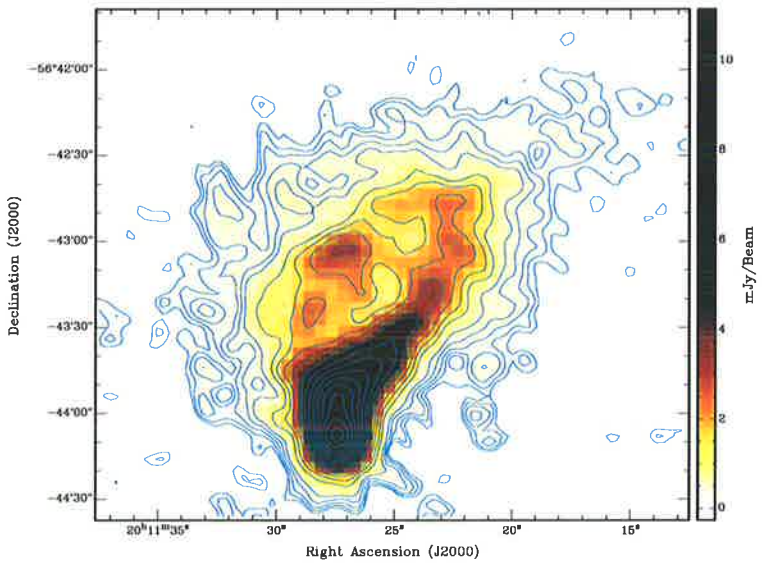

Figure 5.18: The head-tail source B2007-569 shown at 1.4 GHz and 6 arcseconds resolution. Contours are given at 0.14, 0.2, 0.28, 0.4, 0.56, 0.8, 1.1, 1.6, 2.3, 3.2, 4.5, 6.4, 9.0, 13, 18, 26, 36, 51 and 72 mJy beam^{-1}. The total flux for this source is 1.47 $\pm$ 0.01 Jy.

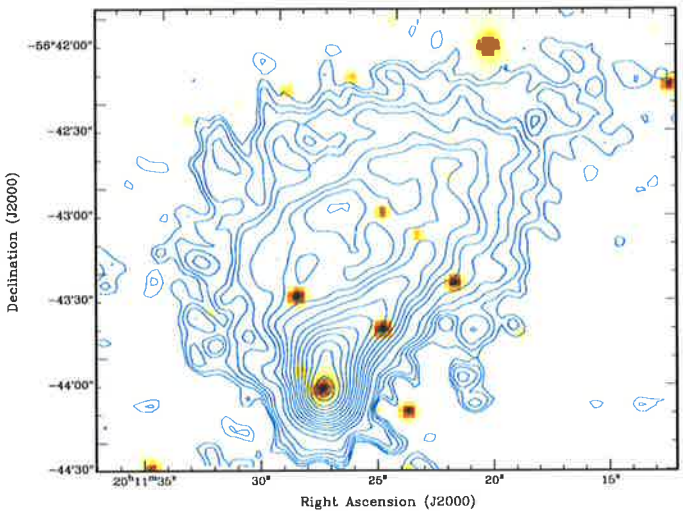

Figure 5.19: DSS image of the head-tail source B2007-569 shown with 1.4 GHz, 6 arcsecond, contours overlaid. Contours are given at 0.2, 0.28, 0.4, 0.56, 0.8, 1.1, 1.6, 2.3, 3.2, 4.5, 6.4, 9.0, 13, 18, 26, 36, 51 and 72 mJy beam^{-1}.

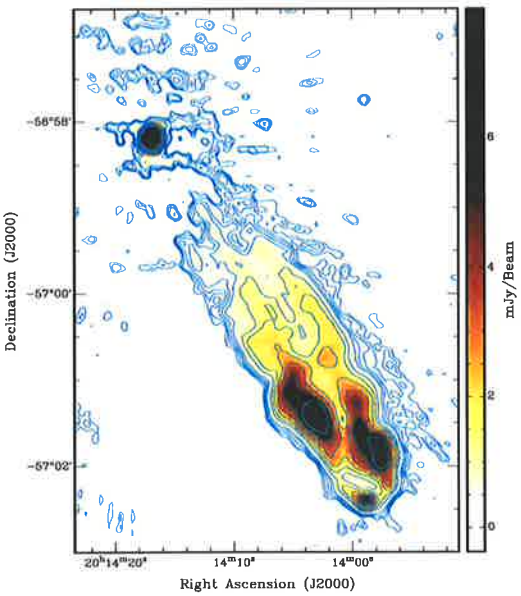

Figure 5.20: The head-tail source J201358.890-570226.00 shown at 1.4 GHz and 6 arcseconds resolution. Contours are given at 0.2, 0.28, 0.4, 0.56, 0.8, 1.1, 1.6, 2.3, 3.2, 4.5 and 6.4 mJy beam^{-1}. The total flux for this source is 1.35 $\pm$ 0.02 Jy.

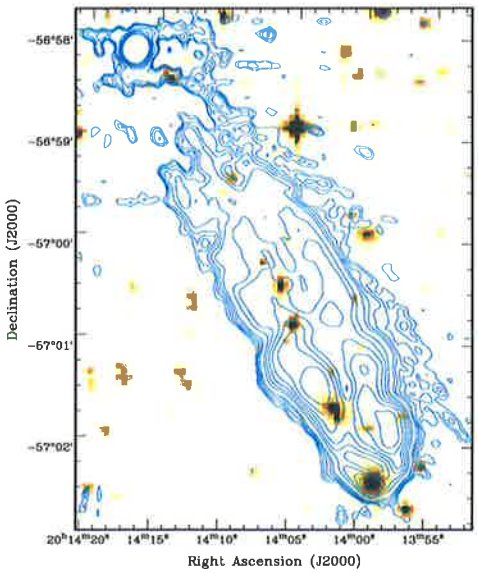

Figure 5.21: DSS image of the head-tail source J201358.890-570226.00 shown with 1.4 GHz, 6 arcsecond, contours overlaid. Contours are given at 0.2, 0.28, 0.4, 0.56, 0.8, 1.1, 1.6, 2.3, 3.2, 4.5 and 6.4 mJy beam^{-1}.

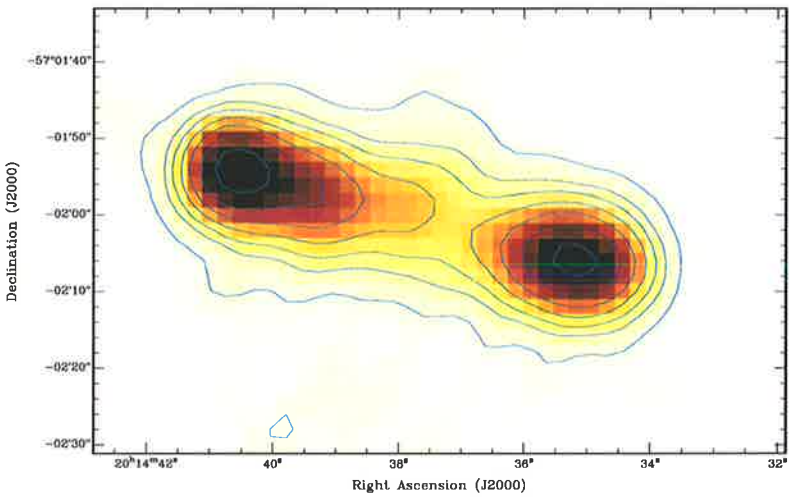

Figure 5.22: The source J201358.890-570226.00 shown at 1.4 GHz and 6 arcseconds resolution. Contours are given at 0.2, 0.28, 0.4, 0.56, 0.8, 1.1, 1.6, 2.3, 3.2, 4.5 and 6.4 mJy beam^{-1}. This source lies behind the Southern diffuse emission.

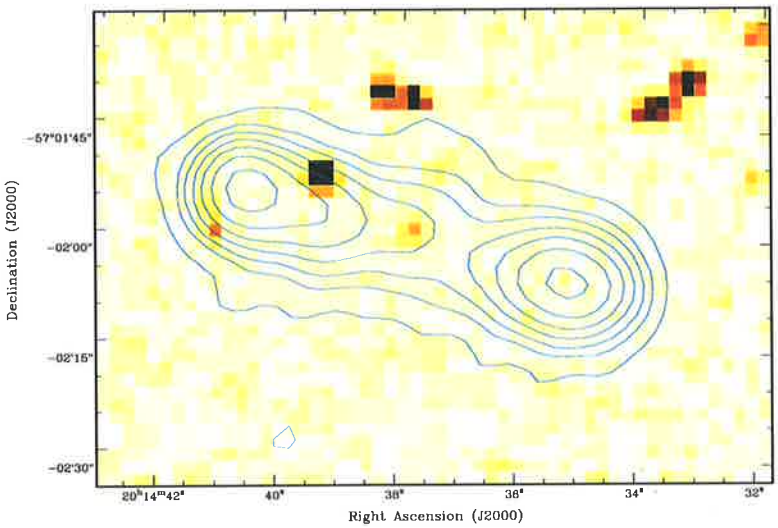

Figure 5.23: DSS image of the head-tail source J201358.890-570226.00 shown with 1.4 GHz, 6 arcsecond, contours overlaid. Contours are given at 0.56, 0.8, 1.1, 1.6, 2.3, 3.2, 4.5 and 6.4 mJy beam^{-1}.

extending from the radio core being swept back either by movement of the object itself or of the cluster medium. The optical counterpart of this object, object 157 from Proust et al. (1988) as shown in the radio optical overlay, Figure 5.21, has magnitude 15.97 and a measured redshift of 0.0524 (Katgert et al. 1998) making it also a cluster member. The movement associated with the jets may again be an indication that there is turbulence within the intra-cluster medium or merging present (Bliton et al. 1998). However, the use of HT galaxies as an indicator of cluster weather is a topic of some contention.

The third radio object of interest, Figure 5.22, is a classic double-lobed radio galaxy. There is an extremely faint optical counterpart for this object, shown in Figure 5.23. Given the faintness of the optical counterpart, which is just detectable in the DSS red image (down to magnitude 21), and the known properties of radio galaxies of this type, it is highly likely to be extremely distant.

One other object of note, is the Seyfert 1 galaxy, Fairall 0339 (Fairall 1981), which can be seen as a strong concentration in the X-ray toward the lower half of Figure 5.9. This object is a cluster member with redshift 0.054 (Hewitt & Burbidge 1991) with radio emission of 4.1 $\pm$ 0.1 mJy at 1.4 GHz. The galaxy is observed as a distant barred spiral (Fairall 1981) of magnitude 16.38 (Sodre et al. 1992). Emission features seen for this object include broad H emission (Véron-Cetty & Véron 1986) and strong emission lines for H and He[II] (Fairall 1981). Fairall 0339 also exhibits several Fe[II] (Sodre et al., 1992; Fairall, 1981) and O[III] emission lines (Sodre et al. 1992) making

it a fairly typical Seyfert.

Other strong X-ray sources shown in Figure 5.9 are associated with stars, the brightest of which is the F5 star SAO 246489 (Sodre et al. 1992). These are not discussed here.

5.7 Total Intensity 4.8 GHz Imaging

The single pointing 4.8 GHz image of the Northern DRER is shown in Figure 5.24 with contours from the 1.4 GHz data overlaid. The restoring beam for this image is 11 by 8 arcseconds and the RMS sensitivity is 0.04 mJy per beam. An enlargement of the brightest part of the strongest filament from the 1.4 GHz is seen in Figure 5.25. The brightest part of the DRER shows a curiously point like core with a possible jet structure and is reminiscent of the radio emission in M87. However, no optical counterpart has been reported at this location.

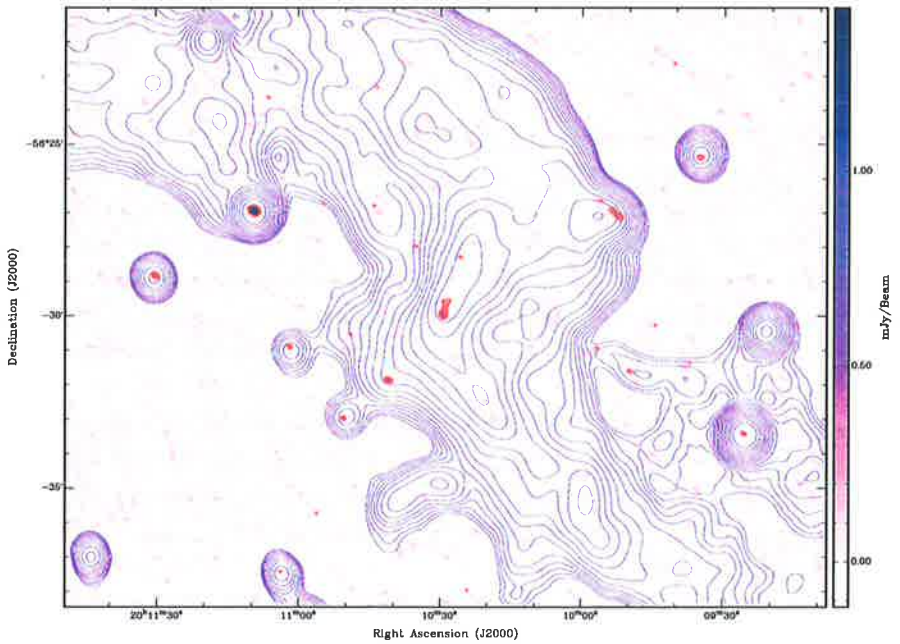

Figure 5.24: 4.8 GHz imaging of the NW diffuse emission in A3667. Contours from the 1.4 GHz low resolution map (see Fig 5.14) are shown in purple while contours for the 4.8 GHz data are given in red at 0.2, 0.28, 0.4, and 0.56 mJy beam^{-1}. The resolution of the 4.8 GHz image is 11 arcseconds and the RMS noise is 0.04 mJy per beam.

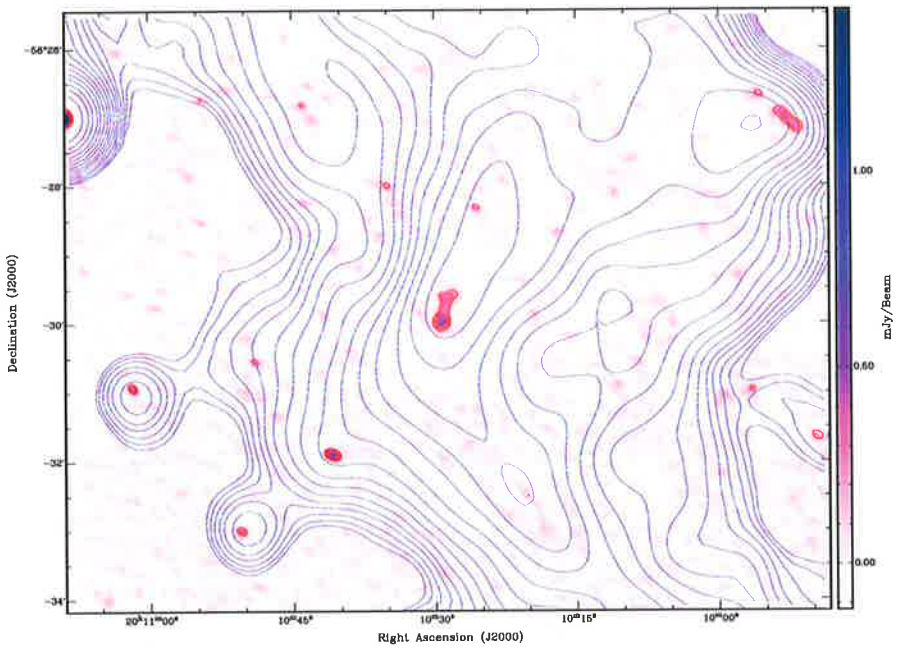

Figure 5.25: Enlargement of Figure 5.24 to better show the point like core of the brightest filament in the Northern diffuse emission region.

5.8 Spectral Indices

The spectral index of the northern DRER was investigated using an 0.8 GHz MOST image kindly provided by Dr. R. W. Hunstead, and the 1.4 and 2.4 GHz ATCA images. As the data were of such high quality it was possible to investigate the spatial variation of the spectral index in different regions, such as the filaments.

Great care was taken to match the resolution of all three images before the final spectral indices were determined. First the higher resolution ATCA data were re-imaged using an appropriate *uv*-taper in order to match the MOST resolution of 43 arcseconds. Then the ATCA images were gridded into the same projection as the MOST data (cosec(δ)). This was accomplished in a two stage process. Firstly *MIRIAD* was used to transform the ATCA images into the same co-ordinate system as the MOST image. Then the Kview package *ko-ord* was used to adjust for a very slight rotational transformation between the ATCA and MOST images which was still present after the *MIRIAD* operation. Ko-ord performs a regridding based on user identified matched pairs of sources. The success of the software depends to some extent on the number of source pairs used to calculate the transformational matrix. In this case 43 point sources common to the image fields were used. Finally, all images were convolved with a Gaussian filter just slightly larger than the MOST beam to ensure any residual effects from differing beam shapes were removed.

This produced a set of three well matched images. An initial investigation of the two spectral index maps produced, (the first between 0.8 and 1.4 GHz and the second

between 1.4 and 2.4 GHz) did not exhibit any of the tell tale signs of poor image matching such as radial and linear gradients across the point sources. Thus, it was assumed that the matching procedure had been performed correctly.

A two point spectral index calculated between 0.8 and 1.4 GHz was produced for the entire cluster using *MIRIAD*. This image is shown as a hue-intensity plot in Figure 5.26. Hue-intensity plots are obtained by assigning the colour scale from one image, in this case the spectral index map, and the intensity from another, in this case the 1.4 GHz ATCA image was used.

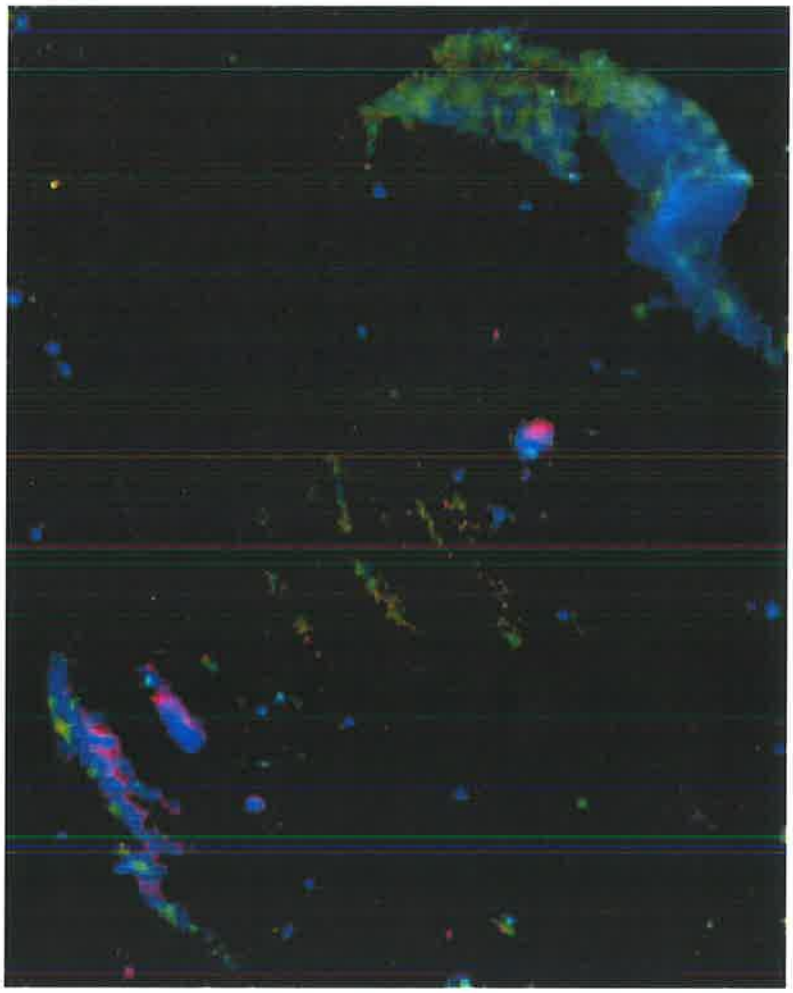

Figure 5.26: Spectral index map for A3667 between 0.8 and 1.4 GHz. Shown here as a hue-intensity plot with the hue corresponding to the spectral index value and the intensity being the total intensity at 1.4 GHz. Values of the spectral index, α, are as follows: yellow (-0.1– -0.5), green (-0.5 – -0.7), blue (-0.7– -1.4), pink (-1.4– -2.1).

Larger images of both DRERs are also shown in Figures 5.27 and 5.28. There are

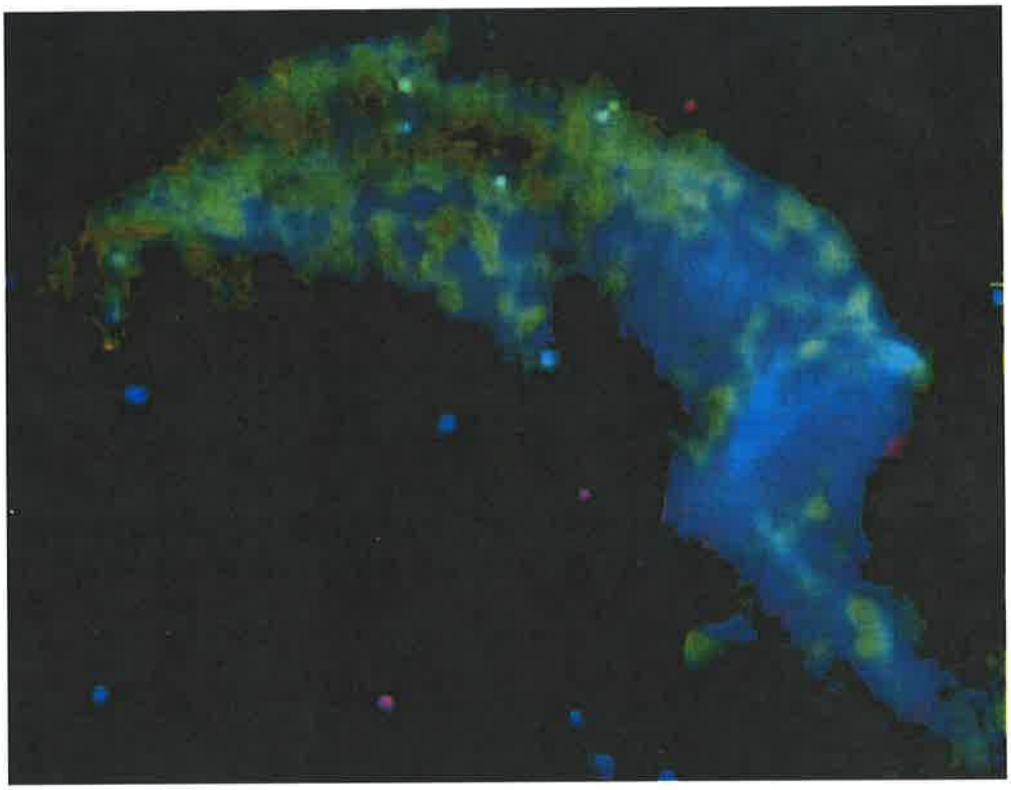

Figure 5.27: Spectral index map for the NW DRER between 0.8 and 1.4 GHz. Shown here as a hue-intensity plot with the hue corresponding to the spectral index value and the intensity being the total intensity at 1.4 GHz. Values of the spectral index, α, are as follows: yellow (-0.1– -0.5), green (-0.5 – -0.7), blue (-0.7– -1.4), pink (-1.4– -2.1).

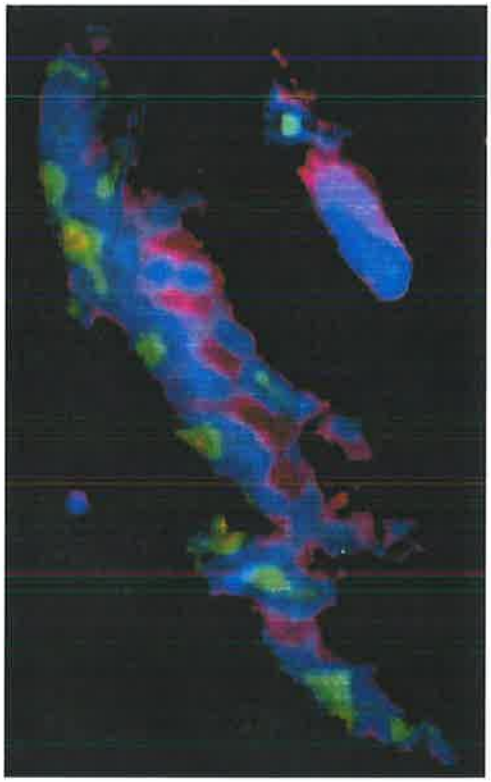

Figure 5.28: Spectral index map for SE DRER between 0.8 and 1.4 GHz. Shown here as a hue-intensity plot with the hue corresponding to the spectral index value and the intensity being the total intensity at 1.4 GHz. Values of the spectral index, α, are as follows: yellow (-0.1– -0.5), green (-0.5 – -0.7), blue (-0.7– -1.4), pink (-1.4– -2.1).

several features in the two-point spectral index map that are worth of discussion. First the flat spectral ridge reported by Röttgering et al. (1997) on the outer edge of the NW source is not apparent. Rather the flattest part of the spectrum appears toward the very north of the source where it is most diffuse. Also there is only a moderate spectral gradient across this source, with the average value across the source at -0.9 ± 0.2. The difference between these new data and the previous image made by Röttgering et al. (1997) appears to be due to more careful matching of the image resolutions. There seems to be a mismatch in the image sizes in the Röttgering et al. data as suggested by the spectral gradients on the point sources, such an effect will commonly produce erroneous results at the edge of a source.

The South eastern source on the other hand shows a well defined spectral index gradient along the major axis of the cluster with the outer parts of the source having the flattest spectra. This, combined with the sharp outer edge, could be interpreted as a slow moving radial expansion of the shockfront theorised by Roettiger et al.. Overall this source is steeper than its Northern counterpart with an average spectral index of -1.2 ± 0.2.

Data were then imported into the SYNAGE++ software package developed by Matteo Murgia at the IRA, Bologna, Italy. SYNAGE++ allows the user to specify regions of the image over which spectral fits are calculated. For the Northern DRER three point spectral index plots were obtained for a series of areas corresponding to the filaments and diffuse regions of the source as well as a plot of $S_{1.4}^{0.8}$ versus $S_{2.4}^{1.4}$ for all parts of the source. Figures 5.29 through 5.34 show the results of the spatial spectral index investigation. For each set of figures there is one showing the location of the boxes used to calculate the three-point spectral index within the source and then a series of 6 plots giving the results. Finally Figure 5.35 show the plot of $\alpha_{1.4}^{0.8}$ versus $\alpha_{2.4}^{1.4}$ for all parts of the source. The box size chosen was slightly larger than the telescope beam and the data were average within each box.

Results of the three point spectral index plots suggest that the filaments follow a power law spectrum with a spectral index value of 1.0 ± 0.1, whereas the rest of the source exhibits the curved spectral gradient signature of simple diffusion. The power law result for the filaments is surprising as this may indicate continuous energy injection, which is difficult to explain given the current models. It should be noted that previously the measurement of a power law spectra for diffuse radio emission has been regarded as suspicious and was thought likely to represent the averaging of different spectral values across a source (Rudnick, L., private communication 2000). However, here the data are of sufficient quality to determine distinct spectral indices for various parts of the source.

One final point to consider is the effect of differing *uv*-plane coverage on the spectral index data, this is of particular importance when comparing the data taken with MOST to that taken with the ATCA. The ATCA has slightly less sensitivity to large scale structure than MOST. This may mean that the ATCA fluxes are slightly lower than would be expected if the instrument had the same *uv*-plane coverage as MOST. This would tend to make the overall spectral index steeper than it should be. However, in the case of the filamentary structure, as this occurs on quite small scales, the spectral

index here is likely not to be strongly affected by the differing *uv* coverage.

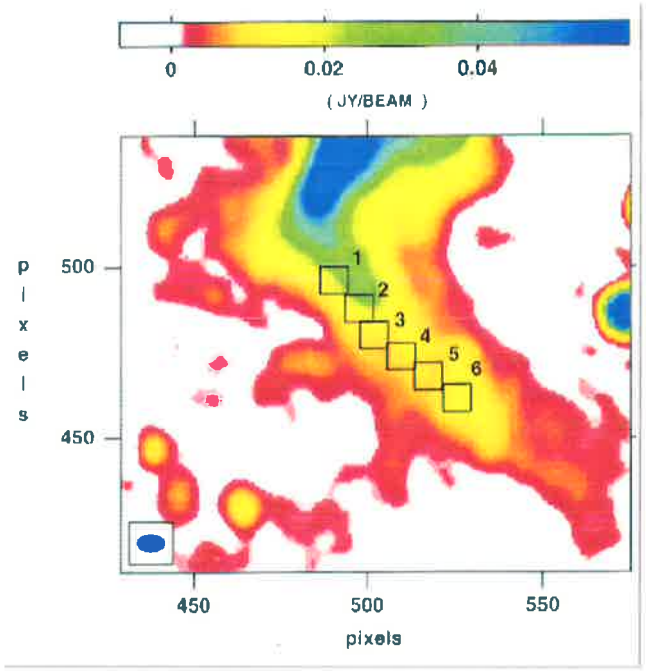

Figure 5.29: Spectral index sample locations in the Southern part of the larger diffuse emission region in A3667. The resultant spectral index plots for these boxes are given in Figure 5.30.

5.9 Polarimetry

Polarisation data were obtained at 1.4 and 2.4 GHz from the ATCA mosaic data. Both diffuse radio features have high levels of polarisation. At 1.4 GHz the percentage polarisation of the Northern feature varies from 10 to 40 percent and appears correlated with the strongest filament while the Southeast source has strong percentage polarisation throughout varying between 30 and 50%. However, these values should be treated with some caution as it is not yet known if all of the total intensity flux is being sampled. As has been shown in the case of the galaxy it is possible to measure a significant polarised flux from very diffuse sources, even where the total intensity has been resolved out (Gaensler et al., 2001; Haverkorn et al., 2002). These values, should for now be regarded as an upper limit. Unfortunately, the 2.4 GHz polarimeteric data were affected by side lobes from the sun in several of the observations. The data have not proved to be very reliable and are not presented here.

Position angle plots were made for all sources with both significant polarisation and extended structure, these can be seen in Figures 5.36, 5.37 and 5.38. These figures show the Northern and Southern DRERs and the head-tail galaxy J201358.890-570226.00,

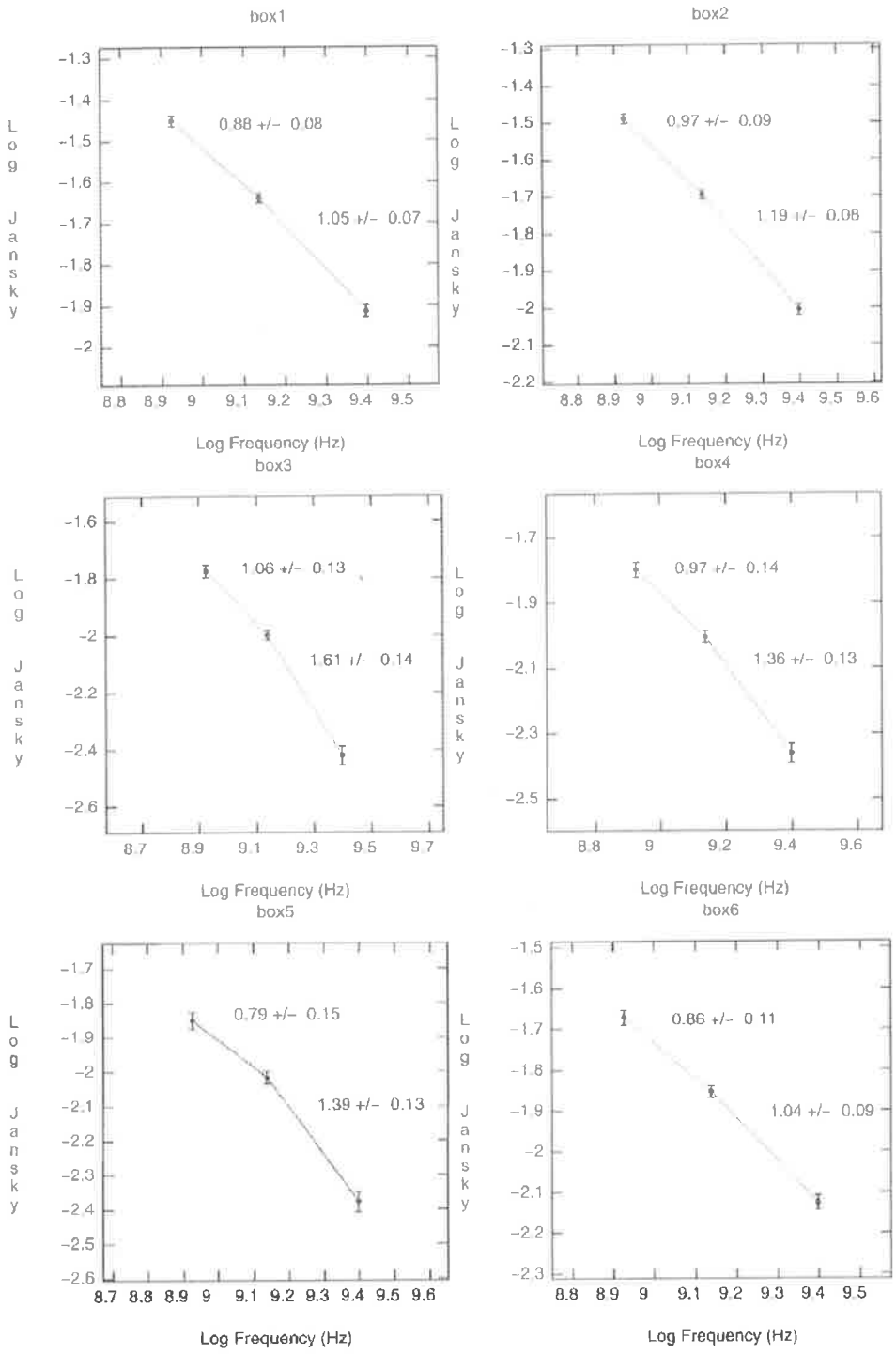

Figure 5.30: Spectral index plots for the Southern part of the larger diffuse emission region in A3667. The corresponding box location is given in Figure 5.29. These regions show a typical curved spectrum related to electron aging.

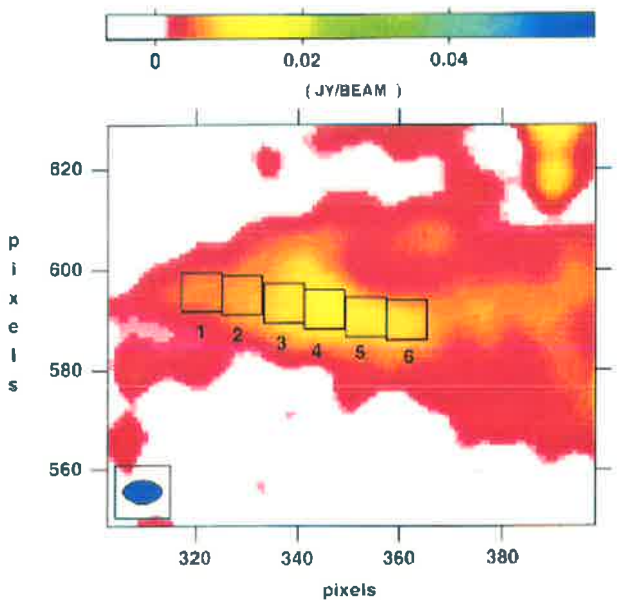

Figure 5.31: Spectral index sample locations in the Northern part of the larger diffuse emission region in A3667. The resultant spectral index plots for these boxes are given in Figure 5.32.

respectively. The position angle pattern is complex for all three sources and doesn't seem to correlate with the intensity in any significant way. In the case of J201358.890-570226.00 the sign of the position angle changes rapidly at certain points. This is further illustrated in Figure 5.39 which shows all positive position angles values in red and all negative values in blue. As these reversals do not seem correlated with the know magnetic field structure in the radio jets it is likely they represent reversal scales for the intracluster magnetic field. In this case field reversals on scale of around 30 – 80 kpc are present.

5.9.1 Rotation Measure Data

In Chapter 3 a statistical search for an enhancement of the rotation measures observed towards the centre of Southern non-cooling flow clusters was conducted. Data obtained in this study for six Southern galaxy clusters were compared to that taken for 24 Northern cluster by Clarke (2000). It was found that the data agreed well between the two datasets. However, there are two anomalous points on the plot of residual RM versus impact parameter (Figure 3.6), which correspond to background sources viewed through the North west DRER in A3667. These points, labelled 1 and 2 on the plot have residual RMs (after galactic correction) of -165.1 and -98.2 rad m^{-2} respectively. Assuming a uniform but extended Faraday screen the magnetic field required to generate such an RM can be estimated using:

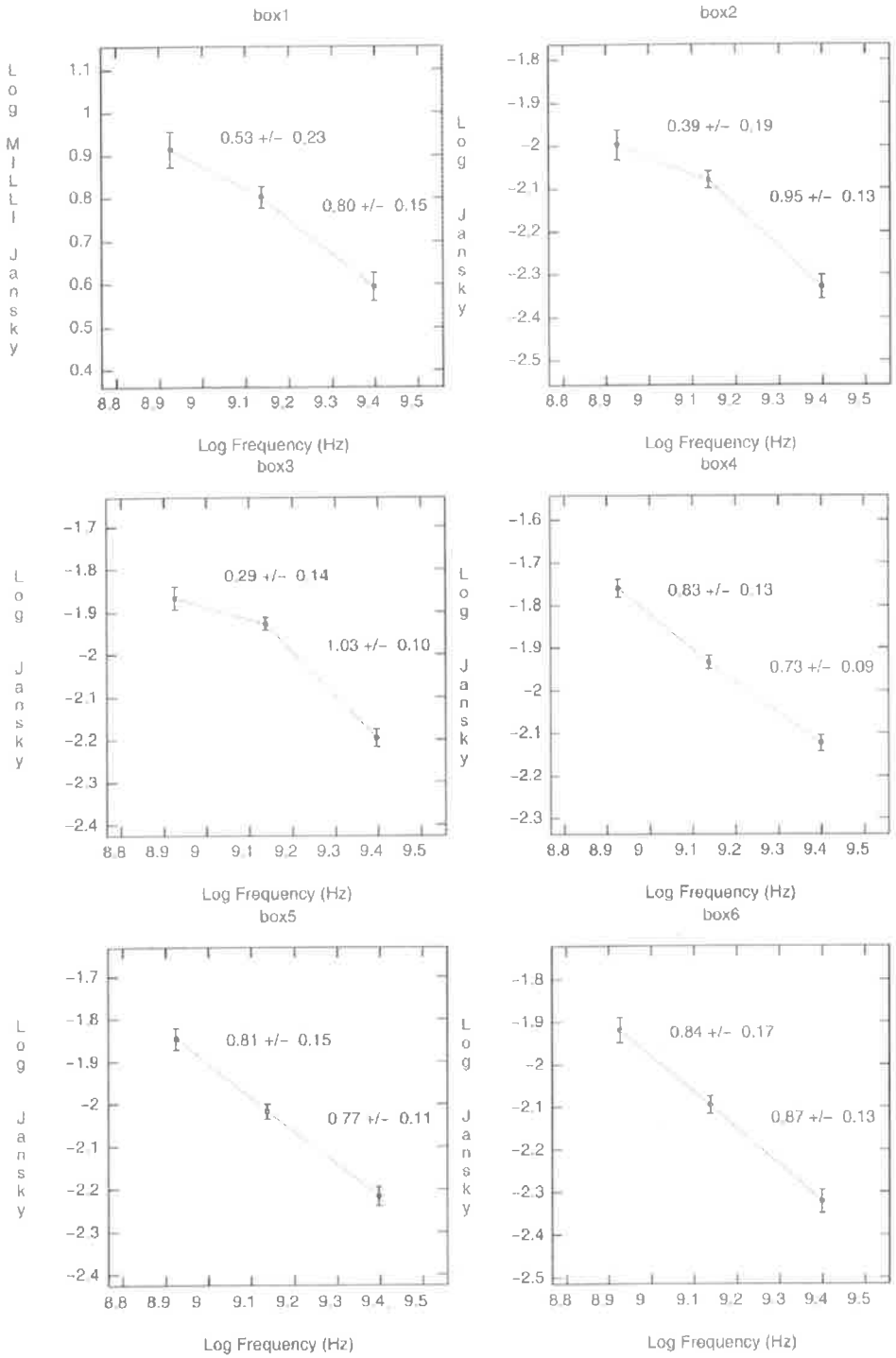

Figure 5.32: Spectral index plots for the Northern part of the larger diffuse emission region in A3667. The corresponding box location is given in Figure 5.31. These regions show a typical curved spectrum related to electron aging.

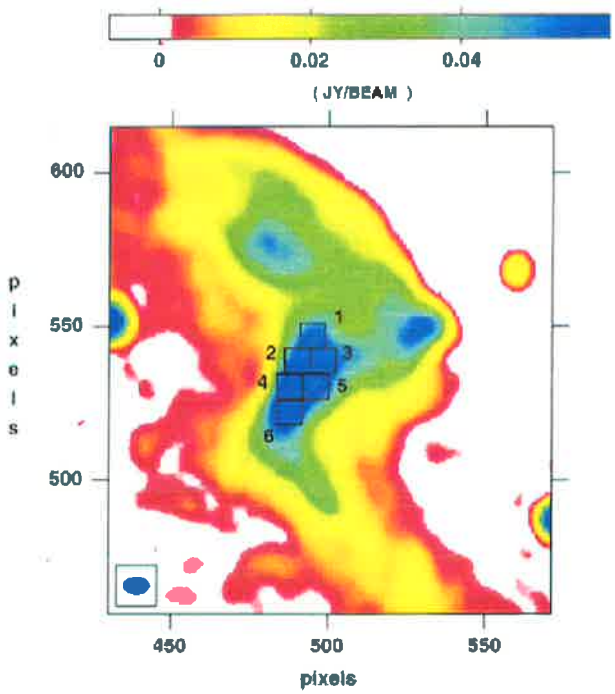

Figure 5.33: Spectral index sample locations in the filamentary parts of the larger diffuse emission region in A3667. The resultant spectral index plots for these boxes are given in Figure 5.34.

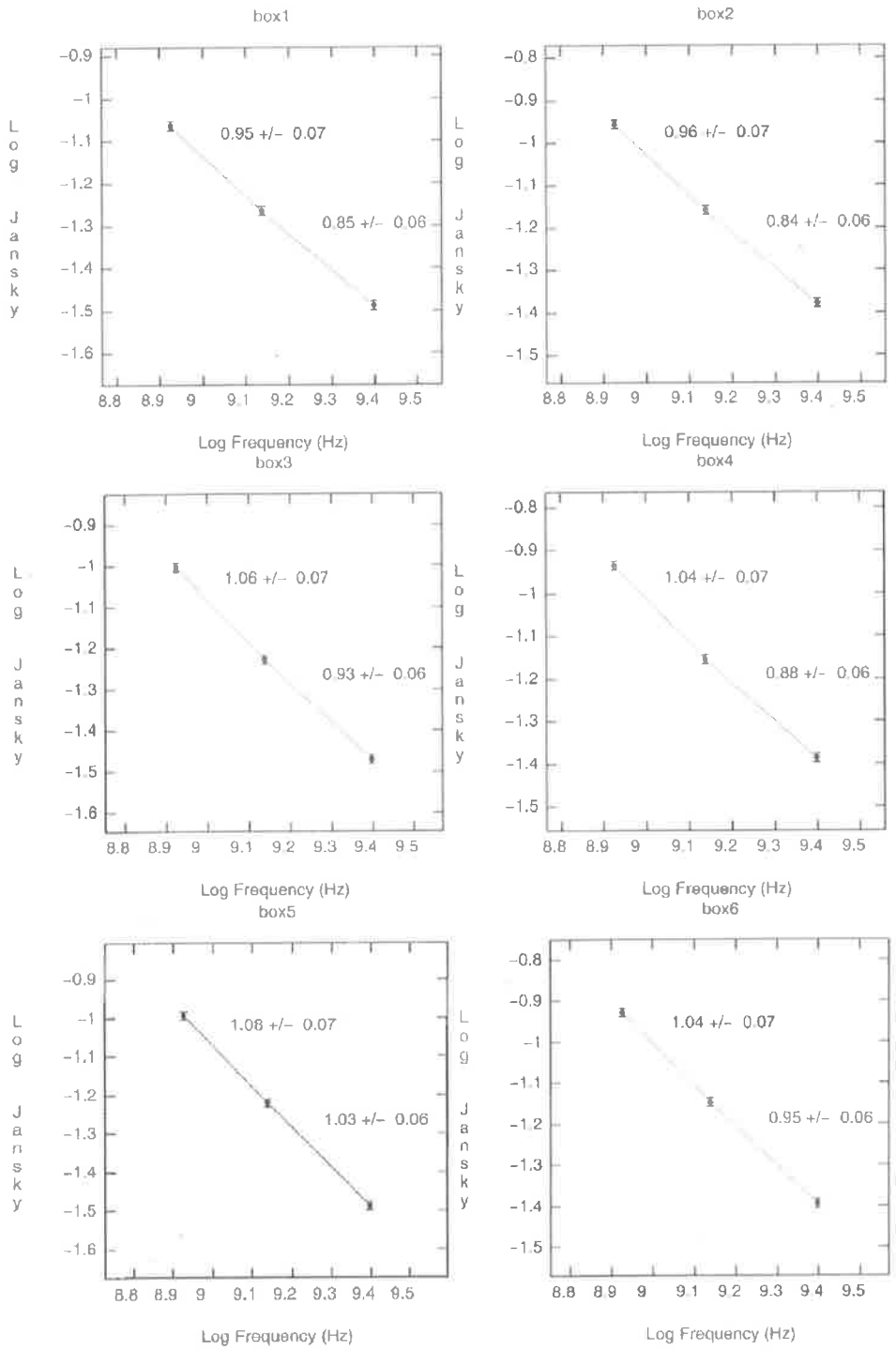

Figure 5.34: Spectral index plots for the filamentary parts of the larger diffuse emission region in A3667. The corresponding box location is given in Figure 5.33. These regions show a power law spectrum with $\alpha_{ave} = 1.0 \pm 0.1$, suggestive of continuous energy injection.

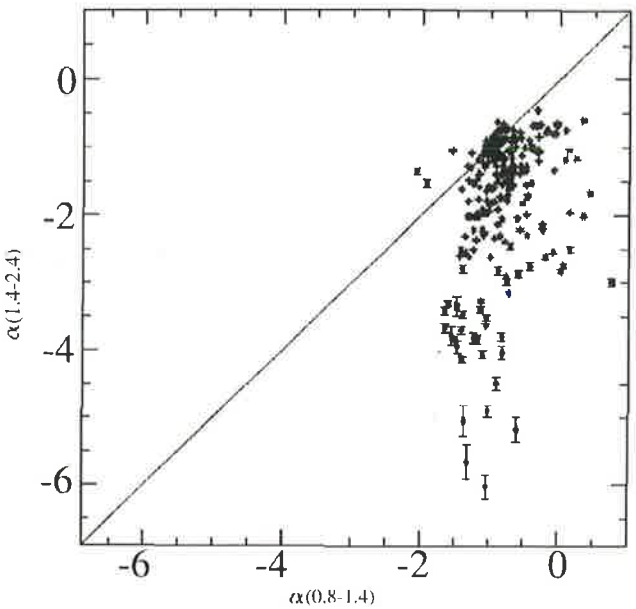

Figure 5.35: $\alpha_{1.4}^{0.8}$ versus $\alpha_{2.4}^{1.4}$ for the all points across the NW DRER in A3667. The points clustered about the line of unity are those from within the source filaments. The other points exhibit the signature of simple diffusion.

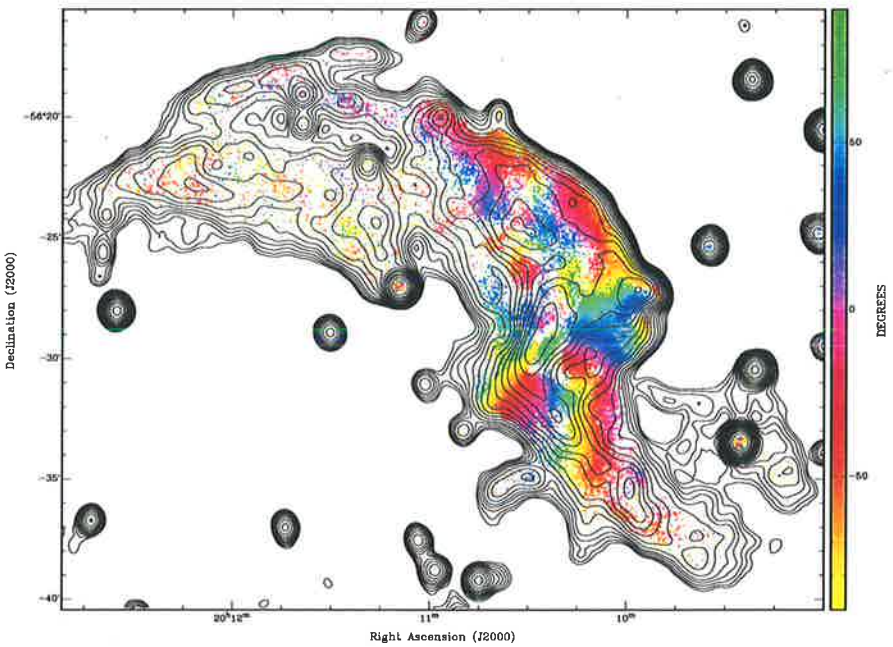

Figure 5.36: 1.4 GHz derived position angle map for the NW diffuse emission in A3667. The image has been blanked below three sigma in total intensity.

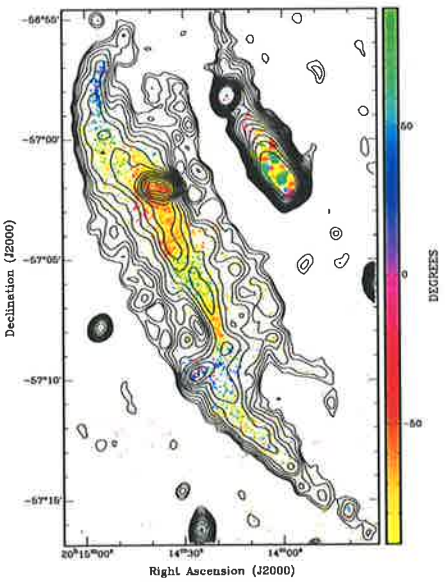

Figure 5.37: 1.4 GHz derived position angle map for the SE diffuse emission in A3667. The image has been blanked below three sigma in total intensity.

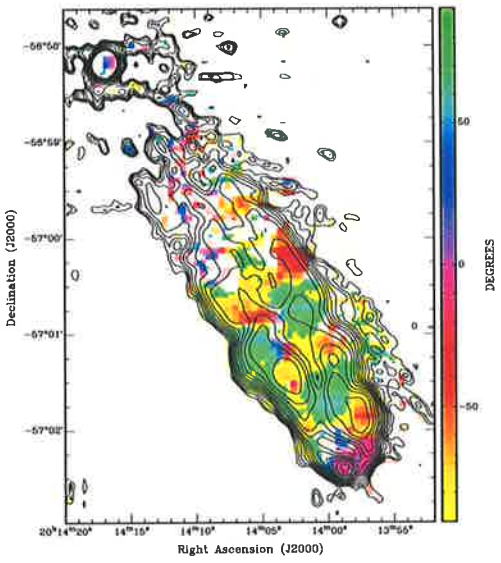

Figure 5.38: 1.4 GHz derived position angle map for the head-tail galaxy J201358.890-570226.00. The image has been blanked below three sigma in total intensity.

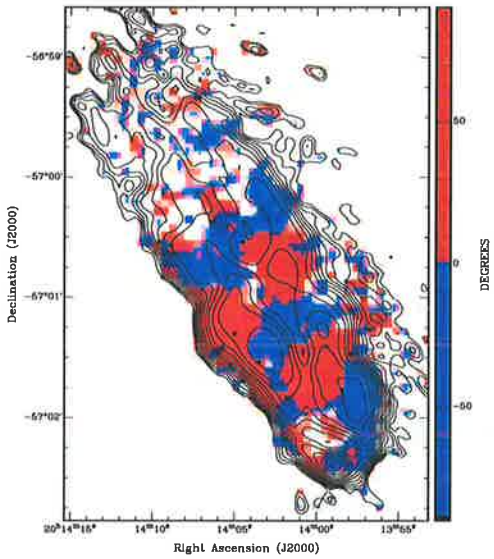

Figure 5.39: 1.4 GHz derived position angle map for the head-tail galaxy J201358.890-570226.00. The image has been blanked below three sigma in total intensity. All positive values are shown in red and all negative values are shown in blue. The reversal scales here are of the order 30 – 80 kpc and are likely associated with the cluster magnetic field.

$$\langle RM \rangle = 812 B_{||} n_e d \tag{5.1}$$

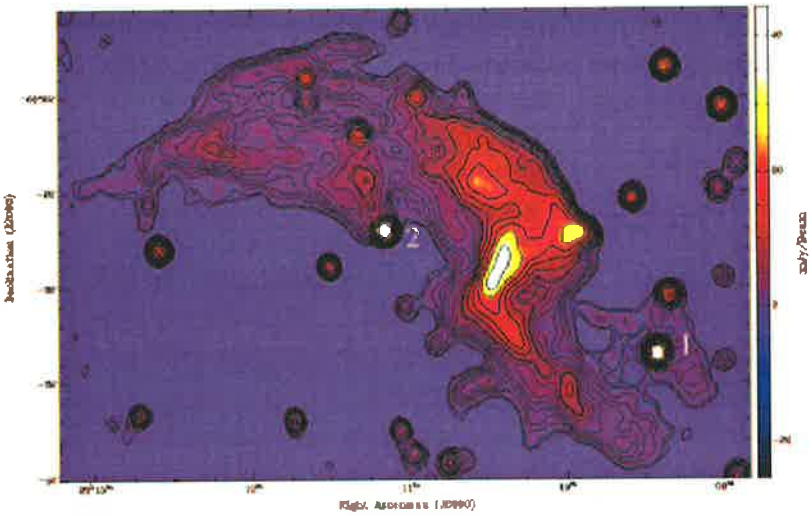

Figure 5.40: Locations of extragalactic objects used to probe the magnetic field in the region of the DRER via Faraday rotation measures. The northern DRER is shown at 1.4 GHz in low resolution (43 × 40 arcseconds) with contours at 0.027, 0.038, 0.054, 0.076, 0.11, 0.15, 0.21, 0.30, 0.42, 0.59, 0.83, 1.2, 1.7, 2.4 and 3.4 mJy beam^{-1}, and the two sources with high RMs are labelled as source 1 and 2.

The lines of sight to both sources are beyond the X-ray emitting region of the cluster. Without a high thermal electron component, a large RM here suggests a very high field strength. For the larger RM value, the background source lies behind the very tenuous part of the northern DRER, as shown in Figure 5.40. Using an electron density of 10^{-4} cm^{-3} (Röttgering et al. 1997) and assuming a spherical geometry of 400 kpc. This gives $\mathbf{B}_{RM} = 5.1$ μG. Assuming similar dimensions, the second RM value gives $\mathbf{B}_{RM}$ =3.0 μG. Performing a standard equipartition magnetic field calculation in the region of the first source gives $\mathbf{B}_{eq} = 2.5$ μG assuming a spectral index of 2 or $\mathbf{B}_{eq} =$ 1.5 μG assuming a spectral index of 1. For the second source where the spectral index is known to be roughly 1.3 an equipartition magnetic field of $\mathbf{B}_{eq} = 1.8$ μG is found. Thus, the equipartion fields strengths are a factor of two lower than the RM derived field. However, as equipartition field strength calculations require many assumption, a factor of two difference is not unreasonable.

As it is not possible to untangle the background source's intrinsic RM from that produced along the line of sight it is not possible to say for certain that these RMs are the result of an enhanced field in the region of the diffuse emission. However, statistical examination of a population of over 900 extragalactic RMs from the literature

(see Chapter 3) suggests that the probability of encountering a purely intrinsic RM greater than 160 rad m^{-2} at this latitude from the galactic plane is 1.7%, whereas the probability of encountering a value of greater than 95 rad m^{-2} is 2.5%. The combined probability of encountering two such high RM from Faraday rotation purely intrinsic to the probe galaxy at such a close separation is 0.04%. This provides a strong argument that the high RM is due to the cluster magnetic field.

The model of Roettiger et al. (1999) predicts a compression of the magnetic field in the vicinity of the bow shock, but gives it strength to be only 0.6 μG . A field compression would normally not be greater than 3–4 times the original field strength. Using this theory it would be possible to explain these high RMs as an enhancement of standard 1–2 μG magnetic fields observed in other galaxy clusters (see Chapter3). However, Kelvin-Helmholtz stability arguments for the cold front observed in the cluster core have already suggested that there is a strong field present in A3667 with values of 7–16 μG being calculated (Vikhlinin et al. 2001). This suggests that there is not a shocked field compression in the cluster periphery as these measured outer field values are too small.

5.10 Comparison to Other Diffuse Sources

A3667 exhibits characteristics common to other diffuse radio sources. The over all steep spectra of the two regions, their high polarimetry and irregular morphology are common to the so-called *radio relic* population. However, as shown here, A3667 also exhibits a highly filamentary structure, with strong polarimetry in the region of the brightest filaments and at the highest resolution a possible jet-like structure. Further, the difference in spectral index between the filaments and diffuse parts of the source is at odds with the current acceleration models.

Comparison to other diffuse sources is difficult, in part due to the low number of specimens, particularly Mpc scale sources and in part due to the natural preference to observe at low resolution. Nevertheless filamentary structure has been reported in a couple of diffuse radio sources. However, such sources such as the source in A85 (Slee et al. 2001) are all relatively small, and it is not surprising to find radio plasma containing the ordered magnetic fields required to maintain filaments on this scale. However, generating and maintain ordered magnetic field of the order of 250 – 400 kpc is problematic. Also, small scale sources such as that in A85, shown to scale next to the emission in A3667 in Figure 5.41, are not sufficiently large to prohibit the relic model of particle diffusion. In fact, Slee et al. (2001) conclude that these small scale regions of emission are in fact true relics, having originated from now dead radio galaxies.

In an effort to search for filaments in other diffuse radio sources a VLA campaign to image 0917+75 was initiated. 0917+75 is an Mpc-scale diffuse radio emission region, which is not associated with a particular cluster but rather with the Rood 27 cluster group. Previous observations hinted at the possibility of filamentary structure and Harris et al. (1993) commented on the inability to fit a single spectral index to the entire emission, suggesting that there might be two different electron populations

present. Data were obtained with the VLA at 1.4 and 5 GHz and forms part of an ongoing collaboration (Johnston-Hollitt (PI) & Clarke). While the data are still only preliminary, the first results are of relevance to this Chapter. Highly polarised, filaments have been detected in 0917+75 as well as a point-like source and jet structure. Figure 5.42 shows the total intensity 5.0 GHz emission. This is the most sensitive image of diffuse emission yet made, the RMS noise here is 10 μJy per beam for an 0.5 arsecond beam. It is possible that this point source is a background source, the combination of this detection and that seen in A3667 are suggestive.

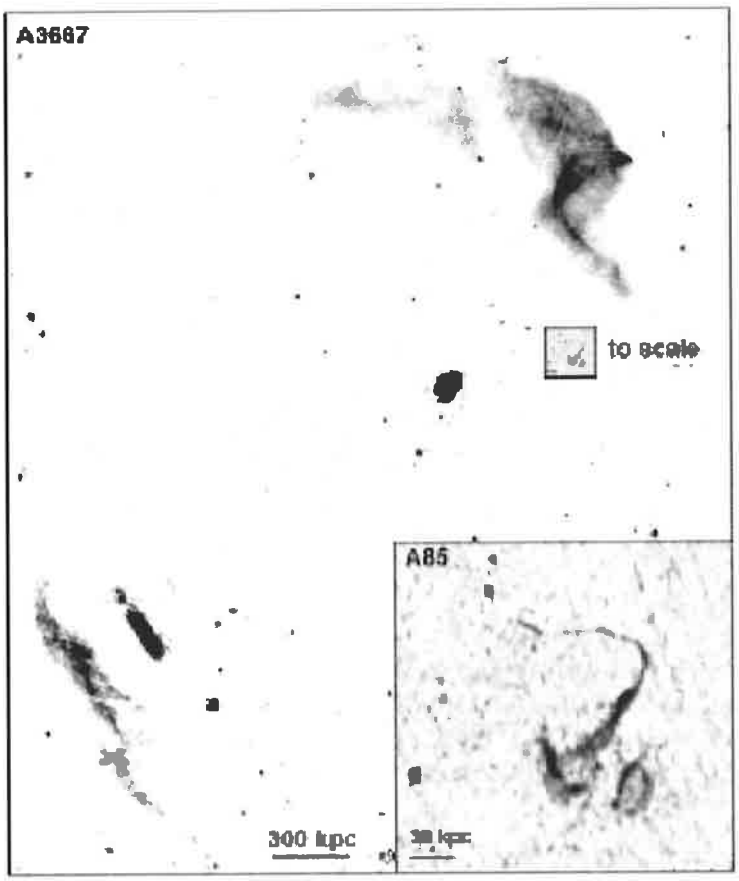

Figure 5.41: Comparison of the diffuse sources in A3667 and A85 (Slee et al. 2001). The diffuse emission in A85 has been scaled to the same size as that of A3667. While both clusters exhibit diffuse emission that is filamentary there is a vast difference in scale.

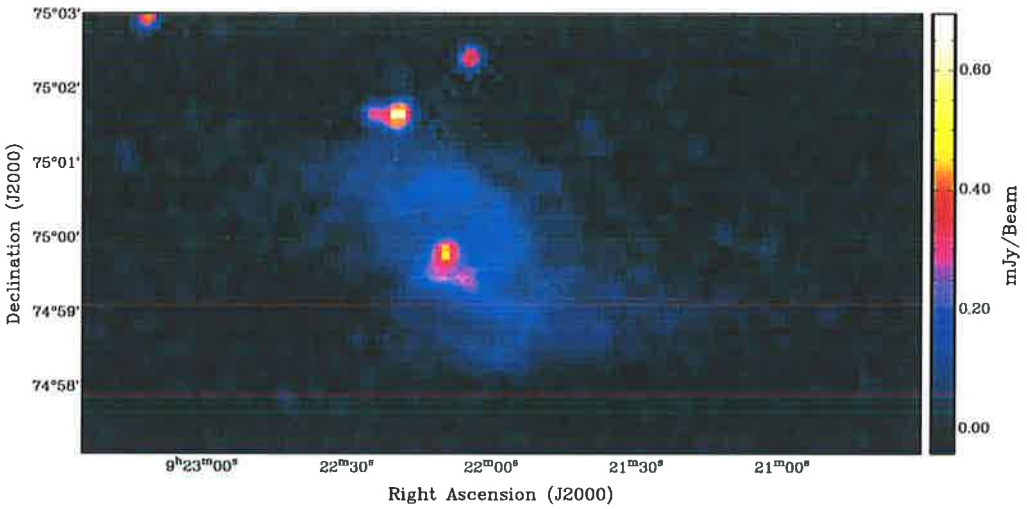

Figure 5.42: The Mpc scaled diffuse emission region, 0917+75, in the Rood 27 cluster group. This data is taken with the VLA at 4.8 GHz and is shown here with a resolution of 0.5 arcseconds. This is the most sensitive emission of a DRER yet produced. It is from the ongoing study of Johnston-Hollitt & Clarke.

5.11 Discussion

Emission by relativistic particles on spatial scales comparable to those observed in clusters such as A3667 is only possible if acceleration takes place within the emission region. Many theories have been put forward for mechanisms that might accelerate particles over such large scales. These include collisions with thermal protons in the cluster, generation by galactic wakes and emission from AGN. None of these theories are tenable in the case of A3667 (see Röttgering et al. 1997 for further discussion). Models specifically designed to explain the emission in A3667 included accretion shocks from in-falling matter due to cosmological structure formation (Enßlin et al. 1998) and cluster merger induced shocks (Roettiger et al. 1999). However, to date none of the predictions of either model have been successfully verified by the data. Enßlin et al. (1998) predicts a maximum percentage polarisation of 30% for the Southern emission region based on their geometrical model, however, the observed percentage polarisation is much higher than this. Also, the particle source is problematic in the original model, as the head-tail galaxy J201358.890-570226.00 does not have the correct alignment with respect to the Southern emission to provide the suitable seed particles, however using the refined theory of *fossil plasma* (Enßlin 1999) goes some way to improving this situation. The merger induced shock model of Roettiger et al. (1999) does somewhat better, by correctly predicting the spectral gradient of the Southern emission (Roettiger, K., private communication 1999) and location of central radio emission. However, the strength of the central radio emission is vastly over estimated and the predicted magnetic field strength severely underestimated. Furthermore, both scenarios are based on shock models wherein the magnetic field is compressed in the region of the shock. This would result in diffuse radio emission which has a very sharp leading edge and a steep spectral gradient in the direction of shock expansion. However, while the Southern emission may fit this profile, the general spectral gradient of the Northern emission is not in the correct direction for this model. Furthermore, the Northern source doesn't exhibit the correct intensity profile of a sharp leading edge. Finally, the filamentary nature of the source and the observed power law spectral index are not readily explained by shock generation.

The current weight of the literature rests firmly with the notion that peripheral diffuse emission associated with galaxy clusters is generated via shocks from cluster-cluster mergers. However, it is intriguing to note the similarities of the emission in A3667 and that in 0917+75. Both are Mpc scale objects, both have a filamentary structure, with high polarisation and both can not be fitted to a single spectral index suggesting two distinct electron populations. At high resolution they both exhibit signs of a central point like source. However, in the case of 0917+75, which is over 5 Mpc from the nearest member of the Rood 27 cluster group, the merger scenario seems unlikely.

In order to better understand the conditions in A3667 a detailed optical investigation into the galaxy redshift distribution was also undertaken. This will be discussed in the next Chapter.

5.12 Summary

Radio observations of the ACO A3667 were presented. These new deeper observations have shown a filamentary structure in the diffuse emission, which appears highly polarised and at the highest resolution may have a point-like core. New results suggesting a possible central halo were presented, along with 3 point spectral index data. These results were discussed in the context of current generation models for diffuse radio emission.

Chapter 6

Optical Data for A3667

6.1 Introduction

As discussed in the previous chapter, it has been suggested that diffuse cluster emission may be generated via shock acceleration due to cluster-wide merger events (Harris et al., 1980; Tribble, 1993). If this model is correct we would expect signatures of the merger activity within the galaxy population in clusters which harbour such diffuse emission.

Previously it has been claimed that substructure in the X-ray emission and lack of a cooling flow provide the necessary evidence for collisional history in a galaxy cluster. However, complex X-ray structure is observed in a large number of clusters, while diffuse radio emission remains relatively rare. Thus, even if the merger model is correct it suggests that either the diffuse radio emission is short-lived or that merger history may be a necessary but not sufficient condition for the generation of large scale diffuse radio emission.

In the majority of cases, diffuse emission is associated with a small redshift range being roughly $0.05 \leq z \leq 0.3$. This is likely to be due in part to selection effects. At low redshifts, diffuse emission is difficult to detect using interferometers. This is due to the lack of short spacings which makes interferometers insensitive to large angular structures. If one assumes diffuse emission to have a typical physical scale of 1 Mpc then instruments such as the VLA which are only sensitive to structures less than 15 arcminutes, will only be able to detect such sources for $z \geq 0.044$. Conversely, two effects will come into play at high redshifts. The first is simply current instruments are not sensitive enough to detect very distant objects. The second and more subtle effect is that blind searches for diffuse emission are not undertaken. All searches to date have made use of the ACO cluster catalogue which is biased to $z \leq 0.3$. Thus, the diffuse emission we are observing either occurs most often fairly late in a cluster's lifetime or the radio emission is very long-lived. However, we know from energy loss arguments from spectral aging in relics that electrons may only emit via the synchrotron process for 0.1 –1 gigayears at centimetre wavelengths. This provides some clue as to the time scale on which diffuse emission can be observed without continuous energy injection.

Observations of starburst galaxies have shown a strong correlation between star

formation and tidal disruption. Such disruption may be either the result of galaxy mergers, such as the famous case of the Antennae galaxies (NGC4038 & NGC4039), or from accretion or merger shocks in the ICM. An excess of starbursts would seem then to indicate a turbulent state, either through more individual galaxy collisions as in the case of CL 1358+62 (Bartholomew et al. 2001), or through shockwave disruption throughout the ICM, possibly resulting in ram pressure stripping. Thus, one might expect that an over density of starburst galaxies would be evidence for a recent cluster merger. However, during the late stages of cluster evolution we know from the Butcher-Oemler effect that cluster constituent galaxies are more likely to be gas-stripped red ellipticals than gas-rich blue spirals. Without an abundance of gas it is unlikely then that starbursts per se would be observed. A more likely indicator of merging would be an excess of the so-called "E+A" galaxies, which are thought to represent post-starburst galaxies in an older elliptical population (Couch & Sharples 1987). "E+A" galaxies are thought to be generated either via galaxy mergers or through ram pressure stripping (Belloni et al. 1995). In either case, the presence of "E+A" galaxies is indicative of past interactions in the cluster.

"E+A" galaxies have spectra that are dominated by a young stellar component indicated by strong Balmer absorption and weak [OII] emission but lack the emission lines characteristic of galaxies with significant ongoing star formation. The term "E+A" is derived from spectral properties, with the "E" denoting an elliptical while "A" is for the Balmer lines which are a characteristic of A stars. Recently the literature has favoured the term "k+a" or "a+k" to describe these systems. This shift reflects the dominance of both K and A star signatures in the spectra.

In order to test further for signatures of a cluster wide merger in the optical population of A3667, a set of spectral observations of objects in the cluster region was undertaken. In this chapter previous optical work will be discussed and placed in the context of the new observations.

6.2 Previous Optical Observations

A3667 has long been considered a merging system based primarily of its bimodal optical density distribution (Proust et al. 1988) and high velocity dispersion (Sodre et al. 1992).

Melnick & Quintana (1981) obtained redshifts for 16 member galaxies of A3667. Following this, Proust et al. (1988) obtained a further 31 redshifts for galaxies in the field of A3667, which they combined with the previous results. Unfortunately this combined sample hereafter, denoted P88, has since been found to contain unreliable redshift values for several of the galaxies in the field (Sodre et al. 1992). Proust et al. (1988) also posited the bimodality of the cluster via an isodensity plot of 423 galaxies with $m_B \leq 19$ in the field of A3667. This plot is shown in Figure 6.1. Two groupings can be seen in the plot. The main group (A3667) was attributed a redshift of 0.0550, being that of the closest galaxy to the centre of the cluster, while the subgroup to the north-west was suggested to be at 0.0563, from redshift value of a near by object. It should be noted that nearly 90% of the galaxies in this plot had unknown redshifts and

inevitably many correspond to either foreground or background objects.

Figure 6.1: Isodensity plot of 423 galaxies with $m_B \leq 19$ in the field of A3667 (Proust et al. 1988).

Sodre et al. (1992) expanded upon the Proust data by taking spectra for 203 galaxies in the vicinity of A3667. Of the 203, redshifts were obtained for 128. This sample, hereafter called S92, included reobservation of almost all but five of the galaxies in the P88 sample. Large discrepancies in velocity were found between the two samples. As neither study published spectra this has made it difficult to determine which was the more accurate; however, in general the S92 sample has smaller errors associated with the measurements and is assumed to be the more reliable of the two. Other data in the literature have provided a further 28 redshifts for objects in the S92 sample bringing the total number of redshifts available in the region of A3667 to 161. Of these, 155 fall between $0.044 \leq z \leq 0.068$ and are likely to be cluster members.

However, neither the S92 nor P88 sample provides information on the galaxy types

within the cluster. The only available information on galaxy types to date comes from either the Digitized Sky Survey, where a morphological guess can be made for the brightest objects, or from two R-band CCD images, observed with the 3.9m Anglo-Australian Telescope by R. W. Hunstead (2001, private communication). These images are located either side of the northwest diffuse radio emission region (DRER). The AAT images, shown in Figures 6.2 and 6.3, seem to exhibit an excess of spiral galaxies compared with the central regions. Though it is not uncommon to find spiral galaxies on the periphery of a rich cluster (Snow 1991) this particular group seems quite dense. In addition, the group is roughly aligned with the northernmost part of the bimodal optical distribution reported by Proust et al. (1988) and could represent an in-falling group. For clarity, the two images have been mosaiced together in Figure 6.4

Girardi et al. (1996) studied A3667 as part of a sample of 37 galaxy clusters used to examine the relationship between velocity dispersion, σ, and X-ray temperature, T. They reasoned that since both σ and T were related to a cluster's gravitational potential there would only be strong correlation between these values for those clusters with both gas and galaxies in dynamical equilibrium with the cluster potential. Using the 123 redshifts from the S92 sample, Girardi et al. (1996) examined A3667 for substructure using both a velocity distribution and velocity gradient analysis. They found neither significant peaks in the velocity distribution, nor a velocity gradient. Using the method of Dressler & Shectman (1988) they computed the probility of substructure as 0.697 where a result above 0.990 was considered significant. An isodensity plot for the S92 sample was generated, this is shown in Figure 6.5. Despite the lack of statistical evidence, this plot is reminscient of the Proust et al. (1988) plot shown in Figure 6.1 and suggests some substructure to the Northwest of the cluster centre. The velocity dispersion was determined to be 1208^{+94}_{-84} km s^{-1}.

Expanding on their previous work, Girardi et al. (1998) used 154 of currently known 155 redshift values for A3667 to compute a maximum cluster radius of 2.22 h^{-1} Mpc, a mean galactocentric redshift of 0.0566 and a global velocity dispersion and associated errors of 971^{+62}_{-47} km s^{-1}. Girardi et al. (1998) also obtained a viralised radius of 1.94 h^{-1} Mpc in which 152 of the galaxies with previously measured redshifts are contained. The total virialized mass was calculated to be $15.98^{+2.18}_{-1.71} \times 10^{14}$ M$_\odot$. They further concluded that the velocity distribution was isotropic. In comparison Knopp et al. (1996) give the X-ray radius of the cluster to be $R_x = 0.80$ h^{-1} Mpc and the X-ray mass at $M_x = 3.50^{+0.30}_{-0.40} \times 10^{14}$ M$_\odot$. Girardi et al. (1998) obtain an optical mass of $M_o = 4.89^{+0.67}_{-0.52} \times 10^{14}$ M$_\odot$ within this X-ray radius. Assuming that the cluster mass follows the gravitation potential, the good agreement between these mass estimates strongly suggests that the cluster is in dynamical equilibrium (Girardi et al. 1998).

6.3 2dF Observations

In order to increase the redshift sample and examine the distribution of galaxy types in the cluster, observations were undertaken with the 2dF spectrographic system (Section 2.7). SuperCOSMOS plate scans were used to obtain a list of suitable galaxies with

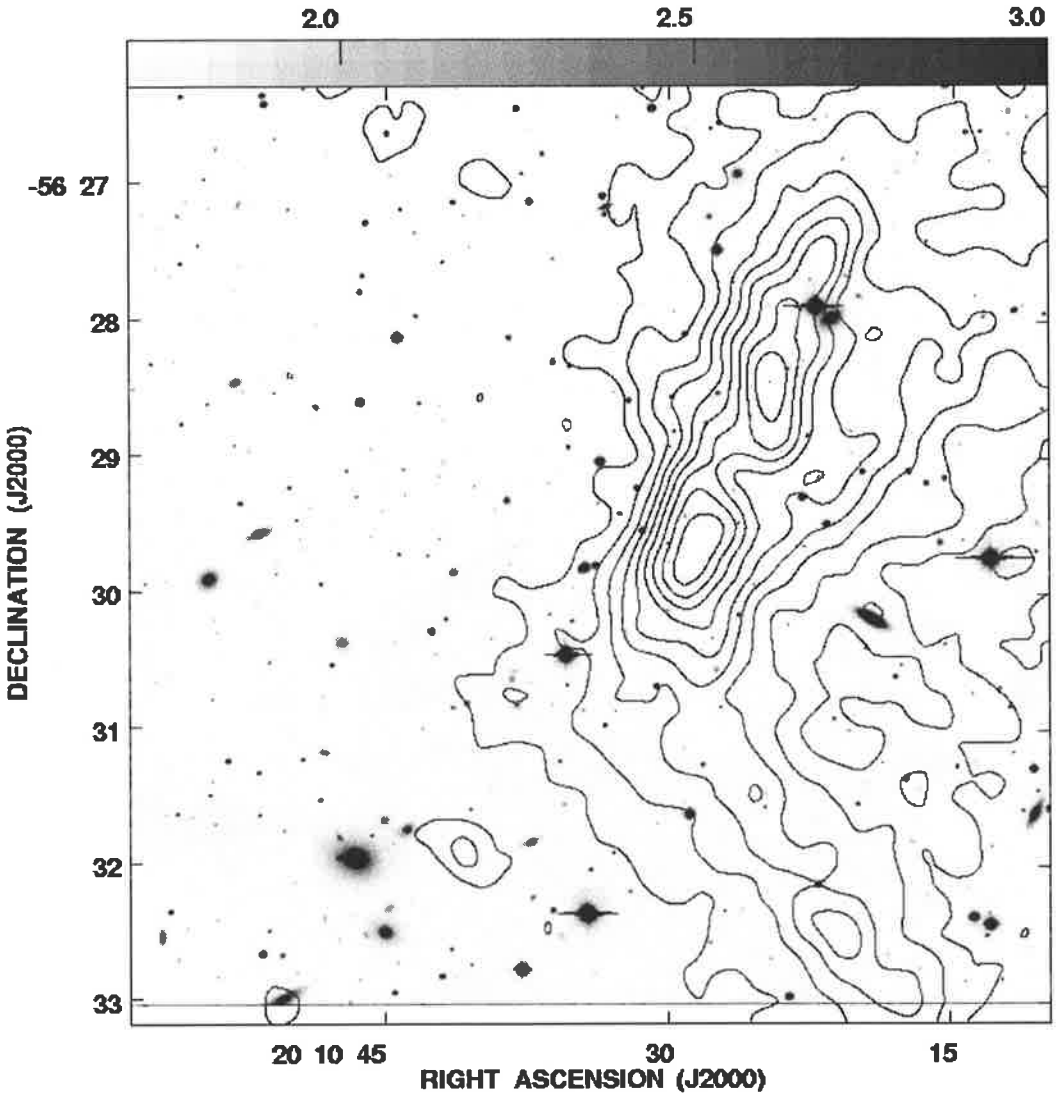

Figure 6.2: R band CCD image of A3667 South of the Northwest DRER (shown as contours from the 1.4 GHz data). The galaxy population is richer in sprials on the outer edge than here closer to the cluster's central region (Hunstead 2001, private communication).

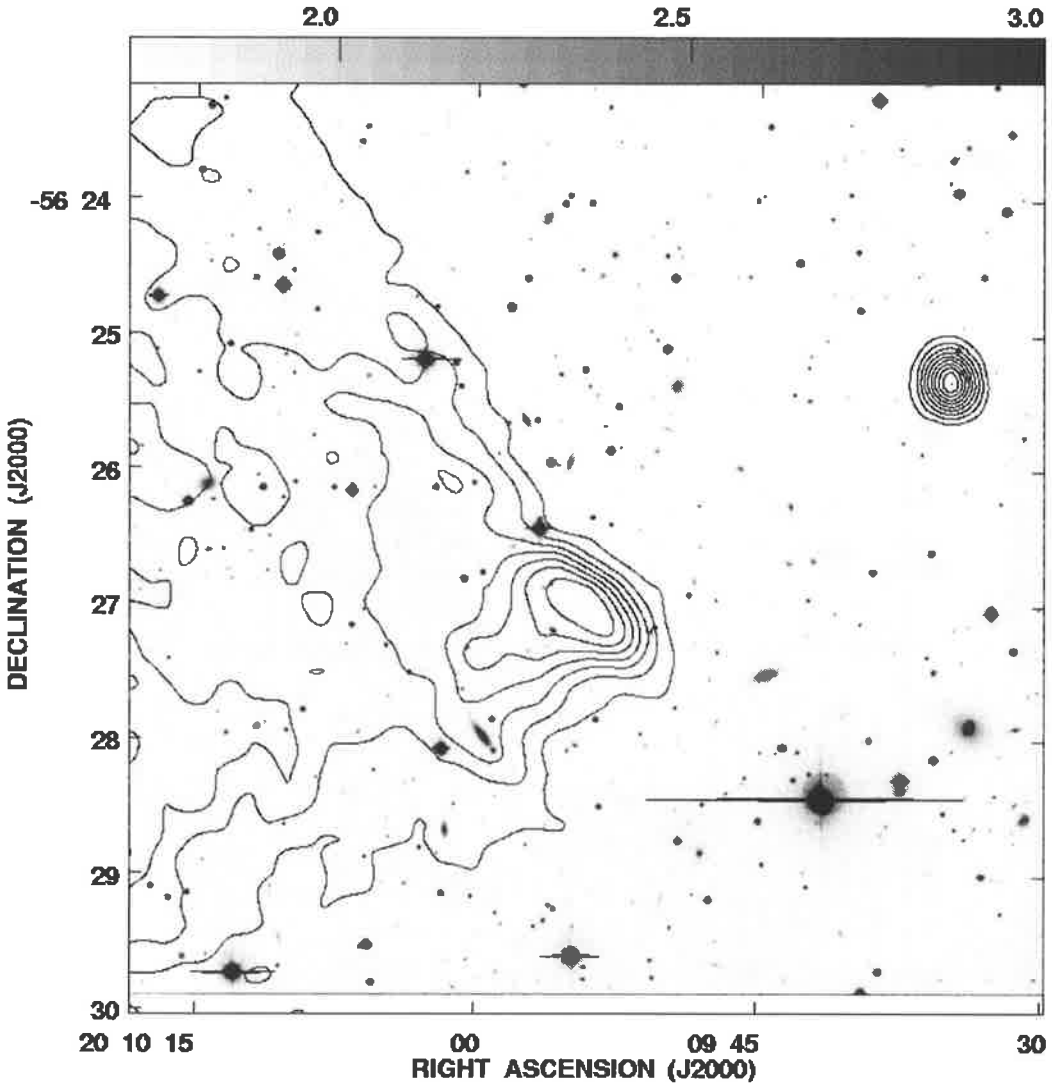

Figure 6.3: R band CCD image of A3667 North of the Northwest DRER (shown as contours from the 1.4 GHz data). The galaxy population here is richer in spirals that the cluster's central region (Hunstead 2001, private communication).

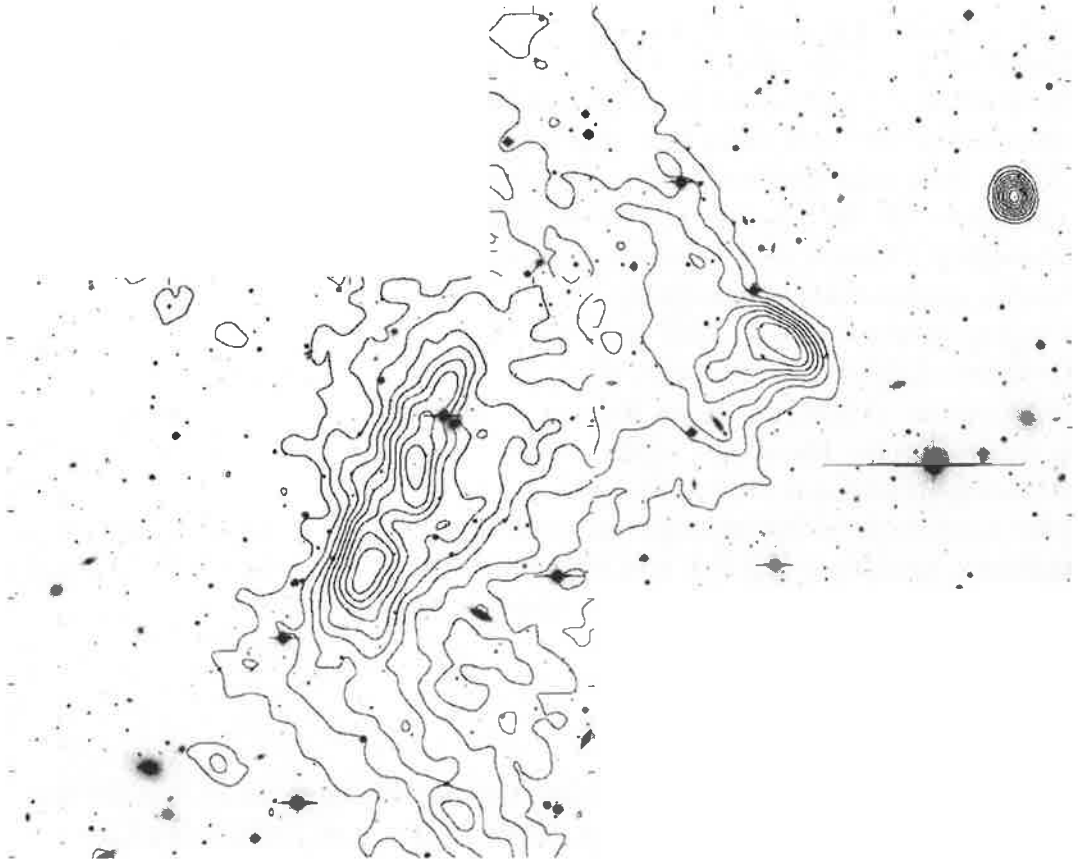

Figure 6.4: The two R band CCD images of A3667 from Figures 6.2 and 6.3 shown as together to give positional perspective. Again the contours are for the 1.4 GHz ATCA data for the diffuse radio emission region to the clusters North.

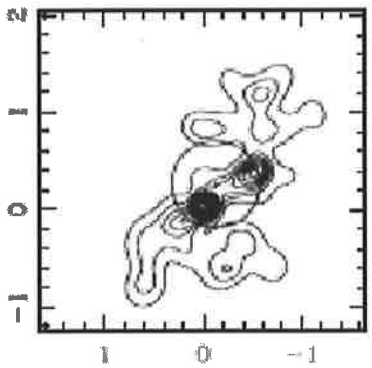

Figure 6.5: Isodensity plot for the S92 sample of 123 galaxies from A3667 with known redshifts Girardi et al. (1998).

$15.5 \leq m_b \leq 18.3$ which had not previously been observed by Sodre et al. (1992). As there is a marked discrepancy between the redshift values for some objects observed by Proust et al. (1988) and Sodre et al. (Sodre et al.) it was decided that a subset of the Sodre et al. (1992) catalogue would be reobserved with 2dF to determine any systematic differences in redshift. The optical counterparts of the radio galaxies in the ATCA data were also included in the target selection. This produced a set of 338 target objects. Of the remaining 62 fibres, 49 were used for guide stars and skys, while the remaining 13 fibres were broken.

Service observations were initially scheduled for 2000 November 01. Unfortunately, poor seeing prevented the A3667 field from being observed. The observations were re-scheduled on 2001 July 20, using the 270R/316R grating. A total integration time of 1.5 hours was obtained in three 30-minute integrations to allow cosmic ray removal via a sigma-clipping algorithm. This gave a wavelength coverage from 3600 to 8000 Angstroms (Å), although this varies between the two spectrographs due to the slightly different dispersions of the gratings and from fibre to fibre on each spectrograph. The instrumental resolution is 9.9 Å and the predicted signal for an $m_B = 18.3$ galaxy at two arcsecond seeing is $\simeq$ 30 counts per pixel at 7000 Å.

6.4 Data Reduction

Data were reduced using the 2dfdr pipeline software package, which was developed for the 2dF Galaxy redshift survey (Colless, 1998; Colless et al., 2001). Data are prepared by performing a number of steps. First the residual effects of any strong atmospheric emission lines at 5577, 5893, 6300 and 7244 Å are removed via masking and the resultant gap of around 20–30 Å is interpolated across. Then the atmospheric absorption bands around 6870 Å (B-band) and 7600 Å (A-band), and the fibre absorption band at 7190 Å are removed by dividing by an appropriate correction. Any bad columns in the CCD are masked and the spectra are then interpolated across these regions.

The software performs two independent redshift estimating procedures based on both the emission and absorption properties of the spectra. For the absorption features the standard technique of cross-correlation (Tonry & Davis 1979) between the spectra and a set of eight known absorption templates is performed. A brief description of the cross-correlation theory is given in Appendix C.

Spectra are prepared for cross-correlation via a six step process that includes: 1) continuum-subtraction; 2) clipping strong emission lines; 3) rebinning to a logarithmic scale; 4) apodization; 5) Fourier transformation and 6) application of an exponential filter. Further details of each process can be found in Colless et al. (2001). Once the spectra are prepared the cross-correlation is computed as the inverse Fourier transform of the product of the Fourier transforms of the galaxy and template spectra.

The highest peak in the cross-correlation function is then fitted with a quadratic equation to obtain its position and height. The ratio of the peak height to the noise level in the cross-correlation function is subsequently computed. This ratio, R, is then used to determine the quality of the redshift estimation, via the assignment of a quality

flag, Q_a, to each spectra. The value of Q_a ranges from 1 to 4 with 4 and 3 meaning a reliable fit (R $\geq$ 5.0 or 4.5), 2 a probable fit (R $\geq$ 4.0) and 1 an unreliable fit (R $>$ 3.5). If no fit is obtained a quality factor of 0 is assigned. For values where Q_a equals 3 and 4, there is an additional requirement that at least four and six of the eight templates respectively, produce a redshift to within 600 kms^{-1}.

For emission features the code performs a Gaussian profile fit to each feature after first subtracting the continuum. Any peaks in the resultant spectrum which are higher than 3.3 times the RMS are marked as candidate emission lines. Gaussians are then fitted to each line in descending order of line strength. After each line is fitted, it is then subtracted from the spectrum in order to reduce the effects of blending. Lines which have fitted FWHMs between 0.7 and 7 pixels and significances higher than 3.5 σ are marked as *good*. Lines that do not meet these criteria are rejected, removing any contamination from unclipped cosmic rays and low significance features. The three strongest lines in each spectrum are then tested in pairs for line separations consistent with a known redshift from a set of common emission lines ([OII], Hβ, [OIII], Hα or [NII]). If a match is found then the rest of the emission lines are matched to that redshift to within 600 kms^{-1}, and the mean redshift is adopted as the emission redshift. If no two emission lines are found to match a particular redshift for a pair of common lines, (or there are fewer than three lines in total) then up to two single-line redshifts are retained for comparison with the absorption derived redshift. A quality flag for this redshift estimate, Q_e, is assigned based on the number of features fitted. This number can take the values 0,1,2,4 with 0 being no lines, 1 for one line, 2 for two lines and 4 for three or more.

The code then compares the redshift obtained via each method and selects the one with the higher quality flag. In the case where $Q_a = Q_e$ the absorption value is selected. The best quality flag , Q_b is then given as the greater of Q_a or Q_e, with two exceptions: 1) if the difference in redshifts derived via the two methods is less than 600 kms^{-1} then Q_b is the maximum of Q_a, Q_e or 3 and 2) if Q_a and Q_e are both less than 2 and the difference in redshifts derived via the two methods is greater than 600 kms^{-1} then Q_b is set to 1.

After the automatic quality flags are assigned the spectra are then manually inspected and interactively re-fitted if necessary. Also at this time the observer may input their own quality flag on a scale of 1 to 5, with 5 being spectra of highest quality.

As it is necessary that an appropriate template spectrum is selected to perform the cross-correlation, the code also outputs which of the eight templates produced the best correlation with each spectrum. This gives information on the objects morphological type, as a number from 1–8. The first five templates are for galaxies, whereas the last three are for stars. Figure 6.6 shows the eight template spectra used in the 2dfdr code. The galaxies used and their morphological types as listed in Colless et al. (2001) are: 1) NGC 3379 (E), 2) NGC 4889 (cD), 3) NGC 5248 (Sbc), 4) NGC 2276 (Sc) and 5) NGC 4485 (Sm/Im). The stellar spectra used are 6) HD 116608 (A1V), 7) HD 23524 (K0V) and 8) BD05°1668 (M5V).

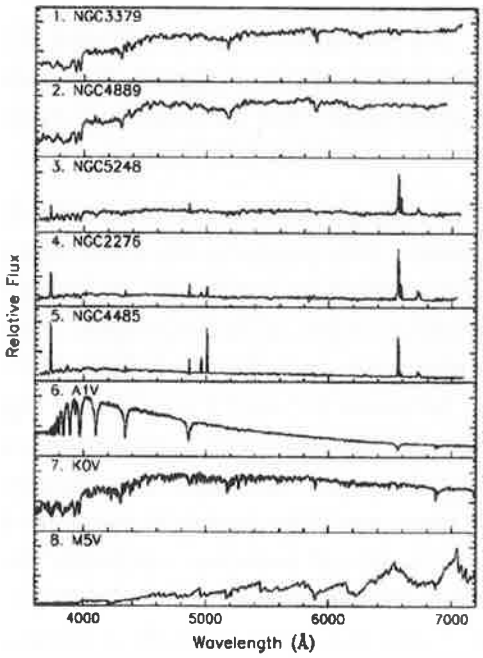

Figure 6.6: Template spectra used for cross-correlation redshift fitting (Colless et al. 2001).

6.5 Results

Of the 338 object spectra obtained, 136 turned out to be misclassified stars. Apparently this was due to a problem with the SuperCOSMOS object discriminator software for bright objects in the pre-release SuperCOSMOS data. In order to fulfill the requirement of having the optical counterparts for the radio galaxies in the target list, the bright magnitude cut off was set at 15.5. This, however, was too bright for the object classification software to distinguish reliably between stars and galaxies. A better strategy would have been to limit the apparent magnitude to $m_B \geq 16.5$ and to add the radio galaxy hosts to the target list individually, rather than selecting the larger magnitude range.

The redshifts obtained from all 387 active fibres were binned at intervals of 0.002 and plotted as a histogram, shown in Figure 6.7. This figure has two main features; the 136 misclassified stars near zero redshift and A3667 at around z= 0.057. The histogram shows remarkably little velocity structure either surrounding the main cluster group or within it. There is no evidence of distinct in-falling groups or other velocity features around the main cluster as have been found in other merging systems like the A3125/A3128 complex (Rose et al. 2002). Then again, perhaps this is not surprising as clusters which harbour DRERs have been shown to be statistically more isolated than clusters of similar X-ray luminosity (Schuecker & Böhringer 1999).

After the stars had been removed, the remaining 202 spectra were examined individually for quality of fit. Spectra for which the quality flag was less than 2 were

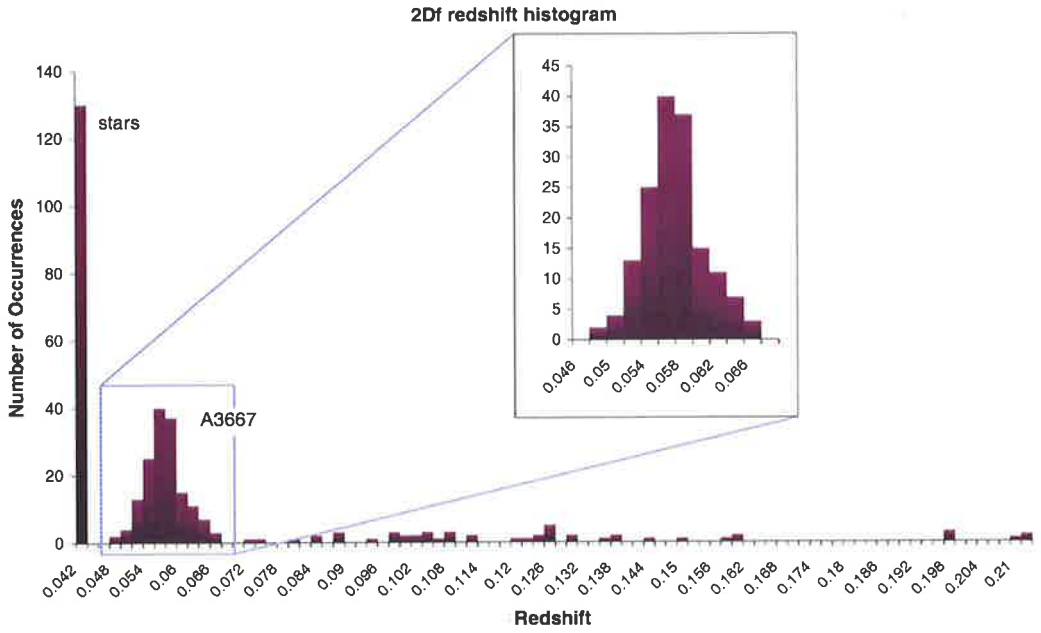

Figure 6.7: 2dF redshift histogram for the A3667 field.

treated with caution. Of the 202 spectra, 143 fell within the range of 0.044 to 0.068 and are considered to be members of A3667. This redshift restricted sample of 143 galaxies is plotted with the 154 values from the literature in Figure 6.8.

There are 67 sources which appear in both the 2dF and literature samples. It can be seen from the Figure 6.8 that there is very good agreement between the datasets in both position and redshift. As noted earlier, the P88 and S92 samples were found to have large redshift discrepancies for some objects. The S92 data were considered more reliable and used in the literature sample. The 2dF data agree well with redshift values in the S92 sample, suggesting that erroneous redshifts were from the P88 sample. To assess any systematic difference between the 2dF and literature samples a plot of measured redshifts from one versus the other was made, this is shown in Figure 6.9. The strong clustering about the line of slope unity suggests that there is no systematic error and the surveys agree well. Analysis of the difference in redshift for the two datasets shows that the median difference is zero and the standard deviation of the differences is 0.00036 this corresponds to a velocity of 109 kms^{-1} which is less than the error in the measurements ($\sim$ 200 kms^{-1}). This suggests that it is acceptable to combine these datasets.

As the spectra used to measure the values in the literature were never published there is no way to directly compare the data quality for a given galaxy. However, for the 2dF data an assessment of the fit quality was already known. The *blunder* rate for spectra measured in the 2dFGRS for which 2dfdr has assigned $Q_b > 2$, is only 1.6% and this depends strongly on magnitude, with almost all blunders occurring for $m_B \geq 18$ (Colless et al. 2001). Thus, for a relatively bright sample such as this one,

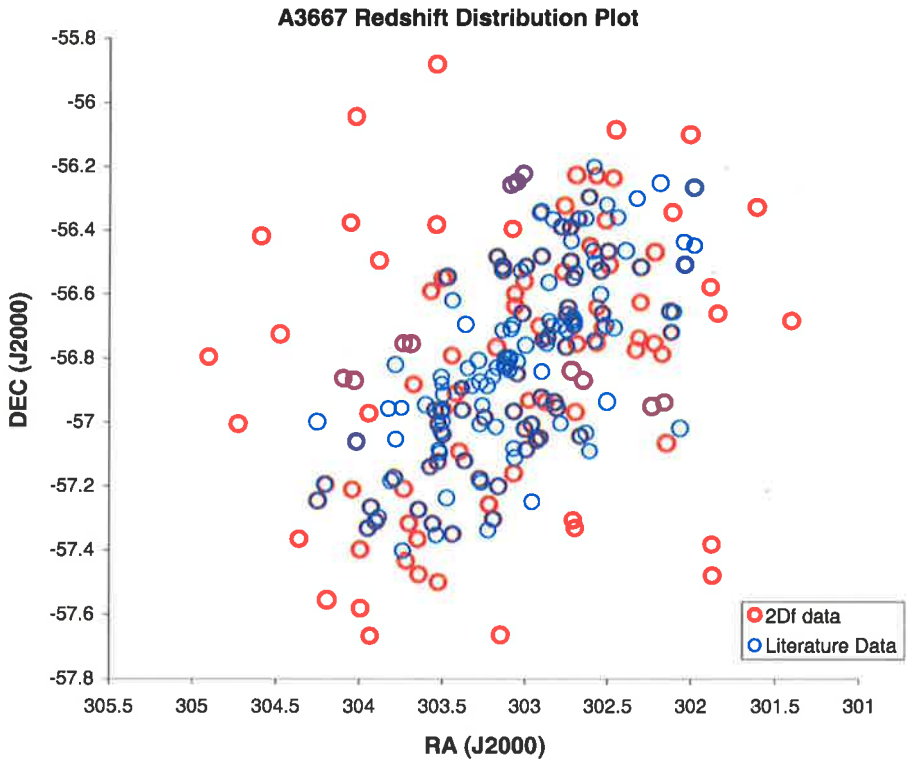

Figure 6.8: Redshift plot for A3667: The axes correspond to the position of the source and the colour of the circle denotes the dataset it belongs to. Red circles are the 2dF data and blue circles are the redshift from the literature. Where the 2dF and literature datasets agree in both position and redshift, the circle becomes purple. Appendix C contains tables of these data.

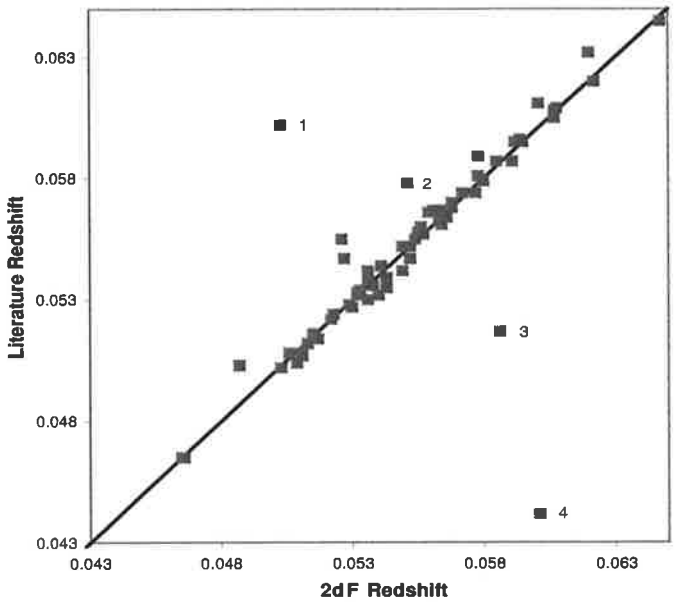

Figure 6.9: Redshift sample difference for A3667: The literature redshift is plotted versus the 2dF redshift for the 67 sources in both samples. Clustering about the slope of unity suggests there is no systematic difference between the two datasets. The four labelled outliers are discussed in the main text.

one can have confidence in the accuracy of the 2dF redshifts. When combining the two datasets for analysis the 2dF data were used in preference to the literature data in all cases where Q_b was greater than two. Of the nine spectra for which Q_b was less than two, seven agreed well with the previously published data and were used as redshifts in the combined dataset. The remaining two spectra had both poor 2dF fit qualities and large differences from the previous data (δ_z =0.0069 and 0.0027 which equates to $\approx$ 2000 and 800 kms^{-1}). These points can be seen on Figure 6.9 as outliers numbered 3 and 2. Both objects were quite bright with magnitudes of 16.90 and 17.39 respectively. The errors quoted in the literature were 61 and 200 kms^{-1} respectively, which doesn't account for the discrepancy with the 2dF result. Having no way to determine which spectrum was the better, the 2dF values were used. The remaining two labelled outliers, 1 and 4, were assigned the highest quality flags for their 2dF values and were thus assumed to be correct. This gave a combined dataset of 231 measured redshifts in the range 0.044 to 0.068, which were then used in the subsequent analysis.

6.5.1 Redshift Distribution

Using the combined dataset the redshift distribution was plotted binned at intervals of 0.0020. This is shown in figure 6.10, overlaid with a Gaussian fit to the central peak. It can be seen that the redshift distribution is well modelled by a Gaussian, but there is some evidence for a subgroup of galaxies at a slightly higher redshift.

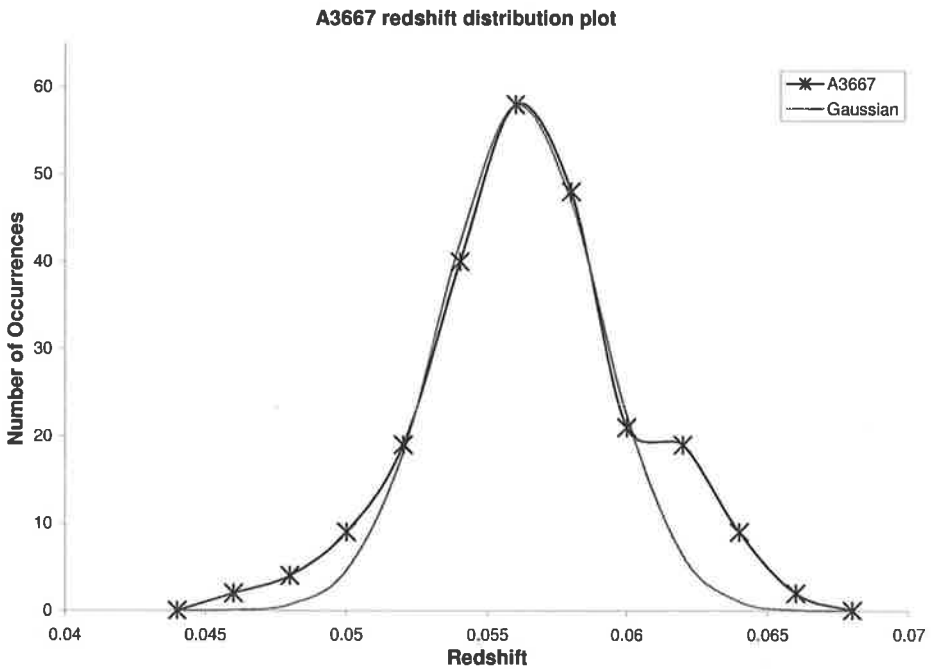

Figure 6.10: Redshift distribution for A3667 with a fitted Gaussian.

Figure 6.10 shows that the potential subgroup does not have a large number of members. In addition, the redshifts which correspond to this "group" are spread out across the entire cluster and not localised to the previously seen sub-group. Nevertheless a three dimensional plot of RA, Dec and z was constructed using Matlab to explore their spatial distribution. It should be noted that such a plot does not give a physical 3D model of the cluster as only the radial velocity can be measured. However, as Matlab allows rotation of the plot it is a useful way to search for associations. Standard redshift versus Δ RA and Δ Dec plots were also made and tested for associations, on the premise that if subgroups are present in the dataset then there will be tight associations between the member galaxies in both plots. Figure 6.11 shows the resultant plots. The cluster appears extremely well mixed and no likely subgroups were found.

Additionally, the Matlab cube was used to search for a velocity gradient across the cluster. If the bimodal distribution report by Proust et al. (1988) is real and the two subgroups are at all inclined from the plane of the sky, a gradient across the cluster should be observed. If a significant difference in velocity between the reported subgroup and A3667 were present this should be visible in the Matlab cube . A gradient was not observed.

Statistical analysis of the dataset gives a mean redshift of 0.0555, (though the Gaussian peaks at approximately 0.0560) and a velocity dispersion, σ_v of 1102 kms^{-1}, which is slightly higher than the previously published values.

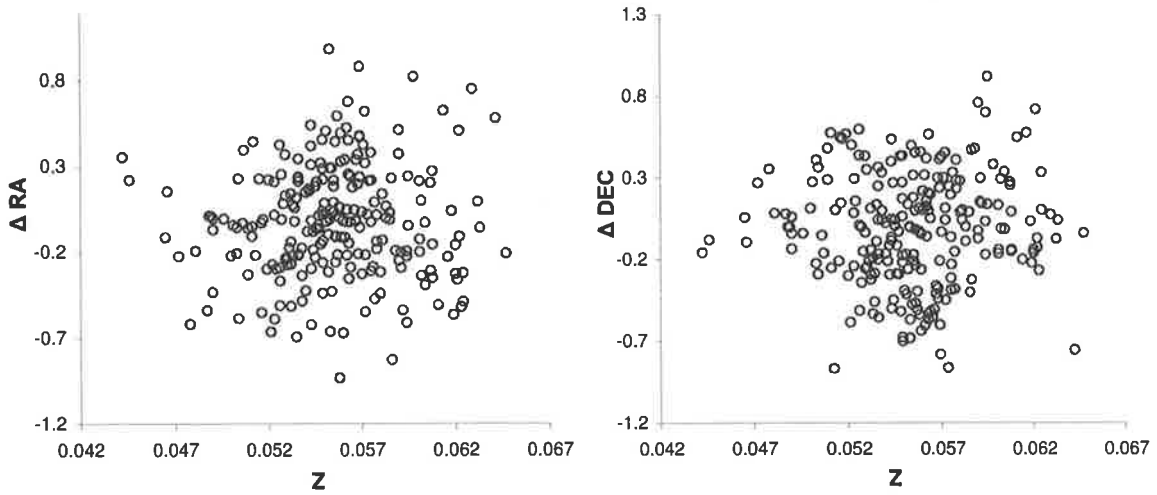

Figure 6.11: Redshift versus RA and Dec, in degrees, relative to the cluster centre.

6.5.2 Bimodality Testing

To further investigate the possibility of bimodality in the redshift data a series of statistical tests were performed.

Kaye's Mixture Model

The first test, a "Kaye's" mixture model algorithm, KMM (Ashman et al. 1994), fits a user-specified number of Gaussian profiles to the data and provides a statistical comparison with a single Gaussian fit to the dataset. The user provides an estimate of the mean value of each peak and a ratio of the members in each peak. The software, provided by Ashman, then assigns each redshift membership to one of the initially supplied Gaussian profiles along with the posterior probabilities of group membership for all profiles. Other outputs include the total number of members in each potential group, the estimate of correct allocation for each group (which is just the mean posterior probabilities for all members assigned to a particular group), an estimate of correct allocation for all redshifts and the average redshift of each fitted peak. Finally, it performs a likelihood ratio test and provides both this and the P-value statistic, which is an estimate of the improvement of the n-group fit over a single Gaussian.

The algorithm was applied for the two-profile case and Table 6.1 summarises the input and output parameters. Of the 231 redshifts measured for A3667, the code assigned all values to be members of the main group centred about z=0.0561. All values were assigned with greater than 88% confidence, with the overall confidence being 94.9%.

Table 6.1: 'Kaye's' mixture model bimodal fitting results for the A3667 redshift sample.

Input Parameters

Mean group z	Proportion	No. of galaxies
0.056	0.9	208
0.062	0.1	23

Output Parameters

Mean group z	Proportion	No. of galaxies
0.0561	1.0	231
-	0	0
Allocation rate	100% to group 1	
Confidence of allocation	94.9%	

Filtering

Figure 6.1 shows the previously published isodensity plot of all galaxies in the vicinity of A3667 (Proust et al. 1988). This figure does not take into account the redshifts of the objects. In order to assess the bimodality of the known redshift sample, Gaussian smoothing was applied to the set of 231 galaxies with redshifts between 0.044 and 0.068. Figure 6.12 shows the galaxy location data smoothed with Gaussian filters ranging in size from 0.20 to 0.35 degrees as pseudocolour plot, while Figure 6.13 shows the same data as a contour plot. The 0.20 degree Gaussian filter image shows a remarkable resemblance to the published isodensity plot in almost all aspects except that the redshift restricted data do not appear to exhibit the significant subgroup structure seen in the Proust et al. (1988) plot. There is a definite elongation of the cluster. The contour plots show there is some evidence of a very small increase in the galaxy density in the region where Proust et al. (1988) show a significant subgroup. However, there is also a feature of equal significance on the southern side of A3667. It is likely that these features result from the elongation rather than distinct subgroups. Neither feature appears if the filter size is increased even marginally.

6.5.3 Galaxy Type Information

As mentioned above, one of the products of the 2dfdr cross-correlation absorption redshift determination is the template which gives the strongest correlation with each measured spectra. This provides information on each galaxy's morphological type. Examination of the physical distribution of various galaxies within the cluster may provide valuable information on the cluster's dynamical history.

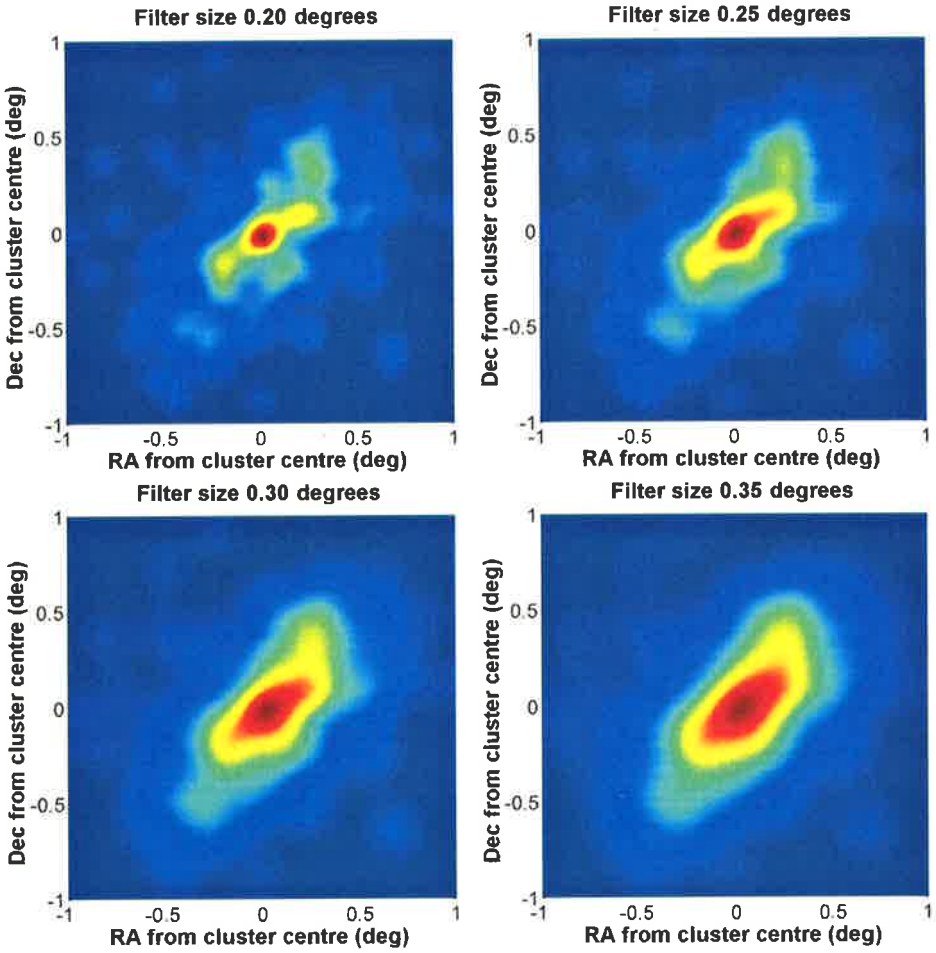

Figure 6.12: Galaxy isodensity plots for A3667, generated by application of Gaussian filters of various sizes to the 231 known cluster members. Shown here as pseudocolour.

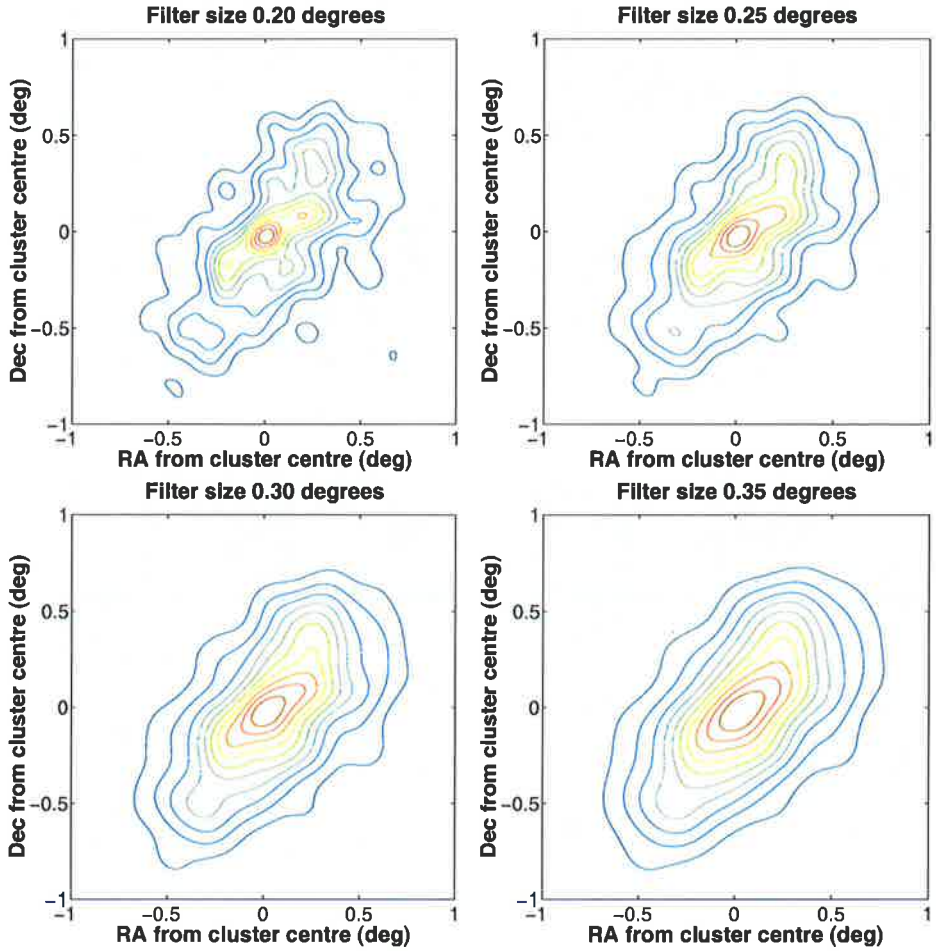

Figure 6.13: Galaxy isodensity plots for A3667, generated by application of Gaussian filters of various sizes to the 231 known cluster members. Shown as contours.

Figure 6.14 shows the distribution of galaxy types in A3667 as defined by the 2dfdr template. The morphological types are elliptical (E), central dominant (cD), spiral (Sc), spiral (Sbc) and Irregular/small (IM/SM). Figure 6.15 shows the same data but with both sets of spirals (Sc and Sbc) and elliptical (E and cD) coloured the same. Not surprisingly the predominant galaxy type in the cluster is elliptical. The spiral population occurs mainly in the northern part of the cluster as suggested by the R band imaging shown in Figures 6.2 and 6.3.

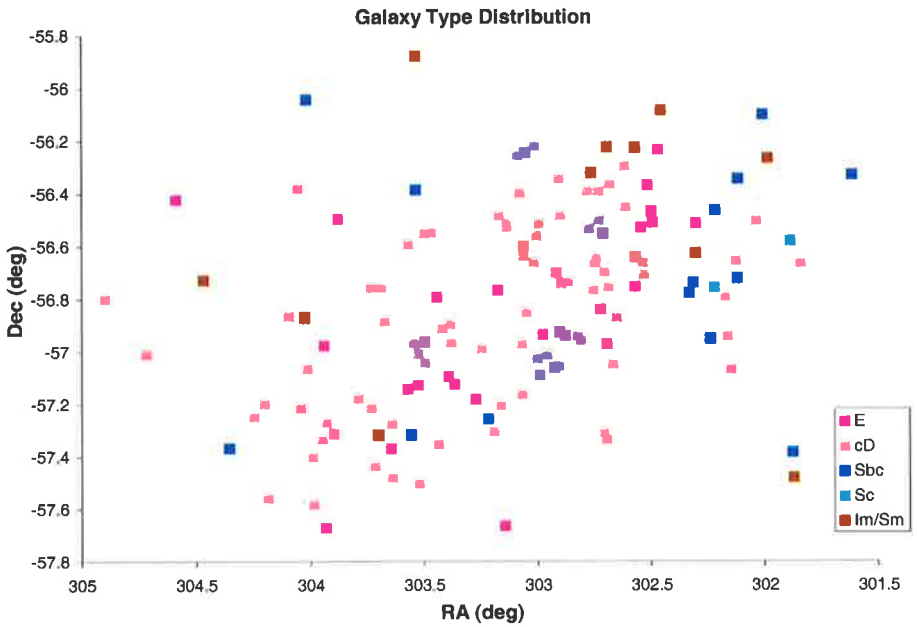

Figure 6.14: Galaxy type distribution for the 143 galaxies in the 2dF dataset. Here the typing is given from the strongest cross-correlation with the 2dfdr template spectra and follows the 2dfdr naming convention.

No E+A galaxies (Section 6.1) were found in the spectra. Perhaps this is not surprising as only 37 have been found so far in a subset of over 15,000 galaxies with strong Hβ, Hγ and Hδ lines from the 2dFGRS, which is an incidence rate of only 0.25 percent (Deeley 2000 in Colless 2000).

6.6 Discussion

A3667 has a mean redshift of 0.0555, a high velocity dispersion (1102 kms^{-1}) and an elongated optical axis. The cluster is typical in that it is dominated by elliptical galaxies, with the second largest population being spirals. There is marginal evidence for a grouping of spirals in the northern part of the cluster. The velocity distribution is well modelled by a single Gaussian, with a weak excess around a redshift of 0.062. There seems to be little or no support for distinct in-falling groups either from the

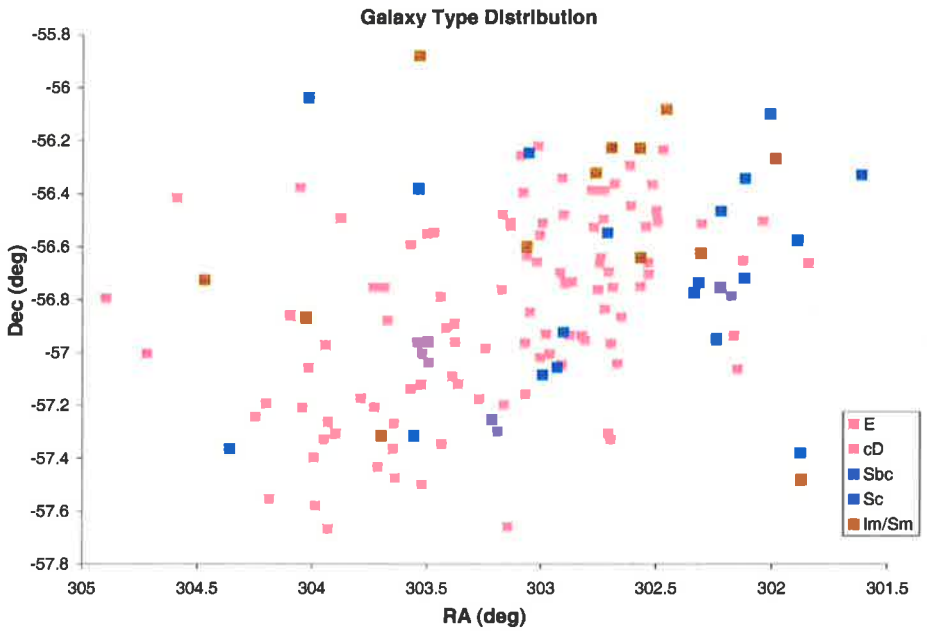

Figure 6.15: Galaxy type distribution for the 143 galaxies in the 2dF dataset, colour coded into ellipticals, spirals and irregulars. Here the typing is given from the strongest cross-correlation with the 2dfdr template spectra and follows the 2dfdr naming convention.

velocity information or the spatial distribution of galaxies with measured redshifts. Moreover there is no evidence for a velocity gradient across the cluster suggested by the previously reported bimodal optical distribution. However, A3667 is a rich cluster and to date only 231 redshift have been obtained for cluster members. This is not a complete sample and further data will be required to categorically rule out the presence of subgroups.

Several authors have claimed that A3667 is observed in a post-merger state. This may be consistent with the high velocity dispersion and mixing in the cluster. If a merger of sufficient magnitude to generate the observed diffuse radio emission is present, it is expected that the merger velocities would be a few thousand km s^{-1}. If such a merger is present, the current data suggest that the merger axis must be entirely in the plane of the sky. This would partly account for the lack of observable subgroup peaks in the velocity data.

However, without any significant evidence in the galaxy population one way or the other it is impossible to distinguish between a pre or post merger system using only the optical data.

6.7 Summary

This chapter gives a discussion of the known optical properties of A3667 and presents the results of a spectral survey of cluster members down to a magnitude of 18.3. Statistical analyses of the data are presented. These data showed that the velocity distribution of the cluster is well modelled by a Gaussian and that the significance of the previously reported subgroup to the North of A3667 has diminished after redshift information was considered. Further, the lack of evidence for subgrouping and a velocity gradient across the cluster has suggested that if a merger is present in A3667 it is entirely within the plane of the sky.

Chapter 7

Conclusions and Future Prospects

7.1 Conclusions

Significant magnetic fields in galaxy clusters have been inferred from both statistical Faraday rotation measure results in a sample of rich, Southern, non-cooling flow clusters and by detection and investigation of diffuse radio emission regions in the cluster A3667.

The statistical rotation measure results discussed in Chapter 3 are consistent with those obtained in the contemporaneous Northern hemisphere study performed by Clarke (2000), suggesting there is a statistical broadening of cluster RMs within 800 kpc of the centre as compared to a control population. Furthermore, the data are consistent with magnetic field strengths of 1–2 μG assuming a tangled cell model with cell sizes of the order of 100 kpc.

Chapter 5 discussed investigations of the radio emission in A3667. The multifrequency data presented there demonstrated the presence of two Mpc scale diffuse radio emission regions (DRERs) at the cluster periphery and a possible weak halo in the cluster core. High resolution imaging of the brighter of the two peripheral DRERs shows clear filamentary structure similar to than seen in radio plasma on much smaller scales. Polarimetry of the region supports the conclusion that these filaments are the result of highly ordered magnetic fields on scales never before seen(100 – 400 kpc). For the first time highly resolved spectral analysis has been undertaken on such an object. Data from 0.8, 1.4 and 2.4 GHz suggests that the filaments exhibit a power law spectrum with $\alpha = 1.1 \pm 0.1$ implying a constant source of energy injection. Emission from the rest of the source follows the curved spectral signature of particle diffusion. RMs have been calculated for the first time for lines of sight passing through diffuse radio emission. These results are strongly suggestive of an enhancement of the magnetic field in the region of the radio emission with the magnetic field strength estimated to be 3.0 – 5.1 μG.

Chapter 6 discussed spectroscopic observations of the galaxies in the field of A3667. These data have increased the number of confirmed cluster members from 154 to 231 and excluded several of the objects in the field from cluster membership. Detailed analysis of the redshift data show that the cluster is highly elongated but substantially

reduces the significance of the previously reported NW subgroup. In fact there is little subgroup structure evident in the velocity data and the distribution is well matched to a Gaussian. These results do not preclude the cluster from being observed in a post-merger state as claimed by several authors, however they do put severe constraints on the merger axis, suggesting that if such a merger has occurred it must have been in the plane of the sky.

Several authors assert that the diffuse radio emission, lack of a cooling flow, high velocity dispersion, optical elongation and previously reported optical subgroups can all be explained by a massive cluster merger resulting in a pair of shock waves propagating throughout the ICM. However, new results presented here including the filamentary nature of the radio emission and the suggested continuous particle injection, coupled with a reduction in confidence of the existence of the optical subgroups throws this interpretation into some doubt. It is not clear from the models of shock generation during cluster mergers how the propagating shocks would produce filamentary radio structure with highly ordered magnetic fields surrounded by diffuse emission with the signature of particle diffusion. Nor is it clear how such a shock could account for the power law spectral index of the filaments, which is indicative of continuous particle injection. Furthermore, in the shock model, the radio emission is expected to have a sharp outer boundary and low spectral index value indicating the presence of newly accelerated electrons as the shock moved through the ICM. Although this is the case for the South eastern DRER, its North western counterpart does not follow this hypothesis. The more complicated structure of the Northern source could be the result of projection effects, however since the optical data constrain the merger axis to the plane of the sky it is expected that projection effects will be minimal. Also, preliminary investigations of the DRER 0917+75 confirm that filamentary structure is not unique to the diffuse emission in A3667. 0917+75 is not associated with a particular cluster, but rather with the Rood 27 cluster group and is located over 5 Mpc from the centre of nearest cluster member. Spectral aging arguments constrain the cluster crossing time to around 1 Giga year. This combined with speed limits imposed on shockwave propagation in plasmas means that it is not possible for a shock to traverse the distance from the centre of the nearest member cluster to the location of 0917+75. This also throws the merger generation scenario into some doubt for this source.

Chapter 4 discussed an estimated all-sky rotation measure map generated from around 900 extragalactic RMs. This was generated in order to facilitate the removal of the Galactic contribution to the measured cluster RMs from Chapter 3. As a by-product of this work some information about the magnetic field structure within the galaxy can be gleaned, although many more data points will be required before a detailed study can be undertaken. Statistical analysis of the high Galactic latitude RM population shows the data has an exponential distribution rather than the previously assumed Gaussian distribution. As this population is expected to reflect only the intrinsic source RMs, this result may provide important information about radio source behaviour.

7.2 Future Work

The statistical investigations of cluster magnetic fields via Faraday rotation measures relies on a relatively small sample of only 39 RMs obtained for sources in the cores of around 30 non-cooling flow clusters. Clearly, this work could be improved with a larger RM source population. Currently the process of measuring the position angle of individual sources at several frequencies in order to obtain an unambiguous RM fit is very labour intensive. However, with the advent of new radio telescopes such as the SKA which will have vastly improved signal-to-noise, due to improved collecting area, it may be possible to obtain a completely unambiguous RM with a single observation. This could be achieved if telescope configurations, combining large bandwidths and flexible correlator designs, which allow the band to be observed in several channels, are employed in future instruments. Currently such observations are possible on the ATCA, but only for bright sources which have enough polarised flux in each of the individual bandwidth channels (Gaensler et al. 1998). As was seen in this study, finding suitably powerful radio sources projected through the cores of galaxy clusters is difficult for even low redshift clusters where the projected sky coverage is large. Once a suitable source sample is obtained, the attrition rate when finding sufficiently polarised sources over a large frequency range is considerable. With future instruments, both the number of detected background sources and the sensitivity to polarised emission will increase. Not only would this make statistical studies more feasible, but in certain cases might provide sufficient background sources to study individual cluster magnetic fields in great detail. This would significantly enhance our understanding of reversal scales in cluster magnetic fields. Moreover, with the advent of new instruments, the number of published RMs for extragalactic radio sources will increase, allowing more detailed modelling of both the RM sky and the Galactic magnetic field.

In the short term, deeper observations of Mpc diffuse radio emission regions may reveal that such structures all have filaments and regions of highly ordered magnetic fields. This will impact on current assumptions about the origin and generation of such sources. A wealth of information has been gathered here on the diffuse radio emission in A3667 and there are several avenues afforded for further exploration of these data. In the immediate future, advances in computation should allow jointly deconvolved, full resolution imaging of the ATCA data. Such images will be more sensitive to large scale structure and may help to confirm the presence of the central radio halo. The addition of single dish data from the Parkes radio telescope may also assist in this endeavour. Observations at an additional frequency in order to obtain another point on the spectral index plots, is also critical to understanding the emission mechanisms at work within the diffuse emission. Detection of the brightest parts of the filaments in the North western source at 6cm will be a valuable starting point in a proposal to map the entire NW DRER at this wavelength. Should such data be obtained, FRM mapping of the relic between 20, 13 and 6cm would provide an excellent comparison to the RMs derived from background sources projected through the region. This would give invaluable information on the location of the diffuse emission with respect to the cluster gas and may in turn help elucidate the issue of projection effects. Similar

observations for the source 0917+75 are already planned.

In the long term, new instruments such as LOFAR and the SKA will improve both the detection rate and the understanding of diffuse radio emission at potentially higher redshifts. Currently, diffuse emission is difficult to detect due to its low surface brightness at centimetre wavelengths. Instruments that probe the universe at low radio frequencies, such as LOFAR, should, in principal sample the population of DRERs that are now dormant at centimetre wavelengths. This may reveal the universe to be teeming with diffuse emission on all scales and at many redshifts. Should a sufficiently large sample of diffuse sources be obtained, it may be possible to undertake evolutionary studies of diffuse emission and its connection to the host cluster.

Advances in these fields will increase rapidly in the coming years and new results will generate new questions for forthcoming students to answer. The words of Velikovsky are as true now as when written in 1952:

Science today, as in the days of Newton, lies before us as a great uncharted ocean, and we have not yet sailed very far from the coast of ignorance. The age of basic discoveries is not yet at its end, and you are not latecomers, for whom no fundamentals are left to discover.

Appendix A

Cluster RM data and Additional Observations

A.1 Cluster Pilot Survey Data

Table A.1: Cluster pilot survey data generated by applying the *MIRIAD* command *UVFLUX* to the pilot survey observations: col 1 gives the name of the cluster; col 2 is the source designation, which is comprised of the cluster name, the object number for that cluster and the observing frequency; col 3 lists the Stokes parameters; col 4 is the theoretcial rms noise for each source in mJy; col 5 is the detected amplitude in mJy; col 6 is the phase in degrees; col 7 is the actual rms noise in mJy and col 8 is the number of correlations.

Cluster Pilot Survey Data							
Cluster	Source	Stokes	RMS_t	A_{mJy}	ϕ_{deg}	RMS_{mJy}	Corr
A3128	a3128_10.4736	I	1.70E-02	50.68	7	2.54E-02	13065
		Q	1.70E-02	1.4	-167	2.06E-02	13065
		U	1.70E-02	1.16	32	2.08E-02	13065
		V	1.70E-02	1.21	-98	2.12E-02	13065
	a3128_10.6528	I	2.88E-02	46.92	8	3.95E-02	11280
		Q	2.88E-02	0.14	-101	3.20E-02	11280
		U	2.88E-02	0.34	84	3.21E-02	11280
		V	2.88E-02	0.36	89	3.20E-02	11280
	a3128_1e.4736	I	1.73E-02	4.1	33	2.45E-02	13975
		Q	1.73E-02	1.68	-159	2.11E-02	13975
		U	1.73E-02	0.34	17	2.12E-02	13975
		V	1.73E-02	1.22	-115	2.15E-02	13975
	a3128_1e.6528	I	2.90E-02	1.59	60	3.27E-02	11880
		Q	2.90E-02	0.42	-78	3.22E-02	11880
		U	2.90E-02	0.69	-105	3.24E-02	11880

continued on next page

continued from previous page

Cluster	Source	Stokes	RMS_t	A_{mJy}	ϕ_{deg}	RMS_{mJy}	Corr
		V	2.90E-02	0.67	-84	3.21E-02	11880
	a3128_3.4736	I	1.74E-02	4.37	30	2.17E-02	13195
		Q	1.74E-02	1.75	-153	2.11E-02	13195
		U	1.74E-02	0.81	26	2.11E-02	13195
		V	1.74E-02	1.24	-90	2.14E-02	13195
	a3128_3.6528	I	2.90E-02	1.01	12	3.23E-02	11100
		Q	2.90E-02	0.7	-13	3.25E-02	11100
		U	2.90E-02	0.54	100	3.25E-02	11100
		V	2.90E-02	0.76	-6	3.26E-02	11100
	a3128_5.4736	I	1.73E-02	46.46	24	4.65E-02	14040
		Q	1.73E-02	2.59	-154	2.11E-02	14040
		U	1.73E-02	1.31	-152	2.11E-02	14040
		V	1.73E-02	1.27	-99	2.11E-02	14040
	a3128_5.6528	I	2.89E-02	28.28	32	4.44E-02	11880
		Q	2.89E-02	1.45	-112	3.25E-02	11880
		U	2.89E-02	2.77	-152	3.21E-02	11880
		V	2.89E-02	0.8	-60	3.20E-02	11880
	a3128_7.4736	I	1.73E-02	3.26	30	2.14E-02	14040
		Q	1.73E-02	1.5	-170	2.11E-02	14040
		U	1.73E-02	0.5	51	2.13E-02	14040
		V	1.73E-02	1.21	-116	2.13E-02	14040
	a3128_7.6528	I	2.89E-02	1.72	14	3.21E-02	11880
		Q	2.89E-02	0.29	69	3.21E-02	11880
		U	2.89E-02	0.39	93	3.22E-02	11880
		V	2.89E-02	0.13	3	3.21E-02	11880
A3266	a3266_1.4736	I	1.74E-02	5.95	-23	2.34E-02	7735
		Q	1.74E-02	0.67	166	2.17E-02	7735
		U	1.74E-02	0.85	27	2.16E-02	7735
		V	1.74E-02	0.77	-105	2.18E-02	7735
	a3266_1.6528	I	2.94E-02	2.76	-34	3.41E-02	8580
		Q	2.94E-02	0.45	75	3.37E-02	8580
		U	2.94E-02	0.92	110	3.37E-02	8580
		V	2.94E-02	0.95	-110	3.40E-02	8580
	a3266_10.4736	I	1.70E-02	23.52	31	2.61E-02	7020
		Q	1.70E-02	0.6	-174	2.12E-02	7020
		U	1.70E-02	0.26	23	2.11E-02	7020
		V	1.70E-02	1.33	-130	2.12E-02	7020
	a3266_10.6528	I	2.91E-02	12.84	22	3.59E-02	8100
		Q	2.91E-02	0.49	161	3.27E-02	8100
		U	2.91E-02	0.98	32	3.27E-02	8100

continued on next page

continued from previous page

Cluster	Source	Stokes	RMS_t	A_{mJy}	ϕ_{deg}	RMS_{mJy}	Corr
		V	2.91E-02	0.04	117	3.30E-02	8100
	a3266_11.4736	I	1.70E-02	10.72	-19	2.85E-02	7020
		Q	1.70E-02	0.44	-168	2.06E-02	7020
		U	1.70E-02	0.38	-79	2.04E-02	7020
		V	1.70E-02	1.02	-83	2.06E-02	7020
	a3366_11.6528	I	2.90E-02	7.51	-27	3.57E-02	8100
		Q	2.90E-02	0.21	-168	3.23E-02	8100
		U	2.90E-02	0.59	-144	3.27E-02	8100
		V	2.90E-02	0.48	-148	3.24E-02	8100
	a3266_2.4736	I	1.72E-02	2.39	8	2.28E-02	8775
		Q	1.72E-02	0.5	-173	2.15E-02	8775
		U	1.72E-02	0.8	13	2.16E-02	8775
		V	1.72E-02	1.02	-101	2.16E-02	8775
	a3266_2.6528	I	2.93E-02	0.78	-24	3.32E-02	9720
		Q	2.93E-02	0.23	-23	3.33E-02	9720
		U	2.93E-02	0.79	34	3.34E-02	9720
		V	2.93E-02	0.2	-161	3.35E-02	9720
	a3266_3.4736	I	1.75E-02	9.46	-15	6.18E-02	7020
		Q	1.75E-02	1.39	-171	2.17E-02	7020
		U	1.75E-02	0.57	-127	2.19E-02	7020
		V	1.75E-02	1.16	-89	2.19E-02	7020
	a3266_3.6528	I	2.93E-02	3.78	-1	4.80E-02	8100
		Q	2.93E-02	0.37	143	3.40E-02	8100
		U	2.93E-02	0.05	122	3.39E-02	8100
		V	2.93E-02	0.02	-99	3.40E-02	8100
	a3266_4e.4736	I	1.74E-02	121.6	21	9.85E-02	7020
		Q	1.74E-02	2.59	-172	2.16E-02	7020
		U	1.74E-02	1.25	-141	2.19E-02	7020
		V	1.74E-02	1.33	-123	2.16E-02	7020
	a3266_4e.6528	I	2.90E-02	77.02	-8	1.26E-01	9540
		Q	2.90E-02	0.88	-167	3.30E-02	9540
		U	2.90E-02	0.79	-61	3.32E-02	9540
		V	2.90E-02	0.39	74	3.30E-02	9540
	a3266_5e.4736	I	1.74E-02	4.73	-47	7.52E-02	6175
		Q	1.74E-02	1.02	171	2.16E-02	6175
		U	1.74E-02	0.7	-129	2.17E-02	6175
		V	1.74E-02	1.57	-118	2.21E-02	6175
	a3266_5e.6528	I	2.89E-02	1.08	138	5.99E-02	8940
		Q	2.89E-02	0.73	159	3.31E-02	8940
		U	2.89E-02	0.56	-23	3.28E-02	8940

continued on next page

continued from previous page

Cluster	Source	Stokes	RMS_t	A_{mJy}	ϕ_{deg}	RMS_{mJy}	Corr
		V	2.89E-02	0.91	93	3.31E-02	8940
	a3266_8.4736	I	1.72E-02	68.96	-12	4.68E-02	6110
		Q	1.72E-02	0.39	-101	2.12E-02	6110
		U	1.72E-02	0.33	-12	2.14E-02	6110
		V	1.72E-02	1.48	-101	2.12E-02	6110
	a3266_8.6528	I	2.91E-02	40.81	1	4.66E-02	7260
		Q	2.91E-02	0.63	-19	3.30E-02	7260
		U	2.91E-02	1.13	169	3.30E-02	7260
		V	2.91E-02	0.44	-160	3.32E-02	7260
	a3266_9.4736	I	1.71E-02	22.4	62	2.87E-02	6955
		Q	1.71E-02	0.7	-160	2.09E-02	6955
		U	1.71E-02	0.17	89	2.07E-02	6955
		V	1.71E-02	1.03	-117	2.07E-02	6955
	a3266_9.6528	I	2.91E-02	14.4	66	3.74E-02	8100
		Q	2.91E-02	0.3	130	3.31E-02	8100
		U	2.91E-02	0.71	-129	3.28E-02	8100
		V	2.91E-02	0.46	-111	3.30E-02	8100
A3558	a3558_10.4736	I	1.87E-02	8.81	18	2.50E-02	8775
		Q	1.87E-02	2.68	-169	2.25E-02	8775
		U	1.87E-02	0.75	-147	2.21E-02	8775
		V	1.87E-02	1.46	-115	2.27E-02	8775
	a3558_10.6528	I	3.04E-02	4.93	26	3.49E-02	8100
		Q	3.04E-02	0.32	-169	3.38E-02	8100
		U	3.04E-02	0.83	148	3.36E-02	8100
		V	3.04E-02	0.35	2	3.41E-02	8100
	a3558_11.4736	I	1.88E-02	3.52	29	2.25E-02	8775
		Q	1.88E-02	2.66	-174	2.28E-02	8775
		U	1.88E-02	0.97	-142	2.23E-02	8775
		V	1.88E-02	1.04	-123	2.31E-02	8775
	a3558_11.6528	I	3.06E-02	0.38	22	3.39E-02	8100
		Q	3.06E-02	0.84	-77	3.42E-02	8100
		U	3.06E-02	0.38	-26	3.41E-02	8100
		V	3.06E-02	0.37	-30	3.39E-02	8100
	a3558_13.4736	I	1.89E-02	10.36	-5	2.51E-02	8710
		Q	1.89E-02	3.01	-165	2.28E-02	8710
		U	1.89E-02	0.73	-124	2.22E-02	8710
		V	1.89E-02	0.38	-109	2.31E-02	8710
	a3558_13.6528	I	3.08E-02	6.44	-12	3.51E-02	8100
		Q	3.08E-02	0.38	-126	3.43E-02	8100
		U	3.08E-02	0.26	46	3.43E-02	8100

continued on next page

continued from previous page

Cluster	Source	Stokes	RMS_t	A_{mJy}	ϕ_{deg}	RMS_{mJy}	Corr
		V	3.08E-02	0.15	165	3.45E-02	8100
	a3558_1e.4736	I	1.86E-02	5.44	4	2.20E-02	8775
		Q	1.86E-02	2.29	173	2.13E-02	8775
		U	1.86E-02	0.15	-172	2.08E-02	8775
		V	1.86E-02	1.26	-124	2.10E-02	8775
	a3558_1e.6528	I	3.04E-02	1.44	-3	3.52E-02	8100
		Q	3.04E-02	0.33	-98	3.44E-02	8100
		U	3.04E-02	0.47	21	3.46E-02	8100
		V	3.04E-02	1.11	-106	3.44E-02	8100
	a3558_2.4736	I	1.85E-02	4.13	-11	3.04E-02	8775
		Q	1.85E-02	3.11	-169	2.28E-02	8775
		U	1.85E-02	0.75	161	2.24E-02	8775
		V	1.85E-02	1.3	-115	2.27E-02	8775
	a3558_2.6528	I	3.03E-02	1.26	-68	3.50E-02	8100
		Q	3.03E-02	1.27	59	3.42E-02	8100
		U	3.03E-02	0.31	45	3.42E-02	8100
		V	3.03E-02	0.39	-99	3.41E-02	8100
	a3558_5.4736	I	1.85E-02	4.45	66	2.46E-02	8775
		Q	1.85E-02	2.66	-175	2.25E-02	8775
		U	1.85E-02	0.75	-169	2.19E-02	8775
		V	1.85E-02	1.27	-113	2.29E-02	8775
	a3558_5.6528	I	3.02E-02	2.64	57	3.47E-02	8100
		Q	3.02E-02	0.55	-108	3.40E-02	8100
		U	3.02E-02	0.34	-73	3.39E-02	8100
		V	3.02E-02	0.43	177	3.40E-02	8100
	a3558_7.4736	I	1.85E-02	36.92	-11	2.86E-02	8775
		Q	1.85E-02	2.15	-164	2.26E-02	8775
		U	1.85E-02	0.96	-169	2.20E-02	8775
		V	1.85E-02	1.22	-112	2.27E-02	8775
	a3558_7.6528	I	3.02E-02	25.78	-15	3.71E-02	8100
		Q	3.02E-02	0.49	-161	3.38E-02	8100
		U	3.02E-02	0.15	162	3.39E-02	8100
		V	3.02E-02	0.57	-147	3.42E-02	8100
	a3558_8.4736	I	1.86E-02	34.45	31	4.05E-02	8775
		Q	1.86E-02	5.66	-166	2.28E-02	8775
		U	1.86E-02	1.28	-135	2.23E-02	8775
		V	1.86E-02	1.28	-109	2.29E-02	8775
	a3558_8.6528	I	3.03E-02	16.05	43	4.45E-02	8100
		Q	3.03E-02	1.71	-132	3.39E-02	8100
		U	3.03E-02	0.27	-179	3.42E-02	8100

continued on next page

continued from previous page

Cluster	Source	Stokes	RMS_t	A_{mJy}	ϕ_{deg}	RMS_{mJy}	Corr
		V	3.03E-02	0.09	43	3.39E-02	8100
A35562	a3562_1.4736	I	1.89E-02	4.45	28	2.37E-02	8775
		Q	1.89E-02	2.4	-173	2.33E-02	8775
		U	1.89E-02	1.08	-121	2.25E-02	8775
		V	1.89E-02	1.04	-98	2.32E-02	8775
	a3562_1.6528	I	3.07E-02	1.85	62	3.54E-02	8100
		Q	3.07E-02	1.42	44	3.47E-02	8100
		U	3.07E-02	0.53	-77	3.46E-02	8100
		V	3.07E-02	0.73	-11	3.44E-02	8100
	a3562_3.4736	I	1.89E-02	5.47	19	2.27E-02	8580
		Q	1.89E-02	3.14	-169	2.34E-02	8580
		U	1.89E-02	0.59	-113	2.23E-02	8580
		V	1.89E-02	0.67	-90	2.30E-02	8580
	a3562_3.6528	I	3.07E-02	2.2	19	3.50E-02	7920
		Q	3.07E-02	0.67	1	3.49E-02	7920
		U	3.07E-02	0.48	-36	3.44E-02	7920
		V	3.07E-02	0.48	-18	3.50E-02	7920
	a3562_4.4736	I	1.72E-02	1.73	25	2.09E-02	7020
		Q	1.72E-02	2.91	-165	2.14E-02	7020
		U	1.72E-02	0.56	96	2.08E-02	7020
		V	1.72E-02	1.12	-89	2.12E-02	7020
	a3562_4.6528	I	2.88E-02	0.13	-170	3.25E-02	6480
		Q	2.88E-02	0.41	116	3.28E-02	6480
		U	2.88E-02	0.54	-150	3.30E-02	6480
		V	2.88E-02	0.76	98	3.32E-02	6480
	a3562_5.4736	I	1.71E-02	4.62	-14	2.07E-02	7020
		Q	1.71E-02	2.61	-171	2.13E-02	7020
		U	1.71E-02	1.15	168	2.02E-02	7020
		V	1.71E-02	1.11	-101	2.12E-02	7020
	a3562_5.6528	I	2.88E-02	2.61	-41	3.25E-02	6480
		Q	2.88E-02	0.7	-139	3.29E-02	6480
		U	2.88E-02	0.97	146	3.25E-02	6480
		V	2.88E-02	0.67	-43	3.26E-02	6480
	a3562_6e.4736	I	1.74E-02	2.99	-27	2.23E-02	5265
		Q	1.74E-02	2.35	-169	2.15E-02	5265
		U	1.74E-02	0.65	119	2.11E-02	5265
		V	1.74E-02	1.17	-102	2.16E-02	5265
	a3562_6e.6528	I	2.92E-02	1.42	-56	3.35E-02	4860
		Q	2.92E-02	0.69	-107	3.33E-02	4860
		U	2.92E-02	1.06	-137	3.29E-02	4860

continued on next page

continued from previous page

Cluster	Source	Stokes	RMS_t	A_{mJy}	ϕ_{deg}	RMS_{mJy}	Corr
		V	2.92E-02	0.36	-160	3.34E-02	4860
	a3562_9.4736	I	1.74E-02	6.46	9	2.16E-02	5265
		Q	1.74E-02	2.43	-167	2.16E-02	5265
		U	1.74E-02	0.86	125	2.10E-02	5265
		V	1.74E-02	0.96	-123	2.14E-02	5265
	a3562_9.6528	I	2.92E-02	2.68	-7	3.24E-02	4860
		Q	2.92E-02	0.36	-20	3.26E-02	4860
		U	2.92E-02	0.79	159	3.26E-02	4860
		V	2.92E-02	1.29	41	3.28E-02	4860
A3667	a3667_1.4736	I	1.87E-02	3.43	76	6.18E-02	8190
		Q	1.87E-02	1.35	168	2.26E-02	8190
		U	1.87E-02	0.29	-173	2.26E-02	8190
		V	1.87E-02	1.41	-118	2.26E-02	8190
	a3667_1.6528	I	3.10E-02	6.64	133	6.10E-02	7560
		Q	3.10E-02	0.41	-125	3.49E-02	7560
		U	3.10E-02	0.29	107	3.45E-02	7560
		V	3.10E-02	0.54	160	3.50E-02	7560
	a3667_11.4736/	I	1.84E-02	1.35	0	2.31E-02	8190
		Q	1.84E-02	1.31	179	2.33E-02	8190
		U	1.84E-02	0.54	37	2.31E-02	8190
		V	1.84E-02	1.61	-129	2.34E-02	8190
	a3667_11.6528	I	3.05E-02	0.79	82	3.69E-02	7560
		Q	3.05E-02	0.39	-113	3.70E-02	7560
		U	3.05E-02	0.28	83	3.69E-02	7560
		V	3.05E-02	0.51	99	3.67E-02	7560
	a3667_16.4736	I	1.89E-02	1.04	19	2.79E-02	8775
		Q	1.89E-02	1.35	-171	2.38E-02	8775
		U	1.89E-02	0.41	-112	2.38E-02	8775
		V	1.89E-02	1.41	-138	2.41E-02	8775
	a3667_16.6528	I	3.12E-02	1.58	135	3.89E-02	8100
		Q	3.12E-02	0.75	156	3.79E-02	8100
		U	3.12E-02	0.35	53	3.81E-02	8100
		V	3.12E-02	0.56	-76	3.82E-02	8100
	a3667_17.4736	I	1.85E-02	4.06	56	2.40E-02	8710
		Q	1.85E-02	1.6	-172	2.26E-02	8710
		U	1.85E-02	0.25	-99	2.29E-02	8710
		V	1.85E-02	1.7	-122	2.31E-02	8710
	a3667_17.6528	I	3.08E-02	2.01	98	3.48E-02	8040
		Q	3.08E-02	0.61	-126	3.50E-02	8040
		U	3.08E-02	0.4	97	3.49E-02	8040

continued on next page

continued from previous page

Cluster	Source	Stokes	RMS_t	A_{mJy}	ϕ_{deg}	RMS_{mJy}	Corr
		V	3.08E-02	0.63	-136	3.50E-02	8040
	a3667_26e.4736	I	1.85E-02	7.54	19	4.67E-02	10530
		Q	1.85E-02	0.8	144	2.40E-02	10530
		U	1.85E-02	1.82	37	2.43E-02	10530
		V	1.85E-02	1.68	-109	2.41E-02	10530
	a3667_26e.6528	I	3.05E-02	10.19	19	4.82E-02	9720
		Q	3.05E-02	0.39	-79	3.68E-02	9720
		U	3.05E-02	0.56	75	3.67E-02	9720
		V	3.05E-02	0.17	101	3.68E-02	9720
	a3667_28.4736	I	1.86E-02	5.29	-5	2.69E-02	8580
		Q	1.86E-02	1.24	165	2.29E-02	8580
		U	1.86E-02	0.61	31	2.31E-02	8580
		V	1.86E-02	1.44	-120	2.30E-02	8580
	a3667_28.6528	I	3.09E-02	3.61	-5	3.75E-02	7920
		Q	3.09E-02	0.3	51	3.59E-02	7920
		U	3.09E-02	0.61	-61	3.58E-02	7920
		V	3.09E-02	0.55	-7	3.61E-02	7920
	a3667_a.4736	I	1.87E-02	7.55	-14	2.46E-02	8710
		Q	1.87E-02	1.05	-170	2.28E-02	8710
		U	1.87E-02	0.79	-66	2.28E-02	8710
		V	1.87E-02	1.23	-116	2.29E-02	8710
	a3667_a.6528	I	3.09E-02	2.92	-17	3.61E-02	8100
		Q	3.09E-02	0.69	-19	3.50E-02	8100
		U	3.09E-02	0.48	55	3.56E-02	8100
		V	3.09E-02	0.61	-50	3.55E-02	8100
	a3667_dif2.4736	I	1.88E-02	4.14	-89	4.46E-02	8775
		Q	1.88E-02	1.06	-175	2.37E-02	8775
		U	1.88E-02	0.21	-3	2.37E-02	8775
		V	1.88E-02	1.27	-127	2.38E-02	8775
	a3667_dif2.6528	I	3.11E-02	4.78	151	5.22E-02	8100
		Q	3.11E-02	0.89	116	3.67E-02	8100
		U	3.11E-02	0.4	49	3.70E-02	8100
		V	3.11E-02	0.68	84	3.67E-02	8100
A3571	a3571_1.4736	I	1.75E-02	6.32	-27	2.14E-02	7020
		Q	1.75E-02	1.94	-168	2.14E-02	7020
		U	1.75E-02	0.79	-177	2.09E-02	7020
		V	1.75E-02	1.51	-102	2.15E-02	7020
	a3571_1.6528	I	2.99E-02	4	-53	3.41E-02	6480
		Q	2.99E-02	0.64	130	3.34E-02	6480
		U	2.99E-02	0.26	60	3.37E-02	6480

continued on next page

continued from previous page

Cluster	Source	Stokes	RMS_t	A_{mJy}	ϕ_{deg}	RMS_{mJy}	Corr
		V	2.99E-02	0.48	-25	3.38E-02	6480
	a3571_3e.4736	I	1.75E-02	26.15	21	2.84E-02	6630
		Q	1.75E-02	5.16	-165	2.18E-02	6630
		U	1.75E-02	1.23	-134	2.10E-02	6630
		V	1.75E-02	1.2	-109	2.18E-02	6630
	a3571_3e.6528	I	3.00E-02	13.32	28	3.62E-02	6120
		Q	3.00E-02	1.23	-106	3.37E-02	6120
		U	3.00E-02	0.44	-137	3.33E-02	6120
		V	3.00E-02	0.66	-134	3.36E-02	6120
	a3571_5e.4736	I	1.74E-02	3.22	23	2.09E-02	7020
		Q	1.74E-02	2.41	-168	2.14E-02	7020
		U	1.74E-02	0.93	-160	2.07E-02	7020
		V	1.74E-02	1.62	-128	2.12E-02	7020
	a3571_5e.6528	I	2.98E-02	0.52	32	3.30E-02	6480
		Q	2.98E-02	0.87	47	3.32E-02	6480
		U	2.98E-02	0.27	16	3.31E-02	6480
		V	2.98E-02	0.73	-114	3.34E-02	6480
	a3571_6.4736	I	1.74E-02	1.88	14	2.09E-02	7020
		Q	1.74E-02	1.76	-173	2.13E-02	7020
		U	1.74E-02	0.64	165	2.06E-02	7020
		V	1.74E-02	1.42	-113	2.14E-02	7020
	a3571_6.6528	I	2.98E-02	0.14	143	3.33E-02	6480
		Q	2.98E-02	0.69	-162	3.35E-02	6480
		U	2.98E-02	0.76	44	3.34E-02	6480
		V	2.98E-02	0.92	-2	3.33E-02	6480
	a3571_8.4736	I	1.75E-02	37.63	-19	2.86E-02	7020
		Q	1.75E-02	2.14	167	2.16E-02	7020
		U	1.75E-02	1.11	-56	2.06E-02	7020
		V	1.75E-02	1.41	-127	2.13E-02	7020
	a3571_8.6528	I	2.98E-02	26.29	-28	3.98E-02	6480
		Q	2.98E-02	0.77	-144	3.30E-02	6480
		U	2.98E-02	0.76	-59	3.29E-02	6480
		V	2.98E-02	0.74	-160	3.32E-02	6480

Table A.2: Cluster pilot survey data obtained using the outputs of the *MIRIAD*task *UVFLUX*: col 1 gives the name of the cluster; col 2 is the source designation, which is comprised of the cluster name, the object number for that cluster and the observing frequency; col 3 lists the Stokes parameters; col 4 is the phase corrected amplitude in mJy; col 5 is the signal-to-noise; col 6 is the total linear polarisation in mJy; col 7 is the percentage polarisation and col 8 is the position angle in degrees. A star in the cluster column indicates that the source was not detected.

Cluster Pilot Survey Data							
Cluster	Source	Stokes	A_{mJy}	σ	P_{mJy}	%P	PA_{deg}
A3128	a3128_10.4736	I	50.3 ± 0.2	226.4	1.7 ± 0.3	3.4	-17.9
		Q	-1.4 ± 0.2	7.6			
		U	1.0 ± 0.2	5.4			
		V	-0.2 ± 0.2	0.9			
	a3128_10.6528	I	46.5 ± 0.4	124.9	0.0 ± 0.4	0.1	-26.3
		Q	0.0 ± 0.3	0.1			
		U	0.0 ± 0.3	0.1			
		V	0.0 ± 0.3	0.0			
	a3128_1e.4736	I	3.4 ± 0.2	16.6	1.6 ± 0.3	46.7	-5.8
		Q	-1.6 ± 0.2	8.8			
		U	0.3 ± 0.2	1.8			
		V	-0.5 ± 0.2	2.8			
⋆	a3128_1e.6528	I	0.8 ± 0.3	2.7	0.2 ± 0.4	24.9	-32.1
		Q	0.1 ± 0.3	0.3			
		U	-0.2 ± 0.3	0.6			
		V	0.1 ± 0.3	0.2			
	a3128_3.4736	I	3.8 ± 0.2	20.0	1.7 ± 0.3	45.5	-12.5
		Q	-1.6 ± 0.2	8.5			
		U	0.7 ± 0.2	4.0			
		V	0.0 ± 0.2	0.0	* phase=90		
⋆	a3128_3.6528	I	1.0 ± 0.3	3.2	0.7 ± 0.4	69.6	-3.9
		Q	0.7 ± 0.3	2.2			
		U	-0.1 ± 0.3	0.3			
		V	0.8 ± 0.3	2.4			
	a3128_5.4736	I	42.4 ± 0.4	108.2	2.6 ± 0.3	6.1	13.2
		Q	-2.3 ± 0.2	13.1			
		U	-1.2 ± 0.2	6.5			
		V	-0.2 ± 0.2	1.1			
	a3128_5.6528	I	24.0 ± 0.4	58.9	2.5 ± 0.4	10.4	38.7
		Q	-0.5 ± 0.3	1.8			
		U	-2.4 ± 0.3	8.3			
		V	0.4 ± 0.3	1.4			
	a3128_7.4736	I	2.8 ± 0.2	15.7	1.5 ± 0.3	53.6	-6.0

continued on next page

continued from previous page

Cluster	Source	Stokes	A_{mJy}	σ	P_{mJy}	%P	PA_{deg}
		Q	-1.5 ± 0.2	8.3			
		U	0.3 ± 0.2	1.8			
		V	-0.5 ± 0.2	3.0			
	a3128_7.6528	I	1.7 ± 0.3	5.7	0.1 ± 0.4	6.4	-5.5
		Q	0.1 ± 0.3	0.4			
		U	0.0 ± 0.3	0.1			
		V	0.1 ± 0.3	0.4			
A3266	a3266_1.4736	I	5.5 ± 0.3	20.6	1.0 ± 0.3	18.2	-24.7
		Q	-0.7 ± 0.2	2.6			
		U	0.8 ± 0.2	3.1			
		V	-0.2 ± 0.2	0.8			
	a3266_1.6528	I	2.3 ± 0.4	6.2	0.3 ± 0.5	14.7	-34.8
		Q	0.1 ± 0.4	0.3			
		U	-0.3 ± 0.4	0.9			
		V	-0.3 ± 0.4	0.9			
	a3266_10.4736	I	20.2 ± 0.3	64.7	0.6 ± 0.4	3.2	-11.0
		Q	-0.6 ± 0.3	2.4			
		U	0.2 ± 0.3	1.0			
		V	-0.9 ± 0.3	3.4			
	a3266_10.6528	I	11.9 ± 0.4	29.9	1.0 ± 0.5	8.0	-30.5
		Q	-0.5 ± 0.4	1.3			
		U	0.8 ± 0.4	2.3			
		V	0.0 ± 0.4	0.1			
	a3266_11.4736	I	10.1 ± 0.3	29.8	0.4 ± 0.3	4.3	-4.8
		Q	-0.4 ± 0.2	1.7			
		U	0.1 ± 0.2	0.3			
		V	0.1 ± 0.2	0.5			
	a3366_11.6528	I	6.7 ± 0.4	16.9	0.5 ± 0.5	7.8	33.2
		Q	-0.2 ± 0.4	0.6			
		U	-0.5 ± 0.4	1.3			
		V	-0.4 ± 0.4	1.1			
	a3266_2.4736	I	2.4 ± 0.2	9.7	0.9 ± 0.3	39.0	-28.7
		Q	-0.5 ± 0.2	2.2			
		U	0.8 ± 0.2	3.4			
		V	-0.2 ± 0.2	0.8			
⋆	a3266_2.6528	I	0.7 ± 0.3	2.1	0.7 ± 0.5	97.2	36.1
		Q	0.2 ± 0.3	0.6			
		U	0.7 ± 0.3	1.9			
		V	-0.2 ± 0.3	0.6			
	a3266_3.4736	I	9.1 ± 0.7	12.4	1.4 ± 0.4	15.4	7.0

continued on next page

continued from previous page

Cluster	Source	Stokes	A_{mJy}	σ	P_{mJy}	%P	PA_{deg}
		Q	-1.4 ± 0.3	5.3			
		U	-0.3 ± 0.3	1.3			
		V	0.0 ± 0.3	0.1			
	a3266_3.6528	I	3.8 ± 0.5	7.1	0.3 ± 0.5	7.9	2.5
		Q	-0.3 ± 0.4	0.8			
		U	0.0 ± 0.4	0.1			
		V	0.0 ± 0.4	0.0			
	a3266_4e.4736	I	114.0 ± 1.2	96.6	2.7 ± 0.4	2.4	10.3
		Q	-2.6 ± 0.3	10.0			
		U	-1.0 ± 0.3	3.7			
		V	-0.7 ± 0.3	2.8			
	a3266_4e.6528	I	76.3 ± 1.3	59.1	0.9 ± 0.5	1.2	-12.1
		Q	-0.9 ± 0.3	2.5			
		U	0.4 ± 0.3	1.1			
		V	0.1 ± 0.3	0.3			
⋆	a3266_5e.4736	I	3.2 ± 1	3.4	1.1 ± 0.4	34.0	11.9
		Q	-1.0 ± 0.3	3.7			
		U	-0.4 ± 0.3	1.6			
		V	-0.7 ± 0.3	2.6			
⋆	a3266_5e.6528	I	-0.8 ± 0.6	1.3	0.9 ± 0.5	-107.1	-18.5
		Q	-0.7 ± 0.4	2.0			
		U	0.5 ± 0.3	1.5			
		V	-0.1 ± 0.4	0.1			
	a3266_8.4736	I	67.5 ± 0.6	112.7	0.3 ± 0.4	0.5	-38.5
		Q	-0.1 ± 0.3	0.3			
		U	0.3 ± 0.3	1.2			
		V	-0.3 ± 0.3	1.0			
	a3266_8.6528	I	40.8 ± 0.5	74.6	1.3 ± 0.5	3.1	-30.7
		Q	0.6 ± 0.4	1.6			
		U	-1.1 ± 0.4	2.9			
		V	-0.4 ± 0.4	1.1			
	a3266_9.4736	I	10.5 ± 0.3	30.6	0.7 ± 0.4	6.3	-0.1
		Q	-0.7 ± 0.3	2.6			
		U	0.0 ± 0.2	0.0			
		V	-0.5 ± 0.2	1.9			
	a3266_9.6528	I	5.9 ± 0.4	14.1	0.5 ± 0.5	8.3	33.2
		Q	-0.2 ± 0.4	0.5			
		U	-0.5 ± 0.4	1.2			
		V	-0.2 ± 0.4	0.5			
A3558	a3558_10.4736	I	8.4 ± 0.3	31.4	2.7 ± 0.3	32.2	6.7

continued on next page

continued from previous page

Cluster	Source	Stokes	A_{mJy}	σ	P_{mJy}	%P	PA_{deg}
		Q	-2.6 ± 0.2	10.9			
		U	-0.6 ± 0.2	2.7			
		V	-0.6 ± 0.2	2.5			
	a3558_10.6528	I	4.4 ± 0.4	11.4	0.8 ± 0.5	17.3	33.0
		Q	-0.3 ± 0.4	0.8			
		U	-0.7 ± 0.4	1.9			
		V	0.4 ± 0.4	0.9			
	a3558_11.4736	I	3.1 ± 0.2	12.8	2.8 ± 0.3	89.4	8.1
		Q	-2.6 ± 0.2	10.9			
		U	-0.8 ± 0.2	3.2			
		V	-0.6 ± 0.2	2.3			
⋆	a3558_11.6528	I	0.4 ± 0.4	0.9	0.4 ± 0.5	109.7	30.5
		Q	0.2 ± 0.4	0.5			
		U	0.3 ± 0.4	0.9			
		V	0.3 ± 0.4	0.9			
	a3558_13.4736	I	10.3 ± 0.3	38.4	2.9 ± 0.3	28.5	4.0
		Q	-2.9 ± 0.2	11.9			
		U	-0.4 ± 0.2	1.7			
		V	-0.1 ± 0.2	0.5			
	a3558_13.6528	I	6.3 ± 0.4	16.1	0.3 ± 0.5	4.6	-19.4
		Q	-0.2 ± 0.4	0.6			
		U	0.2 ± 0.4	0.5			
		V	-0.2 ± 0.4	0.4			
	a3558_1e.4736	I	5.4 ± 0.2	23.1	2.3 ± 0.3	42.0	1.9
		Q	-2.3 ± 0.2	10.0			
		U	-0.2 ± 0.2	0.7			
		V	-0.7 ± 0.2	3.2			
⋆	a3558_1e.6528	I	1.4 ± 0.4	3.7	0.4 ± 0.5	31.0	-42.1
		Q	-0.1 ± 0.4	0.1			
		U	0.4 ± 0.4	1.2			
		V	-0.3 ± 0.4	0.8			
	a3558_2.4736	I	4.1 ± 0.3	12.5	3.1 ± 0.3	77.4	6.6
		Q	-3.1 ± 0.2	12.5			
		U	-0.7 ± 0.2	3.0			
		V	-0.6 ± 0.2	2.3			
⋆	a3558_2.6528	I	0.5 ± 0.4	1.2	0.7 ± 0.5	146.0	9.3
		Q	0.7 ± 0.4	1.7			
		U	0.2 ± 0.4	0.6			
		V	-0.1 ± 0.4	0.2			
	a3558_5.4736	I	1.8 ± 0.3	6.9	2.8 ± 0.3	152.0	7.8

continued on next page

continued from previous page

Cluster	Source	Stokes	A_{mJy}	σ	P_{mJy}	%P	PA_{deg}
		Q	-2.7 ± 0.2	11.0			
		U	-0.7 ± 0.2	3.2			
		V	-0.5 ± 0.2	2.0			
⋆	a3558_5.6528	I	1.4 ± 0.4	3.7	0.2 ± 0.5	13.7	-15.1
		Q	-0.2 ± 0.4	0.5			
		U	0.1 ± 0.4	0.3			
		V	-0.4 ± 0.4	1.1			
	a3558_7.4736	I	36.2 ± 0.3	118.7	2.3 ± 0.3	6.3	12.2
		Q	-2.1 ± 0.2	8.6			
		U	-0.9 ± 0.2	4.0			
		V	-0.5 ± 0.2	1.9			
	a3558_7.6528	I	24.9 ± 0.4	60.4	0.5 ± 0.5	1.9	8.4
		Q	-0.5 ± 0.4	1.2			
		U	-0.1 ± 0.4	0.4			
		V	-0.5 ± 0.4	1.3			
	a3558_8.4736	I	29.5 ± 0.4	68.3	5.6 ± 0.3	18.8	4.7
		Q	-5.5 ± 0.2	22.6			
		U	-0.9 ± 0.2	3.8			
		V	-0.4 ± 0.2	1.7			
	a3558_8.6528	I	11.7 ± 0.5	23.7	1.2 ± 0.5	10.0	6.6
		Q	-1.1 ± 0.4	3.0			
		U	-0.3 ± 0.4	0.7			
		V	0.1 ± 0.4	0.2			
A3562	a3562_1.4736	I	3.9 ± 0.3	15.5	2.4 ± 0.4	62.2	6.6
		Q	-2.4 ± 0.2	9.6			
		U	-0.6 ± 0.2	2.3			
		V	-0.1 ± 0.2	0.6			
⋆	a3562_1.6528	I	0.9 ± 0.4	2.2	1.0 ± 0.5	118.5	3.3
		Q	1.0 ± 0.4	2.7			
		U	0.1 ± 0.4	0.3			
		V	0.7 ± 0.4	1.9			
	a3562_3.4736	I	5.2 ± 0.2	21.1	3.1 ± 0.4	59.7	2.2
		Q	-3.1 ± 0.3	12.2			
		U	-0.2 ± 0.2	1.0			
		V	0.0 ± 0.2	0.0			
	a3562_3.6528	I	2.1 ± 0.4	5.3	0.8 ± 0.6	37.0	15.0
		Q	0.7 ± 0.4	1.7			
		U	0.4 ± 0.4	1.0			
		V	0.5 ± 0.4	1.2			
	a3562_4.4736	I	1.6 ± 0.2	6.3	2.8 ± 0.4	179.5	0.6

continued on next page

continued from previous page

Cluster	Source	Stokes	A_{mJy}	σ	P_{mJy}	%P	PA_{deg}
		Q	-2.8 ± 0.3	11.0			
		U	-0.1 ± 0.2	0.2			
		V	0.0 ± 0.3	0.1			
⋆	a3562_4.6528	I	-0.1 ± 0.4	0.3	0.5 ± 0.6	-388.3	34.6
		Q	-0.2 ± 0.4	0.4			
		U	-0.5 ± 0.4	1.2			
		V	-0.1 ± 0.4	0.3			
	a3562_5.4736	I	4.5 ± 0.2	18.1	2.8 ± 0.4	62.7	11.8
		Q	-2.6 ± 0.3	10.1			
		U	-1.1 ± 0.2	4.7			
		V	-0.2 ± 0.3	0.8			
⋆	a3562_5.6528	I	2.0 ± 0.4	4.9	1.0 ± 0.6	48.8	28.4
		Q	-0.5 ± 0.4	1.3			
		U	-0.8 ± 0.4	2.0			
		V	0.5 ± 0.4	1.2			
	a3562_6e.4736	I	2.7 ± 0.3	8.7	2.3 ± 0.4	87.6	3.9
		Q	-2.3 ± 0.3	7.8			
		U	-0.3 ± 0.3	1.1			
		V	-0.2 ± 0.3	0.8			
⋆	a3562_6e.6528	I	0.8 ± 0.5	1.7	0.8 ± 0.7	100.7	37.6
		Q	-0.2 ± 0.5	0.4			
		U	-0.8 ± 0.5	1.6			
		V	-0.3 ± 0.5	0.7			
	a3562_9.4736	I	6.4 ± 0.3	21.4	2.4 ± 0.4	37.9	5.9
		Q	-2.4 ± 0.3	8.0			
		U	-0.5 ± 0.3	1.7			
		V	-0.5 ± 0.3	1.8			
	a3562_9.6528	I	2.7 ± 0.5	5.7	0.8 ± 0.7	30.5	-32.5
		Q	0.3 ± 0.5	0.7			
		U	-0.7 ± 0.5	1.6			
A3667		V	1.0 ± 0.5	2.1			
⋆	a3667_1.4736	I	0.8 ± 0.7	1.2	1.4 ± 0.4	162.6	6.2
		Q	-1.3 ± 0.2	5.3			
		U	-0.3 ± 0.2	1.2			
		V	-0.7 ± 0.2	2.7			
⋆	a3667_1.6528	I	-4.5 ± 0.7	6.5	0.3 ± 0.6	-5.5	10.1
		Q	-0.2 ± 0.4	0.6			
		U	-0.1 ± 0.4	0.2			
		V	-0.5 ± 0.4	1.3			
	a3667_11.4736	I	1.4 ± 0.3	5.3	1.4 ± 0.4	101.7	-9.1

continued on next page

continued from previous page

Cluster	Source	Stokes	A_{mJy}	σ	P_{mJy}	%P	PA_{deg}
		Q	-1.3 ± 0.3	5.1			
		U	0.4 ± 0.3	1.7			
		V	-1.0 ± 0.3	3.9			
⋆	a3667_11.6528	I	0.1 ± 0.4	0.3	0.2 ± 0.6	140.4	-6.4
		Q	-0.2 ± 0.4	0.4			
		U	0.0 ± 0.4	0.1			
		V	-0.1 ± 0.4	0.2			
⋆	a3667_16.4736	I	1.0 ± 0.3	3.3	1.3 ± 0.4	136.0	3.3
		Q	-1.3 ± 0.3	5.2			
		U	-0.2 ± 0.3	0.6			
		V	-1.1 ± 0.3	4.1			
⋆	a3667_16.6528	I	-1.1 ± 0.4	2.6	0.7 ± 0.6	-63.8	-8.6
		Q	-0.7 ± 0.4	1.6			
		U	0.2 ± 0.4	0.5			
		V	0.1 ± 0.4	0.3			
	a3667_17.4736	I	2.3 ± 0.3	8.8	1.6 ± 0.3	69.9	0.7
		Q	-1.6 ± 0.2	6.6			
		U	0.0 ± 0.2	0.2			
		V	-0.9 ± 0.2	3.6			
⋆	a3667_17.6528	I	-0.3 ± 0.4	0.7	0.4 ± 0.6	-129.6	3.9
		Q	-0.4 ± 0.4	0.9			
		U	-0.1 ± 0.4	0.1			
		V	-0.5 ± 0.4	1.2			
	a3667_26e.4736	I	7.1 ± 0.5	15.7	1.6 ±	22.3	-33.0
		Q	-0.7 ± 0.2	2.8	0.3		
		U	1.5 ± 0.2	6.1			
		V	-0.6 ± 0.2	2.3			
	a3667_26e.6528	I	9.6 ± 0.5	19.7	0.2 ± 0.5	1.7	31.5
		Q	0.1 ± 0.4	0.2			
		U	0.2 ± 0.4	0.4			
		V	0.0 ± 0.4	0.1			
	a3667_28.4736	I	5.3 ± 0.3	18.1	1.3 ± 0.3	24.8	-11.7
		Q	-1.2 ± 0.2	4.9			
		U	0.5 ± 0.2	2.1			
		V	-0.7 ± 0.2	2.9			
	a3667_28.6528	I	3.6 ± 0.4	8.5	0.4 ± 0.6	9.8	28.7
		Q	0.2 ± 0.4	0.5			
		U	0.3 ± 0.4	0.7			
		V	0.5 ± 0.4	1.3			
	a3667_a.4736	I	7.3 ± 0.3	27.8	1.1 ± 0.3	14.8	-8.6

continued on next page

continued from previous page

Cluster	Source	Stokes	A_{mJy}	σ	P_{mJy}	%P	PA_{deg}
		Q	-1.0 ± 0.2	4.2			
		U	0.3 ± 0.2	1.3			
		V	-0.5 ± 0.2	2.2			
	a3667_a.6528	I	2.8 ± 0.4	7.0	0.7 ± 0.5	25.4	11.3
		Q	0.7 ± 0.4	1.7			
		U	0.3 ± 0.4	0.7			
		V	0.4 ± 0.4	1.0			
⋆	a3667_dif2.4736	I	0.1 ± 0.5	0.2	1.1 ± 0.4	1487.4	-5.6
		Q	-1.1 ± 0.3	4.2			
		U	0.2 ± 0.3	0.8			
		V	-0.8 ± 0.3	3.0			
⋆	a3667_dif2.6528	I	-4.2 ± 0.6	7.2	0.5 ± 0.6	-11.3	-17.1
		Q	-0.4 ± 0.4	1.0			
		U	0.3 ± 0.4	0.7			
		V	0.1 ± 0.4	0.2			
A3571	a3571_1.4736	I	5.6 ± 0.3	22.1	2.1 ± 0.4	36.5	11.2
		Q	-1.9 ± 0.3	7.4			
		U	-0.8 ± 0.2	3.1			
		V	-0.3 ± 0.3	1.2			
	a3571_1.6528	I	2.4 ± 0.4	5.7	0.4 ± 0.6	18.0	-8.7
		Q	-0.4 ± 0.4	1.0			
		U	0.1 ± 0.4	0.3			
		V	0.4 ± 0.4	1.0			
	a3571_3e.4736	I	24.4 ± 0.3	70.0	5.1 ± 0.4	20.7	4.9
		Q	-5.0 ± 0.3	18.6			
		U	-0.9 ± 0.3	3.3			
		V	-0.4 ± 0.3	1.5			
	a3571_3e.6528	I	11.8 ± 0.5	25.4	0.5 ± 0.6	4.0	21.7
		Q	-0.3 ± 0.4	0.8			
		U	-0.3 ± 0.4	0.8			
		V	-0.5 ± 0.4	1.1			
	a3571_5e.4736	I	3.0 ± 0.2	11.9	2.5 ± 0.4	84.8	10.2
		Q	-2.4 ± 0.3	9.2			
		U	-0.9 ± 0.2	3.5			
		V	-1.0 ± 0.3	3.9			
⋆	a3571_5e.6528	I	0.4 ± 0.4	1.1	0.6 ± 0.6	147.3	11.6
		Q	0.6 ± 0.4	1.4			
		U	0.3 ± 0.4	0.6			
		V	-0.3 ± 0.4	0.7			
	a3571_6.4736	I	1.8 ± 0.2	7.3	1.9 ± 0.4	101.6	9.8

continued on next page

continued from previous page							
Cluster	Source	Stokes	A_{mJy}	σ	P_{mJy}	%P	PA_{deg}
		Q	-1.8 ± 0.3	6.9			
		U	-0.6 ± 0.2	2.5			
		V	-0.6 ± 0.3	2.2			
⋆	a3571_6.6528	I	-0.1 ± 0.4	0.3	0.9 ± 0.6	-787.8	-19.9
		Q	-0.7 ± 0.4	1.6			
		U	0.6 ± 0.4	1.3			
		V	0.9 ± 0.4	2.2			
	a3571_8.4736	I	35.6 ± 0.3	104.2	2.2 ± 0.4	6.1	-8.3
		Q	-2.1 ± 0.3	8.1			
		U	0.6 ± 0.2	2.5			
		V	-0.9 ± 0.3	3.4			
	a3571_8.6528	I	23.2 ± 0.5	47.0	0.7 ± 0.6	3.2	-16.0
		Q	-0.6 ± 0.4	1.5			
		U	0.4 ± 0.4	1.0			
		V	-0.7 ± 0.4	1.7			

Table A.3: Radio Sources in A3158: col 1 and 2 are the right accension and declination of the sources observed using the J2000 equinox; col 3 is the peak flux density in mJy at 1.4 GHz measured using a 6 arcsecond beam; col 4 is the peak flux density in mJy at 2.4 GHz measured using a 3 arcsecond beam; col 5 gives brief comments for sources with multiple components.

Radio Sources in A3158				
RA_{J2000}	Dec_{J2000}	$S_{1.4}$ (mJy)	$S_{2.4}$ (mJy)	Notes
3 39 43	-53 6 29.0	0.70		
3 41 49	-54 2 5.7	0.55		
3 41 53	-54 2 24.0	0.65		
3 41 41	-53 59 27.0	11.76		
3 42 56	-54 2 32.0	0.92		
3 42 2	-53 36 7.4	15.32	0.72	south lobe
3 42 4	-53 35 7.4	2.00		core
3 42 6	-53 33 59.5	8.83		north lobe
3 42 19	-53 26 13.0	0.63		
3 42 19	-53 26 11.4	0.70		
3 42 34	-53 33 19.0	0.69		
3 42 53	-53 37 53.0	4.11		
3 43 33	-54 11 18.0	1.79		
3 43 7	-53 41 41.0	0.64		
3 43 16	-53 39 36.0	0.85		
3 43 22	-53 28 41.0	1.80		
3 43 23	-53 28 15.0	0.95		

continued on next page

continued from previous page

RA_{J2000}	Dec_{J2000}	$S_{1.4}$ (mJy)	$S_{2.4}$ (mJy)	Notes
3 43 29	-53 41 30.0	0.83		
3 43 45	-53 42 46.0	1.02		
3 43 49	-53 25 26.0	1.26		
3 43 59	-53 55 19.0	1.41		
3 44 16	-54 4 23.0	6.15		
3 44 11	-53 43 35.0	1.95	1.00	
3 44 18	-53 41 52.0	1.59	1.02	
3 44 21	-53 44 30.0	2.12	0.95	
3 44 22	-53 59 22.0	2.26		double
3 44 24	-53 59 44.0	1.91		double
3 44 30	-53 53 12.0	45.00	7.75	double
3 44 30	-53 53 14.0	42.07	4.71	double
3 44 32	-53 52 59.0		8.46	
3 44 41	-53 42 23.0	1.17		
3 44 43	-53 41 55.0	0.70	1.04	
3 44 44	-53 41 45.0	12.96	5.07	
3 45 25	-53 41 29.0	14.52	2.13	double
3 45 27	-53 41 25.0	12.36	2.00	double
3 45 37	-53 40 20.0	1.90		
3 45 42	-53 32 51.2	1.50		
3 45 53	-53 0 46.0	1.53		
3 46 5	-53 15 21.0	2.26		
3 47 3	-53 44 40.0	0.66		

Appendix B

Rotation Measure Catalogue

B.1 RM Data used to produce Interpolated All-Sky RM Map

Table B.1: The dataset used to produce the interpolated all-sky RM maps. Data are collated from several catalogues in the literature and the fit of each source individually verifed. Where a source is observed more than once the most reliable fit was used. Col 1 is the J2000 Galactic Longitude; col 2 the J2000 Galactic Latitude; col 4 is the RM in rad m^{-2}, col 5 is the error in the RM in rad m^{-2} specified in the literature and col 5 shows if the source was used in the final dataset after the two stage culling was performed.

Extragalactic RM Catalogue				
l_{J2000}	b_{J2000}	RM	δRM	Used
0.8	146.9	19	3.4	Y
1.0	48.0	22	2	Y
1.0	140.3	4.1	3.4	Y
1.4	24.2	19	1	Y
1.8	62.2	-16	2	Y
1.8	116.1	40	11.3	Y
1.9	52.5	9	2	Y
2.1	124.2	14	5	Y
2.2	109.7	90	1	Y
2.3	54.3	26	3	Y
2.6	138.9	3	4	Y
2.7	118.8	-1	2	Y
3.9	138.9	12.4	4	Y
4.3	35.1	57	1	Y
4.3	125.1	-130	5	Y
4.7	157.0	-10	5	Y

continued on next page

continued from previous page

l_{J2000}	b_{J2000}	RM	δRM	Used
5.1	59.2	6	2	Y
5.2	132.6	7	2	Y
5.6	94.0	2	3	Y
6.0	19.8	57	4	Y
6.3	46.8	167	20	Y
6.7	96.7	1	5	Y
6.8	82.9	-7	21	Y
7.1	59.0	-10	4	Y
7.4	78.7	-2	0.2	Y
7.7	47.6	81.2	5.8	Y
7.7	56.4	-65	2	Y
7.9	168.2	11	1	Y
8.0	47.5	26	4	Y
8.1	90.0	-270	19	Y
8.1	136.8	14	3	Y
8.3	138.7	14	0.3	Y
8.4	97.0	69	15	Y
8.5	84.3	30	4	Y
8.6	68.2	386	5	N
8.6	113.6	12	10	Y
9.0	153.0	17	7	Y
9.6	53.3	72	4	Y
9.6	89.4	708	8	N
9.7	45.2	91	4	Y
10.0	145.0	25	7	Y
10.4	62.6	-3	1	Y
10.5	111.8	81	3	Y
11.1	98.7	62	2	Y
11.1	126.4	45	2	Y
11.2	103.4	20	2	Y
11.4	44.4	-15	2	Y
11.7	117.9	5	17	Y
11.8	165.0	-3	2	Y
13.1	98.3	71	3	Y
13.2	54.8	-33	5	Y
13.5	58.0	-50	6	Y
13.9	122.6	15	1	Y
14.2	142.3	-130	10	Y
15.2	113.2	5.6	4.9	Y
15.3	56.9	-24.3	3.8	Y

continued on next page

continued from previous page

l_{J2000}	b_{J2000}	RM	δRM	Used
15.5	62.2	22	14	Y
16.5	129.7	38	3	Y
16.6	47.3	19	1	Y
16.6	90.2	-90	2	Y
17.2	61.5	71	2	Y
17.5	68.6	28	1	Y
17.6	75.5	84	3	Y
17.8	128.8	-35	26	Y
17.9	67.2	-7	33	Y
17.9	116.4	20	2	Y
19.4	168.4	-35.4	0.5	Y
19.7	35.1	-336	6	N
20.0	74.6	-13	2	Y
20.2	142.7	42	1	Y
20.4	69.0	41	5	Y
20.6	118.5	43	5	Y
21.3	25.5	6	2	Y
21.5	64.7	-170	17	Y
21.5	159.0	2	17	Y
21.8	108.1	1	3	Y
22.1	104.5	37	6	Y
22.3	101.5	93	4	Y
22.8	104.0	66	1	Y
23.4	105.4	32	4	Y
23.8	104.6	52	3	Y
24.8	100.1	7	2	Y
24.9	48.2	-14	2	Y
25.5	43.7	-36	3	Y
25.8	132.7	13	2	Y
26.1	122.0	10	1	Y
26.5	139.7	26	6	Y
26.8	125.8	-176	2	Y
27.3	122.5	31.1	0.7	Y
27.6	21.5	13	5	Y
27.6	111.8	114	14	Y
28.5	52.2	-144	4	Y
29.6	53.7	53	2	Y
29.8	25.0	5	1	Y
30.3	114.2	54	4	Y
30.7	144.4	-308	32	N

continued on next page

continued from previous page

l_{J2000}	b_{J2000}	RM	δRM	Used
31.9	111.0	89	2	Y
31.9	127.2	31	2	Y
32.3	46.3	-8	4	Y
32.3	156.9	-25	3	Y
33.0	120.0	27	1	Y
33.2	145.7	18	20	Y
33.6	123.6	33	4	Y
33.7	123.2	1510.8	7.8	N
34.0	124.5	140	3	Y
35.4	82.0	111	1	Y
35.4	117.1	-4.4	1	Y
35.8	77.0	93	3	Y
36.5	55.8	17	3	Y
36.5	130.6	22.5	7.3	Y
36.5	138.4	-3	1	Y
36.9	46.8	7	6	Y
37.0	101.4	22	1	Y
37.1	96.2	80	18	Y
37.3	102.8	20	3	Y
37.7	97.2	52	1	Y
37.7	109.0	13	6	Y
37.7	109.1	16	9	Y
38.1	113.0	26	2	Y
38.3	145.5	15.3	0.8	Y
38.9	97.0	41	4	Y
40.0	134.0	-25	5	Y
40.3	55.6	-49	10	Y
40.4	136.0	5	1	Y
40.7	108.6	57	6	Y
41.1	109.5	-24	4	Y
42.4	132.9	101.4	1.5	N
42.5	106.0	-81	16	Y
42.5	153.1	-18.3	4.3	Y
42.6	73.8	63	4	Y
44.1	97.5	-43	6	Y
44.5	39.1	23	6	Y
44.6	39.7	78.4	2.5	Y
44.9	98.7	464	7	N
45.1	139.1	-16	5	Y
45.2	132.7	12	2	Y

continued on next page

continued from previous page

l_{J2000}	b_{J2000}	RM	δRM	Used
45.4	47.6	46	8	Y
45.4	92.9	800	21	N
45.7	107.1	159	12	N
46.1	84.7	200	16	Y
46.4	122.2	47.8	0.9	Y
46.8	108.2	34	34	Y
46.9	13.2	-1	2	Y
47.1	91.0	13	5	Y
47.2	112.1	-11	0.7	Y
47.2	163.8	18	4	Y
47.7	82.3	-1	4	Y
47.8	93.1	-2	11	Y
48.3	61.8	29.3	5.8	Y
48.5	51.1	88	2	Y
48.6	132.3	-7	2	Y
49.0	53.0	46	7	Y
49.0	103.2	-359	9	N
49.4	101.3	-32	5	Y
49.9	77.6	49	2	Y
50.1	128.3	75	11	Y
51.1	15.5	2	12	Y
51.4	102.0	-69	2	Y
51.4	153.6	-7	1	Y
51.6	53.0	4	2	Y
51.8	53.6	-373	3	N
52.1	136.6	141	5	N
52.4	126.8	-11	1	Y
53.1	56.7	3	2	Y
53.1	146.3	26.9	0.6	Y
53.7	85.0	633	5	N
54.0	136.7	50	4	Y
54.9	38.0	16	2	Y
55.6	80.7	216	2	Y
55.7	163.0	16	8	Y
56.5	58.6	6	4	Y
56.6	36.4	30	3	Y
56.7	154.1	8.1	5.9	Y
57.2	107.4	-105	7	Y
57.6	129.0	-20	2	Y
58.1	84.1	154	2	Y

continued on next page

continued from previous page

l_{J2000}	b_{J2000}	RM	δRM	Used
58.2	66.7	393	12	N
58.8	46.7	45	3	Y
59.1	40.7	23	2	Y
59.1	130.8	-6	1	Y
59.4	37.0	-5	6	Y
59.4	155.3	-112	39	Y
60.1	33.0	-2.4	0.4	Y
60.3	33.6	-3	1	Y
60.6	58.3	9	1	Y
61.1	142.7	14.3	3.7	Y
62.3	110.7	9	1	Y
62.4	100.3	199	3	Y
62.9	115.0	-1850	15	N
63.3	102.6	75	4	Y
63.5	70.0	45	4	Y
63.9	98.8	366	2	N
64.1	122.4	35	13	Y
64.7	68.0	0	1	Y
64.8	35.9	91	3	N
65.1	92.8	90	3	Y
66.3	105.0	-104	3	Y
66.6	80.7	203	2	Y
66.8	61.4	48	2	Y
68.3	79.0	-75	8	Y
68.3	85.9	458	1	N
69.4	72.4	44	2	Y
69.5	81.1	242	2	Y
69.8	93.7	-395	9	N
71.5	142.8	-45	1	Y
71.6	55.4	53	2	Y
71.7	157.5	7	2	Y
71.8	103.4	71	2	Y
72.0	51.2	13	2	Y
73.5	27.1	2	4	Y
74.0	144.9	22	4	Y
74.2	34.8	8	2	Y
74.7	54.0	28	1	Y
74.8	159.7	0	3	Y
75.0	171.7	-7	2	Y
75.7	95.7	70	1	Y

continued on next page

continued from previous page

l_{J2000}	b_{J2000}	RM	δRM	Used
75.7	141.3	16	2	Y
75.8	86.8	272	4	Y
76.6	57.8	34	5	Y
76.7	64.7	-5	2	Y
78.3	81.0	458	4	N
79.0	111.8	38	3	Y
79.9	107.1	97	8	Y
80.2	133.4	0	3	Y
81.1	64.4	-232	5	Y
81.7	130.	6	1	Y
82.4	47.6	-268	4	Y
82.4	65.0	64	2	Y
83.0	142.5	95	14.4	N
85.4	97.2	-20	2	Y
86.9	149.1	5	4	Y
88.7	163.4	12	7	Y
89.2	32.0	10	10	Y
89.8	26.5	-27	7	Y
89.9	173.2	-4	0.3	Y
90.6	54.0	28	4	Y
92.5	125.4	18	7	Y
92.5	148.8	1	1	Y
94.2	163.0	26.2	1.2	Y
94.7	87.2	420	4	N
94.8	35.3	21	2	Y
95.2	151.3	4.8	0.8	Y
95.3	102.2	-89	2	Y
95.3	133.6	33	1	Y
95.4	86.1	99	3	Y
95.6	101.8	-37	3	Y
96.1	83.0	185	2	Y
97.5	135.4	-26	1	Y
98.2	164.5	-8	1	Y
100.1	19.5	9	2	Y
101.2	146.4	0	2	Y
101.8	157.4	12	1	Y
103.8	164.5	872	10	N
103.9	114.3	-105	4	Y
104.1	168.9	-27	12	Y
105.0	121.6	-63	2	Y

continued on next page

continued from previous page

l_{J2000}	b_{J2000}	RM	δRM	Used
105.7	118.0	-50	3	Y
106.4	62.8	19	2	Y
106.7	103.4	-12	3	Y
107.0	82.9	-14	2	Y
107.2	118.9	-25	4	Y
107.7	117.5	-42	4	Y
108.9	120.9	-4.3	3.8	Y
109.4	70.1	9	2	Y
109.8	141.7	-3	2	Y
110.0	154.4	2	0.2	Y
111.0	20.8	8	2	Y
113.2	150.0	-52	2	Y
113.4	169.1	-11	1	Y
115.0	18.2	-27	2	Y
115.9	131.0	-29	4	Y
116.2	83.7	-100	3	Y
116.9	106.5	175	5	N
117.5	50.0	36	3	Y
118.2	142.4	13	2	Y
118.4	127.5	-29	2	Y
118.6	148.0	-10	3	Y
120.2	42.0	18	2	Y
120.4	131.6	-81	27	Y
122.4	16.0	-9	2	Y
123.2	161.8	12	3	Y
124.1	140.3	-13	1	Y
124.5	56.1	26	2	Y
125.1	147.1	15	0.3	Y
125.5	168.6	-3	1	Y
126.0	165.5	18.5	0.6	Y
126.6	15.0	2	1	Y
127.0	91.2	185	1	Y
128.6	17.2	-17	4	Y
129.1	130.4	69	9	Y
129.5	109.4	-56	1	Y
130.1	142.8	169.4	5.9	N
130.2	57.2	20.8	2.4	Y
130.5	42.0	47	7	Y
130.8	70.2	38	1	Y
131.2	70.5	-122	11	Y

continued on next page

continued from previous page

l_{J2000}	b_{J2000}	RM	δRM	Used
132.3	8.5	3	6	Y
132.9	152.3	4	5	Y
133.0	67.0	7	2	Y
133.3	118.1	-30	1	Y
133.4	71.1	98	3	Y
133.5	118.1	-29	1	Y
134.0	34.9	18	1	Y
134.3	41.2	28	2	Y
134.4	70.0	49	4	Y
134.7	130.3	12	1	Y
135.6	95.4	-86	3	Y
136.2	109.2	-28	2	Y
137.3	100.8	-41	4	Y
137.7	151.2	11	0.4	Y
137.7	151.2	34.4	4.6	Y
139.2	171.6	4.1	2	Y
139.6	33.5	1	5	Y
140.4	159.1	-3	3	Y
141.0	149.6	0	2	Y
141.3	49.3	37	2	Y
141.4	107.3	116	8	N
141.4	113.0	-37	3	Y
142.8	81.5	52	4	Y
142.8	101.3	11	4	Y
143.2	144.6	-27	6	Y
144.3	132.4	-29	15	Y
145.3	82.8	-124	5	Y
145.3	82.8	247	17	Y
146.3	153.0	1	2	Y
146.7	121.2	-12	4	Y
147.3	32.0	24	3	Y
147.4	67.6	8	2	Y
148.0	162.5	0	1	Y
148.8	109.9	3	3	Y
149.0	137.7	2	2	Y
150.7	69.0	70	2	Y
151.7	74.4	-4	2	Y
153.5	95.3	39	2	Y
153.8	62.0	44	2	Y
153.8	73.0	-186	3	Y

continued on next page

continued from previous page

l_{J2000}	b_{J2000}	RM	δRM	Used
154.2	154.8	-2	3	Y
155.0	33.4	-3	4	Y
155.7	25.9	25	2	Y
155.8	62.0	50	4	Y
155.9	32.8	32	12	Y
156.1	52.7	15	7	Y
156.8	134.4	-15.9	0.7	Y
157.5	146.4	17	19	Y
159.5	36.9	138	5	N
159.8	168.5	2	2	Y
159.9	40.1	21.5	23.5	Y
160.0	51.3	55	4	Y
160.0	55.0	16	4	Y
160.1	111.6	53	5	Y
160.7	117.6	-20	2	Y
162.3	55.8	41	4	Y
162.7	44.7	-3	5	Y
162.8	58.6	-312	4	N
162.8	130.1	-7	2	Y
163.6	125.1	-19	3	Y
163.8	41.2	-62	7	Y
165.3	131.3	39	31	Y
165.8	21.3	30	6	Y
166.1	143.1	64	6	Y
166.2	107.2	-33	11	Y
167.2	160.2	-351	16	N
167.8	102.5	312	18	N
168.4	165.8	-15.2	2.3	Y
168.8	103.3	-48	1	Y
169.7	134.9	0	1	Y
170.2	22.0	43	3	Y
170.5	124.3	-182	14	Y
170.6	113.4	-22	7	Y
171.2	136.6	-7	1	Y
171.3	130.1	-15	1	Y
171.7	74.0	55	3	Y
172.2	63.4	138.2	10.3	Y
172.2	150.7	-42.5	0.8	Y
172.3	151.5	-36	1	Y
172.6	49.6	40	3	Y

continued on next page

continued from previous page

l_{J2000}	b_{J2000}	RM	δRM	Used
173.9	132.9	-25	1	Y
174.3	145.4	-54	30	Y
175.3	74.0	76	5	Y
175.6	28.0	15	2	Y
177.2	41.0	5	2	Y
177.6	104.7	-12	3	Y
178.0	154.0	-3	2	Y
178.3	78.2	160	11	Y
178.5	31.2	-304	8	N
179.6	161.8	6	4	Y
181.6	137.5	-75	3	Y
181.9	120.5	-3	1	Y
182.9	87.2	-390	6	N
183.3	111.1	-87	4	Y
185.1	61.6	-80	3	Y
185.8	148.2	18	4	Y
187.8	54.4	2	1	Y
188.7	94.9	139	3	Y
188.8	16.5	-90	10	Y
189.0	163.0	6.5	0.5	Y
189.2	141.8	15	5	Y
189.4	140.1	257	7	N
189.6	127.7	-23.2	0.6	Y
189.7	6.4	6.8	2.5	Y
190.7	157.6	-1.4	1.1	Y
190.8	130.9	10	1	Y
191.1	126.0	13	3	Y
191.4	144.6	6	3	Y
192.0	100.8	-56	1	Y
192.2	84.5	3	4	Y
192.4	93.8	129	2	Y
192.5	127.8	9	1	Y
192.9	77.2	145	30	Y
194.2	132.2	27.7	1.6	Y
195.6	102.3	55	1	Y
195.7	46.4	28	2	Y
197.8	50.4	13	2	Y
198.1	126.4	8.5	3.2	Y
198.1	157.7	-6	4	Y
198.3	54.7	-19	3	Y

continued on next page

continued from previous page

l_{J2000}	b_{J2000}	RM	δRM	Used
198.9	150.2	41	1	Y
199.5	157.5	-29	1	Y
200.1	107.9	62	6	Y
200.2	39.5	-39	4	Y
201.0	92.0	5	14	Y
201.2	109.6	38	1	Y
201.4	49.8	42	10	Y
201.6	103.0	301	6	N
201.7	58.0	-24	2	Y
202.5	171.0	-58	1	Y
203.0	118.9	21	4	Y
204.3	138.8	13	4	Y
204.4	72.2	-77	1	Y
205.0	78.7	-39	7	Y
205.4	99.8	61	3	Y
206.7	20.3	10	1	Y
207.1	54.0	-8	7	Y
207.2	179.3	6	2	Y
207.9	49.9	-22	2	Y
208.6	140.1	24	3	Y
208.7	101.0	-102	19	Y
209.1	61.8	-60	4	Y
209.1	179.4	-1	2	Y
209.4	90.0	51	4	Y
209.4	113.1	45	8	Y
209.5	73.4	30	1	Y
209.7	79.4	-54	3	Y
210.0	158.5	33	18	Y
211.6	134.5	-1	5	Y
212.8	100.6	-699	2	N
213.2	131.1	41	1	Y
213.3	138.2	24	2	Y
213.7	137.3	58	5	Y
213.9	139.5	14	0.4	Y
215.0	139.2	42	2	Y
215.3	125.8	-32	2	Y
216.0	41.0	12	5	Y
216.6	159.2	9	6	Y
216.7	38.8	-64	38	Y
217.2	143.8	12	1	Y

continued on next page

continued from previous page

l_{J2000}	b_{J2000}	RM	δRM	Used
217.7	105.2	-58	8	Y
218.4	46.7	21	2	Y
218.4	150.2	10	3	Y
218.6	175.6	-4	1	Y
218.9	75.8	257	2	N
219.3	78.0	-58	4	Y
219.4	148.3	-1	0.4	Y
220.2	37.6	1	2	Y
220.5	49.0	-1	1	Y
221.1	95.8	-840	2	N
221.3	130.9	24	1	Y
221.4	132.1	33	3	Y
221.6	177.3	3	1	Y
221.9	44.7	-1	1	Y
222.3	5.8	18	9	Y
222.3	77.7	-36	1	Y
223.7	31.9	-86	9	Y
224.0	151.0	-35	60	Y
224.0	168.5	-10.6	0.8	Y
224.6	63.2	-14.8	16.5	Y
225.4	94.2	274	2	Y
226.0	104.4	125	4	Y
226.2	130.3	34	1	Y
226.7	156.7	8	3	Y
226.8	132.3	18	0.3	Y
227.0	100.5	90	3	Y
227.3	177.1	13	9	Y
228.6	41.2	5	1	Y
229.1	144.9	21	3	Y
229.6	6.7	4	2	Y
229.8	177.2	18	9	Y
231.7	125.1	62	4	Y
232.4	53.5	10	8	Y
232.7	63.4	-11	21	Y
232.7	135.3	2	1	Y
232.8	75.0	-117	3	Y
233.8	68.0	-55	4	Y
234.6	166.1	-3	2	Y
234.6	178.2	-65	7	Y
235.2	38.3	-17	7	Y

continued on next page

continued from previous page

l_{J2000}	b_{J2000}	RM	δRM	Used
235.5	120.6	2	2	Y
236.5	170.7	-1	0.2	Y
237.0	49.1	1	6	Y
237.4	178.1	50	11	Y
238.1	178	-32	10	Y
239.0	41.2	-28	1	Y
239.0	43.4	-7	9	Y
239.0	178.2	47	7	Y
239.4	177.7	45	2	Y
239.9	148.3	10	2	Y
240.4	130.7	19	4	Y
241.1	132.3	28	3	Y
241.3	107.4	148.6	9.7	Y
241.9	43.3	12	2	Y
242.1	74.5	-91	6	Y
242.3	177.5	-37	10	Y
242.3	177.5	0	9	Y
242.4	43.7	483	3	N
242.4	88.9	555.4	1.9	N
242.7	98.5	60	1	Y
242.9	19.5	-5	5	Y
242.9	133.7	-85	9	Y
243.0	101.8	169	1	Y
243.0	129.0	14	4	Y
243.0	133.7	141	1	Y
243.0	177.5	-2	9	Y
243.4	54.0	-30	3	Y
243.4	83.9	1111	3	N
243.4	131.4	45	13	Y
243.5	130.9	22	0.2	Y
243.7	55.9	20.5	0.6	Y
243.7	87.7	-60	8	Y
244.4	79.2	-148	5	Y
245.5	18.1	-19.5	12.8	Y
245.5	134.3	35	3	Y
247.7	81.7	96	2	N
247.9	67.2	-124	4	Y
248.5	117.5	-23.9	4	Y
249.2	86.2	-222	2	Y
249.2	177.9	0	9	Y

continued on next page

continued from previous page

l_{J2000}	b_{J2000}	RM	δRM	Used
249.5	133.6	37	2	Y
249.8	52.4	-13	1	Y
250.9	60.5	-21	5	Y
250.9	61.6	-15	1	Y
251.8	126.2	8	2	Y
252.2	179.2	3	1	Y
253.0	128.2	12	2	Y
253.4	177.9	-55	9	Y
254.5	72.3	-73	1	Y
254.5	103.2	-89	5	Y
254.7	110.2	115.4	9.8	Y
255.1	55.9	-31	3	Y
255.1	178.0	-7	11	Y
255.3	104.0	-13	9	Y
255.3	104.5	-8	1	Y
255.6	103.5	9	6	Y
255.7	103.2	-199	8	Y
255.7	103.4	151	6	Y
255.7	103.5	90	5	Y
255.8	103.1	-9	4	Y
255.8	103.2	-56	3	Y
256.0	112.5	25	1	Y
256.3	103.6	-51	6	Y
256.6	65.2	-37	1	Y
257.2	113.5	15	3	Y
257.4	51.4	-53	0.4	Y
257.9	124.2	10	4	Y
259.5	178.0	10	2	Y
260.2	71.2	-53	0.4	Y
260.4	32.2	-25	2	Y
261.4	20.2	28	16	Y
261.6	48.7	-21	3	Y
262.8	48.1	28	4	Y
262.9	40.2	2.1	3.5	Y
263.0	38.7	-6	1	Y
263.2	60.0	-125	2	Y
263.9	50.8	-3	15	Y
264.3	49.3	7	6	Y
264.9	69.1	-125	1	Y
265.4	28.8	-25.8	1.7	Y

continued on next page

continued from previous page

l_{J2000}	b_{J2000}	RM	δRM	Used
265.7	127.9	-8.4	5.5	Y
265.7	127.9	21.5	0.8	Y
265.8	164.7	-62.8	3.2	Y
266.1	51.8	-57	0.2	Y
266.1	119.2	95	3	Y
266.2	43.6	-12	2	Y
267.4	54.4	-87	0.4	Y
267.9	138.4	-10	2	Y
268.1	141.0	7	3	Y
268.8	96.0	-258	1	Y
269.7	152.3	39	2	Y
270.3	98.2	440	16.5	N
270.5	91.3	-359	1	N
270.5	147.5	18	2	Y
271.6	121.3	28.4	0.5	Y
271.7	29.6	6	12	Y
271.7	59.0	-558	43	N
271.7	90.1	347	3	N
272.1	35.9	6	4	Y
272.6	79.6	-183	0.4	Y
273.1	42.9	-307	3	N
273.3	141.3	-11.1	0.7	Y
273.5	16.3	-4	5	Y
275.4	74.1	-162	1	Y
276.3	134.1	-9	2	Y
276.8	70.5	-231	3	Y
277.3	2.0	92	5	N
277.5	39.9	1	1	Y
277.5	150.8	2250	35	N
277.7	55.3	-60	6	Y
278.1	72.9	-275	1	Y
278.8	130.7	13	2	Y
279.3	29.1	12	3	Y
279.7	58.7	-269	1	Y
279.7	58.8	-254	3	Y
279.7	98.0	-166	4	Y
280.1	119.2	13	4	Y
280.3	99.4	-208	2	Y
280.5	120.7	8	13	Y
281.0	58.0	42.1	4.5	Y

continued on next page

continued from previous page

l_{J2000}	b_{J2000}	RM	δRM	Used
282.1	60.1	-76.6	3.7	Y
282.8	48.3	-55	6	Y
283.2	29.5	-11	2	Y
283.2	139.1	37	4	Y
283.4	163.4	-17	3	Y
283.5	57.0	102	1	Y
283.9	43.9	-22	1	Y
284.9	95.8	-378	2	N
284.9	151.4	22.4	10.2	Y
285.3	117.8	-36	3	Y
285.6	117.9	-30	3	Y
285.7	41.5	-17	2	Y
287.4	41.1	-4	2	Y
288.3	132.2	13.9	7.7	Y
290.0	132.1	63	2	Y
290.6	94.7	9	8	Y
291.0	109.3	19	17	Y
291.4	117.1	-5	1	Y
291.8	145.7	4	7	Y
292.0	43.5	-22	1	Y
293.0	72.2	-20	2	Y
293.6	100.9	-49	2	Y
293.7	78.0	-182	29	Y
294.8	26.2	-12	2	Y
294.9	128.3	-57	10	Y
295.2	25.2	10	3	Y
295.2	128.3	-24	13	Y
295.3	166.8	-24	4	Y
295.7	50.2	-57.1	8.9	Y
296.5	92.6	17	8	Y
296.8	25.5	-24	8	Y
297.0	30.6	-18	2	Y
297.2	33.9	-18	1	Y
297.9	45.9	44	12	Y
298.6	37.3	13	4	Y
299.0	51.3	-1	5	Y
299.3	66.7	-92	9	Y
300.2	159.8	-17	1	Y
300.4	60.3	4	54	Y
300.4	107.3	9.9	3.5	Y

continued on next page

continued from previous page

l_{J2000}	b_{J2000}	RM	δRM	Used
300.6	91.2	409	2	N
301.0	86.1	278	8	N
301.6	79.2	159	2	Y
302.3	17.6	-5	5	Y
302.8	156.6	-12	9	Y
302.9	78.3	-82	2	Y
303.4	95.5	-91	1	Y
304.2	53.5	106	3	N
304.3	100.4	-15	3	Y
304.5	96.6	11	9	Y
306.1	53.1	-34	4	Y
306.4	76.7	-354	6	N
306.5	25.8	1	1	Y
306.9	59.6	-60	2	Y
306.9	176.8	7.2	4.2	Y
307.1	27.3	-1.2	3.3	Y
307.6	59.1	-66	5	Y
308.1	133.6	8	3	Y
309.4	40.7	-12	1	Y
310.4	128.5	-29	1	Y
310.7	93.1	428	1.3	N
310.9	142.2	86	11	Y
311.4	60.9	-66	1	Y
311.5	81.6	-58	3	Y
311.8	29.0	-11	1	Y
312.1	96.2	-36	1	Y
312.4	26.8	8	6	Y
312.4	65.9	-87	1	Y
312.6	56.9	-47	1	Y
312.7	174.9	11	9	Y
313.6	118.9	-14	8	Y
314.0	61.3	-67	7	Y
314.2	51.6	-65	3	Y
314.2	139.7	6	4	Y
314.4	47.1	-55	2	Y
314.5	36.2	-344	17	N
315.0	72.4	-75	3	Y
315.3	14.9	3	2	Y
316.1	30.8	9	11	Y
316.2	89.1	-180	2	Y

continued on next page

continued from previous page

l_{J2000}	b_{J2000}	RM	δRM	Used
316.5	26.3	-13	6	Y
316.8	49.3	-23	1	Y
317.1	31.7	-5	13	Y
317.2	62.7	-31.2	3.3	Y
317.3	38.4	-4	6	Y
318.9	66.2	-2.5	5.6	Y
319.9	58.2	-94	3	Y
320.0	117.3	-29	4	Y
320.2	73.2	-67	3	Y
320.5	34.9	6	2	Y
320.8	164.1	-3	3	Y
321.2	28.2	16	3	Y
321.4	130.6	-225	5	Y
321.5	70.5	-81	2	Y
322.2	27.1	54	7	N
322.3	23.9	-3	1	Y
323.3	11.7	2	3	Y
323.5	124.4	-11	7	Y
323.9	89.0	-130	3	Y
325.1	119.4	10	3	Y
325.4	116.1	86	4	Y
325.6	66.0	-63	2	Y
326.8	59.3	-64	1	Y
326.8	69.2	-81	8	Y
327.0	76.6	612	3	N
327.3	63.6	16	3	Y
327.5	161.4	-1	1	Y
327.8	86.0	-136	1	Y
328.0	118.4	-20	5	Y
329.7	42.5	-21	4.4	Y
330.1	77.0	18	1	Y
330.3	125.5	184.4	6.1	Y
330.6	62.7	-60	5	Y
331.0	140.7	-4	2	Y
334.1	70.7	29	3	Y
334.2	13.6	3	3	Y
334.3	43.5	-6	3	Y
335.4	95.1	17	6	Y
336.6	45.0	5.4	3.8	Y
336.8	50.9	81.2	5.8	Y

continued on next page

continued from previous page

l_{J2000}	b_{J2000}	RM	δRM	Used
336.8	83.4	-42	1	Y
337.5	15.6	9	8	Y
337.8	41.8	-11	2	Y
338.6	137.9	1	1	Y
338.8	97.8	-3	2	Y
339.0	71.2	58	1	Y
339.3	126.9	-15	1	Y
341.0	85.7	45	3	Y
341.7	81.2	-19	2	Y
341.7	100.3	-1510	50	N
342.1	144.4	-11.7	3.6	Y
342.2	112.2	53	2	Y
342.9	64.4	72	47	Y
343.1	54.0	-18	0.3	Y
343.3	44.6	-6	3	Y
344.1	55.5	-19	0.4	Y
344.1	86.3	512	5	N
344.5	107.4	11	3	Y
345.4	103.4	34	3	Y
345.8	69.0	49	1	Y
346.3	170.6	0	0.4	Y
346.6	56.4	246	6	N
347.1	33.0	4	2	Y
347.1	34.8	6	3	Y
347.6	88.1	-21	3	Y
347.6	129.1	0.6	5	Y
348.1	14.0	-7	3	Y
348.1	70.3	42	2	Y
349.6	22.6	11	2	Y
350.3	45.1	-125	10	Y
350.5	143.2	18.5	11.5	Y
350.6	53.8	-15	2	Y
350.6	78.3	-324	14	N
350.7	152.3	19	1	Y
351.1	107.9	30	7	Y
351.2	123.2	-142	5	Y
351.2	123.2	116.8	0.8	Y
351.4	82.2	330	3	N
351.7	170.6	-11.8	2.4	Y
351.9	33.1	157	18	Y

continued on next page

continued from previous page				
l_{J2000}	b_{J2000}	RM	δRM	Used
351.9	70.0	-4	4	Y
352.1	38.1	136.7	7.3	Y
352.5	35.2	12	3	Y
352.6	155.9	-18	3	Y
352.7	124.5	-5	2	Y
353.1	22.7	6	1	Y
353.2	56.7	-2	5	Y
353.9	169.9	4.1	8.4	Y
354.4	34.0	5	1	Y
354.4	134.8	-19	2	Y
354.5	88.7	-1	3	Y
354.9	45.5	14	2	Y
357.0	49.2	145	6	Y
357.3	67.8	-2	3	Y
358.1	41.5	41	1	Y
358.1	85.7	72	4	Y
358.3	132.9	-170	6	Y
358.5	79.5	-22	1	Y
358.9	77.5	-38	1	Y
359.0	108.3	-11	6	Y
359.0	114.0	13	18	Y
359.3	34.0	8	2	Y
359.3	64.3	-55	4	Y
359.7	82.3	-172	2	Y
359.8	59.0	79	1	Y

B.2 Two Dimensional Solutions to Poisson's Equation

A common application of interative methods is the numerical solution of a particular equation to give the value of some measurable in regions were no data is present.

If we consider a two dimensional function $z = f(x, y)$ then when know from calculus that the partial derivatives of the function will describe a curved surface in the xy-plane with a height z at every point (Kreyzig 1994). In situations where data is only given for some points in the xy-plane it is still possible to extrapolate the value of those points to regions where there is not measured data. One such method is the two dimensional solutions to Poisson's equations.

Traditionally Poisson's equation is of the form:

$$\nabla^2 V = -\rho/\epsilon$$

where V is the electric potential and ρ/ϵ is the charge density. Now

$$\nabla^2 V = \frac{\delta^2 V}{\delta x^2} + \frac{\delta^2 V}{\delta y^2} + \frac{\delta^2 V}{\delta z^2}$$

A finite difference solution of the two dimensional Laplace equation ($\nabla^2 V = 0$) can be found in the following manner. Let h represent a small distance from any point (x,y). Then by Taylor series expansion

$$V(x+h,y) = V(x,y) + \frac{h\delta V(x,y)}{\delta x} + \frac{h^2}{2}\frac{\delta^2 V(x,y)}{\delta x^2} + ...$$
$$V(x-h,y) = V(x,y) - \frac{h\delta V(x,y)}{\delta x} + \frac{h^2}{2}\frac{\delta^2 V(x,y)}{\delta x^2} + ...$$

Combining these equations gives

$$\frac{\delta^2 V(x,y)}{\delta x^2} = \frac{V(x+h,y) - 2V(x,y) + V(x-h,y)}{h^2}$$

Similarly the second partial derivative with respect to y can be found. Substituting these partial difference approximations into Laplace's equation gives

$$V(x+h,y) + V(x-h,y) + V(x,y+h) + V(x,y-h) - V(x,y) = 0$$

Now solving for V(x,y) we obtain

$$V(x,y) = \frac{V(x+h,y) + V(x-h,y) + V(x,y+h) + V(x,y-h)}{4} \qquad \text{(B.1)}$$

Solving this on a grid of points with one spacing equal to h says that the function, in this case the potential, is the average of the four points surrounding it, which are in turn the average of the four points surrounding them and so on. Thus, the function can be determined across the entire xy-plane by inserting values where there are measured quantities and then iteratively applying equation B.1 until an unchanging set of values is obtained. Thus, for ever grid point, V_{k+1}(x,y) we have

$$V_{k+1}(x,y) = \frac{V_k(x+1,y) + V_k(x-1,y) + V_k(x,y+1) + V_k(x,y-1)}{4} \qquad \text{(B.2)}$$

The method of succesive approximations used above can be improved by a simple change which causes it to converge more rapidly. This difference is effected by calculating the difference between the current grid point, V_k(x,y), and the average of the four surrounding cells at each iteration. This quantity is multiplied by a number called a relaxation constant, β, which is usually between 1 and 2 and is added to the existing grid potential as shown below:

$$V_{k+1}(x,y) = V_k(x+,y) + \beta(\Sigma_k/4 - V_k) \tag{B.3}$$

The rate of convergence can be increased by choosing a suitable value for the relaxation constant. The optimum value of β varies according to the problem being solved. In the case of the interpolated RM map, the voltage term in the above equation was replaced by a rotation measure value and the co-ordinate system converted into spherical polar co-ordinates. This gave the interpolated RM map seen in Chapter 4.

Appendix C

2dF Redshift Information

C.1 Redshift Data for A3667

Table C.1: 2dF redshift data for A3667: col 1 is the J2000 right accension; col 2 is the J2000 declination; col 3 is the magnitude; col 4 is the absorption derived redshift; col 5 is the emission derived redshift; col 6 is the average redshift between emission and absorption spectral fits and col 7 is the software derived spectral quality, being a number from 1 - 4, 4 being the best quality.

2Df data for A3667						
RA_{J2000}	Dec_{J2000}	Mag	z_{ab}	z_{em}	z_{ave}	Q
20 5 37.49	-56 41 6.1	16.89	0.0558			4
20 6 26.98	-56 19 50.9	18.16	0.0586			1
20 7 22.03	-56 39 44.0	16.41	0.0535			4
20 7 29.09	-57 28 46.2	18.09	0.0553	0.0553	0.0553	4
20 7 30.08	-57 22 58.6	16.75	0.0521	0.0518	0.05195	4
20 7 32.50	-56 34 45.9	17.43	0.0560	0.0557	0.05585	4
20 7 56.06	-56 16 1.3	16.65	0.0543	0.0545	0.0544	4
20 8 1.56	-56 6 7.6	17.60	0.0594	0.0594	0.0594	4
20 8 9.17	-56 30 21.7	16.80	0.0523			4
20 8 27.61	-56 20 42.5	17.79	0.0572	0.0569	0.05705	4
20 8 28.97	-56 43 12.2	16.63	0.0487	0.0486	0.04865	4
20 8 30.27	-56 39 16.7	17.21	0.0592			4
20 8 35.33	-57 3 56.3	18.04	0.0623			4
20 8 39.10	-56 56 24.8	16.90	0.0532			4
20 8 41.88	-56 47 16.4	17.91	0.0526	0.0520	0.0523	4
20 8 52.33	-56 28 5.3	18.22	0.0624	0.0618	0.0621	4
20 8 53.06	-56 45 16.8	18.05	0.0538	0.0542	0.054	4
20 8 56.81	-56 57 4.8	17.72	0.0577			1
20 9 12.53	-56 30 58.5	16.97	0.0580			4

continued on next page

continued from previous page

RA_{J2000}	Dec_{J2000}	Mag	z_{ab}	z_{em}	z_{ave}	Q
20 9 12.93	-56 37 36.0	17.99	0.0549	0.0549	0.0549	4
20 9 15.35	-56 44 12.4	17.88	0.0490	0.0487	0.04885	4
20 9 19.68	-56 46 30.9	17.86	0.0540	0.0537	0.05385	4
20 9 49.45	-56 4 58.6	17.68	0.0621	0.0618	0.06195	4
20 9 52.60	-56 14 13.3	17.73	0.0563			4
20 9 58.26	-56 30 32.2	17.96	0.0602			1
20 9 59.72	-56 27 57.8	17.74	0.0538			1
20 10 3.67	-56 22 7.9	17.67	0.0570			4
20 10 7.63	-56 42 25.4	18.11	0.0580			4
20 10 8.24	-56 39 40.6	16.82	0.0552			4
20 10 10.62	-56 31 36.0	17.67	0.0607			1
20 10 16.06	-56 38 30.4	17.63	0.0524	0.0527	0.05255	3
20 10 16.30	-56 45 10.6	17.54	0.0543			1
20 10 16.79	-56 13 46.2	17.06	0.0519	0.0522	0.05205	4
20 10 26.49	-56 26 55.0	18.20	0.0530			1
20 10 27.50	-56 17 48.4	16.05	0.0522			4
20 10 36.28	-56 52 9.0	17.97	0.0590			3
20 10 40.25	-57 2 40.8	16.95	0.0530			4
20 10 42.90	-56 21 54.8	16.71	0.0529			4
20 10 44.78	-56 45 22.7	18.22	0.0545			4
20 10 46.27	-56 13 38.0	18.07	0.0616	0.0615	0.06155	4
20 10 46.88	-56 58 9.3	18.05	0.0594			1
20 10 47.57	-57 19 53.4	17.26	0.0533			1
20 10 49.20	-56 41 52.5	17.42	0.0513			4
20 10 50.14	-57 18 24.5	17.06	0.0557			1
20 10 50.46	-56 32 59.5	16.66	0.0536	0.0533	0.05345	4
20 10 53.26	-56 50 21.4	16.96	0.0647			4
20 10 54.38	-56 29 54.3	17.39	0.0568			4
20 10 54.66	-56 23 28.4	16.07	0.0503	0.0533	0.0518	4
20 10 57.64	-56 38 38.4	16.71	0.0591			4
20 10 58.91	-56 39 54.5	16.75	0.0601			4
20 11 0.43	-56 45 55.5	15.64	0.0594			4
20 11 2.71	-56 19 22.7	17.14	0.0588	0.0587	0.05875	4
20 11 4.80	-56 31 47.4	17.55	0.0544			1
20 11 6.77	-56 23 23.0	16.39	0.0578			4
20 11 14.06	-56 57 23.5	17.39	0.062			4
20 11 17.20	-56 56 18.1	16.37	0.0608			4
20 11 27.50	-56 44 7.0	16.14	0.0549			4
20 11 30.17	-56 56 16.0	18.27	0.0601			1
20 11 34.74	-56 44 38.2	17.55	0.0465			4

continued on next page

continued from previous page

RA_{J2000}	Dec_{J2000}	Mag	z_{ab}	z_{em}	z_{ave}	Q
20 11 36.15	-56 55 29.8	16.33	0.0622	0.0618	0.0620	4
20 11 36.27	-56 28 56.2	16.92	0.0561			4
20 11 37.82	-56 20 39.6	16.96	0.0556			4
20 11 38.04	-57 2 58.0	16.97	0.0511	0.1584	0.10475	4
20 11 39.57	-56 42 3.5	17.89	0.0556			4
20 11 42.86	-57 3 28.5	16.94	0.0552	0.0545	0.05485	4
20 11 50.63	-57 0 27.4	17.17	0.0541			1
20 11 54.80	-56 55 58.3	17.76	0.0490			2
20 11 58.32	-57 5 12.3	16.00	0.0547	0.0547	0.0547	4
20 11 58.60	-56 30 47.7	16.40	0.0509			4
20 12 0.79	-57 1 20.5	16.57	0.0503			4
20 12 1.27	-56 33 37.0	17.84	0.0569			4
20 12 3.53	-56 13 22.0	16.52	0.0511			4
20 12 4.22	-56 39 38.4	17.75	0.0595			4
20 12 11.60	-56 51 1.2	17.57	0.0506			4
20 12 13.07	-56 14 54.3	17.65	0.0516	0.0516	0.0516	4
20 12 14.92	-56 35 58.8	17.58	0.0564	0.0563	0.05635	4
20 12 15.02	-56 38 18.7	17.43	0.0562			1
20 12 16.52	-56 58 2.9	16.90	0.0551			4
20 12 16.54	-57 9 37.7	17.51	0.0567			4
20 12 18.73	-56 23 54.1	17.91	0.0543			4
20 12 21.24	-56 15 29.6	17.56	0.0517			4
20 12 32.59	-56 31 37.9	17.24	0.0549	0.0549	0.0549	4
20 12 32.99	-56 30 50.7	16.77	0.0578			4
20 12 34.80	-57 39 46.3	17.15	0.0573			4
20 12 38.65	-57 12 4.2	16.78	0.0585			1
20 12 40.95	-56 29 0.2	17.73	0.0555			1
20 12 41.76	-56 45 59.1	18.21	0.0618			4
20 12 46.03	-57 18 12.2	16.84	0.0566			4
20 12 52.21	-57 15 26.0	17.77	0.0534			1
20 12 58.79	-56 59 11.4	16.64	0.0533			4
20 13 5.50	-57 10 43.5	17.28	0.0577	0.0573	0.0575	4
20 13 27.61	-57 7 17.9	16.73	0.0532			1
20 13 30.96	-56 57 48.8	17.23	0.0540			4
20 13 31.55	-56 53 39.2	16.97	0.0466			4
20 13 34.96	-57 5 32.1	18.21	0.0542			3
20 13 40.23	-56 54 37.0	17.80	0.0542			4
20 13 44.76	-57 21 0.1	16.99	0.0565	0.0564	0.05645	4
20 13 46.06	-56 47 33.2	17.70	0.0545			4
20 13 52.67	-56 32 47.0	16.68	0.0607			4

continued on next page

continued from previous page

RA_{J2000}	Dec_{J2000}	Mag	z_{ab}	z_{em}	z_{ave}	Q
20 13 58.67	-57 2 22.6	15.50	0.0523			4
20 13 59.05	-56 57 42.0	16.20	0.0601	0.0596	0.05985	4
20 13 59.63	-56 33 3.2	17.82	0.0574	0.0574	0.0574	4
20 14 5.27	-57 29 58.0	17.76	0.0549			4
20 14 5.80	-57 0 28.0	17.10	0.0515			1
20 14 6.30	-57 7 28.7	17.35	0.0586			4
20 14 8.03	-55 52 54.4	18.30	0.0595			4
20 14 8.66	-56 23 5.6	17.40	0.0569	0.0565	0.0567	4
20 14 10.50	-56 57 49.8	17.39	0.0536			4
20 14 13.40	-57 19 2.9	17.18	0.0564	0.0564	0.0564	4
20 14 16.57	-56 35 30.2	17.74	0.0563			4
20 14 17.45	-57 8 25.0	17.85	0.0527			1
20 14 33.61	-57 28 33.0	17.39	0.0549			1
20 14 34.07	-57 16 24.7	17.32	0.0554			4
20 14 35.26	-57 21 58.4	18.12	0.0553			4
20 14 41.50	-56 52 56.0	17.74	0.0543			4
20 14 44.86	-56 45 24.0	17.33	0.0572			4
20 14 47.97	-57 18 58.7	17.60	0.0548	0.0547	0.05475	4
20 14 51.94	-57 26 0.9	16.63	0.0559			4
20 14 55.39	-57 12 33.5	17.87	0.0567			4
20 14 56.07	-56 45 22.0	16.54	0.0536			4
20 15 9.28	-57 10 31.6	16.40	0.0568			4
20 15 30.53	-56 29 47.2	17.78	0.0571			4
20 15 34.69	-57 18 38.7	17.41	0.0526			1
20 15 42.55	-57 15 59.9	17.40	0.0556			4
20 15 43.65	-57 40 4.6	18.23	0.0512			4
20 15 45.89	-56 58 26.7	18.28	0.0549			1
20 15 47.00	-57 19 56.1	16.71	0.0563			4
20 15 56.67	-57 34 50.1	16.86	0.0569			1
20 15 58.12	-57 23 55.2	17.73	0.0569			4
20 16 3.58	-57 3 39.1	17.37	0.0559			4
20 16 4.41	-56 2 35.4	17.57	0.0590	0.0587	0.05885	4
20 16 6.79	-56 52 9.8	17.42	0.0622			1
20 16 9.80	-57 12 39.0	18.00	0.0551			3
20 16 12.81	-56 22 46.7	17.58	0.0562			1
20 16 22.69	-56 51 45.5	16.71	0.0543			4
20 16 44.88	-57 33 14.9	16.01	0.0642			4
20 16 48.39	-57 11 41.2	15.87	0.0557			4
20 16 59.45	-57 14 45.0	17.39	0.0572			4
20 17 25.75	-57 21 57.9	17.60	0.0563	0.0562	0.05625	4

continued on next page

continued from previous page						
RA_{J2000}	Dec_{J2000}	Mag	z_{ab}	z_{em}	z_{ave}	Q
20 17 52.66	-56 43 33.7	17.65	0.0629	0.0631	0.0630	3
20 18 21.40	-56 25 14.5	18.01	0.0598			3
20 18 52.66	-57 0 21.9	17.42	0.0569			4
20 19 35.34	-56 47 49.4	17.69	0.0553			4

Table C.2: Published redshift data for A3667: col 1 is the J2000 right accension; col 2 is the J2000 declination; col 3 is the velocity; col 4 is the redshift and col 5 is the reference number, here 1 correponds to data from (Sodre et al. 1992) and 2 is data from (Proust et al. 1988). It should be noted that although the velocities are quoted to five significant figures they are only measured with an accuracy of three, thus the redshift values have all been rounded to reflect this.

previously published redshift data for A3667				
RA_{J2000}	$De_{J2000}c$	Velocity	z	ref
20 7 55.8	-56 26 51	14334	0.0478	1
20 7 55.8	-56 15 58	16025	0.0535	1
20 8 9.2	-56 30 22	15706	0.0524	1
20 8 10.3	-56 26 14	15104	0.0504	1
20 8 15.7	-57 1 11	18558	0.0619	1
20 8 25.1	-56 39 23	15456	0.0516	1
20 8 28.6	-56 43 9	15065	0.0503	1
20 8 30.4	-56 39 17	17835	0.0595	1
20 8 38.5	-56 56 23	15960	0.0532	1
20 8 45.7	-56 15 14	18327	0.0611	1
20 9 12.6	-56 30 59	17364	0.0579	1
20 9 19.1	-56 18 5	16610	0.0554	1
20 9 34.1	-56 27 53	18105	0.0604	1
20 9 46.3	-56 21 39	15763	0.0526	1
20 9 51.2	-56 42 22	18215	0.0608	1
20 9 59.8	-56 27 58	16075	0.0536	1
20 10 0.3	-56 56 15	18573	0.0620	1
20 10 1.9	-56 19 14	15250	0.0509	1
20 10 3.4	-56 41 51	18692	0.0624	1
20 10 8.3	-56 39 41	16561	0.0552	1
20 10 10.4	-56 31 35	18146	0.0605	1
20 10 11.0	-56 36 3	17241	0.0575	1
20 10 19.3	-56 30 11	17727	0.0591	1
20 10 19.6	-56 44 46	16921	0.0564	1
20 10 20.7	-56 12 7	15778	0.0526	1
20 10 21.6	-56 27 57	17268	0.0576	1
20 10 26.2	-57 5 29	15940	0.0532	1

continued on next page

continued from previous page

RA_{J2000}	Dec_{J2000}	Velocity	z	ref
20 10 27.6	-56 17 48	15640	0.0522	1
20 10 31.7	-57 2 4	16662	0.0556	1
20 10 32.6	-56 21 48	16462	0.0549	1
20 10 39.9	-57 2 40	15812	0.0527	1
20 10 43	-56 21 55	15817	0.0528	1
20 10 46.8	-56 31 57	14138	0.0472	1
20 10 47.4	-56 41 2	14984	0.0500	1
20 10 49.3	-56 41 53	15361	0.0512	1
20 10 50.5	-56 33 0	15897	0.0530	1
20 10 50.7	-56 40 24	16842	0.0562	1
20 10 51.5	-56 41 2	17145	0.0572	1
20 10 53.3	-56 26 1	16069	0.0536	1
20 10 53.4	-56 50 21	19340	0.0645	1
20 10 54.4	-56 29 54	17031	0.0568	1
20 10 54.7	-56 23 25	15060	0.0502	1
20 10 57.6	-56 38 36	17605	0.0587	1
20 10 59.0	-56 39 55	18320	0.0611	1
20 10 59.8	-56 42 52	14408	0.0481	1
20 11 0.5	-56 45 56	17868	0.0596	1
20 11 6.8	-56 23 20	17650	0.0589	1
20 11 8.3	-57 0 20	15927	0.0531	1
20 11 8.7	-56 41 58	16125	0.0538	1
20 11 13.7	-56 57 23	18940	0.0632	1
20 11 17.3	-56 56 19	18254	0.0609	1
20 11 19.4	-56 21 59	16430	0.0548	2
20 11 20.9	-56 42 3	16893	0.0563	1
20 11 24.8	-56 41 5	15960	0.0532	1
20 11 25.5	-56 33 50	17331	0.0578	1
20 11 27.5	-56 44 8	16543	0.0552	1
20 11 28.6	-56 45 17	17403	0.0581	1
20 11 34.8	-56 44 39	13940	0.0465	1
20 11 36.2	-56 50 31	16764	0.0559	1
20 11 36.3	-56 55 30	18597	0.0620	1
20 11 36.3	-56 28 56	16989	0.0567	1
20 11 36.6	-56 20 28	16749	0.0559	1
20 11 37.9	-56 20 37	16794	0.0560	1
20 11 38.1	-57 2 58	15230	0.0508	1
20 11 43.0	-57 3 29	16411	0.0547	1
20 11 50.3	-57 14 49	16300	0.0544	1
20 11 50.7	-57 0 27	16306	0.0544	1

continued on next page

continued from previous page

RA_{J2000}	Dec_{J2000}	Velocity	z	ref
20 11 58.4	-57 5 12	16361	0.0546	2
20 11 58.7	-56 30 45	15117	0.0504	1
20 11 59.2	-56 45 37	18965	0.0633	1
20 12 0.7	-57 1 20	18050	0.0602	1
20 12 3.7	-56 13 19	15210	0.0507	1
20 12 4.3	-56 39 39	17850	0.0595	1
20 12 6.8	-56 31 38	15030	0.0501	1
20 12 11.6	-56 51 0	15217	0.0508	1
20 12 12.1	-56 48 42	18120	0.0604	1
20 12 15.1	-57 6 42	17244	0.0575	1
20 12 16.3	-57 4 59	16015	0.0534	1
20 12 16.4	-56 58 2	17328	0.0578	1
20 12 18.2	-56 41 48	16800	0.0560	1
20 12 20.9	-56 42 33	17550	0.0585	1
20 12 21.4	-56 15 27	15395	0.0514	1
20 12 21.6	-56 47 55	15790	0.0527	1
20 12 22.0	-56 48 10	16566	0.0553	1
20 12 22.9	-56 50 24	14703	0.0490	1
20 12 23.4	-56 50 18	14878	0.0496	1
20 12 25.7	-56 47 52	17472	0.0583	1
20 12 27.4	-56 49 37	16725	0.0558	1
20 12 29.5	-56 47 59	14669	0.0489	1
20 12 30.1	-56 49 0	16668	0.0556	1
20 12 30.5	-56 47 56	14624	0.0488	1
20 12 30.7	-56 49 36	16396	0.0547	1
20 12 32.7	-56 31 36	16252	0.0542	1
20 12 33.1	-56 42 51	15665	0.0523	1
20 12 33.2	-56 30 48	17410	0.0581	1
20 12 38.7	-57 12 4	17607	0.0587	1
20 12 40.7	-56 49 48	17094	0.0570	1
20 12 40.9	-56 28 59	16740	0.0558	1
20 12 42.2	-57 0 56	16463	0.0549	1
20 12 46.1	-57 18 12	16899	0.0564	1
20 12 46.6	-56 51 28	16850	0.0562	1
20 12 53.4	-57 20 15	16732	0.0558	1
20 12 55.0	-56 53 12	17464	0.0583	1
20 12 58.9	-56 59 11	16015	0.0534	1
20 13 2.0	-56 56 54	15838	0.0528	1
20 13 3.4	-57 11 21	16480	0.0550	1
20 13 5.3	-57 0 28	16630	0.0555	1

continued on next page

continued from previous page

RA_{J2000}	Dec_{J2000}	Velocity	z	ref
20 13 5.3	-56 52 30	18956	0.0632	1
20 13 5.6	-57 10 44	17206	0.0574	1
20 13 8.0	-56 48 30	18045	0.0602	1
20 13 17.0	-56 53 18	16024	0.0535	1
20 13 22.8	-56 49 56	15854	0.0529	1
20 13 26.4	-56 41 43	17418	0.0581	1
20 13 27.7	-57 7 18	15967	0.0533	1
20 13 31.1	-56 57 49	15954	0.0532	1
20 13 31.6	-56 53 39	13955	0.0465	1
20 13 44.9	-57 21 0	17001	0.0567	1
20 13 45.3	-56 37 11	16625	0.0555	1
20 13 53.1	-56 32 45	18223	0.0608	1
20 13 53.1	-57 14 13	17040	0.0568	1
20 13 58.3	-56 54 51	16363	0.0546	1
20 13 58.7	-57 2 23	15709	0.0524	1
20 13 59.3	-56 57 42	13260	0.0442	1
20 13 59.7	-56 59 56	16066	0.0536	1
20 14 0.8	-56 52 49	13370	0.0446	2
20 14 1.3	-56 51 39	17245	0.0575	1
20 14 1.7	-56 58 10	16633	0.0555	1
20 14 1.7	-57 1 41	17244	0.0575	2
20 14 3.0	-57 5 49	15579	0.0520	1
20 14 4.8	-57 5 14	15107	0.0504	1
20 14 5.9	-57 0 28	15484	0.0516	1
20 14 6.6	-57 7 29	15510	0.0517	1
20 14 8.4	-57 21 10	16078	0.0536	1
20 14 10.6	-56 57 50	16114	0.0538	1
20 14 13.8	-57 19 3	16831	0.0561	1
20 14 17.8	-57 8 25	16390	0.0547	1
20 14 23.9	-56 56 51	18234	0.0608	1
20 14 34.1	-57 16 25	16642	0.0555	1
20 14 56.7	-56 45 22	16244	0.0542	1
20 14 57.0	-57 24 9	16827	0.0561	1
20 14 59.8	-56 57 29	13260	0.0442	2
20 15 7.6	-56 49 17	17673	0.0590	1
20 15 8.2	-57 3 12	15847	0.0529	1
20 15 9.4	-57 10 32	17091	0.0570	1
20 15 14.0	-57 11 3	17225	0.0575	1
20 15 18.2	-56 57 36	15213	0.0507	1
20 15 31.6	-57 17 51	16270	0.0543	1

continued on next page

continued from previous page

RA_{J2000}	Dec_{J2000}	Velocity	z	ref
20 15 36.8	-57 18 45	16624	0.0555	1
20 15 42.6	-57 16 0	16717	0.0558	1
20 15 47.1	-57 19 56	16884	0.0563	1
20 16 4.5	-57 3 39	16982	0.0566	1
20 16 23.7	-56 51 45	16159	0.0539	1
20 16 49.7	-57 11 43	16695	0.0557	1
20 16 59.1	-57 14 46	17207	0.0574	1
20 16 59.4	-56 59 57	18416	0.0614	1

Table C.3: Comparison of 2dF and literature redshifts for A3667. Col 1 is the J2000 right accension given by SuperCOSMOS; col 2 is the J2000 declination given by SuperCOSMOS; col 3 is the magnitude; col 4 is the 2Df redsift; col 5 is the published redshift; col 6 is the difference between the 2dF and published redshift and col7 is the 2dF software spectral fit quality, being a number between 1 and 4, 4 being a the best quality.

A3667: Redshift dataset comparison						
RA_{J2000}	Dec_{J2000}	Mag	z_{2Df}	z_{lit}	δ_z	Q
20 7 56.06	-56 16 1.3	16.65	0.0543	0.0535	0.0008	4
20 8 9.17	-56 30 21.7	16.80	0.0523	0.0524	0.0001	4
20 8 28.97	-56 43 12.2	16.63	0.0487	0.0503	0.0016	4
20 8 30.27	-56 39 16.7	17.21	0.0592	0.0595	0.0003	4
20 8 39.10	-56 56 24.8	16.90	0.0532	0.0532	0	4
20 9 12.53	-56 30 58.5	16.97	0.0580	0.0579	0.0001	4
20 9 59.72	-56 27 57.8	17.74	0.0538	0.0536	0.0002	4
20 10 8.24	-56 39 40.6	16.82	0.0552	0.0552	0	4
20 10 10.62	-56 31 36.0	17.67	0.0607	0.0605	0.0002	4
20 10 27.50	-56 17 48.4	16.05	0.0522	0.0522	0	4
20 10 40.25	-57 2 40.8	16.95	0.0530	0.0527	0.0003	1
20 10 42.90	-56 21 54.8	16.71	0.0529	0.0528	0.0001	4
20 10 49.20	-56 41 52.5	17.42	0.0513	0.0512	0.0001	4
20 10 50.46	-56 32 59.5	16.66	0.0536	0.0542	0.0006	4
20 10 53.26	-56 50 21.4	16.96	0.0647	0.0645	0.0002	4
20 10 54.38	-56 29 54.3	17.39	0.0568	0.0568	0	1
20 10 54.66	-56 23 28.4	16.07	0.0503	0.0502	0.0001	1
20 10 57.64	-56 38 38.4	16.71	0.0591	0.0587	0.0004	4
20 10 58.91	-56 39 54.5	16.75	0.0601	0.0611	0.001	4
20 11 0.43	-56 45 55.5	15.64	0.0594	0.0596	0.0002	1
20 11 6.77	-56 23 23.0	16.39	0.0578	0.0589	0.0011	4
20 11 14.06	-56 57 23.5	17.39	0.0620	0.0632	0.0012	4
20 11 17.20	-56 56 18.1	16.37	0.0608	0.0609	0.0001	4

continued on next page

continued from previous page

RA_{J2000}	Dec_{J2000}	Mag	z_{2Df}	z_{lit}	δ_z	Q
20 11 27.50	-56 44 7.0	16.14	0.0549	0.0552	0.0003	4
20 11 34.74	-56 44 38.2	17.55	0.0465	0.0465	0	4
20 11 36.15	-56 55 29.8	16.33	0.0622	0.0620	0.0002	1
20 11 36.27	-56 28 56.2	16.92	0.0561	0.0567	0.0006	4
20 11 37.82	-56 20 39.6	16.96	0.0556	0.0560	0.0004	1
20 11 38.04	-57 2 58.0	16.97	0.0511	0.0508	0.0003	4
20 11 42.86	-57 3 28.5	16.94	0.0552	0.0547	0.0005	4
20 11 50.63	-57 0 27.4	17.17	0.0541	0.0544	0.0003	4
20 11 58.60	-56 30 47.7	16.40	0.0509	0.0504	0.0005	4
20 12 0.79	-57 1 20.5	16.57	0.0503	0.0602	0.0099	4
20 12 3.53	-56 13 22.0	16.52	0.0511	0.0507	0.0004	4
20 12 4.22	-56 39 38.4	17.75	0.0595	0.0595	0	4
20 12 11.60	-56 51 1.2	17.57	0.0506	0.0508	0.0002	4
20 12 16.52	-56 58 2.9	16.90	0.0551	0.0578	0.0027	1
20 12 21.24	-56 15 29.6	17.56	0.0517	0.0514	0.0003	4
20 12 32.59	-56 31 37.9	17.24	0.0549	0.0542	0.0007	4
20 12 32.99	-56 30 50.7	16.77	0.0578	0.0581	0.0003	4
20 12 38.65	-57 12 4.2	16.78	0.0585	0.0587	0.0002	4
20 12 40.95	-56 29 0.2	17.73	0.0555	0.0558	0.0003	4
20 12 46.03	-57 18 12.2	16.84	0.0566	0.0564	0.0002	4
20 12 58.79	-56 59 11.4	16.64	0.0533	0.0534	0.0001	4
20 13 5.50	-57 10 43.5	17.28	0.0577	0.0574	0.0003	4
20 13 27.61	-57 7 17.9	16.73	0.0532	0.0533	0.0001	4
20 13 30.96	-56 57 48.8	17.23	0.0540	0.0532	0.0008	4
20 13 31.55	-56 53 39.2	16.97	0.0466	0.0465	0.0001	4
20 13 44.76	-57 21 0.1	16.99	0.0565	0.0567	0.0002	4
20 13 52.67	-56 32 47.0	16.68	0.0607	0.0608	0.0001	4
20 13 58.67	-57 2 22.6	15.50	0.0523	0.0524	0.0001	4
20 13 59.05	-56 57 42.0	16.20	0.0601	0.0442	0.0159	4
20 14 5.80	-57 0 28.0	17.10	0.0515	0.0516	0.0001	4
20 14 6.30	-57 7 28.7	17.35	0.0586	0.0517	0.0069	1
20 14 10.50	-56 57 49.8	17.39	0.0536	0.0538	0.0002	4
20 14 13.40	-57 19 2.9	17.18	0.0564	0.0561	0.0003	4
20 14 17.45	-57 8 25.0	17.85	0.0527	0.0547	0.0020	4
20 14 34.07	-57 16 24.7	17.32	0.0554	0.0555	0.0001	4
20 14 56.07	-56 45 22.0	16.54	0.0536	0.0530	0.0006	4
20 15 9.28	-57 10 31.6	16.40	0.0568	0.0570	0.0002	4
20 15 34.69	-57 18 38.7	17.41	0.0526	0.0555	0.0029	4
20 15 42.55	-57 15 59.9	17.40	0.0556	0.0558	0.0002	4
20 15 47.00	-57 19 56.1	16.71	0.0563	0.0563	0	1

continued on next page

continued from previous page						
RA_{J2000}	Dec_{J2000}	Mag	z_{2Df}	z_{lit}	δ_z	Q
20 16 3.58	-57 3 39.1	17.37	0.0559	0.0566	0.0007	4
20 16 22.69	-56 51 45.5	16.71	0.0543	0.0539	0.0004	4
20 16 48.39	-57 11 41.2	15.87	0.0557	0.0557	0	4
20 16 59.45	-57 14 45.0	17.39	0.0572	0.0574	0.0002	4

C.2 Cross-correlation

The standard technique to determine redshifts is via cross-correlation between the spectra in question and a template spectra of the same spectral type but at zero redshift (Tonry & Davis 1979). In this case, if g(z) is the function that describes the spectrum of the object at unknown redshift and t(z) is the function describing the template spectra of the same type as the object under investigation, then the cross-correlation function, c(z) is defined, such that:

$$c(z) = g(z) * t(z) \propto \sum_i g(i)t(i-z). \tag{C.1}$$

Here, the amount that the object function, g(z), is displaced from the template function, t(z), is the redshift. If the object function and template function are identical, aside from this displacement, the cross-correlation code will produce a delta function at the redshift value. However, should the object function differ from the template function slightly, a Gaussian peak will be produced centred on the displacement or redshift value will be produced. The size and shape of such a Gaussian will provide information on how closely the object and template spectra match. This gives a quantifiable measure of the error in such a technique.

Bibliography

Abell, G. O., 1958, ApJS, 3, 211

Abell, G. O., Corwin, H. G., Olowin, R. P., 1989, ApJS, 70, 1

Allen, S.W., 1999, in *Diffuse Thermal and Relativistic Plasma in Galaxy Clusters*, Proceedings of the Ringberg workshop held, April 1999, Ringberg Castle, Germany. Eds Böhringer, H., Feretti, L., & Schuecker, P., p129

Ashman, K. A., Bird, C. M., & Zepf, S. E., 1994, AJ, 108, 2348

Athreya, R. M., Kapahi, V. K., McCarthy, P. J., & van Breugel, W., 1997, A&A, 329,809

The Australia Telescope Compact Array Users' Guide, CSIRO ATNF, October 1999 *http://www.narrabri.atnf.csiro.au/observing/users_guide/html/atug.html*

Bailey, J., Glazebrook, K., & Bridges, T., 2002 2dF Users Manual version 2.0

R. M. Baltrusaitis et al, 1985, Nucl. Instr. and Meth. in Phys. Res. A, A240 410.

Bartholomew, L. J., Rose, J. A., Gaba, A. E., Caldwell, N., 2001, AJ, 122m 2913

Beck, R., Berkhuijsen, E. M., & Wielebinski, R., 1978, A&A, 68, L27

Beck, R., Berkhuijsen, E. M., & Wielebinski, R., 1980, Nature, 283, 272

Beck, R., 1982, A&A, 106, 121

Beck, R., 1983, in Internal kinematics and dynamics of galaxies; Dordrecht, D. Reidel Publishing Co., 1983, p. 159, 160.

Beck, R., & Reich, W., 1985, in *The Milky Way Galaxy; Proceedings of the 106th Symposium, Groningen, Netherlands, May 30-June 3, 1983 (A85-46176 22-90)*. Dordrecht, D. Reidel Publishing Co., 1985, p. 239-244.

Beck, R., Krause, M., Klein, U., A&A, 152, 237

Beck, R., 1986, IEEE Transactions on Plasma Science, 14, 740

Beck, R., Wielebinski, R., & Klein, U., 1987, A&A, 186, 95

Beck, R., Loiseau, N., Hummel, E., Berkhuijsen, E. M., Grave, R., & Wielebinski, R., 1989, A&A, 222, 58

Beck, R., Buczilowski, U. R., & Harnett, J. I., 1990, In Galactic and intergalactic magnetic fields; Proceedings of the 140th Symposium of IAU, Dordrecht, Netherlands, Kluwer Academic Publishers, 1990, p. 213, 214.

Beck, R., 1991, in *The interpretation of modern synthesis observations of spiral galaxies; Proceedings of the Workshop, Albuquerque, NM, Mar. 12-15, 1990*, Astronomical Society of the Pacific, 1991, p. 43-56.

Beck, R., 1991, A&A, 251, 15

Beck, R., Carilli, C. L., Holdaway, M. A., & Klein, U., 1994, A&A, 292, 409

Beck, R., Brandenburg, A., Moss, D., Shukurov, A., & Sokoloff, D., 1996, Annu. Rev. Astron. Astrophys. 34, 155

Belloni, P., Bruzual, A. G., Thimm, G. J., & Röser, H.-J., A&A, 1995, 297, 61

Berkhuijsen, E. M., & Brouw, W. N., 1963, Bulletin of the Astronomical Institute of the Netherlands, 17, 185

Berkhuijsen, E. M., Brouw, W. N., Muller, C. A., & Tinbergen, J., 1964, Bulletin of the Astronomical Institute of the Netherlands, 17, 465

Bingham, R. G., McMullan, D., Pallister, W. S., White, C., Axon, D. J., & Scarrott, S. M., 1976, Nature, 259, 463

Blandford, R. D., & Ostriker, J. P., 1978, ApJL, 221, 29

Bliton, M., Rizza, E., Burns, J. 0., Owen, F. N., & Ledlow, M. J., 1998, MNRAS, 301, 609

Brown, J. C, & Taylor, A. R., 2001, ApJ, 563, L31

Bolton, J. G., & Wild, J. P., 1957, ApJ, 125, 296

M. Boratav, 2001, in *Proc. Int. Work. Extremely High Energy Cosmic Rays - Experiments, Theory and Future Directions -, March 22 - 23, 2001, ICRR, Tokyo, Japan*, Journ. of the Phys. Soc. of Japan, Suppl. B, 70

Bowyer, S., & Bergh"ofer, T. W., 1998, ApJ, 506, 502

Bozyan, E. P., ApJL, 152, 155

Bridle, A. H., & Fomalont, E. B., 1976, A&A, 52, 107

Broten, N. W., MacLeod, J. M., & Vallee, J. P., 1988, Ap&SS, 141, 303

Buczilowski, U. R.; Beck, R., 1991, A&A, 241, 47

Burbidge, G. R., 1958, ApJ, 128, 1

Burkard, O., Journal of Geophysical Research, 1961, 66, 3058

Burgess, A. M., & Hunstead, R. W., 1995, PASA, 12, 227

Burn, B. J.,

Chyzy, K. T., Beck, R., Kohle, S., Klein, U., Urbanik, M., 2000, A&A, 355, 128

Clark, B. G. 1999, in *Synthesis Imaging in Radio Astronomy II*, ed. Taylor, G.B, Carilli, C.L., & Perley, R.A., ASP Conf Ser., 80, 1

Clarke, T. E. 2000, *Probing Magnetic Fields in Clusters of Galaxies*, (Ph.D. Thesis, University of Toronto)

Clegg, A. W., Cordes, J. M., Simonetti, J. H., & Kulkami, S. R., 1992, ApJ, 386, 143

Colless, M. M., 1998, in *Looking Deep in the Southern Sky* eds, Morganti, R., & Couch, W. J., Springer Verlag, Berlin p9.

Colless, M., Dalton, G., Maddox, S., Sutherland, W., Norberg, P., Cole, S., Bland-Hawthorn, J., Bridges, T., Cannon, R., Collins, C., Couch, W., Cross, N., Deeley, K., De Propris, R., Driver, S. P., Efstathiou, G., Ellis, R. S., Frenk, C. S., Glazebrook, K., Jackson, C., Lahav, O., Lewis, I., Lumsden, S., Madgwick, D., Peacock, J. A., Peterson, B. A., Price, I., Seaborne, M., & Taylor, K., 2001, MNRAS, 328, 1039

Conway, R. G., & Kronberg, P.P., 1969, MNRAS, 142, 11

Cooper, B. F. C., & Price, R. M., 1962, Nature, 195, 1084

Cordey, R. A., 1985, MNRAS, 215, 437

Cornwell, T. J., 1988, A&A, 202, 316

Cornwell, T., & Braun, R., 1989, in *Synthesis Imaging in Radio Astronomy*, ed. Perley, R. A., Schwab, F. R., & Bridle, A.H., ASP Conf Ser., 6, 167

Couch, W. J., Sharples, R. M., 1987, MNRAS, 229, 423

Crutcher, R. M., & Kazes, I., 1983, A&A, 125, 23

Danziger, I. J, & Goss, W. M., 1983, MNRAS, 202, 703

Davies, R. D., 1964, in *The Galaxy and the Magellanic Clouds*, IAU Symposium no. 20. Ed Kerr, F. J.

Deeley, K., cited in Colless, M. M., 2000, PASA, 17, 215

Dennison, B., 1979, AJ, 84, 725

Dennison, B., 1980, ApJ, 239, 93

Donivan, F. F., Carr, T. D., & Omer, G. C., 1974, ApJ, 187, 11

Dressler, A., & Shectman, S. A., 1988, AJ, 95, 284

Durret, F., Slezak, E., Lieu, R., Dos Santos, S., & Bonamente, M., 2002, A&A, 390, 397

Ebeling, H., Voges, W., Bohringer, H., Edge, A. C., Huchra, J. P., Briel, U.G., 1996, MNRAS, 281, 799

Ekers, R. D. , 1969, Aust. Journal. Phys. Supp. 6, 3

Ekers, R. D., & Rots A. H. 1979, in *Image Formation from Coherence Functions in Astronomy*, IAU Colloquim 49, ed. C. van Schooneveld & C. D. Reidel, p61

Ehle, M., Beck, R., Haynes, R. F., Vogler, A., Pietsch, W., Elmouttie, M., & Ryder, S., 1996, A&A, 306, 73

Elvius, A, 1978, in *Structure and Properties of Nearby Galaxies*; IAU Symposium no. 77, p65, Ed. Berkhuijsen, E.M., and Wielebinski, R., (Dordrecht, D. Reidel Publishing Co)

English, J., Taylor, A. R., Irwin, J. A., Dougherty, S. M., Basu, S., Beichman, C., Brown, J., Cao, Y., Carignan, C., Crabtree, D., Dewdney, P., Duric, N., Fich, M., Gagnon, E., Galt, J., Germain, S., Ghazzali, N., Gibson, S. J., Godbout, S., Gray, A., Green, D. A., Heiles, C., Heyer, M., Higgs, L., Jean, S., Johnstone, D., Joncas, G., Landecker, T., Langer, W., Leahy, D., Martin, P., Matthews, H., McCutcheon, W., Moriarity-Scheiven, G., Pineault, S., Purton, C., Roger, R., Routledge, D., St-Louis, N., Tapping, K., Terebey, S., Vaneldik, F., Watson, D., Willis, T., Wendker, H., Zhang, X., 1998, PASA, 15, 56

Enßlin, T. A., Biermann, P. L., Kronberg, P. P., Wu, X. P., 1997, ApJ, 477, 560

Enßlin, T. A., Biermann, P. L., Klein, U., & Kohle, S., 1998, A&A, 332, 395

Enßlin, T. A, 1999, in *Diffuse thermal and relativistic plasma in galaxy clusters* Proceedings of the Ringberg Workshop, held April 1999, Ringburg Castle, Germany. Eds Böhringer, H., Feretti, L., & Schuecker, P., p275

Fabian, A. C., Nulsen, P. E. J., Stewart, G. C., Ku, W. H.-M., Malin, D. F., Mushotzky, R. F., 1981, MNRAS, 196, 35

Fairall, A. P., 1981, MNRAS, 196, 417

Felten, J. E., Gould, R. J., Stein, W. A., & Woolf, N. J., 1966, ApJ, 146, 955

Felten, J. E, & Morrison, P., 1966, ApJ, 146, 686

Feretti, L., & Giovannini, G., 1996, in *Extragalactic radio sources: proceedings of the 175th Symposium of the International Astronomical Union, held in Bologna, Italy, 10-14 October 1995*, Edited by Ron D. Ekers, C. Fanti, and L. Padrielli. Published by Kluwer Academic Publishers, p. 333.

Feretti, L., Dallacasa, D., Govoni, F., Giovannini, G., Taylor, G. B., & Klein, U., 1999, A&A, 344, 472

Forman, W., Kellogg, E., Gursky, H., Tananbaum, H., & Giacconi, R., 1972, ApJ, 178, 309

Frater, R. H., & Brooks, J. W. 1992, Special issue of J. Electr. Electron. Eng. Australia, Vol. 12, No. 2

Frick, P., Stepanov, R., Shukurov, A., & Sokoloff, D., 2001, MNRAS, 325, 649

Friedman, H., & Byram, E. T., 1967, ApJ, 147, 399

Galt, J. A., Slater, C. H., & Shuter, W. L. H., MNRAS, 120, 187

Gaensler, B. M., Manchester, R. N., & Green, A. J., 1998, MNRAS, 296, 813

Gaensler, B. M., Dickey, John M., McClure-Griffiths, N. M., Green, A. J., Wieringa, M. H., & Haynes, R. F., 2001, ApJ, 549, 959

Gavazzi, G., 1978, A&A, 69, 355

Gavazzi, G., 1979, A&A, 72, 1

Girardi, M., Fadda, D., Giuricin, F., Mardirossian, Mezzetti, M., & Biviano, A., 1996, ApJ, 457, 61

Girardi, A., Giuricin, G., Mardirossian, F., Mezzetti, M., & Boschin, W., 1998, ApJ, 505, 74

Goldshmidt, O., & Rephaeli, Y., 1993, ApJ, 411, 518

Giovannini, G., Feretti, L., & Andernach, H., 1985, A&A, 150, 302

Giovannini, G., & Feretti, L., 2000, in *Cluster Mergers and their Connection to Radio Sources*, proceedings of Joint Discussion 10 of the XXIVth IAU General Assembly, held August 14 2000, Manchester, UK. Ed Feretti, L., p15.

Gorenstein, P., Bjorkholm, P., Harris, B., & Harnden, F. R., 1973, ApJL, 183, 57

Govoni, F., Taylor, G. B., Dallacasa, D., Feretti, L., & Giovannini, G., 2001, 379, 807

Goss, W. M., Ekers, R. D., Skellern, D. J., & Smith, R. M., 1982, MNRAS, 198, 259

Gräve, R., & Beck, R., 1987, in *Interstellar magnetic fields: Observation and theory; Proceedings of the Workshop, Tegernsee, Federal Republic of Germany, Sept. 8-12, 1986* Springer-Verlag, 1987, p47

Gursky, H., Kellogg, E., Murray, S., Leong, C., Tananbaum, H., & Giacconi, R., 1971, ApJ, 167, L81

Gursky, H., Solinger, A., Kellogg, E. M., Murray, S., Tananbaum, H., Giacconi, R., Cavaliere, A, 1972, ApJ, 173, L99

Haigh, A. J., Roberston, J. G., & Hunstead, R. W., 1997, PASA, 14, 221

Han, J.-L., & Qiao, G. J., 1994, A&A, 288, 759

Han, J.-L., Manchester, R. N., Berkhuijsen, E. M., & Beck, R., 1997, A&A, 322, 98

Han, J.-L., Manchester, R. N., & Qiao, G. J., 1999, MNRAS, 306, 371

Han, J.-L., Beck, R., Ehle, M., Haynes, R. F., & Wielebinski, R., 1999,A&A, 348, 405

Hanisch, R. J., Matthews, T. A., & Davis, M. M., 1979, AJ, 84, 946

Hanisch, R. J., 1980, AJ, 85, 1565

Hanisch, R. J., 1982, A&A, 116, 137

Hanisch, R. J., Storm, R. G., & Jaffe, W. J., 1985, A&A, 153, 9

Harris, D. E., & Romanishin, W., 1974, ApJ, 188, 209

Harris, D. E., & Miley, G. K., 1978, A&AS, 34, 117

Harris, D. E., Kapahi, V. K., & Ekers, R. D., 1980, A&AS, 39, 215

Harris, D. E., Stern, C. P., Willis, A. G., & Dewdney, P. E., 1993, AJ, 105, 769

Haverkorn, M., Katgert, P., & de Bruyn, G., A&A, 356, L13

Heeschen, D. S., 1973, ApJ, 179, L93

Heiles, C.,& Stevens, M., 1986, ApJ, 301, 331

Hennessy, G. S., Owen, F. N., & Eilek, J. A., 1989, ApJ, 347,144

Hewitt, A., & Burbidge, G., 1991, ApJS, 75, 297

Høg, E., Fabricius, C., Makarov, V. V., Bastian, U., Schwekendiek, P., Wicenec, A., Urban, S., Corbin, T., Wycoff, G., 2002, A&A, 357, 367

Horellou, C., Beck, R., & Klein, U., 1990 in *Galactic and intergalactic magnetic fields; Proceedings of the 140th Symposium of IAU, Dordrecht, Netherlands*, Kluwer Academic Publishers, p. 211,

Horellou, C., Beck, R., Berkhuijsen, E. M., Krause, M., & Klein, U., 1992, A&A, 265, 417.

Inoue, H., Koyama, K., & Tanaka, Y. 1983, in *Supernova Remnants and their X-ray Emission, IAU Symposium No. 101*, ed. J. Danziger & P. Gorenstein (Dordrecht: Reidel), 535

Jaffe, W. J., Valentijn, E. A., & Perola, G. C., 1976, A&A, 49, 179

Jaffe, W.J., 1977, ApJ, 212, 1

Jaffe, W., 1980, ApJ, 241, 925

Jones, P. A., & McAdam, W. B., 1992, ApJS, 80, 137

Katgert, V., Mazure, A., den Harthog, R., Adami, C., Biviano, A., & Perea, J., 1998, A&AS, 129, 399

Kellogg, E., Gursky, H., Leong, C., Schreier, E., Tananbaum, H., & Giacconi, R., 1971, ApJ, 165, L49

Killeen, N. E. B., 1993, *Analysis of Australia Telescope Compact Array Data with AIPS, 4th ed.*, (Australia Telescope National Facility)

Killeen, N. E. B., Flukes, C. J., Zhao, J.-H., & Ekers, R. D., MNRAS, (in preparation)

Kim, K.-T., 1988, (Ph.D. Thesis, University of Toronto)

Kim, K.-T., Kronberg, P. P., Dewdney, P. E., & Landecker, T.L., 1990, ApJ, 355, 29

Kim, K.-T., Tribble, P. C., & Kronberg, P. P., 1991, ApJ, 379, 80

Klein, U., Urbanik, M., Beck, R., & Wielebinski, R., A&A, 127, 177

Knopp, G. P., Henry, J. P., & Briel, U. G., 1996, ApJ, 472, 125

Krause, M., Klein, U.& Beck, R., A&A, 138, 385

Kreyzig, E., 1994, *Advanced Engineering Mathematics*, 6^{th} Edition. Wiley & Son, New York.

Kronberg, P. P., & Simard-Normandin, M., 1976, Nature, 263, 653

Large, M. I., Mills, B. Y., Little, A. G., Crawford,D. F., & Sutton, J. M., 1981, MNRAS 194, 693

Lawler, J. M., & Dennison, B., 1982, ApJ, 252, 81

Lewis, I. J., Cannon, R. D., Taylor, K., Glazebrook, K., Bailey, J. A., Baldry, I. K., Barton, J. R., Bridges, T. J., Dalton, G. B., Farrell, T. J., Gray, P. M., Lankshear, A., McCowage, C., Parry, I. R., Sharples, R. M., Shortridge, K., Smith, G. A., Stevenson, J., Straede,J. O., Waller, L. G., Whittard, J. D., Wilcox, J. K., & Willis, K. C., 2002, MNRAS, 333, 279

Liang, H., Hunstead, R. W., Birkinshaw, M., Andreani, P., 2000, ApJ, 544, 686

Loiseau, N., Hummel, E., Beck, R., & Wielebinski, R., 1987, in *Interstellar magnetic fields: Observation and theory; Proceedings of the Workshop, Tegernsee, Federal Republic of Germany, Sept. 8-12, 1986 (A88-35776 14-90)*. Springer-Verlag, 1987, p42

Longair, M., 1981, *High energy astrophysics: an informal introduction for students of physics and astronomy*, 1st Edition, Cambridge University Press

Longair, M., 1997, *High energy astrophysics: an informal introduction for students of physics and astronomy*, 3rd Edition, Volume 2, Cambridge University Press

Lyne, A. G., & Smith, F. G., 1989, MNRAS, 237, 533

MacLeod, J. M., Vallee, J. P., & Broten, N. W., 1988, A&ASS, 74, 63

Malina, R. F., Bowyer, C. S., Lea, S. M., & Lampton, M., 1978 ApJ, 219, 795

Manchester, R. N., Han, J.-L., & Qiao, G. J., 1998, MNRAS, 295, 280

Markevitch, M., Sarazin, C. L., Vikhlinin, A., 1999, ApJ, 521, 526

McClure-Griffith, N. M., Green, A. J., Dickey, J. M., Gaensler, B. M., Haynes, R. F., & Wieringa, M. H., 2001, ApJ, 551, 394

Melnick, J., & Quintana, H., 1981, AJ, 86, 1567

Meyer, W.F., 1919, *A Study of Certain Nebulae for Evidences of Polarization Effects* (Ph.D. Thesis, University of California, Berkeley)

Miley, G. K., Perola, G. C., van der Kruit, P. C., & van der Laan, H., 1972, Nature, 237, 269

Mills, B. Y., Slee, O. B., & Hill, E. R., 1961, Aust. J. Phys., 14. 497

Morris, D., Radhakrishnan, V., & Seielstad, G. A., 1964, ApJ, 139,551

Neininger, N., Klein, U., Beck, R., & Wielebinski, R., 1991, Nature, 352, 781.

Neininger, N., Beck, R., Sukumar, S., & Allen, R. J., 1993, A&A, 274, 68

Norris, R. P., Kesteven, M. J.,& Calabretta, M. R., 1992, J. Electr. Electron. Eng. Australia, 12, 205

Öhman, Y., 1942, PASP, 54, 720

Piddington, J. H., 1964, MNRAS, 128, 345

Plante, R. L., Lo, K. Y., Crutcher, R. M.,& Killeen, N. E. B., 1994, in *The Nuclei of Normal Galaxies: Lessons from the Galactic Center, Proceedings of the NATO Advanced Research Workshop*, (Dordrecht: Kluwer Academic Publishers), Ed Genzel, R. and Harris, A. I., NATO Advanced Science Institutes (ASI) Series C, 445, 205

Proust, D., Mazure, A., Sodre, L., Capelato. H., & Lund, G., 1988, A&AS, 72, 415

Rand, R. J., & Lyne, A. G., 1994, MNRAS, 268, 497

Rayner, D. 2000, *Circular Polarisation in AGN*, (Ph.D. Thesis, University of Tasmania)

Reid, A. D., Hunstead, R. W., Lemonon, L., & Pierre, M. M., 1999, MNRAS, 302, 571

Rephaeli, Y., 1979, ApJ, 227, 364

Reynolds, J. E. 1994, A Revised Flux Scale for the AT Compact Array, (ATNF Internal Report AT/39.3/040)

Ricker, P. M., & Sarazi, C. L., ApJ, 561, 621

Roettiger, K., Burns, K. O., & Stone, J. M., 1999, ApJ, 518, 603

Roland, J., 1981, A&A, 93, 407

Rose, J. A., Gaba, A. E., Christiansen, W. A., Davis, D. S., Caldwell, N., Hunstead, R. W., Johnston-Hollitt, M., 2002, AJ, 123, 1216-1246

Röttgering, H. J. A., Wieringa, M. H., Hunstead, R. W., & Ekers, R. D., 1997, MNRAS, 290, 577

Rudnick, L., & Jones, T. W., 1983, Astron. J., 88, 518

Ruzmaikin, A. A, & Sokoloff, D. D, 1979, A&A, 78, 1

Rybicki, G. B., & Lightman, A. P., 1979 *Radiative processes in astrophysics*, Wiley-Interscience, New York

Ryle, M., & Windram, M. D., MNRAS, 138, 1

Sarazin, C. L., & Lieu, R., 1998, ApJ, 494, L177

Sarazin, C. L., 1999, ApJ, 520, 529

Sastry, Ch. V., & Shevgaonka R. K., 1983, JÀstrophysÀstr; 4, 47

Sault, R. J., & Wieringa, M. H., 1994, A&AS, 108,585

Sault, R. J., Teuben, P. J., & Wright, M. C. H. 1995, ADASS IV, ed. Shaw, R., Payne, H.E., & Hayes, J. J. E., ASP Conf Ser., 77, 433

Sault, R. J., Staveley-Smith, L., & Brouw, W. N., 1996, A&AS, 120, 375

Sault, R. J., & Killeen, N. E. B., 1998, (CSIRO)

Scarrott, S. M., White, C., Pallister, W. S., & Solinger, A. B., 1977, Nature, 265, 32

Schilizzi, R. T., & McAdam, E. B., 1975, MNRAS, 79, 1

Schlickeiser, R, Sievers, A., & H., Thiemann, 1987, A&A, 182, 21

Schuecker, P., & Böhringer, H., 1999, in *Diffuse Thermal and Relativistic Plasma in Galaxy Clusters*, Proceedings of the Ringberg workshop held, April 1999, Ringberg Castle, Germany. Eds Böhringer, H., Feretti, L., & Schuecker, P., p43

Schwarz, U. J., & Lasenby, J., 1990, in *Galactic and Intergalactic Magnetic Fields. IAU Symposium No. 140*, ed. R. Beck, P.P. Kronberg, & R. Wielebinski (Kluwer Academic Publishers: Dordrecht, The Netherlands)

Serlemitsos, P. J., Smith, B. W., Boldt, E. A., Holt, S. S., & Swank, J. H., 1977, ApJ, 211, L63

Shapley, H., & Ames, A., 1932, Annals of Harvard College Observatory, Cambridge, Mass. : Astronomical Observatory of Harvard College

Simard-Normandin, M., Kronberg, P. P., & Button, S., 1981, ApJS, 45, 97

Slee, O. B., Roy, A. L., Murgia, M., Andernach, H.,& Ehle, M., 2001, AJ, 122, 1172

Snow, T. P., 1991, *The Dynamical Universe*, West Publishing

Sodre, L., Capelato, H. V., Steiner, J. E., Proust, D., & Mazure, A., 1992, MNRAS, 259, 233

Sofue, Y., Klein, U., Beck, R., & Wielebinski, R., 1986, Ap&SS, 119, 191

Sofue, Y., & Beck, R., 1987, PASJ, 39, 541

Sokoloff, D. D., Bykov, A. A., Shukurov, A., Berkhuijsen, E. M., Beck, R., & Poezd, A. D., 1998, MNRAS,299,189

Staveley-Smith, L., Sault, R. J., Hatzidimitriou, D., Kesteven, M. J., & McConnell, D., 1997, MNRAS, 289, 225

Stokes, G., Trans. Camb. Phil. Soc., 9, 399

Tabara, H., & Inoue, M., 1980, A&AS, 39, 379

Taylor, J. H., & Cordes, J. M., 1993, ApJ, 411, 674

Taylor, G. B, Barton, E. J., & Ge, J.-P., 1994, Astron. J., 107, 1942

Thompson, A. R., Moran J. M., & Swenson, G. W., 1986, *Interferometry and Synthesis in Radio Astronomy*, John Wiley & Sons

Tonry, J., & Davis, M., 1979, AJ, 84, 1511

Tribble, P. C., 1991, MNRAS, 250, 726

Tribble, P. C., 1993, MNRAS, 263, 31

Vallée, J. P., MacLeod, J. M., & Broten, N. W., 1986, A&A, 156, 386

Vallée, J. P., 1990, ApJ, 360, 1

Vallée, J. P., 1991, ApJ, 366, 450

Vallée, J. P., 1996, A&A, 308, 433

Vallée, J. P., 1997, Fund. Cos. Phys. 19, 1

Véron-Cetty, M.-P., Véron, 1986, A&AS, 65, 241

Vidal, N. V., 1975, PASA, 2 327

Vikhlinin, A., Markevitch, M., & Murray, S. S., ApJ, 551, 160

Vinokur, M., 1965, Annales d'Astrophysique, 28, 412

Wardle, J. F. C., & Kronberg, P. P., 1974, ApJ, 194, 249

Weinreb, S., 1962, ApJ, 136, 1149

Welter, G. L., Perry, J. J., & Kronberg, P. P., 1984, ApJ, 279, 19

Westerhout, G., Brouw, W. N., Muller, C. A., & Tinbergen, J., 1962, AJ, 67, 590

Wielebinski, R., Shakeshaft, J. R., & Pauliny-Toth, I. I. K., 1962, The Observatory, 82, 158

Wielebinski, R., & Shakeshaft, F. R., 1962, MNRAS, 128, 19

Wilson, M. A. G., 1970, MNRAS, 151, 1

Zeeman, P., 1897, ApJ, 5, 333

Zwicky, F., Herzog, E., & Wild, P., 1968, *Catalogue of galaxies and of clusters of galaxies*, Pasadena: California Institute of Technology (CIT)